Magnetic Resonance Imaging of Spin-Polarized ^{3}He and ^{129}Xe

Sina Tafti
B.A. Physics, Kalamazoo College, Kalamazoo, MI 2013

A Dissertation presented to the Graduate Faculty
of the University of Virginia in Candidacy for the degree of
Doctor of Philosophy

Department of Physics
University of Virginia
September 2020

Professor G. Wilson Miller
Research Advisor

Professor Gordon Cates

Professor Xiaochao Zheng

Professor John Mugler

Abstract

This thesis describes two applications of magnetic resonance imaging (MRI) of spin-polarized (i.e. hyperpolarized) noble gases. One application is to explore the feasibility of using inertial confinement fusion (ICF) polymer shells to load and seal in spin-polarized ^{3}He suitable for cryogenic injection into the plasma core of a tokamak fusion reactor. This feasibility study is a step towards the first proof-of-principle *in-situ* test of polarization survival, inside the DIII-D tokamak. The other application is in lung imaging of human subjects with chronic obstructive pulmonary disease (COPD). In this research study, we use apparent diffusion coefficient (ADC) measurements obtained from diffusion-weighted MRI of inhaled hyperpolarized ^{3}He and ^{129}Xe to characterize emphysema, a smoking-induced chronic disease responsible for destruction of lung parenchymal tissue.

The main objectives of the feasibility study of ICF polymer shells in loading of spin-polarized ^{3}He were to determine (1) the polarization loss inherent to permeation through the shell wall, (2) the absolute polarization of the gas that has been loaded into the pellet, and (3) how fast the polarization decays after it has been loaded. For these measurements, we used nuclear magnetic resonance (NMR) and MRI techniques to measure the signal generated by the polarized helium gas during and after the permeation process, using a 1.5-Tesla clinical MRI scanner.

We developed a mathematical model that describes the polarization density of the helium gas inside and outside the pellet as a function of time. We then determined the measured signal evolution to our model. We report $81\% \pm 2$ and $62\% \pm 2$ polarization retention in the permeation process for shells with wall thickness of 15 μm and 26 μm, respectively. To determine the absolute polarization of the helium sealed inside the polymer shell, we calibrated the MRI signal obtained from hyperpolarized ^{3}He to the signal obtained from thermally polarized ^{3}He inside the precisely known field strength of a clinical 1.5-Tesla scanner. We measured the absolute polarization of

the permeated ^{3}He sealed inside a 15-μm shell to be 22.1% $\pm$ 1.1 , with starting polarization of $\sim$48%, prior to the permeation process. The T_1 of the polarized helium inside the shell at 77 K is 83 hours $\pm$ 10.

In the diffusion-weighted lung MRI project, we introduced and tested a quantitative framework within which to characterize emphysema burden based on hyperpolarized ^{3}He and ^{129}Xe ADC maps and compared its diagnostic performance with CT-based emphysema metrics and pulmonary function tests. Twenty-seven patients with mild, moderate, or severe COPD and 13 age-matched healthy control subjects participated in this study. Participants underwent CT and multiple b-value diffusion-weighted ^{3}He and ^{129}Xe MRI examinations and standard pulmonary function tests. ADC-based emphysema index was computed separately for each gas and b-value as the fraction of lung voxels with ADC values greater than in the healthy group 99^{th} percentile. The resulting values were compared with quantitative CT results (relative lung area , < -950 HU) as the reference standard.

We found that emphysema indices based on ^{3}He and ^{129}Xe ADC were strongly correlated ($r = 0.95$, $P < .001$) and both showed strong correlation with relative lung area with low attenuation (RA) on CT images ($r \geq 0.85$, $P < .001$). The ^{3}He-based and ^{129}Xe-based ADC emphysema indices were also highly repeatable (intraclass correlation coefficient > 0.99) and showed highly significant differences between healthy, mild-moderate, and severe COPD groups, independent of the b-values used ($P < .01$). Both ^{3}He-based and ^{129}Xe-based ADC emphysema indices were also correlated with pulmonary function metrics used to characterize emphysema, including diffusing capacity of lung for carbon monoxide ($r \geq 0.80$, $P < .001$) and residual lung volume divided by total lung capacity ($r \geq 0.61$, $P < .002$), with a degree of correlation similar to that of quantitative CT ($r \geq 0.57$, $P < .001$). We conclude that emphysema index based on hyperpolarized ^{3}He or ^{129}Xe diffusion MRI provides a robust and highly repeatable measure of emphysema burden that may offer higher sensitivity to early stage lung disease than quantitative CT or standard pulmonary function metrics.

Acknowledgments

First and foremost, I would like to thank my advisor, Wilson Miller, for his incomprehensible support throughout my graduate career in his lab. It was truly an honor and a privilege to have worked for and been trained by such a patient, caring, enthusiastic, humble, and humorous teacher and researcher. Four years ago when I joined his lab, I had no idea why such strong magnetic fields are needed for *magnetic* resonance imaging (MRI), and frankly, couldn't care less about MR physics and MRI research. It was Wilson's genuine enthusiasm and curiosity for the world of MR that got me interested not only in the field of MR, but also in scientific research and the systematic approach to understanding and tackling a problem. I am genuinely excited for his current and future graduate students. If you are a new/current student in his lab, hang on to your hat, it's going to be an incredible journey!

It is through Wilson that I learned how to ask the right and relevant questions in designing an experiment and analyzing MR data. Wilson challenged me to be a much better writer and provided me with the resources to independently design an experiment, acquire and analyze data, and draw conclusions based on the results of the analysis. I am forever indebted for him for taking a chance on me. Without his mentorship, I do not think that I would have succeeded, nor would have enjoyed graduate school at the University of Virginia.

I would also like to thank my thesis committee members, Drs. Gordon Cates, John Mugler, and Xiaochao Zheng, for their support and invaluable guidance in my thesis projects. John's help in preparing the manuscript on ADC-based emphysema index based on diffusion-weighted MRI of inhaled hyperpolarized ^{3}He and ^{129}Xe was a tremendous asset and improved the quality of our paper considerably. Xiaochao's guidance and suggestions for the spin-polarized fusion project made me a better researcher and helped me sharpen my analysis skills. Gordon's probing questions in research meetings strengthened my critical thinking. I am privileged to have had such

amazing mentors.

There are a number of other researchers, faculty members, and graduate students to whom I am indebted for their support. Drs. Andy Sandorfi and Xiangdong Wei set up much of the experimental apparatus for the gas dispense mechanism we used to fill glass tubes with ^{3}He for permeation, absolute polarization, and decay time constant measurements at 1.5 T. Additionally, Drs. Mike Shim, Alan Ropp, and Ed deLange lended us their vast expertise in radiology and pulmonology that helped us with the clinical perspective and utility in preparing the ADC-based emphysema index manuscript. I thank Will Garrison for lending me much of his time to discuss my results of the analysis of the diffusion-weighted MRI data and for helping me with the statistics section of the ADC-based emphysema index paper. Zack Carson helped me with Latex and saved me hours of tedious work by showing me cool tricks with Latex formatting, and for that I am deeply grateful.

Additionally, I am thankful for Dr. Max Bychkov for making me a better teacher through dozens, if not hundreds of hours of one-on-one training and mentorship. It wasn't until I worked for Max that I truly appreciated the subtleties and intricacies of setting up an experiment. In the end of the second summer of my graduate career, I had to make the very difficult decision of switching research groups. I am grateful for Dawn Shifflett's support and guidance throughout this transition. Of course, I cannot forget the UVA physics department professors who taught the core and elective graduate physics courses. I am thankful for their instruction.

I am forever indebted to my parents, Mahnaz and Jafar, and my brothers, Mohsen and Ehsan for their unconditional support and love throughout my graduate career. Particularly, while writing my thesis, my parents' support has been a tremendous asset, and without their help, completing my dissertation would have been difficult. Additionally, I thank Hashem and SuzAnne Akhavan Tafti who offered me the opportunity to attend Kalamazoo College and start my higher education journey. Through examples and personal experiences, they instilled in me the willingness to work hard and take educated risks, and they taught me the value of paying forward my privileges.

I attribute much of my success to SuzAnne and Hashem's mentorship.

And last, but not least, I thank my partner and soulmate, Gen Schmitt. Her support and love for the past four years have been incredibly energizing, and her encouragement throughout the final years of graduate school was phenomenal. I am grateful for all that she has done for me, from making me dinners and snacks through late nights writing abstracts and manuscripts to conversations and words of encouragement when I was feeling down. Graduate school without her support would have been more difficult, and she was always there for me, and for that I am eternally grateful.

List of abbreviations

ADC	Apparent diffusion coefficient, or, analog-to-digital converter
FFT	Fast Fourier transform
iFFT (or FFT^{-1})	Inverse fast Fourier transform
FWHM	Full width at half max
TE	Echo time
TR	Repetition time
Voxel	Volume element
PFT	Pulmonary function test
RV	Residual volume (of the lung)
FEV$_1$	Forced expiratory volume in one second (of the lung)
FVC	Forced vital capacity (of the lung)
HU	Hounsfield units
TLC	Total lung capacity

List of symbols

γ	Gyromagnetic ratio of the said nucleus
f_0	Resonant frequency
ω_0	Resonant angular velocity
B	Magnetic field
θ	Flip angle, or, polar angle
T_1	Longitudinal signal decay/recovery time constant to thermal equilibrium polarization
T_2	Transverse signal decay time constant
T_2^*	Transverse signal decay time constant including local magnetic field inhomogeneity
ρ	Pressure, or, density
P	Polarization
Γ	Polarization retention rate, or, polarization rate
φ	Magnetic field scalar potential
ϕ	Azimuthal angle, or, phase between real and imaginary channels
r	Polar arm (of the polar coordinates)
α	Constant of proportionality between polarization and signal
μ	Magnetic moment, or, magnetic permeability
χ	Magnetic susceptibility
N	Number of spins
$N_\uparrow(N_\downarrow)$	Number of spins aligned (anti-aligned) w external field
h	Planck constant
K	Boltzmann constant
T	Temperature, or, tritium
${}^1H$	hydrogen
${}^3He$	Helium-3
${}^{129}Xe$	Xenon-129
D	Deuterium
S	Spin
V	volume

Contents

List of Figures

List of Tables

Chapter 1

Introduction

Nuclear induction and resonance absorption by magnetic moments, which led to development of nuclear magnetic resonance (NMR) techniques, were pioneered by Bloch [1] and Purcell [2] in the mid 1940's. In 1973, seminal papers by Lauterbur [3] and Mansfield [4] were published which demonstrated that magnetic field gradients can be used to create a spatial map of an object and led to the development of magnetic resonance imaging (MRI) as we know it today. Their invention, which earned them the Nobel Prize in Medicine in 2003, gave rise to a new era of non-invasive imaging and by the late 1980's, MRI had entered routine clinical practice.

The magnetic moment of a nucleus in the presence of an external magnetic field precesses about the field with a resonant frequency that depends on the field strength and the gyromagnetic ratio γ of the nucleus. This phenomenon is the basis of nuclear magnetic resonance. If a collection of nuclei with nonzero spin are placed in an external magnetic field, due to the spin-lattice interactions the net magnetization generated by the ensemble of spins tends to align with the external field's direction while precessing about the field. For spin-1/2 particles placed in an external magnetic field, there are two energy eigenstates corresponding to spins aligned and anti-aligned with the external field. For an ensemble of such particles with $N_\uparrow$ spins aligned and

$N_\downarrow$ spins anti-aligned with the field, the polarization P is given by

$$P = \frac{N_\uparrow - N_\downarrow}{N_\uparrow + N_\downarrow}, \tag{1.1}$$

where at thermal equilibrium, the number of spins in each state is determined by the Boltzmann distribution which depends on the temperature of the system. The thermal equilibrium polarization for this ensemble is given by

$$P = \tanh \frac{\gamma h B_0}{4\pi k T}, \tag{1.2}$$

where k is the Boltzmann constant, T is the temperature in Kelvin, B_0 is the field strength, and h is the Planck constant. For hydrogen nuclei at field strength $B_0 = 1.5$ T and temperature $T = 310$ K (corresponding to body temperature), for example, the thermal polarization is 4.9×10^{-6} (only a few parts per million). The signal in a conventional MRI scan is generated by the magnetic moment of the hydrogen nuclei (^{1}H) in the water and fat molecules inside the body. More specifically, the signal arises from the net magnetization of the precessing spins, which is the vector sum of the precessing spins' magnetic moments. This precessing signal can be detected in the form of an electromotive force induced in a nearby conducting loop. The reason we can make MR images of the human body despite minuscule thermal equilibrium polarization of hydrogen is the copious abundance of hydrogen molecules ($\sim 90,000$ moles per cubic centimeter) [5].

In 1960, Bouchiat et al. introduced a technique called spin-exchange optical pumping (SEOP) to produce polarization levels orders of magnitude higher than the thermal equilibrium polarization in ^{3}He [6]. Using this technique, Bouchiat et al. demonstrated ^{3}He polarization levels of $\sim 0.1\%$, whereas the thermal equilibrium polarization of ^{3}He at room temperature is only $\sim 0.0004\%$ at 1.5 Tesla. Hybrid-alkali SEOP [7] is a more recent technique that employs potassium in addition to rubidium, which greatly increases the efficiency of spin transfer to the helium nucleus. Using

hybrid-alkali SEOP, liter-scale volumes of ^{3}He can be polarized to levels approaching 70% [8, 9]. This increased polarization allows detection of MRI signal of hyperpolarized gases like ^{3}He at densities in the order of 50 mole per cubic centimeter. For example, at 1.5 Tesla, MRI signal generated by one cubic centimeter of ^{3}He nuclei (at standard temperature and pressure) polarized to 50% is ∼50 times higher than the MRI signal generated from hydrogen nuclei in one cubic centimeter of tissue at thermal equilibrium polarization.

Similar to ^{3}He, ^{129}Xe, which is the only other stable spin-1/2 noble gas, can also be polarized by means of SEOP [10, 11]. In 1994, the potential benefits of polarized ^{3}He and ^{129}Xe in medicine was realized when Albert et al. demonstrated *in-vivo* imaging of hyperpolarized ^{129}Xe in mouse lungs [12]. Since then, numerous research studies have shown clinical value for MRI of inhaled hyperpolarized ^{3}He and ^{129}Xe in characterizing lung impairment caused by various lung diseases [13].

Polarized ^{3}He may also be useful in thermonuclear fusion research, in the efforts towards designing a self-sustained energy production scheme. Thermonuclear fusion has been an active area of research for tens of decades [14–19] with the hope of generating a clean and sustainable method for large scale energy production, although no avenue has yet been proven successful. Theoretically, one approach that can possibly help get us to the point of self-sustained nuclear reactions with the potential for practical large-scale energy production was introduced by Kulsrud in 1982 [20]: Spin-polarized fusion, in which the reactant nuclei's spins assume preferential direction and are aligned parallel to one another (hence "polarized"), has a fusion cross-section that is 50% higher than the fusion cross-section of randomly oriented nuclei for the same reaction. This boost in the cross-section, and consequently, fusion energy release, may just be the missing piece for achieving energy production through thermonuclear fusion, and is deserving of experimental research.

In the work presented in this thesis, we explore application of hyperpolarized gas MRI in a step toward the first spin-polarized thermonuclear fusion experiment, and

in characterizing emphysema, a disease that causes destruction of lung parenchyma. The next two sections provide the motivation for the work presented herein.

1.1 Spin-polarized thermonuclear fusion

Research endeavors in energy production from thermonuclear fusion has a long history dating back to the early 1950's. However, to date, the fusion community's efforts for self-sustained energy production in large-scale reactors remain unsuccessful, as the generated fusion power is less than the input power [21].

Fusion ignition, which is the point at which a fusion reaction becomes self-sustained, is required for practical power generation. That is to say, power generation using thermonuclear fusion is only feasible once the energy produced by the fusion reactions heats the plasma faster than all mechanisms responsible for cooling it, to maintain favorable conditions for fusion. Of the many strategies explored for confining and controlling the fusion process, magnetic confinement within a tokamak reactor is the most advanced [21] and appears to be nearing the ignition point with the International Thermonuclear Experimental Reactor (ITER)'s commissioning on the horizon [19] along with the Joint European Torus (JET) [22]. A tokamak is a reactor built in a shape of the torus that uses powerful magnetic fields (in the order of several Tesla) to confine the fusion plasma in a circular beam of current. Tokamak is generally considered to be the leading candidate for practical fusion reactor, and both JET and ITER projects are based on tokamak reactors.

A critical consideration for energy production in thermonuclear fusion is the energy yield of the fusion reaction from which the energy is harnessed. Some candidate fusion reactions that have been explored for energy production are: [21]

$$\mathrm{D} + \mathrm{D} \rightarrow {}^{3}\mathrm{He} + n + 3.27\,\mathrm{MeV}, \tag{1.3}$$

$$\mathrm{D} + \mathrm{D} \rightarrow T + p + 4.03\,\mathrm{MeV}, \tag{1.4}$$

$$\mathrm{D} + \mathrm{T} \rightarrow \alpha + n + 17.59\,\mathrm{MeV} \tag{1.5}$$

$$\mathrm{D} + {}^{3}\mathrm{He} \rightarrow \alpha + p + 18.3\,\mathrm{MeV}, \tag{1.6}$$

where 3.27 MeV, 4.03 MeV, 17.59 MeV, and 18.3 MeV are the energy released in the respective reactions. It is evident that the D + ^{3}He and D + T reactions have much higher energy yields among those listed. Further, these two reactions are favorable because (1) deuterium is abundant and easily available, and (2) the resulting α particles are charged and can be magnetically confined by the tokamak's field, which is a favorable process in retaining the fusion temperature [23].

The fusion reaction cross-section $\sigma(v, \theta)$ is a measure of the probability to undergo fusion as a function of the polar-angle θ and the relative velocity v (or kinetic energy) of the two reactant nuclei. Angle-integrated cross-sections for select fusion processes are shown in Fig 1.1 as a function of their total center-of-mass (cm) kinetic energy ε_{cm}^{Tot} [24]. It can be seen from Fig 1.1 that an advantage of the *D*-*T* reaction compared to the *D*-^{3}He reaction is its large cross-section in the low energy regime (< 50 KeV), which is the plasma energy levels at which most tokamak reactors operate. For reference, ITER's projected mean and peak temperatures are 12 KeV and 18 KeV, respectively [21, 22].

The average fusion reaction rate is proportional to the reactivity $\langle \sigma v \rangle$:

$$\langle \sigma v \rangle = \int p(v)\sigma(v)v dv. \tag{1.7}$$

Here, $p(v)$ is the velocity probability distribution. An excellent approximation of the reactivity for the D + T $\rightarrow \alpha + n$ reaction for the tritium polarization $P_T \in [-1, 1]$, the deuteron vector polarization $P_D^V \in [-1, 1]$, and the deuteron tensor polarization

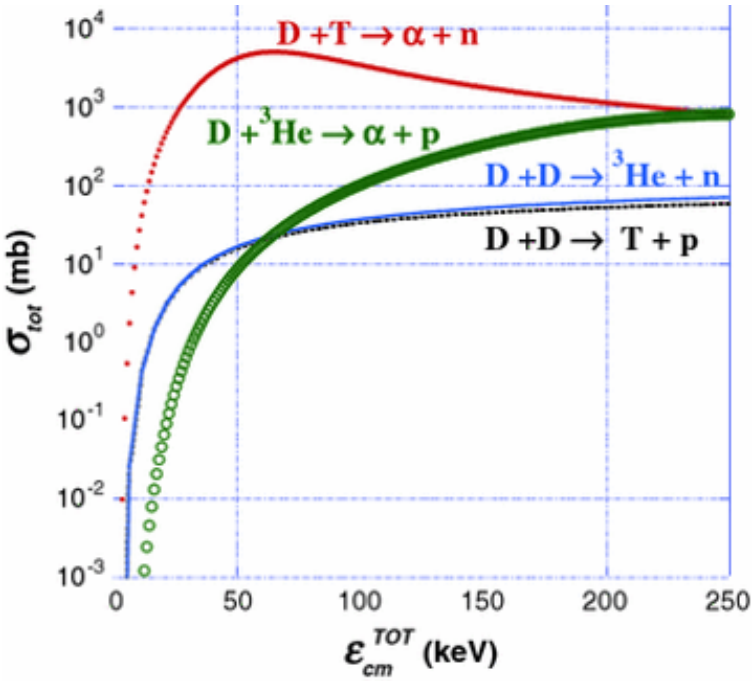

Figure 1.1: Angle-integrated cross-sections for the main fusion processes as a function of their total center-of-mass (cm) kinetic energy ε_{cm}^{Tot}. Plot courtesy of [25].

$P_D^T \in [-2, 1]$ is given by [21]

$$\begin{aligned}\langle d\sigma(\theta)v\rangle &= \frac{1}{4\pi}\langle\sigma_0 v\rangle W(\theta) \\ &= \frac{1}{4\pi}\langle\sigma_0 v\rangle \left\{1 - \frac{1}{2}P_D^V P_T + \frac{1}{2}\left[3P_D^V P_T \sin^2\theta + \frac{1}{2}P_D^T\left(1 - 3\cos^2\theta\right)\right]\right\}.\end{aligned} \tag{1.8}$$

If P_T is replaced by $P_{^3He}$, the above expression gives the reactivity for D+^{3}He $\rightarrow \alpha + p$ reaction instead. The term $\frac{1}{4\pi}\langle\sigma_0 v\rangle$ is the isotropic reactivity for randomly oriented spins. The angular term $W(\theta)$ is a function of the reactant nuclei's polarization, and in the absence of spin polarization of the reactant nuclei, where spins are randomly oriented in the plasma, $W(\theta)$ is equal to 1 [21]. The polar angle θ is measured relative to the local magnetic field, which is a transient toroidal field with toroidal and poloidal field components that form a helical pattern [21].

Integrating Eq 1.8 over all polar and azimuthal angles yields [21]

$$\langle \sigma v \rangle = \langle \sigma_0 v \rangle \left\{ 1 + \frac{1}{2} \vec{P}_D^V \cdot \vec{P}_{T \text{ or } {}^3He} \right\}. \tag{1.9}$$

It is evident from the above expression that if the fusing nuclei, in this case deuterium and tritium or ^{3}He, are aligned parallel to each other, the reactivity is inherently 50% higher than when the spins are randomly oriented (i.e. unpolarized). Thermonuclear fusion with polarized reactant nuclei is referred to as spin-polarized fusion and its mathematical treatment yielding Eq 1.9 was first introduced by Kulsrud et al [20] in 1982 and further developed by the same group in the following years [26]. In addition, Kulsrud et al. predicted time scales for polarization loss in a plasma that were much longer than the characteristic fuel burn-up period, establishing the theoretical practicality for spin-polarized fusion.

Evidently, an exciting avenue that may dramatically increase the thermonuclear energy output is spin-polarized fusion, in which the spins of the fusing nuclei are aligned. Unfortunately, to date, demonstration of spin-polarized fusion in a tokamak reactor has not yet been carried out due to several logistical challenges. In particular, delivering polarized fuels to the fusion plasma has not yet been established or shown due to lack of a method for encapsulating the polarized fuel suitable for injection into the tokamak plasma. However, notable developments in polarization techniques both in SEOP and dynamic nuclear polarization [27], polymer pellets used for inertial confinement fusion (ICF), and injection guns for cryogenic fuel delivery into the reactor plasma have advanced far enough that an *in-situ* spin-polarized fusion experiment may in fact be feasible [21].

Our group at the University of Virginia in collaboration with the Jefferson National Laboratory and General Atomics recently introduced a polarized fuel delivery strategy based on the fusion reaction D + ^{3}He $\rightarrow \alpha + p$ [21, 23, 25, 28, 29]. The reason for developing a testbed for the D-^{3}He reaction instead of the D-T reaction is as follows. First, tritium is not used in research-scale reactors with the exception

of the JET facility. A mainstream polarization mechanism for tritium has not been developed yet and substantial research and development is required to produce polarized tritium [21]. On the other hand, deuterium can be highly polarized in solid HD form [27] and liter-amounts of highly polarized ^{3}He is produced routinely at UVA [9] and Jefferson National Lab. Lastly, ^{3}He handling is simpler than the radioactive tritium for preliminary tests of the technique.

Our group's strategy was introduced with the goal of performing a direct spin-polarized experiment in the DIII-D tokamak in San Diego, which is operated by General Atomics. In this approach, polymer shells (i.e. pellets) originally developed for ICF experiments [30] will be used for encapsulation and cryogenic injection of the polarized D and ^{3}He. At room temperature, the ICF pellets are permeable to ^{3}He and D gases with a time constant in the order of minutes, but become practically impermeable at cryogenic temperatures. Our group's plan is to permeate deuterium into the pellets and then polarized to $\sim$ 40% in the form of frozen HD crystals using the HDice group's facility at JLab [31] and store in a liquid nitrogen cryostat for shipment to the DIII-D facility [29]. To use optical pumping for polarizing the ^{3}He fuel using a laser, ^{3}He must be polarized first and then permeated into the ICF shells. Cryogenic injection guns recently developed by the Oak Ridge National Laboratory (ORNL) can inject ICF shells into the plasma core of the tokamak with high efficiency [32]. We propose to use the same apparatus to cryogenically inject ICF pellets loaded with polarized ^{3}He and D maintained at 77 K into the tokamak plasma core.

Currently, within our group's proposed framework to deliver polarized fuel to the fusion chamber of the tokamak, there are several technical obstacles that need be addressed before actually performing an initial spin-polarized test at the DIII-D tokamak. First, a robust method of permeating polarized ^{3}He into the shells must be established, and the degree of polarization retention in the permeation process must be determined. Second, how fast the ^{3}He decays inside the shells at 77 K must

be determined. Third, the absolute polarization level achieved inside the shells must be determined. Fourth, a method for shipment of the cryostat containing the shells loaded with polarized D and ^{3}He in the presence of a holding field (to keep spins polarized), must be established, and all polarization loss mechanisms associated with the shipment must be understood. Fifth, a robust experimental procedure for cryogenic injection of the shells loaded with polarized helium and deuterium using ORNL's injection guns must be developed. This includes understanding the polarization loss mechanisms involved in loading the guns with the shells, and the injection process itself, and minimizing polarization loss created by each mechanism. And lastly, the polarization survival associated with the path of travel from the injection gun to the fusion chamber of the tokamak must be determined, which also includes determining polarization loss mechanisms, such as that associated with field inhomogeneities along the path of travel. The presented thesis is concerned with the first three challenges, and the other obstacles are outside the scope of this dissertation.

In the work presented in Part A of this thesis, we describe our development of an MRI-based testbed for monitoring the ^{3}He permeation process and report preliminary results of permeation and polarization survival experiments designed to address some of the technical challenges remaining on the path to performing the first spin-polarized fusion experiment at the DIII-D tokamak. First, in Chapter 3, we present the iterative calculation of magnetic field gradients and simulations of diffusion of ^{3}He molecules in the presence of field gradients applied for imaging as well as static field inhomogeneities pertinent to our experimental setup for the permeation of polarized ^{3}He into ICF shells. We performed several polarized ^{3}He permeation experiments using MRI, and specifically chemical shift imaging, to determine the polarization decay of the permeation process and the mechanisms that affect the efficiency, which is the topic of Chapter 4. Further, we measured the longitudinal relaxation rate of the polarized ^{3}He inside the pellets at room temperature and at 77 K in the holding field of a whole-body clinical 1.5-T MRI scanner. Additionally, we designed and

performed an experiment to measure the absolute polarization of the permeated ^{3}He gas inside the pellet. This was done by calibration to thermal equilibrium polarization measurements (Chapter 5). And lastly, we discuss the direction for future work, improvements, and challenges of our proposed and partially developed technique to deliver polarized fuel to the tokamak plasma for achieving spin-polarized fusion.

1.2 Diffusion-weighted MRI in Lungs

Conventional lung MRI is difficult because of the strong field inhomogeneities created by the tissue-air boundaries of the parenchymal tissue structure, as well as low ^{1}H density inside the lung [13]. Recently developed MRI techniques such as ultrashort echo time imaging of the lung parenchyma show promise for addressing these problems [33,34], although to date, computed tomography (CT) remains the prominent imaging technique for noninvasive visualization of the lung parenchyma.

Invention of spin-exchange optical pumping and further developments of the technique allow detection of signal generated by hyperpolarized noble gases, namely, ^{3}He and ^{129}Xe, at number densities that are orders of magnitude lower than number density of ^{1}H in the body. Both ^{3}He and ^{129}Xe are inert gases and can be inhaled without harm to the body. Once inhaled, MRI of hyperpolarized ^{3}He or ^{129}Xe provide a direct image of the ventilated lung airspaces. As such, MRI of inhaled hyperpolarized ^{3}He and ^{129}Xe has emerged as a clinical research tool to assess lung function and structure.

Although the first *in-vivo* MRI of hyperpolarized gas was done using ^{129}Xe [12], most hyperpolarized gas lung MRI research studies immediately thereafter used ^{3}He as the inhaled contrast medium for the following reasons [13]. First, since the gyromagnetic ratio of helium is larger than that of xenon, higher MRI signal is generated from helium than xenon for the same number density and polarization level. And second, much higher degrees of polarization were initially in ^{3}He as compared to ^{129}Xe. However, this trend reversed within the past 15 years due to scarcity of ^{3}He, which

moved the Department of Energy to start rationing the supply of ^{3}He for research [35]. Whereas the primary source of ^{3}He is tritium decay in nuclear warheads [36,37], ^{129}Xe is a naturally abundant isotope of xenon and can be isotopically enriched for hyperpolarization. Additionally, circa 2006, liter-quantities of ^{129}Xe can be polarized to nearly 50% [11].

An image of hyperpolarized gas inside the airspaces of the lung obtained using MRI is referred to as ventilation image. Ventilation images of the inhaled gases in the lung airspaces can provide insight into lung impairment related to air flow obstruction in diseases such as asthma [38] and chronic obstructive pulmonary disease (COPD) [39]. An example of inhaled hyperpolarized ^{129}Xe ventilation image set is shown in Fig 1.2.

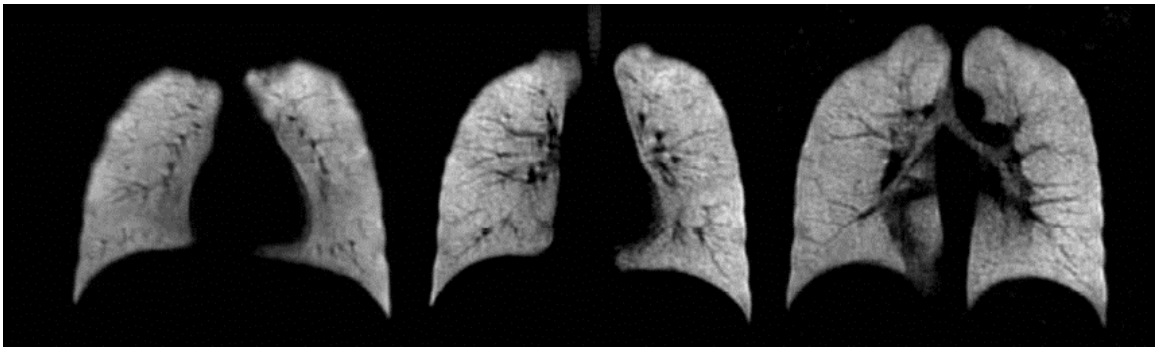

Figure 1.2: Example coronal ventilation images of inhaled hyperpolarized ^{129}Xe of a healthy subject. Images reproduced from [40].

A brief overview of the lung anatomy and physiology can help us understand the capability of hyperpolarized gas MRI in lung disease. The trachea, which is the primary airway leading into the lungs, divides into two secondary airways (called bronchi) that lead to each lung. These airways continue to bifurcate into smaller airways for 23 generations, leading to the terminal bronchioles, which are the smallest conducting airways in the respiratory tree. The terminal bronchioles lead to pulmonary acini, which consist of a collection of alveolar sacs, which are responsible for gas exchange. A schematic diagram of the respiratory tree is given in Fig 1.3.

An essential property of the lung is its large surface-to-volume ratio achieved by the

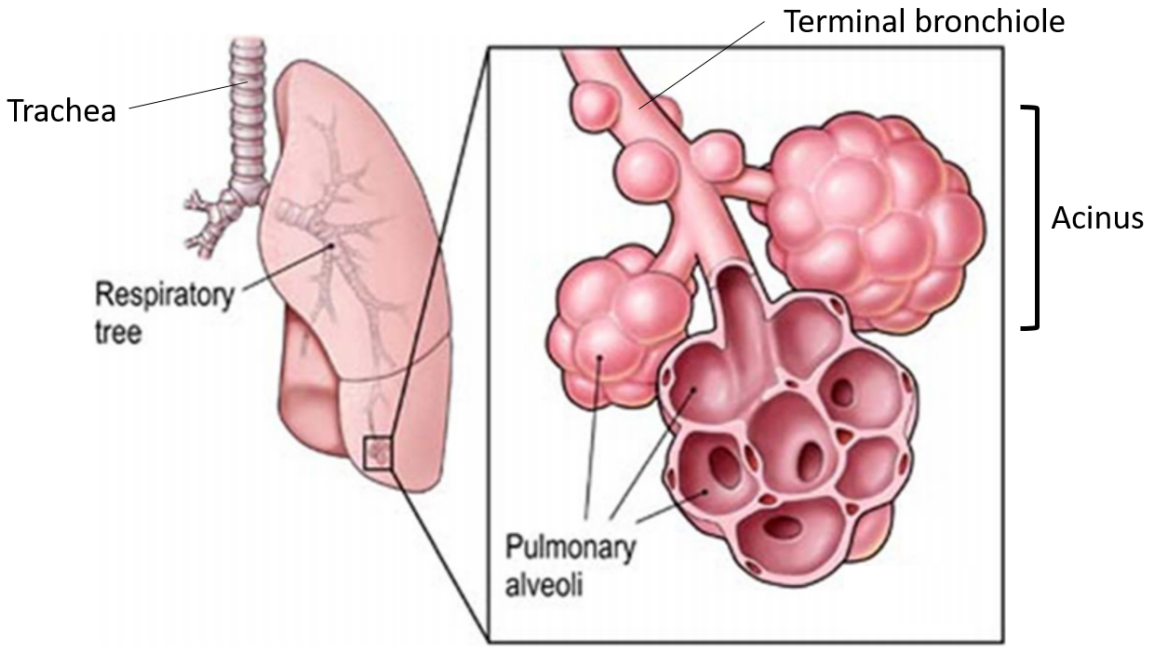

Figure 1.3: Schematic diagram of the respiratory tree. Illustration reproduced from [41].

described bifurcation pattern that is crucial to gas exchange between the alveolar airspaces and the bloodstream flowing through the alveolar walls. In the lung disease known as emphysema, the alveolar walls become destroyed, which in turn reduces the surface-to-volume ratio of the affected acini. Therefore, patients with emphysema suffer from impaired gas exchange carried out by the lungs, which ultimately results in shortness of breath. In addition to gas exchange impairment, the irreversible destruction of alveolar walls causes loss of lung elastic recoil, which makes breathing more difficult in patients with emphysema.

To date, clinical diagnosis of emphysema is primarily done via standard pulmonary function tests that provide a global measure of lung function [42], and the parenchymal damage caused by emphysema is visualized using CT scans [42–44]. However, a hyperpolarized noble gas MRI technique known as diffusion-weighted MRI has be-

come an increasingly promising clinical research tool for emphysema characterization since its initial clinical potential was realized [45]. Diffusion-weighted MRI of inhaled hyperpolarized gases exploits the Brownian motion of the gas molecules within the alveoli to probe the lung microstructure. The measured quantity, which is referred to as the "apparent diffusion coefficient" (ADC), characterizes the mean-squared-displacement of the gas particles inside the lung during the measurement time. As such, ADC values can be used as a relative measure of the degree of restriction to the movement of the gas particles imposed by the alveolar microstructure. Diffusion in healthy lungs is more restricted than diffusion in emphysematous lungs, due to the substantial destruction of alveolar walls in this disease. Therefore, regions of the lung with emphysematous destruction of alveolar walls have higher measured ADC values than healthy regions of the lungs. Elevated ADC values have been established to represent airspace enlargement due to emphysematous tissue destruction in animal [46–48] and human studies using hyperpolarized ^{3}He [45, 49–51] and hyperpolarized ^{129}Xe [13, 52–58].

Numerous studies have compared elevated ADC values from hyperpolarized gas diffusion MRI with results of quantitative CT [39, 54–56, 59] and pulmonary function tests [39, 45, 50, 53, 55–57, 59]. Recent efforts have focused specifically on establishing the capabilities of ^{129}Xe [39, 54, 55, 57, 60] due to the extremely limited availability of ^{3}He [13]. Although the clinical usefulness of diffusion-weighted MRI of hyperpolarized noble gases has become apparent in the recent years, whole-lung quantitative ADC metrics beyond mean and standard deviation have not yet been developed to assess emphysema burden.

Part B of this thesis consists of one chapter (Chapter 6) that introduces and describes a technique for quantifying emphysema burden in patients with COPD, which we developed based on measured diffusivity values of ^{3}He and ^{129}Xe obtained from diffusion-weighted hyperpolarized gas MRI in human lungs. In this chapter we also present the peer-reviewed results of the introduced technique based on the

diffusion-weighted MRI of inhaled hyperpolarized ^{3}He and ^{129}Xe in healthy subjects and patients with COPD.

Chapter 2

Magnetic resonance theory

In the present chapter we lay the theoretical groundwork for the experiments described in this thesis. In Sec 2.1, we describe the origin of MR signal, including polarization level (which determines amount of signal available for excitation), its magnetization dynamics once excited, and its detection to obtain a nuclear magnetic resonance (NMR) signal. We start with quantum mechanical treatment of the magnetic moment to derive the thermal equilibrium polarization, and to discuss the basis of hyperpolarization via spin-exchange optical pumping. Thereafter, since any detectable signal in MRI acquisitions is macroscopic in scale, only classical consideration of MR physics is presented throughout the rest of this chapter. In Sec 2.2, we give the expression for NMR signal and its corresponding frequency spectrum obtained from Fourier transformation. Next, in Sec 2.3 we present the theoretical and practical basis of MRI that relies on frequency- and phase- encoding in "k-space" using magnetic field gradients. In Sec 2.4 and Sec 2.5 we describe the theoretical and practical basis of diffusion-weighted MRI, which can be used to characterize Brownian motion of particles in a gaseous or liquid sample. Diffusion-weighted MRI of hyperpolarized ^{3}He and ^{129}Xe gas is implemented in the experiment presented in Part B to probe parenchymal damage in human lungs due to emphysema, a chronic lung disease. And lastly, in Sec 2.6, we describe a fully phase encoded imaging technique, also known as chemical shift imaging, that is used to image identical spins that ex-

perience different local magnetic field strengths due to their magnetic environments. Chemical shift imaging of thermally polarized and hyperpolarized ^{3}He is used in experiments presented in Part A, where we quantify polarization loss of hyperpolarized ^{3}He permeating into ICF shells, and their survival time once inside the shells.

2.1 Magnetic resonance signal

In nuclear magnetic resonance (NMR) and MRI, the source of magnetization and hence signal originates from the magnetic moment of the nucleus. All nuclei possess quantum number called spin (S) associated with the spin angular momentum $\vec{S}$, and magnetic moment $\vec{\mu}$ along the direction of their spin. The relationship between the spin angular momentum and the magnetic moment is given as

$$\vec{\mu} = \gamma \vec{S}, \tag{2.1}$$

where γ is the gyromagnetic ratio of the nucleus. In quantum mechanics, spin quantization implies that nonzero spins placed in an external magnetic field are in a superposition of the eigenstates of the spin quantum operator S.

Consider a $S = 1/2$ particle, such as the nucleus of ^{1}H, ^{3}He, or ^{129}Xe, placed in an external magnetic field $\vec{B} = B_0\hat{z}$. For such a particle, the wave functions $\psi_\pm$ of the spin component operator S_z have eigenvalues $m_s\hbar = \pm\frac{1}{2}\hbar$ such that

$$S_z\psi_\pm = \pm\frac{1}{2}\hbar\psi_\pm, \tag{2.2}$$

where $\hbar = \frac{h}{2\pi}$ is the reduced Planck constant. These eigenvalues correspond to spin projection alignment parallel or anti-parallel with the field. The energy levels $\epsilon_\pm$ of the spin can be written as

$$\epsilon_\pm = -\vec{\mu}\cdot\vec{B} = -\gamma m_s\hbar B_0 = \pm\frac{\hbar\omega_0}{2}, \tag{2.3}$$

where $\omega_0 = \gamma B_0$ is the resonant frequency of the spins and is often called the Larmor precession frequency. Therefore, the energy difference between parallel and anti-parallel spins is

$$\Delta\epsilon = \hbar\omega_0. \tag{2.4}$$

The amount of magnetization per unit volume due to N spins in a volume V immersed in a magnetic field depends on the polarization level P of the spin population and is given by

$$\vec{M} \equiv \frac{1}{V}\sum_i \vec{\mu_i} = \frac{NP\vec{\mu}}{V}. \tag{2.5}$$

This expression for $\vec{M}$ is valid for both thermally-polarized and hyperpolarized cases, which will be discussed in the following sections.

2.1.1 Thermal equilibrium polarization

For an ensemble of N spin-1/2 particles in a static magnetic field B_0, the measured spin projections along the field axis are either aligned or anti-aligned with the holding field. We refer to the number of spins aligned with the field as $N_\uparrow$ and those anti-aligned as $N_\downarrow$, where the total number of spins is given by $N = N_\uparrow + N_\downarrow$. Since the energy difference between aligned and anti-aligned spins is $\hbar\omega$, the Boltzmann distribution for this 2-state energy system hence dictates that

$$\frac{N_\downarrow}{N_\uparrow} = e^{-\frac{\Delta\epsilon}{kT}} = e^{-\frac{\hbar\omega_0}{kT}}, \tag{2.6}$$

where k is the Boltzmann constant and T is the temperature in Kelvin. In terms of these quantities, the thermal-equilibrium polarization (P) of the ensemble (Eq 1.1) can be written as:

$$P \equiv \frac{N_\uparrow - N_\downarrow}{N_\uparrow + N_\downarrow} = \frac{1 - \frac{N_\downarrow}{N_\uparrow}}{1 + \frac{N_\downarrow}{N_\uparrow}}$$

$$= \frac{1 - e^{-\frac{\Delta\epsilon}{kT}}}{1 + e^{-\frac{\Delta\epsilon}{kT}}} = \frac{1 - e^{-\frac{\hbar\omega_0}{kT}}}{1 + e^{-\frac{\hbar\omega_0}{kT}}}$$
$$= \tanh(\frac{\gamma h B_0}{4\pi kT}) \tag{2.7}$$

In the limit of $\hbar\omega_0 \ll kT$, the thermal equilibrium polarization is approximated by the argument of the hyperbolic tangent as

$$P = \tanh(\frac{\gamma h B_0}{4\pi kT}) \approx \frac{\gamma h B_0}{4\pi kT}. \tag{2.8}$$

The thermal equilibrium polarization levels along with gyromagnetic ratio and resonance frequency of ^{1}H, ^{3}He, and ^{129}Xe at 1.5 Tesla are given in Table 2.1. Although

Nucleus	$\frac{\gamma}{2\pi}$ $[\frac{MHz}{T}]$	f_0 @ 1.5 T [MHz]	Thermal pol @ 1.5 T, 20°C [ppm]	Thermal pol @ 1.5 T, 37°C [ppm]
^{1}H	42.56	63.67	5.23	4.94
^{3}He	−32.43	48.50	3.98	3.76
^{129}Xe	−11.78	17.62	1.45	1.37

Table 2.1: Gyromagnetic ratio and thermal polarization levels of ^{1}H, ^{3}He, and ^{129}Xe at 1.5 T, and 20°C (normal temperature and pressure, NTP) and 37°C (body temperature).

the thermal polarization of hydrogen nuclei at body temperature is only ~ 5 ppm, it is the overwhelming abundance of water molecules in the body that make signal acquisition and MRI of the human body possible.

At thermal equilibrium, the magnetization per unit volume (as introduced in Eq 2.5) of N spins in a volume V immersed in a static field $\vec{B} = B_0\hat{z}$ is therefore given by

$$\vec{M_0} = \frac{NP\vec{\mu}}{V} \approx n \cdot \frac{\gamma h B_0}{4\pi KT} \cdot \gamma m_z \hbar \hat{z} = n\frac{\gamma^2\hbar^2 B_0}{4kT}\hat{z}, \tag{2.9}$$

where $n = N/V$ is the number density. For a large volume with spatially varying spin

population density, $|\vec{M}_0|$ is given by

$$|\vec{M}_0(\vec{r})| \approx n(\vec{r})\frac{\gamma^2\hbar^2 B_0}{4kT}. \tag{2.10}$$

The magnetization given in the above expression is directly proportional to the measured MR signal which will be discussed in Sec 2.1.3.

2.1.2 Hyperpolarization

Hyperpolarization is a technique that achieves orders-of-magnitude higher polarization levels than the thermal equilibrium value at a given field strength and temperature. This can be done by creating highly non-Boltzmann spin population distributions using techniques including spin exchange optical pumping (SEOP) [6], metastability optical pumping (MEOP) [61], and dynamic nuclear polarization (DNP) [62]. SEOP in particular has been used extensively for polarized target experiments to study neutron structure as done in [63] and [64]. In the work presented in this thesis, only ^{3}He and ^{129}Xe polarized using the SEOP technique is used in our experiments and as such, we focus on the basics of SEOP.

Hyperfine interaction between the polarized valence electron of an alkali metal such as ^{87}Rb or ^{39}K and spin-1/2 nucleus like ^{3}He or ^{129}Xe is at the core of spin exchange optimal pumping. Optical pumping with circularly polarized laser light is used to polarize the alkali valence electron, and the spin polarization of the valence electron of the alkali metal transfers to ^{3}He nucleus during collisions between the noble gas and alkali atoms. Rubidium is an ideal candidate for optical pumping since it has a wide energy spacing between its D1 and D2 transition states (so it is easy to target only one transition), it vaporizes at a relatively low temperature, and lasers tuned to its D1 transition (794.8 nm) are commercially available.

The physics of ^{87}Rb optical pumping is summarized in Fig 2.1. The source of angular momentum for polarizing the valence electron of the ^{87}Rb atoms is a circu-

larly polarized laser with wavelength centered at 794.8 nm. For right (left) circularly

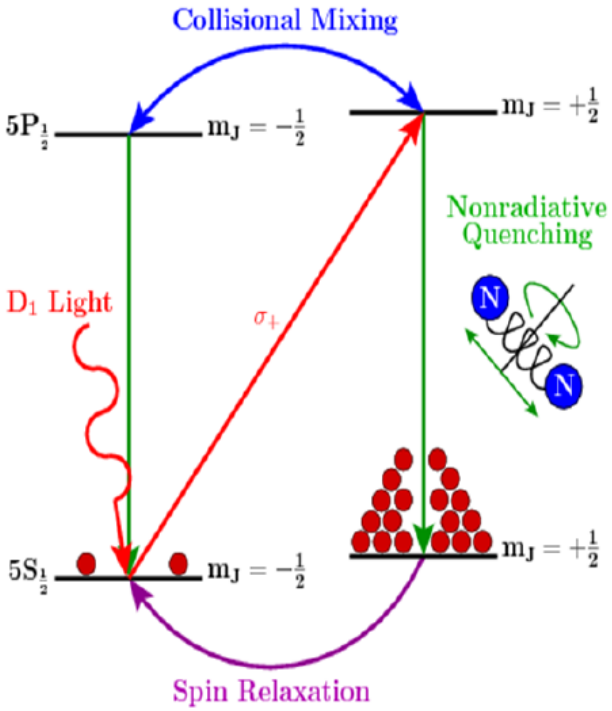

Figure 2.1: Optical pumping of rubidium vapor valence electron using right circularly polarized photons. Illustration reproduced from [5].

polarized laser light, only excitations with $m_J = +1$ ($m_J = -1$) are permitted by the dipole selection rule, since all excitations must obey conservation of angular momentum of the photon-electron system. Therefore, application of circularly polarized light produced by diode lasers, which corresponds to the D1 transition frequency of the rubidium electrons, selectively depletes one of the m_J sublevels of the ground state. For example, in the presence of the holding field, right circularly polarized photons (σ^+) constantly excite the $m_J = -1/2$ sublevel population of the $5S_{\frac{1}{2}}$ ground state to the $m_J = +1/2$ sublevel population of the $5P_{\frac{1}{2}}$ state as shown in Fig 2.1, systematically depleting the $m_J = -1/2$ ground state.

The excited electrons can radiatively decay to the ground state, and consequently emit a photon. This fluorescence would depolarize the electron spins, but N_2 is used

to absorb the energy which increases its rotational degrees of freedom and allows non-radiative quenching of the excited electrons [65]. Some of the electrons in the ground state $m_J = +1/2$ sublevel undergo spin relaxation and switch to the $m_J = -1/2$ sublevel. However, since the $m_J = -1/2$ population is constantly being depopulated as it gets pumped to the excited state, there will be a net polarization build up of the ^{87}Rb valence electrons in the $m_J = +1/2$ state.

After some time, the rubidium polarization approaches its saturation value P_{Rb}^{sat} given by [8]

$$P_{Rb}^{sat} = \frac{R}{R + \Gamma}, \tag{2.11}$$

where the optical pumping rate R is the product of the photon flux density and the photon absorption cross section, and Γ is the spin relaxation rate.

The polarized rubidium electrons can then transfer their polarization to the ^{3}He nuclei via binary collisions with spin exchange rate γ_{se}. After some time, the polarization saturation level of ^{3}He, which depends on the saturated rubidium polarization level (Eq 2.11), is given by

$$P_{^3He} = P_{Rb}\frac{\gamma_{se}}{\gamma_{se} + \Gamma_{\mathrm{Rb}}}, \tag{2.12}$$

where $\Gamma_{Rb} = \Gamma_{collisions} + \Gamma_B + \Gamma_{wall}$ is the spin destruction rate with three major contributors: spin-spin collisions, field inhomogeneity, and spin-wall collisions [5].

The "spin-exchange efficiency" η_{se} is the ratio of the rate at which the angular momentum of the polarized photons is transferred to the ^{3}He nuclei to the rate at which it is lost by the alkali atoms through various relaxation mechanisms, and is mathematically defined as [7]

$$\eta_{\mathrm{se}} = \frac{\gamma_{\mathrm{se}}\,[^3\mathrm{He}]}{[\mathrm{Rb}]\Gamma_{\mathrm{Rb}}} \tag{2.13}$$

where $[^3\mathrm{He}]$ and [Rb] are the concentrations of ^{3}He and ^{87}Rb, respectively. It is noteworthy that the spin exchange efficiency between rubidium electrons and helium nuclei is only ~2%. In a refinement to the basic SEOP technique known as hybrid-alkali spin exchange optical pumping, potassium is added to the ^{3}He-^{87}Rb mixture to

improve the spin exchange efficiency [7]. Since the rubidium valence electron readily transfers its polarization to the potassium valence electron with near-perfect efficiency, and since the potassium electrons can transfer their spin to ^{3}He nucleus with spin exchange efficiency of up to 25%, the saturation polarization of ^{3}He is dramatically increased.

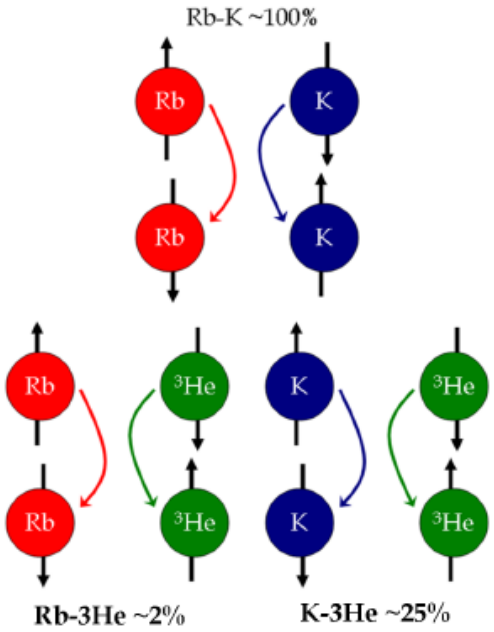

Figure 2.2: Hybrid spin-exchange between helium-3 and rubidium or potassium. Illustration reproduced from [5].

Practical details of producing polarized ^{3}He using our ^{87}Rb-^{39}K hybrid alkali SEOP polarizer are given in the following. Our glass polarizing cell was initially charged with ^{3}He, ^{87}Rb and ^{39}K plus $50-100$ Torr partial pressure of N_2. The ^{87}Rb and ^{39}K stay behind when polarized ^{3}He is dispensed from the cell, so this valved cell can be recharged with ^{3}He and N_2 for each new batch of polarized gas. Safe operating total pressure of the cell can be up to $\sim$ 10 atm at room temperature, though the ^{3}He pressure is set usually at 120 psi (gauge). The cell sits inside an oven to heat the rubidium to vaporize it for optical pumping. A $\sim$27 Gauss holding field is on at all times when polarizing or maintaining the polarization of the ^{3}He inside the

cell. For the hyperpolarized ^{3}He gas experiments presented in this thesis, we used our hybrid-alkali polarizer and were able to consistently achieve polarization levels of 40-60% in 2.5-liter batches.

The fundamental spin exchange mechanism via the hyperfine interaction is the same for both ^{3}He and ^{129}Xe [66]. The larger number of protons in the ^{129}Xe nucleus (than in the ^{3}He nucleus) more strongly attracts the electron cloud of the alkali metal, which consequently increases the spin exchange rate between the ^{129}Xe nuclei and the alkali electrons, such that [67]

$$\gamma_{se}^{^{129}\mathrm{Xe}} \simeq 5000\gamma_{se}^{^{3}\mathrm{He}}. \tag{2.14}$$

Despite the much higher spin exchange rate between the ^{129}Xe nuclei and the alkali electrons, at high pressures, the net optical pumping rate is lower for ^{129}Xe than ^{3}He. That is because ^{129}Xe's many electrons act to depolarize the rubidium valence electrons, and as such, the optical pumping rate of the alkali electrons is low at high ^{129}Xe pressures. Therefore, a closed polarizing cell with high pressures of ^{129}Xe cannot be used to achieve high polarization. Instead, liter-quantities of ^{129}Xe can be polarized to levels approaching 50% in a process where ^{129}Xe gas continually flows through the polarizing cell (which is not a closed cell) at low partial pressures. The outflowing polarized ^{129}Xe is cryogenically accumulated in a section of glass tubing immersed in a liquid nitrogen bath where the ^{129}Xe freezes into crystals maintaining its polarization [10]. This method is capable of producing liter quantities of ^{129}Xe polarized to nearly 50% in $\sim$ 1 hour [11], while same amount of ^{3}He can be polarized to $\sim$60% in $\sim$ 20 hours using the hybrid alkali SEOP technique. For the hyperpolarized ^{129}Xe gas experiments presented in this thesis, we used commercial polarizers manufactured by Xemed or Polarean. Using either of the commercial polarizers, we were able to consistently produce polarization levels of 30-50% in $\sim$ 2-liter batches.

2.1.3 Magnetization dynamics: Signal generation and detection

In the previous two sections we described how longitudinal spin polarization (or magnetization) arises in both the thermally polarized and hyperpolarized cases. In the present section, we describe how this longitudinal magnetization can be converted into a detectable NMR signal. We start with the Bloch equation, which encapsulates the classical description of magnetization dynamics in NMR. We then describe how longitudinally oriented magnetization can be tipped away from alignment with the externally applied magnetic field in order to generate an NMR signal. Finally, we discuss how the amplitude of this signal can be related back to the initial longitudinal magnetization, which will allow us to draw a direct correspondence between the thermally polarized and hyperpolarized cases.

The Bloch equation describes the behavior of the magnetization if perturbed from thermal equilibrium. In the laboratory frame of reference, the Bloch equation can be written as

$$\frac{d\vec{M}}{dt} = \gamma\vec{M} \times \vec{B}_{ext} + \frac{1}{T_1}\left(M_0 - M_z\right)\hat{z} - \frac{1}{T_2}\vec{M}_{\perp}, \tag{2.15}$$

where $\vec{M}$ is the magnetization vector with longitudinal and transverse components $M_z\hat{z}$ and $\vec{M}_{\perp}$, respectively, $\vec{B}_{ext} = B_0\hat{z}$ is the external holding field, T_1 is the longitudinal spin relaxation time constant, and T_2 is the transverse spin relaxation time constant. The first term describes the magnetization behavior in the absence of interactions between neighboring spins, which is pure Larmor precession about the field direction. The second term describes the longitudinal relaxation of the net magnetization vector toward thermal equilibrium magnetization M_0. The longitudinal component of the vector solution to the Bloch equation is given by

$$M_z(t) = M_z(0)e^{-t/T_1} + M_0\left(1 - e^{-t/T_1}\right). \tag{2.16}$$

The time constant T_1, which is also known as "spin-lattice relaxation time", must be determined empirically. For thermal equilibrium polarization, $M_z(0)$ is the starting longitudinal magnetization given by Eq 2.10 where $M_z(0) \leq M_0$ and $M_z(0)$ regrows to M_0 with the regrowth time constant T_1. For a hyperpolarized sample, on the other hand, $M_z(0)$ is the starting magnetization where $M_z(0) \gg M_0$, and $M_z(0)$ decays to M_0 with same time constant T_1.

The third term in the Bloch equation describes the transverse relaxation of the net magnetization due to spin-spin interactions. The magnitude of the transverse component of the solution to the Bloch equation is given by

$$M_\perp(t) = M_\perp(0)e^{-t/T_2}. \tag{2.17}$$

Since this decay arises from the spin-spin interactions, the time constant T_2 is also referred to as "spin-spin relaxation time". Let us now describe the effects of local field inhomogeneities on transverse magnetization: Spins experience local magnetic fields. Since variations in local fields translate to variations in local frequencies (meaning neighboring spins can be resonating at different frequencies), individual spins get out of phase with each other over time. This loss of coherence between spins, whether regional or throughout the sample, is a phenomenon referred to as "dephasing" or "fanning out". Since the net magnetization is the vector sum of the magnetic moments of the spins in the sample, dephasing reduces the net magnetization vector, as shown in Fig 2.3. The net transverse magnetization decay caused by magnetic field inhomogeneities can be characterized by a separate time constant $T_2^{'}$. The total relaxation time constant can thusly be defined as the combination of the two time constants T_2 and $T_2^{'}$ such that

$$\frac{1}{T_2^*} \equiv \frac{1}{T_2} + \frac{1}{T_2^{'}}. \tag{2.18}$$

Therefore, to account for the field inhomogeneities, T_2 may be replaced by T_2^* in

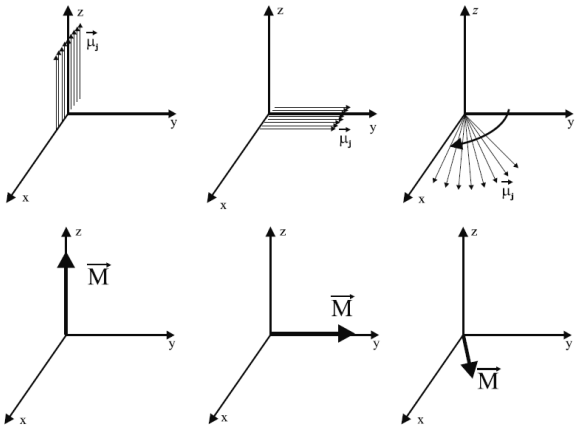

Figure 2.3: The upper sequence shows a 90° tip of a set of spins (isochromats) into the transverse plane such that they all lie along the y-axis (laboratory frame) at some instant in time, as shown in the middle figure. Precession of the individual spins in the x-y plane immediately follows (the recovery of longitudinal magnetization is ignored since the focus is on transverse magnetization dephasing effects). The lower sequence shows the same process in terms of the net transverse magnetization which decreases in magnitude during the precession because of the fanning out of the spins. Cartoon reproduced from Haacke [68].

Eq 2.17.

Let us now describe how purely longitudinal magnetization can be tipped away from $\hat{z}$ via application of an RF field, to have some or all component in the transverse plane. It is more convenient to discuss the RF field and its effect on the magnetization if we consider them in the rotating frame. We define the rotating frame, which we denote by primed parameters, to be a frame of reference that shares the same z axis with the laboratory frame (i.e. $\hat{z}$ and $\hat{z}^{'}$ are aligned), but with $x^{'}$ and $y^{'}$ axes rotating about the z axis clockwise (negative angular velocity).

Consider an ensemble of ^{1}H nuclei oriented along the static field $\vec{B} = B_0\hat{z}$, which generates magnetization along the z axis. A circularly polarized RF field $\vec{B_1}$ that is constant in the rotating frame has the form

$$\vec{B_1} = B_1(\hat{x}\cos\omega t - \hat{y}\sin\omega t) \tag{2.19}$$

in the lab frame but is simply

$$\vec{B_1} = B_1\hat{x}' \tag{2.20}$$

in the rotating frame. Therefore, the total magnetic field in the rotating frame is given by:

$$\vec{B}'_{ext} = (B_0 - \omega/\gamma)\hat{z}' + B_1\hat{x}' \tag{2.21}$$

$$= \frac{1}{\gamma}(\omega_0 - \omega)\hat{z}' + \omega_1\hat{x}' \tag{2.22}$$

Invoking the Bloch equation and Eq 2.22 both in the rotating frame, and ignoring T_1 and T_2 relaxations (which is a reasonable assumption given that RF fields are "instantaneous" with respect to relaxation mechanisms), and substituting the value of $\vec{B}_{ext}$ given in Eq 2.21, we write [68]

$$(\frac{d\vec{M}}{dt})' = \vec{M} \times [(\omega_0 - \omega)\hat{z}' + \omega_1\hat{x}']$$

$$= \gamma\vec{M} \times \vec{B}_{eff} \tag{2.23}$$

where $\omega_0 \equiv \gamma B_0$ is the resonant frequency (Larmor frequency), ω is the RF frequency in the lab frame, $\omega_1 \equiv \gamma B_1$ is the spin-precession frequency about the $\hat{x}'$ generated by the circularly polarized RF field, and $\vec{B}_{eff} \equiv [(\omega_0 - \omega)\hat{z}' + \omega_1\hat{x}']/\gamma$. That is to say, $\vec{B}_{eff}$ is defined as the superposition of the static field and the applied oscillating field along the $\hat{x}'$ direction, which usually is orders of magnitude smaller in amplitude than that of the static field. In the event that the RF field is applied at the resonant frequency such that $\omega = \omega_0$, in the lab frame, $\vec{B}_{eff}$ points ever so slightly away from the static field. However, in the rotating frame, $\vec{B}_{eff}$ becomes simply the oscillating field with the only component in the transverse plane. Therefore, the equation of motion which describes the fate of the magnetization becomes

$$(\frac{d\vec{M}}{dt})' = \vec{M} \times \omega_1\hat{x}'. \qquad \text{(when } \omega = \omega_0\text{)} \tag{2.24}$$

The solution to Eq 2.24 is given by

$$\begin{aligned} M_{x'}(t) &= M_{x'}(0) \\ M_{y'}(t) &= M_{y'}(0)\cos\theta + M_{z'}(0)\sin\theta \\ M_{z'}(t) &= -M_{y'}(0)\sin\theta + M_{z'}(0)\cos\theta, \end{aligned} \tag{2.25}$$

where $\theta \equiv \int_0^t dt^{'}\omega_1(t^{'})$ is determined by the waveform of the RF field. That is to say, in the rotating frame, the magnetization simply precesses about the applied B_1 field, whose direction is constant (in the rotating frame). We refer to θ as the 'tip-angle' or 'flip-angle' (about the axis of the applied RF field), and use this term throughout the thesis.

For example, if RF pulse is applied such that $\theta = \int_0^t dt^{'}\omega_1(t^{'}) = \pi/2$, then in the rotating frame the magnetization is rotated 90° about the x axis granted B_1 is applied along $\hat{x}$. Thusly, if the longitudinal magnetization component prior to the application of the excitation RF pulse is M_z^- (recall that an initial assumption of this treatment is that prior to the RF application, there is no transverse magnetization, i.e. $M_\perp^- = 0$), then the resulting transverse component of the magnetization $M_\perp^+$ is given by

$$M_\perp^+ = M_z^- \sin\theta, \tag{2.26}$$

where we have adopted the notation that "$-$" and "$+$" refer to the time immediately before and after the application of the excitation RF pulse, respectively. Similarly, the remaining longitudinal magnetization M_z^+ (after application of the excitation RF pulse) is given by

$$M_z^+ = M_z^- \cos\theta. \tag{2.27}$$

In MRI terminology, "exciting" spins refers to tipping spins away from the longitudinal direction via application of an RF pulse to create transverse magnetization, and the same terminology will be used throughout this thesis.

It is the transverse magnetization created by the excitation RF pulse that generates the signal in NMR and MRI, which can be understood as follows. The transverse magnetization in the lab frame, and therefore the magnetic field produced by this magnetization, precesses about the longitudinal axis with resonant frequency determined by the magnetic field strength and the gyromagnetic ratio of the spins that create the magnetization. If a radiofrequency coil tuned to the resonant frequency of the spins is oriented such that its axis lies in the transverse plane, the changing magnetization in the transverse plane induces an electromotive force (emf) in the coil. This emf is a result of the change in magnetic flux through the coil and is given by Faraday's law of induction:

$$emf = -\frac{d\Phi}{dt}, \tag{2.28}$$

where the magnetic flux Φ is defined as $\Phi \equiv \int_{\text{area}} \vec{B} \cdot d\vec{S}$. Invoking Stokes' theorem, using the magnetic vector potential, and invoking a vector identity (please see Appendix A for a detailed derivation), we can write the flux in terms of the magnetization vector as

$$\Phi_M(t) = \int_{\text{sample}} d^3r \, \overrightarrow{\mathcal{B}}^{receive}(\vec{r}) \cdot \vec{M}(\vec{r}, t), \tag{2.29}$$

where $\overrightarrow{\mathcal{B}}^{receive}(\vec{r})$ is defined as the magnetic field per unit current that would be produced by the coil, and is essentially a spatial map of the receive field coil sensitivity.

The observed signal is proportional to the voltage induced in the coil and we write

$$Signal \propto emf = -\frac{d}{dt} \int_{\text{sample}} d^3r \vec{M}(\vec{r}, t) \cdot \overrightarrow{\mathcal{B}}^{receive}(\vec{r}). \tag{2.30}$$

We note that the time-derivative concerns only the transverse component of the magnetization precessing about the static field axis, because the time course of the longitudinal component is much slower (than that of the transverse component). As such, longitudinal component of the magnetization (including T_1 relaxation) is not included in the following. Using complex notation, the magnetization vector is given

by the Bloch equation as

$$\vec{M}(\vec{r},t) = e^{-t/T_2^*(\vec{r})} e^{i[-\omega_0 t + \phi_0(\vec{r})]} M_\perp^+(\vec{r},0) \tag{2.31}$$

where phase ϕ_0 and magnitude $M_\perp^+(\vec{r},0)$ are determined by the initial RF pulse. Replacing the value of $\vec{M}(\vec{r},t)$ given in Eq 2.32, and computing the dot product, Eq 2.30 can be written as

$$Signal \propto -\int_{\text{sample}} d^3r \frac{d}{dt}\left[e^{-t/T_2^*(\vec{r})} e^{i[-\omega_0 t + \phi_0(\vec{r})]}\right] M_\perp^+(\vec{r},0)\mathcal{B}_\perp^{receive}(\vec{r}). \tag{2.32}$$

Invoking Eqs 2.5 and 2.26, $M_\perp^+(\vec{r},0)$ is given by

$$|M_\perp^+(\vec{r},0)| = M_z^-(\vec{r},0)\sin\theta(\vec{r}) = n(\vec{r})\mu P \sin\theta(\vec{r}) \tag{2.33}$$

where $n(\vec{r}) \equiv N/V$ is the number density (which spatially varies), P is the polarization, and μ is the magnitude of the magnetic moment of the nucleus of interest. Here we assumed that flip-angle varies spatially, to account for coil sensitivity non-uniformity.

We now compute the time derivative of the terms $e^{-t/T2}$ and $e^{-i\omega_0 t}$ in Eq 2.32. We note that for ^{1}H and ^{3}He in static fields in the order of a Tesla, the Larmor frequency ω_0 is at least four orders of magnitude larger than typical values of $1/T_2^*$. Therefore, time-derivative of the e^{-t/T_2^*} factor can be neglected, compared to the derivative of the $e^{-i\omega_0 t}$ factor. With this approximation, and defining $\rho(\vec{r}) \equiv n(\vec{r})\mu$, we rewrite Eq 2.32 as

$$Signal \propto \omega_0 \int_{\text{sample}} d^3r e^{-t/T_2^*(\vec{r})} e^{i[-\omega_0 t + \phi_0(\vec{r})]} \rho(\vec{r}) P \sin\theta \mathcal{B}_\perp^{receive}(\vec{r}). \tag{2.34}$$

Lastly, we define the parameter Λ to encapsulate any constants or gains from the

electronics of the scanner and we write

$$Signal = \omega_0 \Lambda P \int_{\text{sample}} d^3r e^{-t/T_2^*(\vec{r})} e^{i[-\omega_0 t + \phi_0(\vec{r})]} \rho(\vec{r}) \sin\theta(\vec{r}) \mathcal{B}_\perp^{receive}(\vec{r}). \tag{2.35}$$

This expression for signal will be used in Chapter 5 to directly relate the measured signal generated from a ^{3}He sample at thermal equilibrium polarization to the measured signal from a hyperpolarized ^{3}He sample, where the measured signal in both cases were obtained using the same RF coil (i.e. Λ is the same for both). Because the two samples have different geometries and encompass different regions in the coil, flip-angle maps are obtained (when applicable) for a faithful comparison between the signals.

It is also noteworthy that the signal is proportional to the volume integral of the effective spin density, which will be relevant when we define imaging voxel size in Sec 2.3.3.

2.2 Free induction decay and NMR spectroscopy

In this section we discuss the mathematical form of the NMR signal acquired from precessing transverse magnetization following an excitation RF pulse. We begin by considering the signal as a function of time, which is known as a free induction decay or FID.

Consider exciting a sample of identical spins immersed in a static field $B\hat{z}$ to generate transverse magnetization. If the initial magnetization is purely longitudinal such that $\vec{M} = M_\parallel \hat{z}$, and the flip-angle of the excitation RF pulse is θ, the magnitude $M_\perp$ of the generated transverse magnetization is given by

$$M_\perp = M_\parallel \sin\theta. \tag{2.36}$$

This transverse magnetization will begin precessing about the static field direction

with frequency $f = \gamma B$, generating an oscillating signal which can be detected using an RF coil. In general, the resulting complex signal will have an initial phase ϕ_0 determined by the orientation of the RF coil, and an initial amplitude A determined by the size of $M_\perp$. Due to spin-spin interactions as well as local field inhomogeneities, the amplitude of the oscillating signal will decay with time constant T_2^*. Combining all these factors, the complex FID signal can be written as:

$$S(t) = Ae^{i\phi_0}e^{-i2\pi ft}e^{-t/T_2^*}, \tag{2.37}$$

In practice, the MRI scanner outputs a demodulated version of the complex signal, in which the nominal resonant frequency f_0 has been subtracted off. That is, the oscillation frequency of the signal seen by the user is $f^{'} = f - f_0$, and the complex signal given in Eq 2.37 should instead be written with f replaced by $f^{'}$. This situation is equivalent to viewing the NMR signal in a reference frame rotating clockwise at frequency f_0. To simplify the notation, we will keep writing the complex signal using f rather than $f^{'}$, but it should be recognized that f represents the oscillation frequency in the rotating frame.

If there exists several distinct populations of identical nuclei, with each population precessing at a different resonant frequency due to local magnetic field differences or chemical shifts, the detected FID signal will be the sum of several decay curves each of which will in general have its own initial phase and decay time constant T_2^*. For n such populations, we can write:

$$S(t) = \sum_{k=1}^{n} A_k e^{i\phi_k} e^{-i2\pi f_k t} e^{-t/T_{2,k}^*}. \tag{2.38}$$

Next we consider the Fourier transform of the FID signal, which is often used to identify the different frequency components of the transverse magnetization.

In this section we exploit the Fourier relationship between time and frequency to obtain the frequency spectrum corresponding to an NMR signal (i.e. FID). The

Fourier ($\mathscr{F}$) and inverse Fourier ($\mathscr{F}^{-1}$) transformation between Fourier conjugate parameters t (representing time) and ν (representing frequency) is given by

$$\mathscr{F}(S(t)) = \hat{S}(\nu) = \int_{-\infty}^{\infty} S(t)e^{-2\pi i\nu t}dt. \tag{2.39}$$

$$\mathscr{F}^{-1}(\hat{S}(\nu)) = S(t) = \int_{-\infty}^{\infty} \hat{S}(\nu)e^{2\pi i\nu t}d\nu \tag{2.40}$$

To obtain the frequency spectrum, we must take the Fourier transform of the FID. We can write

$$\begin{aligned}
\mathscr{F}(S(t)) &= \int_{-\infty}^{\infty} S(t)e^{-i2\pi\nu t}dt \\
&= \int_{0}^{\infty} Ae^{i\phi_0}e^{-i2\pi(f+\nu)t}e^{-t/T_2^*}dt \\
&= Ae^{i\phi}\int_{0}^{\infty} e^{-t(1/T_2^*+i2\pi(f+\nu))}dt \\
&= \left[-Ae^{-i\phi}\frac{e^{-t'(1/T_2^*+i2\pi(f+\nu))}}{1/T_2^*+i2\pi(f+\nu)}\right]_0^{\infty} \\
&= \frac{Ae^{-i\phi}}{1/T_2^*+i2\pi(f+\nu)}.
\end{aligned} \tag{2.41}$$

Equation 2.41 is the form of a Lorentzian function. If there exists several samples of identical nuclei experiencing different magnetic environments, the frequency will consist of sum of Lorentzian curves. Eq 2.41 is derived under the assumption that the measured signal extends from time zero to infinity. In practice, the acquired signal ends at some point, resulting in a truncated time-domain signal. Therefore we also derive the Fourier transform of a truncated time-domain signal assuming an finite time of acquisition t_{ADC}. Depending on the application of the FID used in an experiment, t_{ADC} is commonly in the order of T_2^*. For a truncated complex decay, the frequency response can be computed as

$$\mathscr{F}(S(t)) = \int_{0}^{t_{ADC}} Ae^{i\phi}e^{-t/T_2^*}e^{-i2\pi(f+\nu)t}dt$$

$$= \left[-Ae^{i\phi} \frac{e^{-t(1/T_2^* + i2\pi(f+\nu))}}{1/T_2^* + i2\pi(f+\nu)} \right]_0^{t_{ADC}}$$
$$\boxed{= Ae^{i\phi} \frac{1 - e^{-t_{ADC}(1/T_2^* + i2\pi(f+\nu))}}{1/T_2^* + i2\pi(f+\nu)}}. \tag{2.42}$$

The corresponding Fourier transform of the signal generated by several samples of spins each with a different resonant frequency is a sum of complex Lorentzian distributions given by

$$\mathscr{F}(S(t)) = \sum_{k=1}^{n} A_k e^{i\phi_k} \frac{1 - e^{-t_{ADC}(1/T_{2,k}^* + i2\pi(\nu + f_k))}}{1/T_{2,k}^* + i2\pi(\nu + f_k)}. \tag{2.43}$$

An example of a simulated sum of two truncated complex decay curves, one with frequency offset $f = 0$ Hz, $A = 1$ arb. units, $\phi = 1$ rad, and $T_2^* = 50$ ms, and the other with frequency offset $f = 40$ Hz, $A = 0.8$ arb. units, $\phi = 1$ rad, and $T_2^* = 10$ ms, and its associated Fourier transform with the form of a sum of two Lorentzian distributions is given in Fig 2.4. That is to say, we simulated the resulting signal and spectroscopy from two distinct spin populations, one with zero frequency, and the other with frequency of 40 Hz, after demodulation. Note that the off resonance behavior in the frequency spectrum is observed as several peaks corresponding to each off resonance distribution of spins.

The area under the frequency spectrum is proportional to the spin density, and can be used to relate signal strength from different samples of spins, which will be discussed in Sec 2.6. This concept will be extensively used in Chapters 4 and 5, where we compare signal strengths obtained from fitted areas of the frequency spectra.

2.3 Magnetic resonance imaging

The fundamental basis of image acquisition in MRI is linear mapping between position and frequency which is done by applying magnetic field gradients. In this section, we

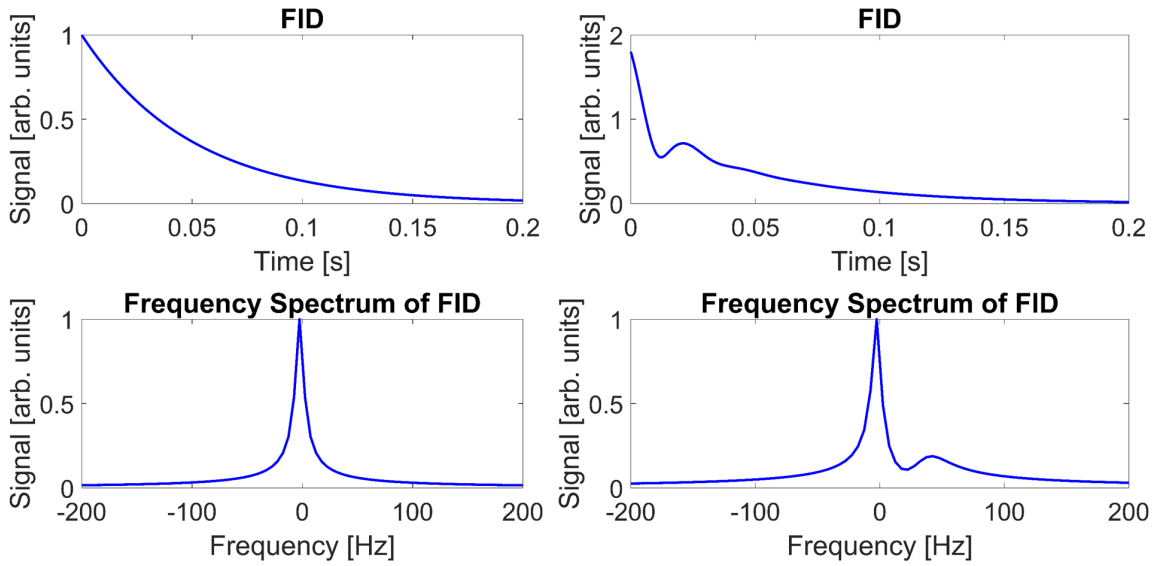

Figure 2.4: Top left figure depicts a simulated truncated complex decay curve representing detected signal for an FID experiment with the following parameters: frequency offset $f = 0$ Hz, $A = 1$ arb. units, $\phi = 1$ rad, and $T_2^* = 50$ ms. Bottom left figure shows the corresponding Fourier transform of the decay, which takes the form of a complex Lorentzian function. On the top right figure is depicted a simulated sum of two truncated complex decay curves, one with the parameters mentioned earlier, and the other with frequency offset $f = 40$ Hz, $A = 0.8$ arb. units, $\phi = 1$ rad, and $T_2^* = 10$ ms. The ripples are caused by the difference in resonant frequencies of the two samples. The Fourier transform of the sum of two truncated complex decays is given in the bottom right figure, which takes the form of a sum of complex Lorentzian functions. Note that the ripples due to the frequency offset in the decay manifests itself in the form of frequency offset from the resonant frequency by 40 Hz. All curves shown here are magnitudes.

explain the theoretical basis of gathering spin density information spatially, as well as practical considerations in image acquisition.

The mathematical treatment for position encoding using gradients will be given in Sec 2.3.1. In practice, the basis for spatial location encoding can be achieved via two methods which will be introduced and discussed in Sec 2.3.2. In Sec 2.3.3, we discuss the practical applications of position encoding. Next, in Sec 2.3.4, we present how only a slice of a 3D object can be imaged. And lastly, in Sec 2.3.5, we exploit slice-selection and position encoding techniques to discretely sample the k-space signal to

form a 2D slice-selective image.

2.3.1 Position encoding using gradients

Recall from Sec 2.1.3 that the transverse magnetization precesses with frequency determined by the strength of local magnetic field $B(\vec{r})$, and the frequency is given by

$$\omega(\vec{r}) = \gamma B(\vec{r}). \tag{2.44}$$

If a linear gradient of the form $\vec{G} \equiv \frac{\partial B_z}{\partial x}\hat{x} + \frac{\partial B_z}{\partial y}\hat{y} + \frac{\partial B_z}{\partial z}\hat{z}$ is superimposed on top of a uniform static field $B_0\hat{z}$, the total magnetic field is given by

$$B_z(\vec{r}) = B_0 + \vec{G}(\vec{r}) \cdot \vec{r}, \tag{2.45}$$

which results in position-dependent precession frequencies given by

$$\omega(\vec{r}) = \omega_0 + \omega_G(\vec{r}), \tag{2.46}$$

where $\omega_G(\vec{r}) \equiv \gamma\vec{G}(\vec{r}) \cdot \vec{r}$. The magnetic field gradient can be turned on and off in time, and to generalize Eq 2.46, we write

$$\omega(\vec{r}, t) = \omega_0 + \omega_G(\vec{r}, t) \tag{2.47}$$

The MR signal derived in Sec 2.1.3 can be expressed as

$$s(t) \propto \int d^3r \rho(\vec{r}) e^{i(\phi(\vec{r},t))}, \tag{2.48}$$

where $\phi(\vec{r}, t)$ is the phase accrued by transverse spins at location $\vec{r}$ and time t after the excitation RF pulse. The position-dependent precession frequencies originating from the magnetic field gradient is manifested in the MR signal in the form of this phase accrual, which depends on the strength and the duration of the gradient, and

is given by

$$\begin{aligned}\phi(\vec{r},t) &= -\int_0^t dt'\omega_G\left(\vec{r},t'\right) \\ &= -\gamma\int_0^t dt'\vec{G}\cdot\vec{r}\left(t'\right). \end{aligned} \tag{2.49}$$

It is now convenient to define $\vec{k}(t)$ as

$$\vec{k}(t) \equiv \frac{\gamma}{2\pi}\int_0^t dt'\vec{G}\left(t'\right). \tag{2.50}$$

Using the definition of $\vec{k}(t)$, up to a constant, the signal can be expressed as

$$s(\vec{k}(t)) = \int d^3r\rho(\vec{r})e^{-i2\pi\vec{k}(t)\cdot\vec{r}}. \tag{2.51}$$

This shows that up to a constant, the signal expressed as a function of $\vec{k}$ is simply the Fourier transform of the spin-density distribution. This means that if magnetic field gradients are used to acquire signal measurements in "k-space", which is the Fourier conjugate to "position space" $\vec{r}$, then, the spin density can be recovered simply by taking the inverse Fourier transform of the acquired k-space data:

$$\rho(\vec{r}) = \int d^3ks(\vec{k})e^{+i2\pi\vec{r}\cdot\vec{k}}. \tag{2.52}$$

Until now we have written $\vec{k}$ as a three dimensional vector. Since there are actually 3 sets of physical gradients of the MRI system, one along each of the principal axes in the lab frame, and each can be turned on and off separately, it is convenient to break down $\vec{G}$, and therefore $\vec{k}$, into their principal components:

$$k_x(t) \equiv \frac{\gamma}{2\pi}\int_0^t dt'G_x\left(t'\right) \tag{2.53}$$

$$k_y(t) \equiv \frac{\gamma}{2\pi}\int_0^t dt'G_z\left(t'\right) \tag{2.54}$$

$$k_z(t) \equiv \frac{\gamma}{2\pi} \int_0^t dt' G_y(t') \,. \tag{2.55}$$

In this notation, the signal can be rewritten as

$$s(k_x, k_y, k_z) = \int dx dy dz \rho(x, y, z) e^{-i2\pi(k_x x + k_y y + k_z z)}, \tag{2.56}$$

and the generalized spin density can be recovered as

$$\begin{aligned} \rho(x, y, z) &= \int dk_x dk_y dk_z s(k_x, k_y, k_z) e^{+i2\pi(k_x x + k_y y + k_z z)} \\ &= \mathscr{F}^{-1}(s(k_x, k_y, k_z)). \end{aligned} \tag{2.57}$$

As derived and written, the limits of integration in both Eqs 2.56 and 2.57 are assumed $(-\infty, \infty)$ and position and spatial frequencies are assumed continuous (i.e. with infinitesimally small dr and dk).

2.3.2 Frequency encoding vs phase encoding

As established in the previous section, the basis of MRI relies on position encoding using magnetic field gradients, which creates intentional position-dependence of the Larmor frequency. There are two ways of implementing the position encoding using gradients, "frequency encoding" and "phase encoding". This section is concerned with introducing and using these two implementation techniques based on discrete k-space sampling for imaging.

Equations 2.56 and 2.57 established a theoretical three-dimensional linear mapping between position space and its Fourier conjugate, k-space. To collect the k-space signal for Fourier transformation into the corresponding spin density map (i.e. form an image), the k-space signal must be sampled at all spatial frequencies, or said differently, all k-space points. Sampling the k-space at arbitrarily fine increments requires infinite time. Therefore, in practice, the k-space is sampled discretely and

for a limited range to make data acquisition feasible.

In the case of discrete transformation, the continuous integral becomes a discrete sum over a limited range and discrete sampling bins, in both conjugate spaces. Parallel with Eqs 2.56 and 2.57, the relationship between the discretely sampled k-space and its corresponding density map using the three-dimensional discrete Fourier transform is given by

$$S\left(p_x\Delta k_x, p_y\Delta k_y, p_z\Delta k_z\right) = \sum_{q_x=-N_x/2}^{N_x/2-1}\sum_{q_y=-N_y/2}^{N_y/2-1}\sum_{q_z=-N_z/2}^{N_z/2-1}\rho[q_x\Delta x, q_y\Delta y, q_z\Delta z]e^{-i2\pi(p_xq_x\Delta x\Delta k_x+p_yq_y\Delta y\Delta k_y+p_zq_z\Delta z\Delta k_z)} \tag{2.58}$$

$$\rho\left(q_x\Delta x, q_y\Delta y, q_z\Delta z\right) = \frac{1}{N_xN_yN_z}\sum_{p_x=-N_x/2}^{N_x/2-1}\sum_{p_y=-N_y/2}^{N_y/2-1}\sum_{p_z=-N_z/2}^{N_z/2-1}S[p_x\Delta k_x, p_y\Delta k_y, p_z\Delta k_z]e^{+i2\pi(p_xq_x\Delta x\Delta k_x+p_yq_y\Delta y\Delta k_y+p_zq_z\Delta z\Delta k_z)}. \tag{2.59}$$

Here N_x, N_y, and N_z are the number of k-space samples along k_x, k_y, and k_z dimensions, respectively, and k_x, k_y, and k_z are the spatial frequency variables corresponding to their Fourier conjugate spatial variables x, y, and z, respectively. The discrete sums in the above expressions have increments Δr and Δk with limited ranges $(-r_{max}, r_{max})$ and $(-k_{max}, k_{max})$. This discretization effectively creates volume elements (voxels) with dimensions Δr and Δk in image- and k- spaces, respectively. Please note that "image space" and "position space" are used interchangeably throughout this thesis.

There are two ways to collect signal throughout the k-space. One method, called frequency encoding, is to turn on gradients to traverse k-space on a line extending from one edge of k-space FOV to the other while acquiring the signal. In this case, assuming that the gradients applied during signal measurement maintain constant amplitude, the sample signal represents the signal intensity and phase to be allocated to uniformly sampled k-space locations along a line. If only a gradient is applied

along the x direction while the signal is being collected, then the signal corresponds to k-space locations along k_x.

The other method of k-space sampling is to turn on and off appropriate gradients before acquiring the signal to traverse to a particular location in k-space, and arrive at a desired *spatial* frequency location (i.e. k-space point). Typically, this technique is used in one direction, e.g. y direction, to arrive at a different starting position for the frequency encode line, then acquire signal during application of x gradient to perform frequency encoding along a different k-space line, as shown in Fig 2.8. It is also posssible to perform phase encoding without frequency encoding, in wich the signal is acquired at a particular k-space location, without any gradient being applied at the sme time. An imaging pulse sequence configured in this way is called a "fully phase encoded" pulse sequence. As discussed in Sec 2.6, this type of pulse sequence can be used to acquire spatially resolved spectral information, and is often termed "chemical shift imaging" or CSI. The signal can then be read out at that spatial frequency and assigned accordingly, while no gradients are on. Whereas the spatial frequency $k(t)$ in frequency-encoding is a function of time while the gradient is on, in phase-encoding the spatial frequency being sampled is independent of time. That is to say, depending on the gradient amplitudes, if it takes time τ to apply the appropriate gradients to arrive at the desired k-space location, once the gradients are turned off, the spatial frequency $k(\tau)$ remains constant while being acquired.

In summary, frequency encoding is done by acquiring signal while the gradients are on. In contrast, phase encoding is done by applying gradients first, with the option to acquire signal using frequency encoding or without, after the phase-encoding gradients are complete.

2.3.3 Practical considerations of frequency and phase encoding

In this section, we provide the practical aspects of discrete k-space sampling using frequency and phase encoding. In order to appropriately collect and allocate k-space signal, an evenly spaced grid of k-space points is considered for sampling.

Recall that in frequency encoding, k-space signal along a line is acquired while the gradients are on, and the direction of the line is determined by the axis of the applied gradients. Consider application of a gradient along G_x to read out signal along a given 2D k-space line k_y, from one end of the line at spatial frequency $-k_x^{max}$ to the the other end at spatial frequency k_x^{max}. On an evenly-spaced sampling scheme, the signal should be allocated to discrete points with spatial frequency spacing Δk_x along the k_y line. If the length of the line is $2k_x^{max}$, then the signal is divided into $\frac{2k_x^{max}}{\Delta k_x}$ bins and allocated chronologically to the k-space points along the line as the signal is being read out. This signal readout scheme along a k-space line can be extended to any arbitrary dimension, as long as the appropriate gradients are applied to define the arbitrary dimension.

On the other hand, consider phase-encoding, in which the gradients are turned on (in the absence of signal readout) to traverse k-space to arrive at the desired k-space coordinate (spatial frequency). If the signal is read out after the gradients have been turned off, all of the measured signal is available for allocation to the current k-space coordinate. This can either be done by averaging over the available signal, or storing the entire signal at each location which will be discussed explicitly in Sec 2.6.

For 1D imaging, a line of k-space signal must be acquired. Similarly, for 2D and 3D imaging, a plane, and a "slab" of k-space points must be acquired, respectively. Since it is natural to acquire signal along a line of k-space using frequency encoding, for 2D and 3D imaging schemes, frequency encoding can be used to acquire parallel lines of k-space preceded by phase encoding in the other dimension(s). Combining frequency and phase encoding is the basis of gradient-echo imaging, which will be

presented in Sec 2.3.5.

The Fourier transform property dictates that

$$\Delta r = \frac{1}{2k_{max}}, \tag{2.60}$$

along a particular dimension. Or given in components

$$\begin{aligned} \Delta x &= \frac{1}{2k_x^{max}} \\ \Delta y &= \frac{1}{2k_y^{max}} \\ \Delta z &= \frac{1}{2k_z^{max}}. \end{aligned} \tag{2.61}$$

This is to say that the resolution of the image is determined by the outer most edge of the sampled k-space (the higher desired resolution, the further in k-space should data be sampled). Since Fourier transform is a linear mapping between the two reciprocal spaces, the inverse of Eq 2.60 holds along any given dimension

$$\Delta k = \frac{1}{2r_{max}}, \tag{2.62}$$

which implies that for large (in volume) distribution of spins, finer sampling rate should be used. We define image field-of-view as $FOV = r_{max} - (-r_{max}) = 2r_{max}$. If Eq 2.62 is violated such that

$$FOV > \frac{1}{\Delta k}, \tag{2.63}$$

i.e. if FOV is smaller than the size of the spin distribution (size of the object being imaged), part of the image will be "wrapped-back" onto the image, a phenomenon coined "aliasing". For example, if a square box of spins with side ℓ is to be imaged with $FOV = 0.7\ell$, the 0.3ℓ that did not "fit" inside the FOV will get wrapped-back onto the image. An example of the aliasing phenomenon is demonstrated in Fig 2.5. This makes sense: The RF pulse that excites the spins in the box tips all of the spins

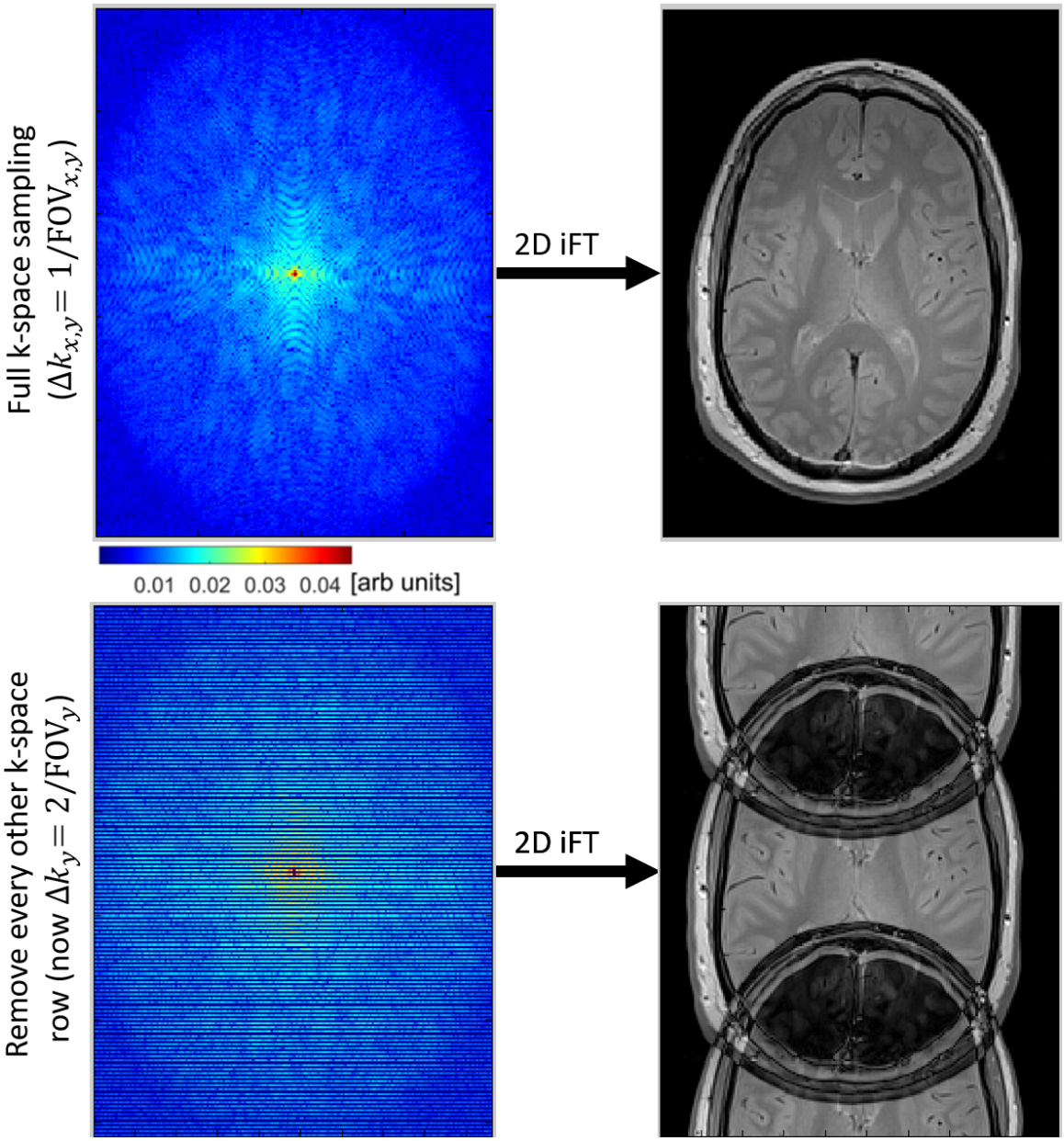

Figure 2.5: Example of aliasing due to under-sampling of the k-space along the phase encode dimension. The top row shows the fully sampled k-space image with its corresponding Fourier conjugate map, the image of a brain. If the k-space is under-sampled, like done in the bottom row, which is equivalent to saying if the FOV of the image is insufficient determined by the Nyquist criterion, part of the image will be aliased, or "folded-back" onto itself. Note that under-sampling the k-space by a factor of 2 in image space is manifested by a copy of the image superimposed on itself, but offset by $\frac{FOV}{2}$. Diagram courtesy of Prof. Miller and obtained in BME 8783 coursework.

(assuming no flip-angle profile) into the transverse plane where the magnetization and therefore signal emanated by the spins is picked up by the coil regardless of the size of the field-of-view. Since all spins are position encoded, and their spin density still appears in FOV, but superimposed unfavorably onto other parts of the image. Therefore, one should design the imaging parameters such that

$$\text{size of imaged object} \leq \frac{1}{\Delta k}, \tag{2.64}$$

where Eq 2.64 is known as the Nyquist theorem which states that k-space should be sampled at least as finely as the reciprocal of the minimum necessary FOV.

It is worth mentioning that aliasing is only a practical concern when employing phase encoding. Along the frequency encoding direction, the k-space can be sampled arbitrarily finely at no additional acquisition time. Whereas in phase-encoding, signal in each k-space point must be acquired independently with dedicated excitation and gradient encoding, applications of which are time-consuming.

Other notable imaging parameters and their dependencies on image quality are as follows. As derived in Eq 2.35, the MR signal can be expressed as the following

$$S \propto \int_{\text{sample}} d^3r \rho(\vec{r}) e^{-t/T_2^*(\vec{r})} e^{[i(\omega_0)t + i\phi_0(\vec{r})]}. \tag{2.65}$$

Evidently, the signal is directly proportional to the volume integral of effective spin density. Therefore, if the spin density is uniformly distributed throughout the sample, the signal is directly proportional to the imaging voxel size. The bigger the imaging voxel, the higher the net number of spins in the voxel, and the higher the magnetization and consequently, the higher the signal. This will be relevant in Chapter 5, where the imaging voxel size in signals generated from thermally polarized and hyperpolarized ^{3}He samples are different and need consideration when comparing the two signals.

Another consideration in MRI is noise σ. Similar to any other application of

signal processing, $\sigma \propto \sqrt{(t_{ADC})^{-1}}$, where t_{ADC} is the measurement time (ADC = analog-to-digital converter). An important image quality that can be experimentally controlled, and is of great importance is signal-to-noise ratio (SNR) defined as SNR $\equiv \frac{S}{\sigma}$. SNR depends on the size of the voxel in each dimension Δx, Δy, and Δz, and number of acquisition N_{acq} (for averaging), number of voxels along each dimension N_x, N_y, and N_z, and data-sampling duration of each k-space point Δt

$$\text{SNR/ voxel } \propto \Delta x \Delta y \Delta z \sqrt{N_{acq} N_x N_y N_z \Delta t}. \tag{2.66}$$

Note that for frequency encoding time $t_{ADC} = N_x \Delta t$, and $V_{voxel} = \Delta x \Delta y \Delta z$, Eq 2.66 can be rewritten as

$$\text{SNR/ voxel } \propto V_{voxel} \sqrt{N_{acq} N_y N_z t_{ADC}}. \tag{2.67}$$

For the same voxel size in phase encoding and frequency encoding methods, much higher SNR can be achieved using phase encoding. In phase encoding, the duration of signal acquisition t_{ADC} can be arbitrarily long with the only limitation being T_2^* decay of the signal. Therefore, the noise level in signal acquired using phase-encoding is substantially lower than the noise level using frequency encoding, if longer $t_{ADC}/voxel$ is exploited in phase-encoding. Whereas in frequency encoding, with the same t_{ADC}, the same measured signal must be divided into $2k^{max}/\Delta k$ bins, and allocated accordingly to the k-space points along the measurement line. However, this advantage comes at a cost, which is elongated acquisition time, at least by a factor of $2k^{max}/\Delta k$. Of course, additional time is required for each excitation and gradient encoding, which is done once for each line in frequency encoding, but done for k-space traversal every phase encoding step.

2.3.4 Slice selection

Commonly in MRI, images are acquired in 2D "slices" to obtain cross-sectional views of an object, for instance, the human body. This is done by simultaneous application of an RF pulse and a gradient normal to the plane of desired image, combination of which selectively excites only a region of space with spins contained within a slice. We define the slice-select axis as the direction perpendicular to the plane of the desired slice. Here we discuss slice-selection along the z axis. We saw earlier in Sec 2.3.1 that application of a gradient along an axis (G_z in this case), causes the precession frequency to be a linear function of position along the slice-select axis as

$$f(z) = f_0 + \gamma G_z z. \tag{2.68}$$

Since the goal is to excite a uniform slice such that all spins in the slice see the same flip-angle and experience the same initial phase after excitation, the profile of the excitation in frequency space should ideally be a boxcar function. To excite an infinitesimal slice through z_0, for example, the RF frequency should be tuned to $f(z_0)$, which is the frequency of the spins at z_0. To excite a region of spins with finite thickness Δz, however, the RF should be tuned to the range of frequencies $\Delta f = f_{z+\frac{\Delta z}{2}} - f_{z-\frac{\Delta z}{2}}$ corresponding to the desired slice. Therefore the bandwidth of the RF pulse BW_{RF} in frequency domain is given by

$$\begin{aligned} BW_{RF} &\equiv \Delta f \\ &= (\gamma/2\pi G_z z_0 + \gamma/2\pi G_z \Delta z/2) - (\gamma/2\pi G_z z_0 - \gamma/2\pi G_z \Delta z/2) \\ &= \gamma/2\pi G_z \Delta z. \end{aligned} \tag{2.69}$$

Therefore, to excite a slice with thickness $TH \equiv \Delta z$, the appropriate bandwidth BW_{RF} and gradient G_z should be applied such that the following holds:

$$TH = \frac{BW_{RF}}{\gamma/2\pi G_z}. \tag{2.70}$$

The relationship between the frequency bandwidth and thickness along the slice-select axis is demonstrated in Fig 2.6. The RF pulse that is simultaneously applied with

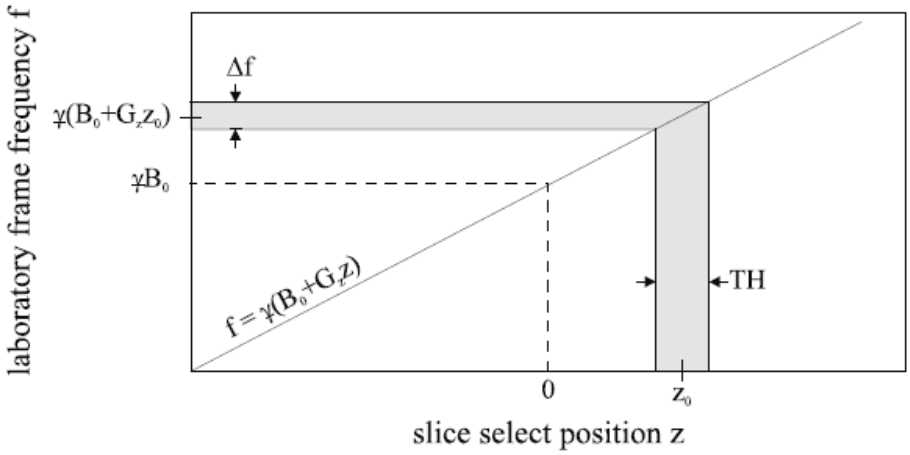

Figure 2.6: The precession frequency (f) in the laboratory frame as a function of position along the slice select axis when a gradient G_z is applied along the z-direction. The frequency bandwidth $\Delta f \equiv BW_{RF}$ (the shaded horizontal strip) is such that the slice region of thickness Δz (the shaded vertical strip) is symmetrically excited. Since the slice is offset from the origin in the z direction by z_0, the center frequency of the rf pulse is offset from the static Larmor frequency $\frac{\gamma}{2\pi}B_0$ by $\frac{\gamma}{2\pi}G_z z_0$ as indicated. Diagram courtesy of Haake [68].

the slice-select gradient ideally has a boxcar profile with sharp edges such that all and only spins within the slice are excited and all spins outside the slice remain along the longitudinal direction. For this reason, an RF pulse with envelope-waveform of a $\text{sinc}(\gamma B/BW) \equiv \frac{\sin(\gamma B/BW)}{\gamma B/BW}$ in the time domain is used since the Fourier transform of a sinc with infinite lobes is a perfect boxcar. An example of a simulated sinc waveform with its corresponding Fourier conjugate, with is the frequency response, is given Fig 2.7. Although, for practical purposes concerning duration of acquisition,

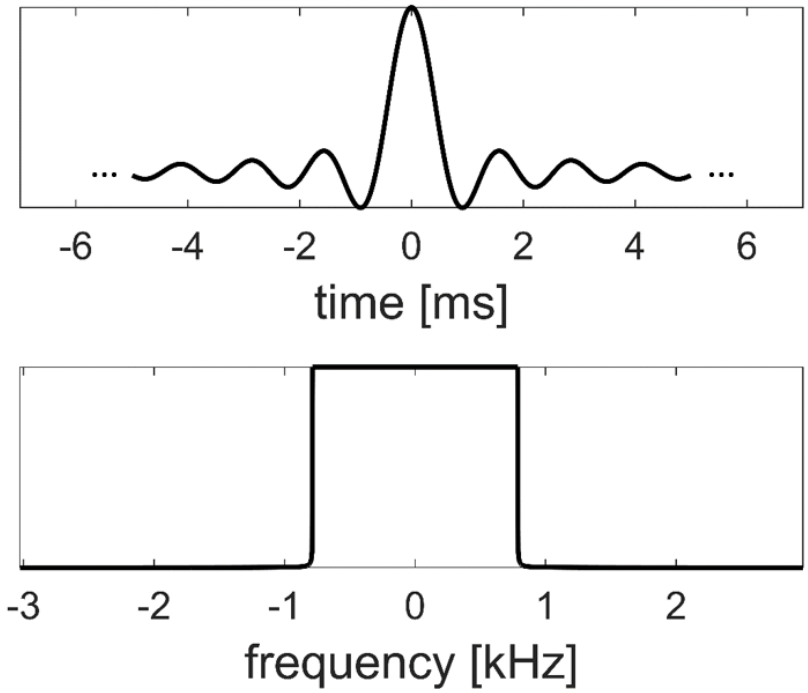

Figure 2.7: Simulated sinc RF pulse and its corresponding frequency response. If this pulse is applied for excitation, only spins resonating with Larmor frequencies that fall within the nonzero frequency range ($\sim -875\,\text{Hz} < f < 875\,\text{Hz}$) of the corresponding boxcar waveform are excited.

the excitation pulse is truncated such that the pulse in the time domain has just a few side-lobes.

2.3.5 Slice-selective gradient-echo imaging

A "pulse sequence" describes the ordering of application of RF pulses, magnetic field gradients, and signal readout mechanism (data acquisition system, DAQ, also known as analog-to-digital converter, ADC). Here we describe a 2D slice-selective pulse sequence for data acquisition on a line-by-line basis. The gradient-echo pulse sequence is composed of series of "event blocks" with repetition time (TR) as shown in Fig 2.8, and will be discussed in the following. After application of an RF pulse during which the flat top of the slice-select gradient G_z (also referred to as G_{ss}) is

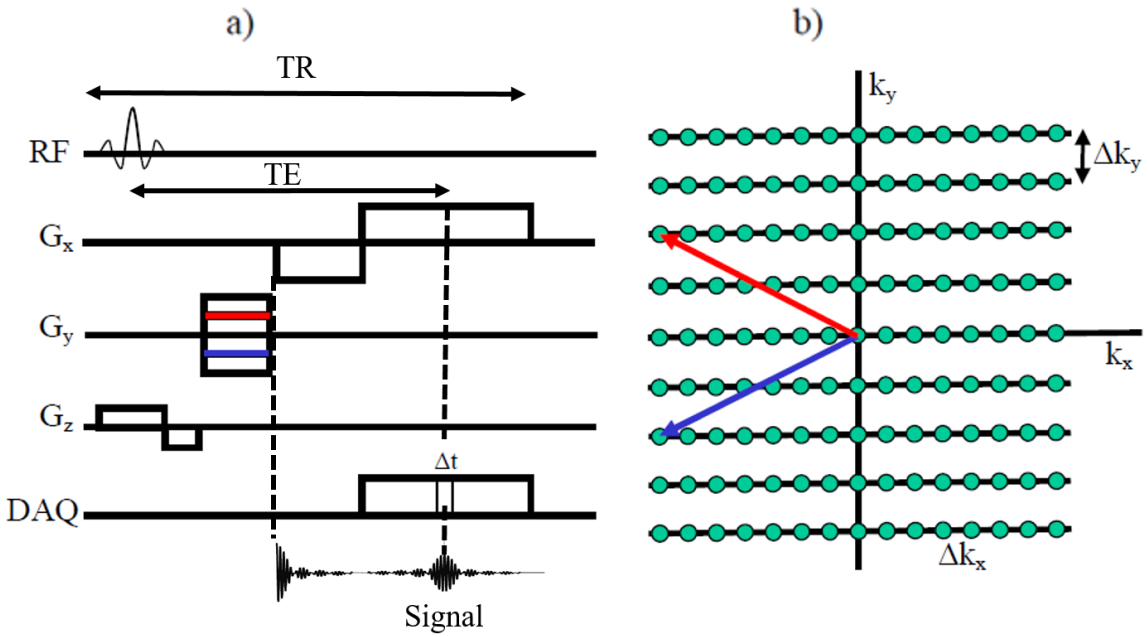

Figure 2.8: a) Pulse sequence diagram for a 2D slice-selective Cartesian k-space acquisition. b) Corresponding k-space trajectory. One horizontal line is acquired per RF excitation. Diagram reproduced and combined from [68] and [5] and modified slightly.

applied, the subsequent gradients G_x and G_y are applied to traverse the k-space. In the convention presented here, which is also the common convention in the field, the frequency encoding is done using G_x and the phase encoding is done using G_y. First, G_y ("phase-encode" gradient) is applied to move up or down along the k_y axis to get to the desired line of k-space.

After the application of G_y, which is indicated by the first vertical dashed line, the negative lobe of G_x ("frequency-encode" gradient) is turned on to move to the left-most edge of k-space. This can be done simultaneously with G_y, and in fact is commonly done in most pulse sequences. However, for separating the explanation of the phase encoding step from frequency encoding step, the two are applied at different times. Recall that application of a gradient dephases spins along its direction (coherent dephasing if particles are not allowed to move), which in turn reduces the net transverse magnetization, and consequently the signal. Therefore, the negative

lobe G_x acts to dephase the signal such that its amplitude decays while the gradient is on. It can be seen in the signal waveform in Fig 2.8 that the amplitude drops close to zero, but does not entirely diminish. Instead, it traces out the Fourier transform of the spin distribution, which due to coherent loss of alignment between spins in the transverse plane caused by the gradient, happens to have a much lower (but nonzero) amplitude away from k-space center ($k = 0$). After G_y and the negative lobe of G_x gradients are applied, the opposite lobe of G_x (positive polarity in Fig 2.8) is turned on to traverse k-space from left edge all the way to the right edge along k_x during which the signal is read out using the DAQ (or ADC). The positive lobe of G_x, on the other hand, acts to recover loss of coherence done by the negative lobe of G_x, in turn increasing the signal that was coherently decayed. Therefore, the T_2-decayed signal forms an "echo" at the center of k_x, indicated by the second dashed line in Fig 2.8.

The time between the center of the RF pulse and the center of echo reached at the k_x center is called "echo-time" (TE). This procedure is then repeated exactly the same way, but instead a different k-space line is read out (k_x line with a different k_y coordinate). Two examples of k-space lines are color-coded red and blue in Fig 2.8.

Discrete Fourier transformation (and its inverse transformation) is computationally intensive with computation time $(n^2)^d$, if n is the number of operations for d-dimensional image sets. Fast Fourier transform (FFT) and iFFT (inverse Fourier transform) are much more efficient algorithms that can be used instead to go between one domain and its frequency domain with computation time $(n \ln n)^d$, substantially reducing computational time needed for transformation between the two conjugate spaces. An example of a 2D image obtained from inverse fast Fourier transform of a 2D k-space data is shown in the top row of Fig 2.5. Notice that the majority of the signal in the k-space map is concentrated near the center.

2.4 Diffusion attenuation of MR signal

This section is concerned with the behavior of MR signal generated by spins that are moving in space during application of a magnetic field gradient superimposed on the static field.

In gases and liquids, individual particles diffuse within the medium via Brownian motion. The rate at which particles become displaced from their initial positions is characterized by the diffusion coefficient, also called diffusivity, usually labeled by the variable D. Mathematically, the diffusion coefficient D for an ensemble of identical particles in gaseous and liquid media is given by

$$D(t) \equiv \frac{\left\langle |\vec{r}(t) - \vec{r}(0)|^2 \right\rangle}{2t \cdot N_d}, \tag{2.71}$$

where $\vec{r}(0)$ and $\vec{r}(t)$ are the position of a given particle at times 0 and t, respectively, N_d is the dimensionality, and the brackets represent the ensemble average. The above expression is just the mean squared displacement of an ensemble of particles in a region of space, per unit time per dimension. If the only impediment to diffusion is collision with other diffusing particles, this situation is called free diffusion and the diffusion coefficient $D(t)$ becomes a constant, usually labeled D_0, that is an inherent property of the medium.

From kinetic theory of gases, for a pure (unmixed) gas one can write

$$D_0 = \frac{1}{3}\ell v_T = \frac{2}{3}\sqrt{\frac{k_{\mathrm{B}}^3}{\pi^3 m}}\frac{T^{3/2}}{Pd^2}, \tag{2.72}$$

where $\ell = \frac{k_{\mathrm{B}}T}{\sqrt{2}\pi d^2 P}$ is the mean free path, $v_T = \sqrt{\frac{8k_{\mathrm{B}}T}{\pi m}}$ is the mean thermal speed of the gas, k_B is the Boltzmann constant, T is the temperature, and P is the pressure of the gas with particles of diameter d and mass m. The inverse relationship between diffusivity and pressure is of importance in our experiments presented in Chapter 4, because the pressure of ^{3}He dispensed in the tubes is different for each experiment.

At one atmospheric pressure and standard temperature, for example, the empirical free diffusivity of pure ^{3}He is $D_0 = 1.98$ cm^2/s.

However, if the medium is contained in some sort of structure that impedes its particles' diffusivity, such as ^{3}He gas inside a pellet or ^{3}He or ^{129}Xe gas inside the lungs, then this situation is referred to as restricted diffusion. Under conditions of restricted diffusion, the Diffusivity computed using Eq 2.71 is no longer a constant and is always smaller than the free diffusivity D_0, because the mean squared displacement is restricted by the confining structure. Obviously, the extent of diffusion in a medium depends on the degree of restriction imposed by this confining structure, i.e. the more confined its surrounding, the lower diffusivity of the medium, and the smaller D is compared with D_0.

In the present section we derive an expression describing the time evolution of the MR signal arising from an ensemble of freely diffusing spins during the application of a specific type of gradient waveform. The waveform of interest is composed of two opposite lobes applied back-to-back along a chosen axis. We will see that diffusion of transverse spins during such a bipolar gradient attenuates the MR signal, and the degree of attenuation depends on the particle diffusivity. We will derive a quantitative expression for signal attenuation under such circumstances, which serves as the technical basis for diffusion-weighted MRI discussed in Sec 2.5.

Let us assume that we have already excited a region of gas, and in turn created transverse magnetization, and consequently, signal S_0 generated by the excited spins, which can be expressed as:

$$S_0 \propto \int d^3r e^{-i\phi(\vec{r})}. \tag{2.73}$$

Consider the bipolar gradient depicted in Fig 2.9, with each lobe having exactly the same duration Δ and amplitude G. This gradient waveform is referred to as the "diffusion-sensitizing gradient". In the following mathematical treatment, we derive the equation for signal at the end of the gradients denoted as S_b.

The amplitude of the signal at the end of the diffusion-sensitizing gradient wave-

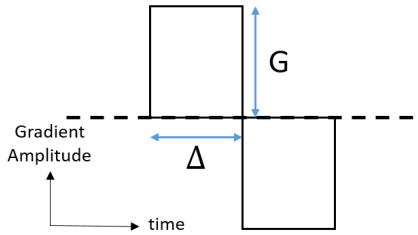

Figure 2.9: Waveform of the diffusion-sensitizing bipolar gradient. Both lobes of the gradient waveform share the same flat-top time Δ and the gradient amplitude G. The net area of the gradient is zero.

form will depend on the net phase accrual of individually diffusing spins during the application of the gradients. Since the phase accrual varies only along the axis of the gradient, one can model the diffusion of the molecules in 1D. We will model diffusion as a discrete random walk along a 1D grid of equally spaced locations with fixed time step. Therefore, the signal expressed in Eq 2.73 can be written in the form of a discrete sum:

$$S_0 \propto \sum_n S_{0,n} \propto \sum_n e^{-i\phi_n}, \tag{2.74}$$

where $S_{0,n}$ is the signal generated by the n^{th} spin. We seek to determine the signal at the end of the gradients by computing ϕ_n.

In our model, at each time step, the particles can move one distance step (δ) per time step (τ). Invoking Eq 2.71, we know that the diffusivity of the particle at time τ is given by $D = \frac{\delta^2}{2\tau}$. Let us consider one particle and follow its phase accrual as it moves along the gradient axis while the diffusion gradients are on. We assume the particle takes M steps during diffusion time $t = 2\Delta = 2M\tau$. The starting position of the particle is chosen to be $x_0 = 0$, the position of the particle at j^{th} time step is $x_j = \delta \sum_{k=1}^{j} \epsilon_k$, and $\epsilon_k = \pm 1$ decides the direction of the k^{th} time step completely randomly. Recall from Eq 2.49 that the phase accrual during application of a linear gradient is given by $\phi(\vec{r}, t) = -\gamma \int_0^t dt' \vec{G} \cdot \vec{r}(t')$. Invoking Eq 2.49, and realizing that the phase accrual has opposite polarity during each lobe of the gradient, we write

$$\begin{aligned}\phi(2M\tau) &= \sum_{j=1}^{2M} \Delta\phi_j \\ &= \gamma G\tau \sum_{j=1}^{M} x_j - \gamma G\tau \sum_{j=M+1}^{2M} x_j \\ &= \gamma G\tau (\sum_{j=1}^{M} \delta \sum_{k=1}^{j} \epsilon_k - \sum_{j=M+1}^{2M} \delta \sum_{k=1}^{j} \epsilon_k) \\ &= \gamma G\tau\delta (\sum_{j=1}^{M} \sum_{k=1}^{j} \epsilon_k - \sum_{j=M+1}^{2M} \sum_{k=1}^{j} \epsilon_k). \end{aligned} \tag{2.75}$$

For an ensemble of many spins, the mean squared phase is given by

$$\left\langle \phi(2M\tau)^2 \right\rangle = \gamma^2 G^2 \tau^2 \delta^2 \left\langle \left(\sum_{j=1}^{M} \sum_{k=1}^{j} \epsilon_k - \sum_{j=M+1}^{2M} \sum_{k=1}^{j} \epsilon_k \right)^2 \right\rangle. \tag{2.76}$$

As done in Haacke [68], it can be shown that

$$\left\langle \left(\sum_{j=1}^{M} \sum_{k=1}^{j} \epsilon_k - \sum_{j=M+1}^{2M} \sum_{k=1}^{j} \epsilon_k \right)^2 \right\rangle \approx 2\frac{M^3}{3}, \tag{2.77}$$

and Eq 2.76 becomes

$$\left\langle \phi(2M\tau)^2 \right\rangle = \frac{2}{3}\gamma^2 G^2 \tau^2 \delta^2 M^3. \tag{2.78}$$

Substituting $\Delta = M\tau$ and $D = \frac{\delta^2}{2\tau}$, the mean squared phase of an ensemble of spins is given by

$$\begin{aligned}\left\langle \phi(2\Delta)^2 \right\rangle &= \frac{2}{3}\gamma^2 G^2 2\frac{\delta^2}{2\tau}(M\tau)^3 \\ &= \frac{4}{3}\gamma^2 G^2 D\Delta^2. \end{aligned} \tag{2.79}$$

Recall that our goal is to determine the relative strength of the signal generated by the entire ensemble of spins at the end of the diffusion gradients.

The net phase is the result of sum of *large* number of random steps, therefore, the central limit theorem is invoked, which states that the distribution of the phases in the ensemble takes the form of a Gaussian distribution, and one can write

$$P(\phi_n) = \frac{1}{\sigma\sqrt{2\pi}} \int e^{\frac{-\phi_n^2}{2\sigma^2}}, \tag{2.80}$$

where σ is the variance in the phase and $\sigma^2 = \langle \phi_n^2 \rangle$.

Using the above probability distribution and integrating over all spin phases, shifting from discrete to continuous treatment, the net signal can be rewritten as

$$\begin{aligned} S &\propto \int_{-\infty}^{\infty} P(\phi_n) e^{i\phi_n} d\phi_n \\ &= \frac{1}{\sigma\sqrt{2\pi}} \int_{-\infty}^{\infty} e^{\frac{-\phi_n^2}{2\sigma^2}} e^{i\phi_n} d\phi_n. \end{aligned} \tag{2.81}$$

Next, we complete the square for the exponent $(\frac{-\phi_n^2}{2\sigma^2} + i\phi_n)$ and write

$$\begin{aligned} \frac{-\phi_n^2}{2\sigma^2} + i\phi_n &= -\frac{1}{2\sigma^2}\left(\phi_n^2 - i2\sigma^2\phi_n + i^2\sigma^4\right) + \frac{i^2\sigma^2}{2\sigma^2} \\ &= -\frac{1}{2\sigma^2}(\phi_n - i\sigma^2)^2 - \frac{\sigma^2}{2}. \end{aligned} \tag{2.82}$$

Plugging Eq 2.82 into Eq 2.81, we write

$$S \propto \frac{1}{\sigma\sqrt{2\pi}} \int_{-\infty}^{\infty} e^{-\frac{1}{2\sigma^2}(\phi_n - i\sigma^2)} e^{-\frac{\sigma^2}{2}} d\phi_n. \tag{2.83}$$

Use of a simple change of variables $\phi = \phi_n - i\sigma^2$, which gives $d\phi = d\phi_n$, enables us to rewrite Eq 2.83 as

$$S \propto \frac{1}{\sigma\sqrt{2\pi}} e^{-\frac{\sigma^2}{2}} \int_{-\infty}^{\infty} e^{-\frac{\phi^2}{2\sigma^2}} d\phi. \tag{2.84}$$

Realizing that $\frac{1}{\sigma\sqrt{2\pi}} \int_{-\infty}^{\infty} e^{-\frac{\phi^2}{2\sigma^2}} d\phi = 1$ is a normalized Gaussian distribution, the net signal can be written as

$$S \propto e^{\frac{\sigma^2}{2}}. \tag{2.85}$$

Lastly, recall that $\sigma^2 = \langle \phi_n^2 \rangle = \frac{4}{3}\gamma^2 G^2 \Delta^3 D$, and the signal is given by

$$S \propto e^{-\frac{1}{2}\frac{4}{3}\gamma^2 G^2 \Delta^3 D} = e^{-\frac{2}{3}\gamma^2 G^2 \Delta^3 D}. \tag{2.86}$$

It is convenient at this point to define the b-value for the bipolar diffusion-sensitizing gradient $b \equiv \frac{2}{3}\gamma^2 G^2 \Delta^3$ to rewrite the signal as

$$S_b \propto e^{-bD}. \tag{2.87}$$

The above proportionality expression is for the signal at the end of the bipolar diffusion gradient, generated by spins that underwent Brownian motion along the gradient axis. D is the diffusivity of gas, and b-value encapsulates the gradient waveform including its timing and amplitude. Therefore, it can be seen in expression Eq 2.87 that with the application of such gradient, the b-value and its corresponding signal can be used to probe the diffusivity of the gas or the liquid being imaged. This process inherently sensitizes the motion of the particles, and the extent to which the particles diffuse can be used to assess degree of confinement as seen by the liquid or the gas. The proportionality constant in expression 2.87 is S_0 prior to the gradient application, and one can write

$$S_b = S_0 e^{-bD}. \tag{2.88}$$

In the above mathematical treatment, we derive the equation for signal at the end of the gradients denoted as S_b, in the absence of T_2 and T_2^*, to show the motion-sensitization achieved by the bipolar diffusion-sensitizing gradient. This equation is at the heart of diffusion-weighted MRI, which is the topic of next section.

2.5 Diffusion-weighted MRI

Diffusion-weighted MRI is a technique that exploits Eq 2.88 to probe the motion of the gas or liquid particles being imaged. Diffusion-weighted imaging can be performed

based on a variety of pulse sequences, here, we describe one based on slice-selective 2D gradient-echo sequence. This technique uses a set of at least two gradient-echo images, one with and one without application of a bipolar diffusion-sensitizing gradient. Diffusivity is then recovered in comparing the signal intensities in the images.

Consider taking two 2D images back-to-back, first with pulse sequence identical to that introduced in Sec 2.3.5, and the latter with a bipolar gradient as indicated in Fig 2.10. This technique employs the same gradient waveform as the one introduced

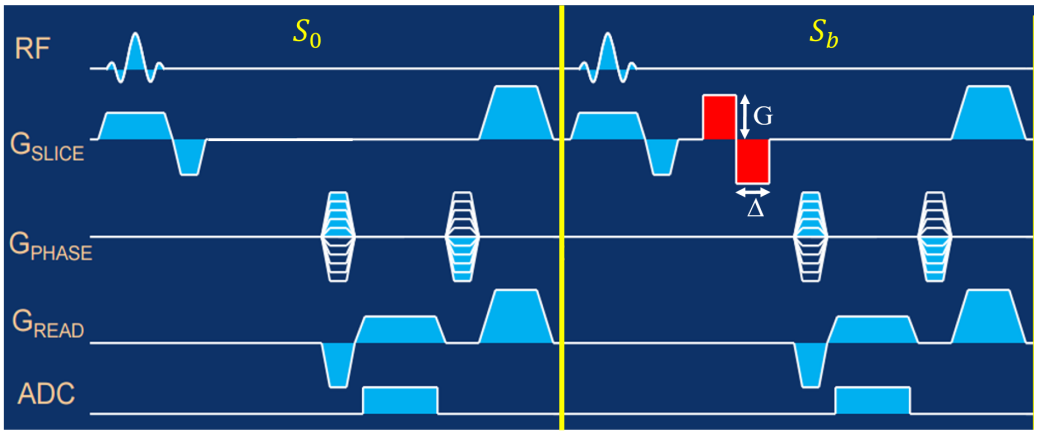

Figure 2.10: Left diagram represents the pulse sequence for the first 2D slice-selective gradient-echo image (S_0) and the right diagram shows the same sequence but with application of a bipolar diffusion-sensitizing gradient color coded red for the diffusion-weighted image (S_b). The yellow vertical line separates the two pulse sequences. Diagram courtesy of Prof. Miller and obtained in BME 8783 coursework.

in Fig 2.9 to create sensitivity to motion. The idea is to acquire the first image to obtain signal S_0, followed by the second image with the motion-sensitizing gradient, to obtain signal S_b. Therefore, the diffusivity of the spin ensemble being imaged is probed by experimentally measuring D from Eq 2.88.

The b-value is a parameter that can be carefully chosen in the experiment and depends on the diffusion gradient timing (scales with Δ^3) and the amplitude of the gradient (scales with G^2), therefore the gradient waveform is of great concern and can severely impact diffusion measurement. Depending on the time-scale of interest

in probing diffusion, the b-value can be tweaked to adjust the range of diffusion sensitivity of the technique. The goal is to design a gradient waveform with b-value resulting in degree of attenuation that spans the available dynamic range, such that $0.1 \lesssim e^{-bD} \lesssim 0.9$. The b-value for an arbitrary motion-sensitizing bipolar gradient waveform is given by [69]

$$\begin{aligned} b &= \gamma^2 \int dt \left(\int_0^t G(t')dt' \right)^2 \\ &= (2\pi)^2 \int dt \left(\gamma/2\pi \int_0^t G(t')dt' \right)^2 \\ &= (2\pi)^2 \int \left(k(t)\right)^2 dt. \end{aligned} \tag{2.89}$$

Note that b-value scales with γ^2. This is an important consideration in pulse sequence design implemented in Part B, where diffusion-weighted MRI of both ^{3}He and ^{129}Xe gases are performed.

The diffusivity is measured using the diffusion-attenuated signal for restricted diffusion, and is termed "apparent diffusion coefficient" (ADC), which depending on the degree of confinement deviates from free diffusion constant D_0. ADC is exploited in characterizing the degree of microstructure damage inside healthy and diseased lungs, and serves as the key quantity in Chapter 6.

2.6 Chemical shift imaging

Chemical shift imaging (CSI), or fully phase-encoded imaging, is a technique that obtains spatial and spectral distribution of nuclei that experience different local magnetic field strengths. Whereas this technique is normally used to acquire images of identical nuclei experiencing different local magnetic environments due to chemical bonds, we use this technique to acquire images of identical nuclei with different magnetic environments due to magnetic susceptibility differences.

Let us first examine a simple FID experiment (see Sec 2.1). Application of an excitation RF pulse with wide enough bandwidth to excite all of the spins in our sample generates an NMR signal, the strength of which is proportional to the number of excited spins, sine of the flip angle, and polarization level. The transverse signal decays with time constant T_2^*, which is the effective decay time constant that includes the additional decay due to field inhomogeneities across the sample. Taking the Fourier transform of the FID would therefore yield the frequency spectrum contained in the signal, and therefore the entire distribution of field inhomogeneities present in the excited region. Also, since there were no gradients applied prior to acquiring this FID, in the context of imaging presented in Sec 2.3, the amplitude and phase of the time-domain signal corresponds to the $k = 0$ sample (zero spatial frequency) in k-space.

The fully phase-encoded technique extends the acquisition of FID and its corresponding frequency spectrum to all of the spatial frequencies, i.e. all of k-space, by phase encoding along all dimensions. This is achieved by first exciting the spins in the region of interest, then applying s gradient pulse of appropriate strength and duration along each principal direction to create a desired spatial frequency (k-space location), and finally acquiring the signal during the ADC. Once signal acquisition is complete, the same gradient but with opposite polarity is applied to "unwind" the spatial frequency and return to the center of k-space. Then this process is repeated until all desired spatial frequencies (k-space locations) have been sampled. Therefore, all k-space trajectory is completed via phase-encoding, and not combination of both frequency and phase encoding like done in gradient-echo imaging. An example of the CSI pulse sequence is given in Fig 2.11.

Like all MRI techniques, the fully phase-encoded k-space data contains gradient-encoded position information that can be used to form an image. However, the fully phase encoded data has the added benefit that it also contains spectral information corresponding to the distribution of magnetic field shifts within each imaging voxel.

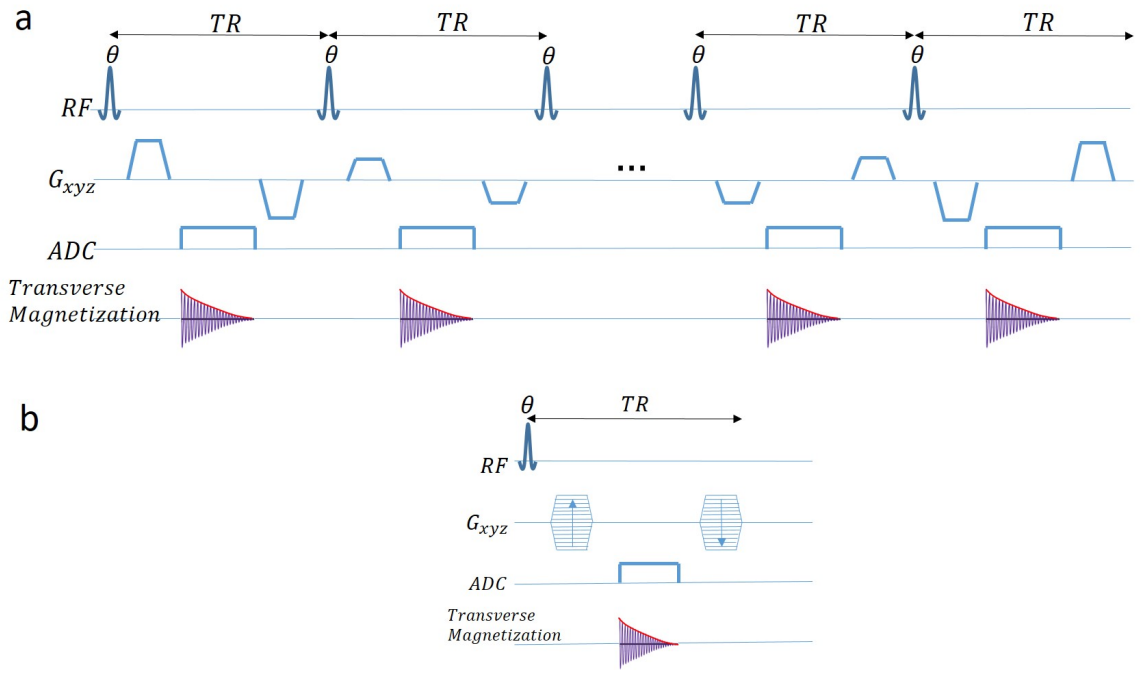

Figure 2.11: (a) Schematic diagram of a Cartesian fully phase-encoded pulse sequence obtaining FID data with a sequential order from one corner of the k-space to the opposite corner. (b) Compact form of the same pulse sequence. θ is the RF flip angle, TR is the repetition time, G_{xyz} are the gradients applied along x, y, and z (not simultaneously), and ADC is the analog-to-digital converter. Although not depicted here, a fully phase-encoded pulse sequence usually includes RF- and gradient spoiling, if TR is short compared with T1.

Consider a 4D data set, for example, with three of the dimensions corresponding to x, y, and z axes, and the other corresponding to time-domain signal of each FID. Each point in 3D k-space is encoded with three phase encoding tables, one along the x, one along the y, and one along the z axes. After each spatial phase encoding, the data is sampled at desired number of time points each with the same dwell time (which determines the spectral field-of-view), and for a finite length of time. The time of acquisition, i.e. ADC duration, determines the spectral resolution. To resolve the frequency information, one can take the Fourier transform in the time domain as described in Sec 2.2. To resolve the spatial density information, one must take the

inverse Fourier transform along each of the spatial dimensions. Therefore, the 4D data set can be resolved to a 3D image along with frequency spectrum available at each voxel.

Part A

Spin-polarized fusion

Chapter 3

Magnetostatics, diffusion, and imaging simulations

As described in Sec 2.6, the chemical shift imaging (CSI) technique provides both spectral and spatial information about the imaged spin density distribution. We will use CSI for permeation and absolute polarization measurements in the experiments presented in this thesis, because the differing magnetic susceptibilities between gas, glass, and pellet material cause slight shifts in the local magnetic fields, and thus slight shifts in the NMR frequency, that allow us to separately track ^{3}He inside and outside the pellet during the permeation process. In order to fully understand such effects toward formulating a sound approach to these experiments, in this chapter we develop a numerical simulation to study the magnetic field shifts caused by materials with nonzero magnetic susceptibility placed in an otherwise uniform static magnetic field B_0. First, we develop a method for numerical calculation of field disturbances caused by an arbitrary geometric arrangement of materials with differing magnetic susceptibilities in the scanner's 1.5 T magnetic field, based on Maxwell's equations under magnetostatic conditions, and apply this calculation to the specific geometry of our experimental setup.

Next, we develop a simulation of ^{3}He gas particles undergoing restricted diffusion within the geometry of our experimental setup and its associated field disturbances, and further study the effects of this motion on the resulting NMR signal. Lastly,

we add imaging gradients to the mix and simulate the acquisition of k-space data in order to better understand the effects of field inhomogeneity and ^{3}He diffusion on 2D slice-selective gradient-echo and CSI image acquisition.

3.1 Magnetostatics numerical calculation

In this section, we develop an iterative algorithm for calculating field disturbances caused by an arbitrary geometrical arrangement of materials with differing magnetic susceptibilities immersed in an otherwise uniform magnetic field. To do so, we first present the theoretical derivation of the iterative algorithm, as well as an iterative "telescoping" procedure in Sec 3.1.1. We then present a validation of our algorithm for a shell of magnetic permeability μ immersed in an otherwise uniform magnetic field, which has a known analytic solution in Section 3.1.2. And lastly, in Sec 3.1.3, we use the algorithm to calculate the field disturbances unique to the geometry of our experimental setup.

3.1.1 Theory and derivation of the iterative algorithm

Here we derive an iterative algorithm for calculation of magnetic field created by an arbitrary geometry immersed in an otherwise static magnetic field, from first principles. This will be the topic of Sec 3.1.1.1. To resolve the field disturbances in the geometry of our experimental setup, large-matrix (matrix size $> 1000 \times 1000 \times 1000$) operations are needed. Matrix operations of this size are computationally challenging. To address this issue, we develop an iterative "telescoping" field-of-view algorithm in Sec 3.1.1.2, which as we will see, can reduce the matrix size and computation time greatly.

3.1.1.1 Derivation of the iterative algorithm to determine scalar potential

Consider an empty region of space with static, perfectly uniform magnetic field B_0. Addition of material with magnetic susceptibility $\chi \simeq 0$ introduces field inhomogeneity throughout the region, while the material gains magnetization M. We can write the resulting magnetic field as

$$\mathbf{B}(\vec{r}) = \mu_0(\mathbf{H}(\vec{r}) + \mathbf{M}(\vec{r})) = \mu_0(1 + \chi(\vec{r}))\mathbf{H}(\vec{r}) = \mu\mathbf{H}(\vec{r}), \tag{3.1}$$

where μ_0, $\mathbf{B}(\vec{r})$, $\mathbf{H}(\vec{r})$, and $\mathbf{M}(\vec{r})$ are vacuum permeability, magnetic induction, magnetic field, and induced magnetization respectively. Among these quantities, only B_0 and $\chi(\vec{r})$ are known a priori. All the others must be determined from Maxwell's equations. Since Maxwell's equations can be solved analytically only for relatively simple geometries, we develop here a numerical calculation based on finite differences that can be applied to an arbitrary susceptibility map $\chi(\vec{r})$ defined on a discrete grid of spatial locations. The relevant Maxwell equations are:

$$\nabla \cdot \mathbf{B}(\vec{r}) = 0 \tag{3.2}$$

$$\nabla \times \mathbf{H}(\vec{r}) = J_f(\vec{r}) + \frac{\partial \mathbf{D}(\vec{r})}{\partial t}, \tag{3.3}$$

with constitutive equation

$$\mathbf{B}(\vec{r}) = \mu(\vec{r})\mathbf{H}(\vec{r}),, \tag{3.4}$$

where $J_f(\vec{r})$ is the free surface or volume current and $D(\vec{r}) = \epsilon(\vec{r})\mathbf{E}(\vec{r})$, where $\epsilon(\vec{r})$ and $\mathbf{E}(\vec{r})$ are electric permeability and the electric field, respectively. In the absence of changing electric fields and the absence of surface and volume currents (which is the situation for our experiments presented in Ch 4) Eq 3.3 reduces to

$$\nabla \times \mathbf{H}(\vec{r}) = 0. \tag{3.5}$$

One approach to solving for $\mathbf{B}(\vec{r})$ (or $\mathbf{H}(\vec{r})$) in equations 3.2, 3.3, and 3.4 would be to find the magnetic vector potential $\mathbf{A}(\vec{r})$ given by

$$\mathbf{B}(\vec{r}) = \nabla \times \mathbf{A}(\vec{r}). \tag{3.6}$$

And then, compute magnetic induction $\mathbf{B}(\vec{r})$ from the vector potential. However, our experimental set up is a special case of magnetostatics where there are no surface or volume currents. Thus we can use a magnetic scalar potential $\varphi(\vec{r})$ instead, which simplifies the mathematical formulation greatly. The relationship between the magnetic field strength and the scalar potential is given by

$$\mathbf{H}(\vec{r}) = -\nabla\varphi(\vec{r}). \tag{3.7}$$

Substituting Eq 3.4 in Eq 3.2 yields

$$\nabla \cdot (\mu(\vec{r})\mathbf{H}(\vec{r})) = 0. \tag{3.8}$$

Substituting Eq 3.7 in Eq 3.8 yields

$$\begin{aligned} \nabla \cdot (\mu(\vec{r})(-\nabla\varphi(\vec{r}))) &= 0 \\ -\mu(\vec{r})\nabla^2\varphi(\vec{r}) - \nabla\varphi(\vec{r}) \cdot \nabla\mu(\vec{r}) &= 0 \\ \nabla^2\varphi(\vec{r}) + \frac{1}{\mu(\vec{r})}\nabla\varphi(\vec{r})\nabla\mu(\vec{r}) &= 0. \end{aligned} \tag{3.9}$$

The basic strategy of our numerical algorithm is to solve Eq 3.9, which can be solved for $\varphi(\vec{r})$ using finite difference procedure. This is done by an iterative process in which an initial value of $\varphi(x, y, z)$ is assumed, and then the values of $\varphi(x, y, z)$ are updated in each iteration based on its neighboring values $\varphi(x \pm \Delta x, y \pm \Delta y, z \pm \Delta z)$ and $\mu(x \pm \Delta x, y \pm \Delta y, z \pm \Delta z)$, consistent with the finite difference formulation of Eq 3.9. For large number of iterations and by imposing boundary conditions, $\varphi(r)$

is expected to approach its correct value. To derive the necessary finite difference formulation of Eq 3.9, we multiply both sides of Eq 3.9 by $\mu(\vec{r})$ to write

$$\begin{aligned}(\frac{\partial\mu(\vec{r})}{\partial x}\frac{\partial\varphi(\vec{r})}{\partial x}+\mu(\vec{r})\frac{\partial^2}{\partial x^2}\varphi(\vec{r}))+(\frac{\partial\mu(\vec{r})}{\partial y}\frac{\partial\varphi(\vec{r})}{\partial y}+\mu(\vec{r})\frac{\partial^2}{\partial y^2}\varphi(\vec{r}))\\ +(\frac{\partial\mu(\vec{r})}{\partial z}\frac{\partial\varphi(\vec{r})}{\partial z}+\mu(\vec{r})\frac{\partial^2}{\partial z^2}\varphi(\vec{r}))=0.\end{aligned} \tag{3.10}$$

Under finite difference formulation, first derivatives are such that computation at each point, or pixel, is done using the current (i.e. center) pixel and one other neighboring pixel, or using two neighboring pixels but not the center pixel. Therefore, iterative calculations based on first derivatives alone creates a directional bias. On the other hand, second differences are such that at each point, the parameter of interest can be computed based on *both* neighboring points' parameter values. Therefore, a mathematical formulation that uses both first and second derivatives will have no directional bias in computation of the parameter of interest. The goal in this derivation is to isolate the center point in terms of surrounding points.

With that in mind, let us now spell out the derivative and second derivative terms of Eq 3.10 to write

$$\frac{\partial\mu}{\partial x}=\frac{\mu(x+\Delta x)-\mu(x)}{\Delta x}=\frac{\mu(x+\Delta x)-\mu(x-\Delta x)}{2\Delta x} \tag{3.11}$$

$$\frac{\partial\varphi}{\partial x}=\frac{\varphi(x+\Delta x)-\varphi(x)}{\Delta x}=\frac{\varphi(x+\Delta x)-\varphi(x-\Delta x)}{2\Delta x} \tag{3.12}$$

$$\mu\frac{\partial^2}{\partial x^2}\varphi=\mu\frac{\varphi(x+\Delta x)-2\varphi(x)+\varphi(x-\Delta x)}{\Delta x^2}, \tag{3.13}$$

where Eqs 3.11, 3.12, and 3.13 are valid for principal dimensions x, y, and z. From hereon forward, the dimensions that are normal to the dimension along which the derivative is being computed are dropped (e.g. $\mu(x+\Delta x)\equiv\mu(x+\Delta x,y,z)$ and $\mu\equiv\mu(\vec{r})=\mu(x,y,z)$), which allows for more compact expressions without any consequences. Substituting Eqs 3.11, 3.12, and 3.13 for x, y, and z in Eq 3.10 results

in the following

$$\frac{\mu(x+\Delta x)-\mu(x-\Delta x)}{2\Delta x}\frac{\varphi(x+\Delta x)-\varphi(x-\Delta x)}{2\Delta x}+\mu\frac{\varphi(x+\Delta x)-2\varphi(x)+\varphi(x-\Delta x)}{\Delta x^2}$$
$$+\frac{\mu(y+\Delta y)-\mu(y-\Delta y)}{2\Delta y}\frac{\varphi(y+\Delta y)-\varphi(y-\Delta y)}{2\Delta y}+\mu\frac{\varphi(y+\Delta y)-2\varphi(y)+\varphi(y-\Delta y)}{\Delta y^2}$$
$$+\frac{\mu(z+\Delta z)-\mu(z-\Delta z)}{2\Delta z}\frac{\varphi(z+\Delta z)-\varphi(z-\Delta z)}{2\Delta z}+\mu\frac{\varphi(z+\Delta z)-2\varphi(z)+\varphi(z-\Delta z)}{\Delta z^2}$$
$$=0. \tag{3.14}$$

Lastly, rearranging and isolating $\varphi(x,y,z)$ we write

$$\varphi(x,y,z)=\frac{1}{6\mu(\frac{1}{\Delta x^2}+\frac{1}{\Delta y^2}+\frac{1}{\Delta z^2})}\times$$
$$[\frac{(\mu(x+\Delta x)-\mu(x-\Delta x))(\varphi(x+\Delta x)-\varphi(x-\Delta x))}{4\Delta x^2}+\mu\frac{\varphi(x+\Delta x)+\varphi(x-\Delta x)}{\Delta x^2}$$
$$+\frac{(\mu(y+\Delta y)-\mu(y-\Delta y))(\varphi(y+\Delta y)-\varphi(y-\Delta y))}{4\Delta y^2}+\mu\frac{\varphi(y+\Delta y)+\varphi(y-\Delta y)}{\Delta y^2}$$
$$+\frac{(\mu(z+\Delta z)-\mu(z-\Delta z))(\varphi(z+\Delta z)-\varphi(z-\Delta z))}{4\Delta z^2}+\mu\frac{\varphi(z+\Delta z)+\varphi(z-\Delta z)}{\Delta z^2}]. \tag{3.15}$$

Note that in the above expression, we have successfully written $\varphi(x,y,z)$ in terms of values of φ and μ of its immediate neighboring points, $\varphi(x\pm\Delta x, y\pm\Delta y, z\pm\Delta z)$ and $\mu(x\pm\Delta x, y\pm\Delta y, z\pm\Delta z)$. In our numerical calculation, Eq 3.15 is used to iteratively compute and update the map of φ values, one spatial location at a time. That is, $\varphi(x,y,z)$ is computed and updated at each iteration, based on the φ map of the previous iteration of $\varphi(x\pm\Delta x, y\pm\Delta y, z\pm\Delta z)$ values. Note that the μ map, i.e. map of magnetic permeabilities of interest, is constant from one iteration to the next because it is a known input parameter to the calculation. From the final computed φ map, the magnetic field induction B can be obtained simply using $B(\vec{r})=-\mu(\vec{r})\nabla\varphi(\vec{r})$, where the gradient is computed using finite differences of the magnetic scalar potential.

Let us now address the initial condition and boundary condition of the proposed iterative algorithm. For an object of limited spatial extent with magnetic permeability μ immersed in an otherwise static magnetic field, the field perturbations far away from the object diminishes. That is, the static field far away from the object is unperturbed. For uniform field $\mathbf{B} = B_0\hat{z}$, the scalar potential is simply given by $\varphi(x, y, z) = -\frac{1}{\mu_0}B_0 z$. Therefore, the appropriate boundary condition is $\varphi = -\frac{1}{\mu_0}B_0 z$ as $\vec{r} \to \infty$. Furthermore, since the potential in the absence of any field is also $\varphi = -\frac{1}{\mu_0}B_0 z$ for $\vec{r} \in \mathbb{R}$, this is a reasonable starting point for the iterative calculation. Please note, that from hereon forward, we adopt the convention that we call the magnetic field induction $\mathbf{B}$ 'magnetic field', i.e. when we refer to magnetic field, we mean $\mathbf{B}$, not $\mathbf{H}$, throughout the chapter, and elsewhere in the thesis. A specific example of a starting φ map , which satisfies the initial condition, is given in Fig 3.2 of Sec 3.1.3.

Because our calculation cannot actually stretch to infinity, we cannot enforce the boundary condition exactly. Instead, we endeavor to stretch out spatial extent far enough that the level of perturbations at the furthest extent are small compared with perturbations near the introduced material. In practice, we enforce the boundary condition by fixing the values of φ at the outer edge of the field-of-view matrix, such that those values are not allowed to get recomputed and updated for any of the iterations. For example, for a three-dimensional square field-of-view, the φ values in the outer box or "rim" of the field-of-view (which contains 6 planes) are not recomputed or updated. Ideally, the field-of-view would be large enough so that the boundary condition could be satisfied by enforced uniform field at the edge of the field of view. But in order to achieve acceptable spatial resolution near the material, the matrix size would need to be prohibitively large. To address this practical limitation, we develop and implement the "telescoping" procedure described in the next section.

3.1.1.2 Telescoping field-of-view algorithm

In the previous section, we established that the boundary condition for the iterative algorithm requires enforcing the condition the field perturbations far away from the object diminishes. Enforcing this condition along with having desirable voxel size requires the size of the matrices containing the magnetic scalar potential and permeability values to be prohibitively large. In this section, we resolve this issue by developing a "telescoping" field-of-view in which we start by populating the desired field-of-view with magnetic permeability values, i.e. creating a μ-map, corresponding to the geometry of interest. We then "zoom out" in increments of factor of 2, where the central half of a new matrix the same size as the previous matrix but double the field-of-view is populated by the "low resolution" version of the previous matrix. We continue this "zooming out" process until the geometry of interest reduces to a few voxels at the center of the final field-of-view. Therefore, the number of voxels along a dimension of the matrix is always $N = 2^{n_z+1}$, where n_z is the number of times the "telescoping" step is repeated (i.e. number of zooms). We point out that there is no fundamental reason why the "zooming" factor must be two, but because each zooming step is essentially an interpolation, using a factor of two makes it very straightforward and robust to implement the "telescoping" procedure.

The boundary condition, that no field perturbation should prevail at 'infinity', is enforced at the outer boundary (i.e. 'rim') of the final (zoomed-out) field-of-view which then becomes the first field-of-view in which the iterations begin. For a specified number of iterations N_{iter}, once the φ-map in the zoomed-out field-of-view is recomputed and updated N_{iter} times, the field-of-view is zoomed in by a factor of 2, and the φ map in the newly zoomed-in field-of-view is recomputed and updated another N_{iter} times. Note that the boundary condition at each "telescoping" step is applied at its outer voxels where the values set in those voxels are the central 'rim' of the zoomed-out map. This process continues until the necessary field-of-view covering the geometry of interest is reached. N_{iter} is determined by trial and error, with the

condition that field disturbances are accurate within 1 ppm. That is, the difference between the numerically calculated field disturbances and the analytically calculated field disturbances should be $\lesssim 10^{-6}$ times the field strength, in a simple geometry for which an analytical solution exists. This is done by validation of the iterative magnetostatics formulation with analytic solution for a simple geometry, which is done in the following section.

We note that it is the φ map that gets recomputed and updated at each iteration and telescoping step. The μ map only gets updated between telescoping steps to change the pixel resolution. A concrete example of the μ-map undergoing the telescoping procedure is given in Fig 3.3 of Sec 3.1.3.

3.1.2 Validation with analytic solution: field perturbations of spherical shell

In this section, we confirm proper operation of the numerical algorithm developed in the previous section, by computing the field disturbance due to magnetic material arranged in a simple geometry (a spherical shell) for which an analytic solution is known.

Consider a spherical shell of inner radius a and outer radius b with magnetic permeability μ immersed in an otherwise static magnetic field B_0 (this is a problem partially solved in Jackson [70]). The field map, including the inhomogeneities created by the presence of the shell superimposed onto the static field, can be analytically solved using the scalar magnetic potential. Assuming that the center of the coordinate system coincides with the center of the shell, in spherical coordinates, one can start from Legendre polynomial form of the scalar potential to write

$$\varphi(r,\theta) = \begin{cases} -H_0 r\cos\theta + \dfrac{\alpha}{r^2}\cos\theta, & r > b \quad (3.16) \\ (\beta r + \gamma\dfrac{1}{r^2})\cos\theta, & a < r < b \quad (3.17) \\ \delta r\cos\theta, & r < a \quad (3.18) \end{cases}$$

where r and θ, are the radial distance and the polar angle, respectively. No azimuthal angle ϕ is at play due to azimuthal symmetry. Magnetic field can be obtained from this expression for the scalar potential using $B = -\mu\nabla\varphi$, and one can write

$$B(r,\theta) = \begin{cases} (H_0 + \frac{2\alpha}{r^3})\cos\theta\,\hat{r} + (H_0 - \frac{\alpha}{r^3})\sin\theta\,\hat{\theta}, & r > b \quad (3.19) \\ (\frac{2\gamma}{r^3} - \beta)\cos\theta\,\hat{r} - (\beta + \frac{\gamma}{r^3})\sin\theta\,\hat{\theta}, & a < r < b \quad (3.20) \\ -\delta\cos\theta\,\hat{r} + \delta\sin\theta\,\hat{\theta}, & r < a. \quad (3.21) \end{cases}$$

Conversion of the spherical coordinates to Cartesian coordinates is made possible by writing spherical parameters $\hat{r}$, $\hat{\theta}$, and $\hat{\phi}$ in terms of $\hat{x}$, $\hat{y}$, $\hat{z}$ as the following:

$$\hat{r} = \sin\theta\cos\phi\,\hat{x} + \sin\theta\sin\phi\,\hat{y} + \cos\theta\,\hat{z} \quad (3.22)$$

$$\hat{\theta} = \cos\theta\cos\phi\,\hat{x} + \cos\theta\sin\phi\,\hat{y} - \sin\theta\,\hat{z} \quad (3.23)$$

$$\hat{\phi} = -\sin\phi\,\hat{x} + \cos\phi\,\hat{y}. \quad (3.24)$$

Lastly, substituting Eqs 3.22, 3.23, and 3.24 into Eqs 3.19, 3.20, and 3.21, the magnetic field in and around the shell immersed in an otherwise static field is given by

$$B(r,\theta) = \begin{cases} (H_0 + \frac{2\alpha}{r^3})\cos\theta(\sin\theta\cos\phi\,\hat{x} + \sin\theta\sin\phi\,\hat{y} + \cos\theta\,\hat{z}) \\ \quad +(H_0 - \frac{\alpha}{r^3})\sin\theta(\cos\theta\cos\phi\,\hat{x} + \cos\theta\sin\phi\,\hat{y} - \sin\theta\,\hat{z}), & r > b \quad (3.25) \\ (\frac{2\gamma}{r^3} - \beta)\cos\theta(\sin\theta\cos\phi\,\hat{x} + \sin\theta\sin\phi\,\hat{y} + \cos\theta\,\hat{z}) \\ \quad -(\beta + \frac{\gamma}{r^3})\sin\theta(\cos\theta\cos\phi\,\hat{x} + \cos\theta\sin\phi\,\hat{y} - \sin\theta\,\hat{z}), & a < r < b \quad (3.26) \\ -\delta\cos\theta(\sin\theta\cos\phi\,\hat{x} + \sin\theta\sin\phi\,\hat{y} + \cos\theta\,\hat{z}) \\ \quad +\delta\sin\theta(\cos\theta\cos\phi\,\hat{x} + \cos\theta\sin\phi\,\hat{y} - \sin\theta\,\hat{z}), & r < a, \quad (3.27) \end{cases}$$

where the constants are solved by applying boundary conditions in the form of continuity at $r = a$ and $r = b$ and found to be $\alpha = \frac{2(\mu+1)(\mu-1)}{(2\mu+1)(\mu+2)-2\frac{a^3}{b^3}(\mu-1)^2}(b^3 - a^3)H_0$, $\delta = \frac{9\mu}{(2\mu+1)(\mu+2)-2\frac{a^3}{b^3}(\mu-1)^2}H_0$, $\beta = 2/3(1 + \frac{1}{2\mu})\delta$, and $\gamma = \alpha(\delta - \beta)$.

Using the analytic solution in Eqs 3.25, 3.26, and 3.27, we compute the field

in and around a shell of inner radius $a = 10\,\mu$m and outer radius $b = 20\,\mu$m, with permeability $\mu = -11$ ppm, immersed in an otherwise static field strength of $B_0 = 1.5$ Tesla. The isotropic resolution and field-of-view are one cubic micron and 128 cubic micron, respectively. A cross-section view of the calculated field distribution is given in the left panel of Fig 3.1.

We now use our numerical algorithm to compute the magnetic field in the exact same geometry as described above. Number of iterations used is 5000 per telescoping step, and the number of telescoping steps is 6. The result is given in the right panel of Fig 3.1. The difference between the numerical solution and the analytic solution was then computed for validation of our proposed technique. The cross-sectional view of the difference field map is shown in the bottom panel of Fig 3.1. It is evident from this plot that with the chosen parameters and large enough number of iterations, the iterative field calculation converges to the correct values. In general, we found that for a matrix size of $128 \times 128 \times 128$, based on trial and error, 5000 iterations per "telescoping" step is adequate, yielding results such that $\frac{\Delta B}{B_0} < 0.1$ ppm, where $\Delta B = B_{\text{numerical}} - B_{\text{analytic}}$. That is, the difference between the numerical and the analytic solutions of the magnetic field is less than $\sim 0.1\ \mu$T. This is a definitive confirmation that the resulting field maps obtained from iterative calculation of φ maps of more complex geometries are to be trusted with the exception of the voxels at the boundary of any object. As indicated by the difference map, a caveat of our proposed technique is incorrect field values at the boundary voxels between regions with different magnetic permeability. This "pixelation" is an unavoidable discrepancy, though small enough to be inconsequential.

3.1.3 Calculation of field perturbations in our experimental setup

Let us use our numerical algorithm to calculate field perturbations in the geometry that most resembles our actual experimental setup. In our experiments, we use a

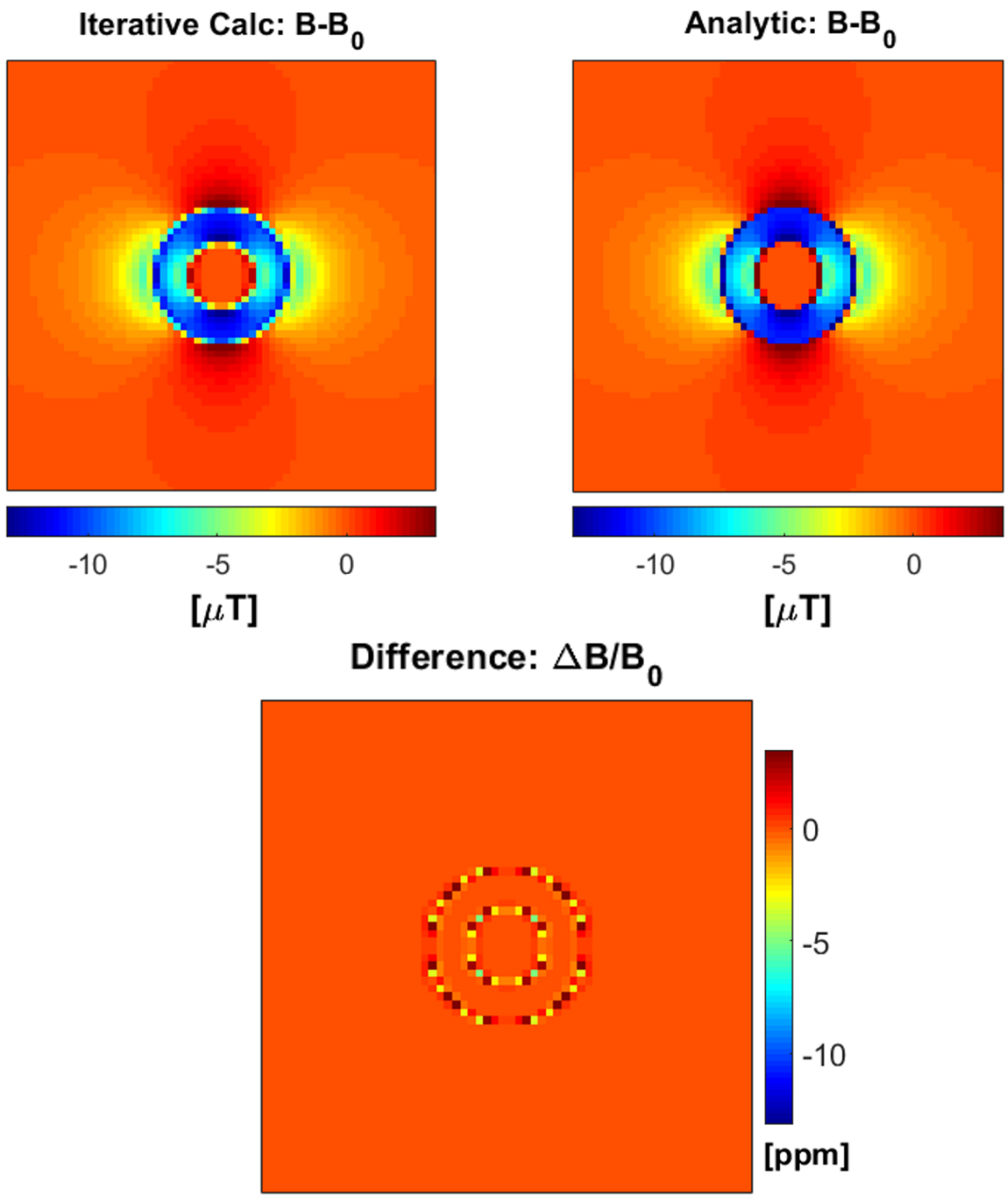

Figure 3.1: Comparison between analytic and simulated central cross-sectional view of the magnetic field map of a shell of permeability $\mu = -11$ ppm with inner radius $a = 10\,\mu$m and outer radius $b = 20\,\mu$m immersed in an otherwise static uniform field of strength $B_0 = 1.5$ T. Number of iterations used in this simulation is 5000 per "telescoping" step, and the resolution and the field-of-view are $1\,\mu$m and $128\,\mu$m, respectively. Field inhomogeneities created by presence of the shell appear to be in the order of a few ppm. It is evident that the simulation results are accurate up to at least 1 ppm from the difference map (right panel). Only unavoidable discrepancy occurs at the boundary voxels, which is inconsequential for our geometries.

Borosilicate glass tube with inner diameter of 3-4 mm and wall thickness of ~ 1 mm filled with ^{3}He. The tube contains a 2.2-mm diameter spherical bead made of borosilicate glass that elevates a 2-mm diameter polymer shell with wall-thickness of 15-26 μm. Magnetic permeability of Borosilicate and polymer are similar and reported to be $\mu \simeq -11$ ppm [71], although the polymer shell's contribution to the field inhomogeneities is minuscule compared with that of the tube and the bead since the thicknesses are ~ 2 orders of magnitude different.

For this geometry, a $128 \times 128 \times 128$ matrix with original field-of-view of 10.24 mm (-5.12 mm $< x, y, z < 5.12$ mm) and isotropic resolution of $\Delta x = \Delta y = \Delta z = 80\mu$ is chosen. This matrix size is compatible with maximum of 6 "telescoping" steps with the out most field-of-view of 32.8 cm. The same "telescoping" is applied to the φ map, of course, with the initial values $\varphi(x, y, z) = -\frac{1}{\mu} B_0 z$. An example of the most zoomed out (i.e. having largest field-of-view) φ map is given in Fig 3.2.

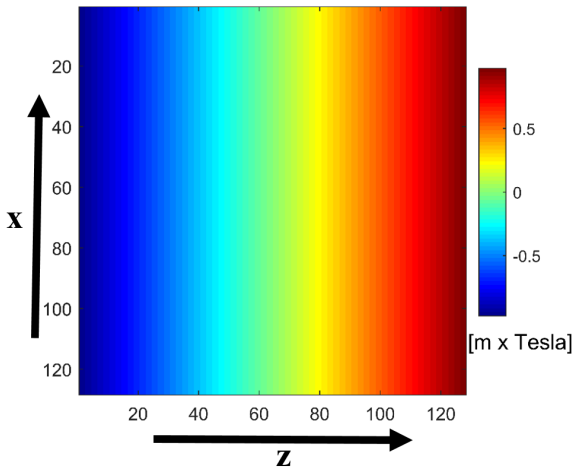

Figure 3.2: Central cross-sectional view of the starting φ map showing a constant gradient along $\hat{z}$. Iterations are done on this map and zoomed in once iterations on each "telescoping" step is completed until reaching the original field-of-view. This map satisfies $B_0 = 1.5$ T $= -\mu \nabla \varphi$.

An example of susceptibility map in the form of $(1 - \mu)$ map undergoing the "telescoping" procedure is shown in Fig 3.3. Here, we assume that the permeability

of ^{3}He is the same as that of vacuum (i.e. μ_0). Regardless of the number of zooms or the resolution, one problem which will persist is the incorrect field computed at the boundary between regions with different magnetic permeability. To minimize the magnitude of this "pixelation" problem, we assign the weighted mean of μ_0 and μ to the values of voxels that contain partial volume of both the object with permeability μ and ^{3}He with permeability μ_0. An example of the weighted mean μ values at the boundary voxels is shown in the enlarged region of the original field-of-view (i.e. zoom $\times$ 1) shown in Fig 3.3.

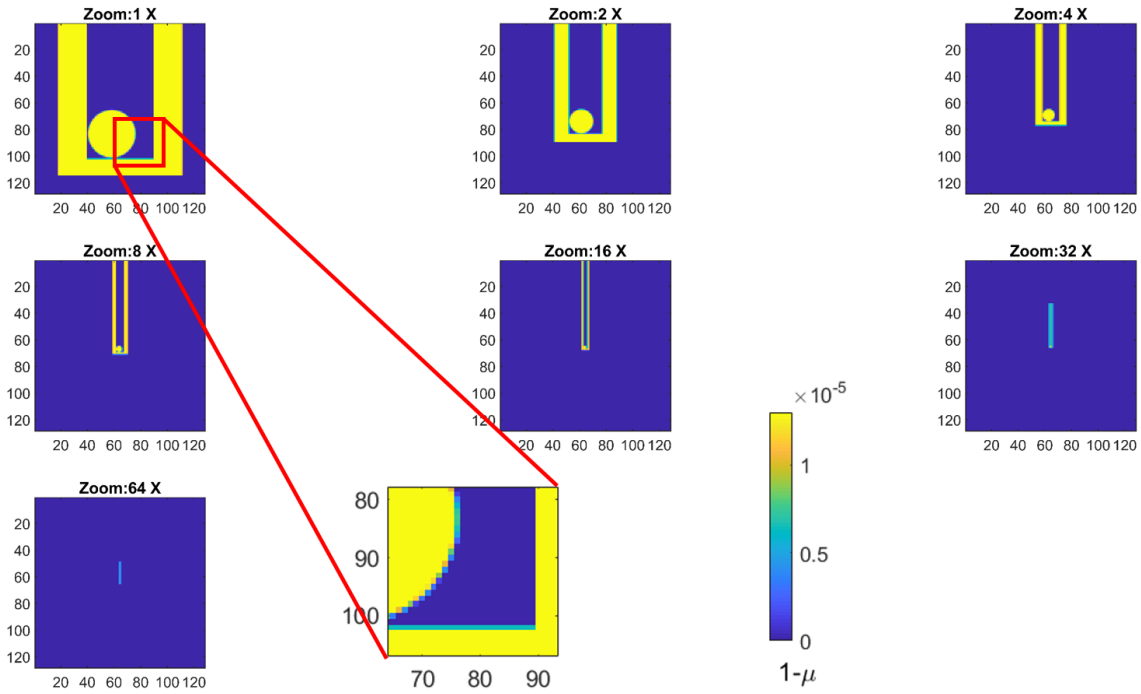

Figure 3.3: Central cross-sectional views of $1-\mu$ maps showing 6 "telescoping" steps (i.e. zooms) for a μ-map of size $128 \times 128 \times 128$. The enlarged region demonstrates that the boundary voxels between the objects and ^{3}He (which we assume has permeability that of vacuum μ_0) are given permeability values based on the weighted mean of μ and μ_0 depending on the volume of each in the voxel. The permeability of borosilicate glass is $\mu = -11$ ppm, hence the colorbar shows the value inside the glass to be $1-\mu = 11 \times 10^{-5}$. All panels including the enlarged map share the same color scale.

Since the target quantity of interest is the span of ^{3}He resonance frequencies caused

by the magnetic field inhomogeneities, one can compute the frequency as

$$f = \frac{\gamma}{2\pi} B, \tag{3.28}$$

where γ is the gyromagnetic ratio of ^{3}He in units of rad·s^{-1}T^{-1}.

Central cross-sectional views of the frequency distribution in our simulated geometry is given in Fig 3.4. For the views including the polymer shell, since the thickness

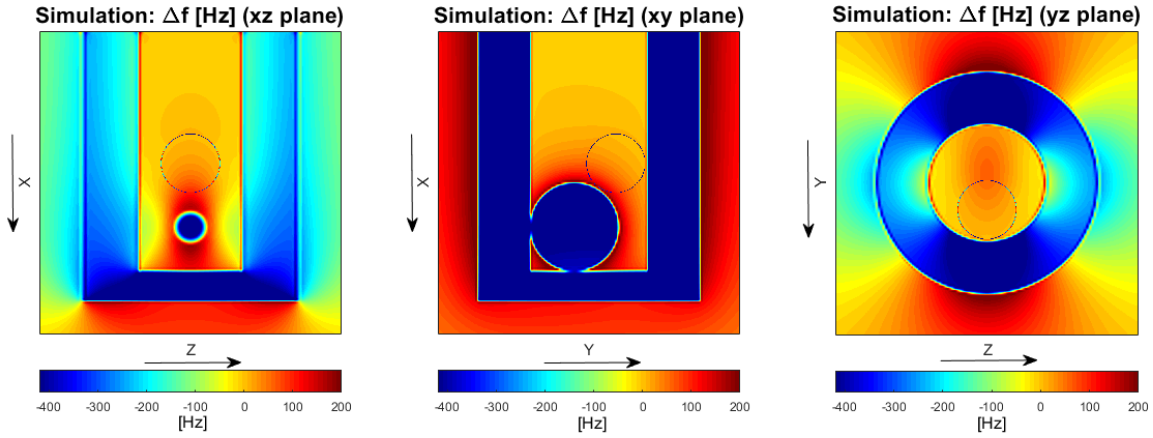

Figure 3.4: Central cross-sectional views along principal axes of the frequency distribution in and around the polymer shell resting on top of a bead at the bottom of a flat-tube. Simulation parameters are: number of iterations = 5000, $\mu_{shell} = \mu_{glass} = -11\,\mu$, side wall thickness = 2 mm, bottom thickness = 1 mm, bead OD = 3 mm, shell OD = 2 mm, shell wall thickness = 15 μm, field-of-view = 10 mm, and resolution = 78 μm. Since the thickness of the shell is smaller than the resolution, the frequency distribution solely due to presence of the shell is calculated analytically on a $1024 \times 1024 \times 1024$ matrix to provide finer resolution. The simulated frequency distribution obtained from the tube is resized (interpolated) from a $128 \times 128 \times 128$ matrix to a $1024 \times 1024 \times 1024$ matrix and the superposition of the two maps is shown for demonstration only (otherwise the pellet itself would be invisible since its thickness (15-26 μ) is smaller than the resolution (= 80 μ)

of the shell is so small compared to the size of the tube, it is impossible to resolve the field perturbation caused by the shell in our simulations unless matrices with size of at least $1000 \times 1000 \times 1000$ are used to allocate a few voxels across the shell. Importantly, computational time of an iterative calculation done on a $1024 \times 1024 \times 1024$

matrix is $8^3 = 512$ times longer than that done on a $128 \times 128 \times 128$ matrix. We note that depending on the number of iterations (3500-5000), the simulation on a matrix size of $128 \times 128 \times 128$ on a computer with Intel core i7 processing unit and 64 GB of RAM takes 3-4 hours. Therefore, field disturbance and its frequency distribution is instead calculated analytically for the shell using Eqs 3.25, 3.26, and 3.27. To superimpose the two frequency distributions, the frequency distribution map computed analytically (rather than numerically) for the shell is resized (interpolated) onto a $128 \times 128 \times 128$ matrix, and using superposition of the two, the composite frequency map is obtained (see Fig 3.4).

3.2 ^{3}He diffusion simulation

In the previous section, we developed a mathematical formulation to calculate the magnetic field distributions in our experimental setup, which consists of a polymer pellet elevated by a spherical glass bead which rests at the bottom of a glass tube filled with ^{3}He. Since ^{3}He is in gaseous phase, to understand the magnetic field distribution seen by the ^{3}He particles, not only do we need to compute the static field inhomogeneities, but also simulate diffusion of gas through these inhomogeneities, which will alter the frequency distribution of the NMR signal generated by the ^{3}He nuclei. In this section we develop a diffusion simulation, which we perform in MATLAB, based on three-dimensional Brownian motion of an ensemble of particles on a grid of points. The goal of this section is to develop and validate simulation of ^{3}He gas particles through space based on 3D Brownian motion. The results of the simulation will help determine the extent of motion of the ^{3}He gas particles in the presence of field inhomogeneities presented in Sec 3.1. We note that in this simulation, density gradient plays no role in the motion of the particles, instead only 3D random Brownian motion of particles is the implemented phenomenon (i.e. bulk flow is not addressed).

In liquid or gaseous media, free diffusion of particles is a physical phenomenon characterized by free diffusivity constant denoted by D_0 which is an intrinsic characteristic of the said gaseous or liquid medium. Free diffusivity is defined as motion of particles in gas or liquid without any confining structure to hinder the particles' random Brownian motion. Restricted diffusion, on the other hand, is defined as motion of gas or liquid particles confined within a rigid structure that restricts particles' motion at the rigid structure's boundaries. In general, the diffusivity constant D for particles in gaseous and liquid media, which applies to both free and restricted diffusion, depends on the mean-squared-displacement of the ensemble of particles and is given by

$$D(t) \equiv \frac{\left\langle |\vec{r}(t) - \vec{r}(0)|^2 \right\rangle}{2t \cdot N_d}, \tag{3.29}$$

where $\vec{r}(0)$ and $\vec{r}(t)$ are the displacement of the particles at times 0 and t, respectively (see Sec 2.5).

Consider a one-dimensional random walk with the displacement after the N^{th} step given by $x_N = \sum_{j=1}^{N} \epsilon_j \delta$, where δ is the step size and ϵ_j takes its values $\epsilon_j = \pm 1$ completely randomly. The average displacement for this random walk is

$$\langle x_N \rangle = \left\langle \sum_{i=1}^{N} \epsilon_j \delta \right\rangle = \sum_{j=1}^{N} \delta \langle \epsilon_N \rangle = 0, \tag{3.30}$$

i.e. the particles collectively take as many $\epsilon_j = -1$ steps as they do $\epsilon_j = 1$ steps. The mean squared displacement, however, is a non-zero quantity computed as

$$\begin{aligned} \left\langle x_N^2 \right\rangle &= \left\langle \left(\sum_{j=1}^{N} \epsilon_N \delta \right)^2 \right\rangle = \delta^2 \left\langle \left(\sum_{j=1}^{N} \epsilon_i \right)^2 \right\rangle \\ &= \delta^2 \left\langle \sum_{j=1}^{N} \epsilon_j^2 + 2 \sum_{j \neq k} \epsilon_j \epsilon_k \right\rangle = \delta^2 \left(\left\langle \sum_{j=1}^{N} \epsilon_j^2 \right\rangle + \cancelto{0}{\left\langle 2 \sum_{j \neq k} \epsilon_j \epsilon_k \right\rangle} \right) = N\delta^2. \end{aligned} \tag{3.31}$$

Therefore, the one-dimensional free diffusivity of gaseous or liquid particles with N δ-

sized steps during time t is $D = \frac{N\delta^2}{2t}$, which establishes that in the limit of unrestricted random walk, Eq 3.29 approaches D_0. To implement the Brownian motion in the simulation, we define free diffusivity D_0 in terms of step size δ, dimensionality N_d, and step time Δt as $D_0 \equiv \frac{\delta^2}{2N_d\Delta t}$.

We carry out a discrete 3D Brownian motion on a grid of equally-spaced $128 \times 128 \times 128$ points to be compatible with the magnetostatics simulation field maps. Free diffusivity of the particles is set to $D_0 = 0.495$ cm^2/s corresponding to that of pure ^{3}He gas at 4 atm (a representative pressure for our experiments). Spatial spatial step size dx and time step size dt are chosen such that $dx = \sqrt{2N_{dim}dtD_0}$ holds and is in accordance with the same FOV as that for the simulated field maps presented in Sec 3.1. A spatial mask representing the geometry of our experimental set up is defined to only allow particles in certain regions (i.e. inside the tube particles are allowed, in the walls of the tube and outside it, particles are not allowed). Only one step at a time per particle is permitted and all steps are taken along the principal axes (i.e., $\pm\hat{x}$, $\pm\hat{y}$, or $\pm\hat{z}$) chosen completely at random.

We use a large number of particles (M) in the simulation, where we initially populate the particles evenly by placing 10 particles at each allowable location. We store the location of the particles in a $3 \times M$ size matrix, and keep track of the position of the M particles. At each step, every particle takes a step from their current grid point to an immediate neighboring grid point determined by a random integer in $[1, 6]$ each corresponding to a step either in $\pm\hat{x}$, $\pm\hat{y}$, or $\pm\hat{z}$ direction . If the new grid point is a forbidden one (i.e. inside the tube wall or the solid bead, as determined by the mask) the step is reversed such that the position of that particle remains unchanged. At each time point, the mean squared displacement of the entire ensemble is computed as $\left\langle |\vec{r}(t) - \vec{r}(0)|^2 \right\rangle = \left\langle (x_{diff}^2 + y_{diff}^2 + z_{diff}^2) \right\rangle$, where $x_{diff} = x(t) - x(0)$, $y_{diff} = y(t) - y(0)$, and $z_{diff} = z(t) - z(0)$. Number of iterations N is determined such that the desired time of diffusion is carried out ($t = Ndt$).

Here is the summary of the step-by-step procedure we use to implement the 3D

Brownian motion:

- Initialize parameter constants dx, dt, FOV, D_0, dimensionality N_{dim}, number of iterations N, number of particles M, and pressure P
- Create a mask of allowed and forbidden regions based on the gridded points
- Initialize and populate the matrix comprised of the position of all particles based on the mask
- Iterate the following N times:
  - For each of the M particles, choose a random integer between 1 and 6, where each integer corresponds to a direction along either of the principal axes, for each particle (this is done vectorwise on a vector of size M)
  - Move the position of the particles one grid point based on the random integer, reverse step if new position is forbidden for any of the particles
  - Compute mean squared displacement for all particles

To validate our simulation, let us simulate a simple situation, in which we place the entire ensemble of particles at a single point within a cylindrical, closed-bottom tube, and let them diffuse out starting at time $t = 0$. Since at each iteration we compute mean-squared-displacement of the ensemble, we can plot it as a function of time. The slope of the line of mean-squared-displacement vs time is the measured diffusivity.

We populate the center point of the field-of-view of a grid of $128 \times 128 \times 128$ points with $M = 225,000$ (i.e. the initial position of all particles is $\vec{r}(t = 0) = (x, y, z) = (0, 0, 0)$). The center point is positioned near the bottom of the tube. The geometry is designed for the field-of-view to include the bottom part of a 3-mm inner diameter tube with the bottom being a semi-sphere of the same diameter. The particles are allowed to undergo restricted Brownian motion starting at time $t = 0$ for 17 ms.

Diffusion simulation snapshot results shown at time instances of 2, 6, and 17 ms are depicted in Fig 3.5.

It can be seen that the first few milliseconds of diffusion is purely free but sometime between 5-6 ms after diffusion starts, the walls of the tube start restricting the free diffusion which can be seen in the bottom-row panels of Fig 3.5, and in Fig 3.6 where the diffusivity curve starts deviating from the line of free diffusion (free diffusivity is the slope of the line). Toward the beginning of the diffusion process where the particles diffuse freely, on the other hand, mean squared displacement vs time curve coincides with the line of free diffusivity. It is evident that in less than 17 ms, the particles that all started at the center of the field-of-view have now filled the entire lower region of the tube almost uniformly due to rapid diffusion of the gas particles. This phenomenon is completely independent of pressure-gradient bulk-flow motion of particles and the simulation is carried out assuming that both the pressure and the density of the gas inside the tube is at 4 atm and remains stable, i.e. there are no leaks or addition of the gas during the diffusion time and gas is assumed at equilibrium.

Here, we have successfully developed a diffusion simulation based on 3D Brownian motion of particles in space. The plot of mean-squared-displacement as a function of time in Fig 3.6 serves as a validation of our developed simulation.

3.3 Simulation of imaging gradients

As we saw in Secs 2.3, 2.5, and 2.6, in order to obtain the spatial distribution of the spins in a sample (i.e. acquire an image of the sample), one needs to traverse and acquire signal at the appropriate k-space points. To visit different points of k-space, magnetic field gradients need be applied to superimpose a field gradient across the desired dimension to traverse the k-space along the said dimension. The result of these gradients is phase accrual over the course of an applied gradient due to alteration of the resonant frequency of the spins across the dimension the gradients

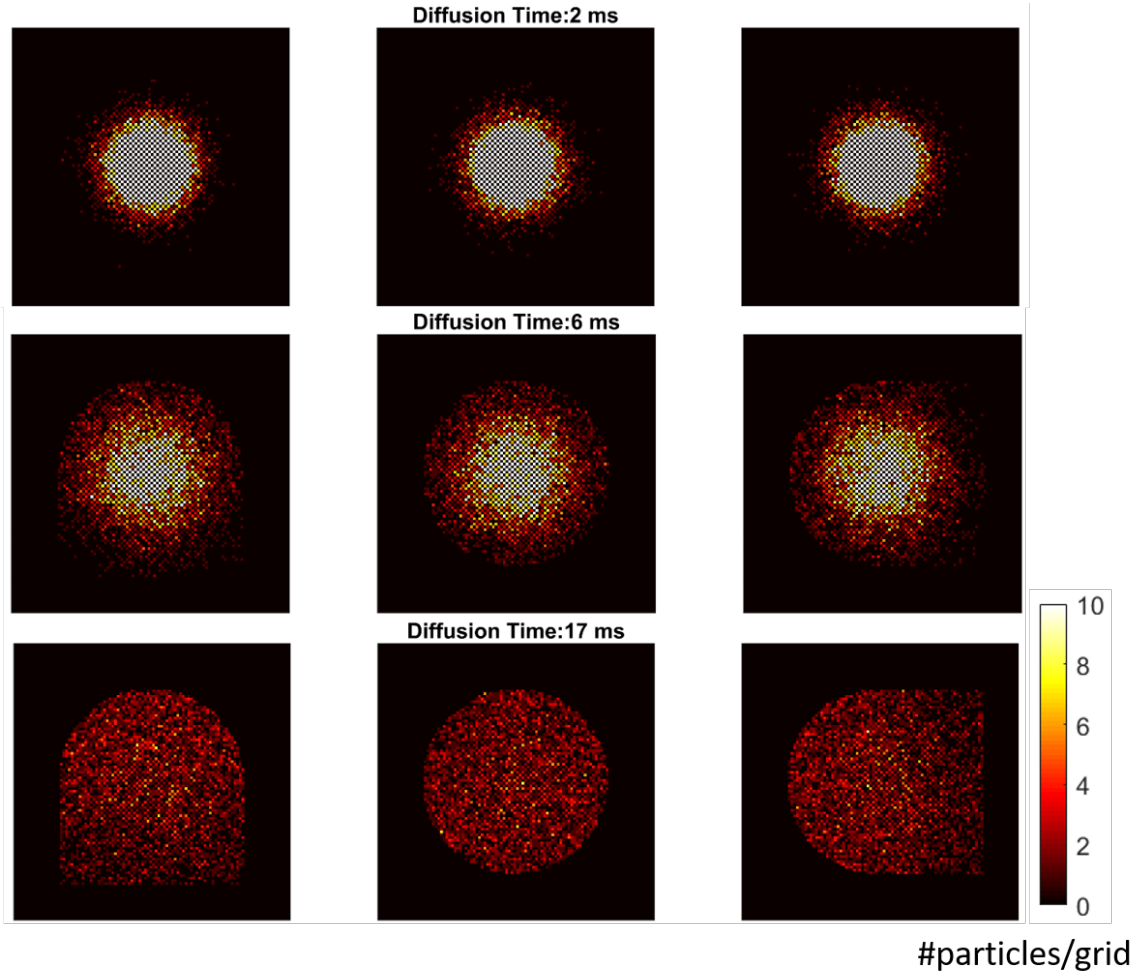

Figure 3.5: Central cross-sectional views of ^{3}He diffusion simulation results along the principal axes with the following parameters: $M = 225,000$, grid size $= 128 \times 128 \times 128$, $D_0 = 1.98/4$ cm^2/s, FOV $= 5$ mm, $N_{dim} = 3$. The particles undergo free diffusion for the first ~ 5 ms, after which the outer edge of the spreading particles meet the tube walls and diffusion becomes obstructed. All panels share the same color scale.

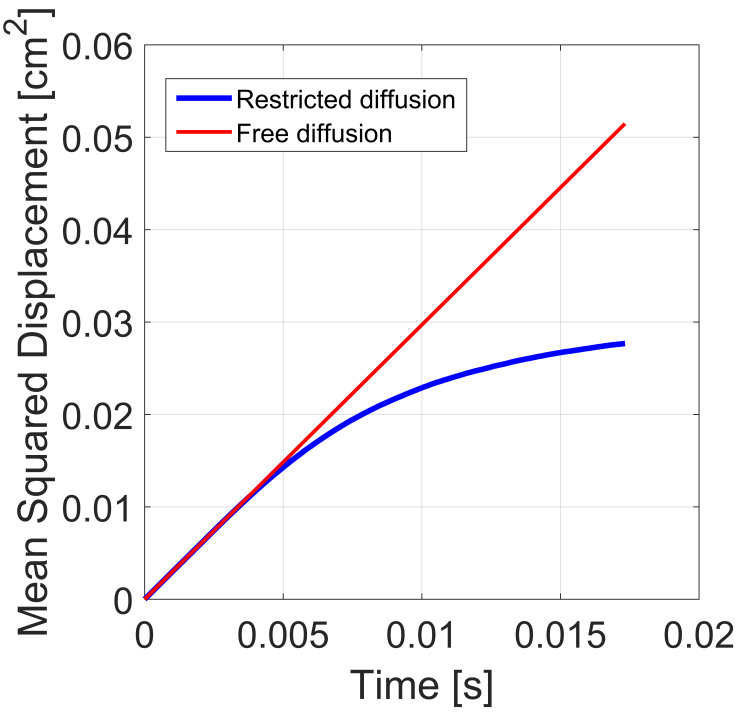

Figure 3.6: Mean squared displacement plotted as a function of time for ^{3}He diffusing from a point source at 4 atm inside a tube. Note that for the beginning stages of the diffusion process where the particles have not reached the boundaries of the tube, the diffusion is unrestricted and the curve coincides with line of free diffusivity and diverges away as more particles approach the walls and undergo obstructed diffusion instead.

are applied. Consequently, in our experiments presented in Chapter 4 where we use imaging techniques to monitor the permeation process, gas molecules diffuse through the time-dependent field gradients applied for imaging, therefore experiencing change in their precession frequency, in addition to the frequency change created by the susceptibility-induced magnetic field inhomogeneities presented earlier in Sec 3.1.

In this section, we simulate the imaging gradients needed to acquire signal at all appropriate spatial frequencies as a function of time for gradient-echo and chemical shift imaging pulse sequences, which are the two techniques used in experiments in Chapters 4 and 5. In the context of gradient application, recall from Secs 2.3 and 2.6 that the difference between gradient-echo and CSI sequences is that in gradient-echo

imaging, signal in a line of k-space is acquired by application of a gradient along a certain dimension (while ADC is on), whereas in a CSI acquisition, travel to the desired k-space location is complete, then the signal is read out. Nonetheless, both imaging techniques require application of gradients.

To be compatible with both magnetostatics and diffusion simulations, all imaging gradient simulations are also done on the same matrix size ($128 \times 128 \times 128$). The timing of the gradients are also designed to ensure compatibility. It is important to note here that target amplitude of a gradient is not achievable instantaneously since currents in the coils have to build up to a certain level to produce them. This is a hardware-specific limitation and for the system that we use for all of our experiments (Avanto, strength 1.5 T), the maximum achievable slew rate is 170 mT/m/ms. Therefore, all gradients presented in this chapter are of trapezoidal form with maximum slew rate and gradient amplitude of 170 mT/m/ms, and 40 mT/m, respectively. Since it is the time-integral of the gradients that determine displacement in k-space, it is the responsibility of the sequence developer to ensure that the sides of the trapezoid are included properly in computing the relationship between k-space location and area under gradient waveform as a function of time.

Recall from Sec 2.3 that the k-space location at time t, the image resolution, and the image field-of-view are given as

$$k(t) = \int^{t} \frac{\gamma}{2\pi} G(t')dt' \tag{3.32}$$

$$\Delta r = \frac{1}{2k_{max}} \tag{3.33}$$

$$FOV = \frac{1}{\Delta k}, \tag{3.34}$$

respectively. Therefore, all imaging gradients must be simulated in accordance with Eqs 3.32, 3.33, and 3.34 to obtain the correct resolution and field-of-view in imaging of the ^{3}He gas particles.

An example of simulated traces of gradients applied for gradient-echo imaging

as a function of time is shown in Fig 3.7 for maximum gradient strength of $G_{xyz} =$ 40 mT/m and maximum slew rate of 170 mT/m/ms corresponding to the optimal scanner capability. The application of RF pulse in this simulation is assumed instant,

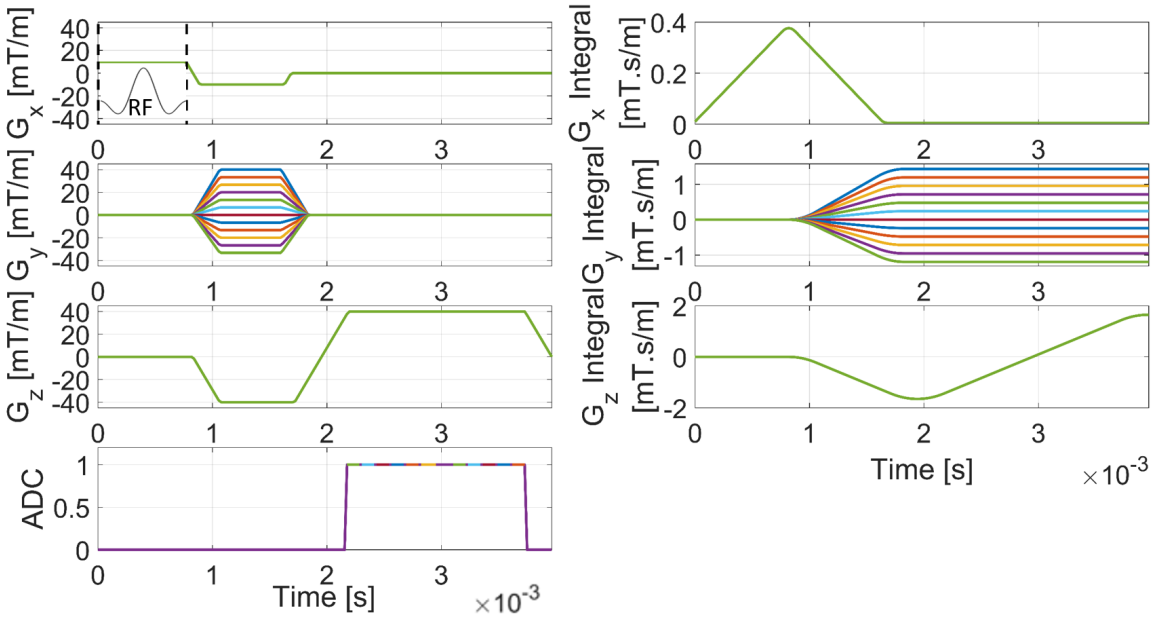

Figure 3.7: Simulated gradients applied for slice-selective 2D gradient-echo imaging. The application of RF pulse in each TR is assumed instantaneous (but shown on the plot for reference where the RF pulse would have been if not instantaneous). Slice selection is done along the x axis, phase encoding along the y axis, and frequency encoding along read or z direction.

and gradients are not rewound after signal has been acquired at each repetition time period, instead perfect "spoiling" is assumed at the end of each TR period. Spoiling is an MRI term used to refer to application of strong field gradients, which could be applied along either or all directions, to deliberately force loss of coherence of the precessing spins, i.e. dephasing the spins, and consequently reducing the net signal in the transverse plane to zero. The effect of perfect spoiling on available signal is equivalent to increasing TR to infinity (in practice, a large value).

Conventionally, since MRI scanners are used to image the human body, slice-selective axis is understood to be along the z-axis, i.e. along the static field direction.

In our experiments, we choose the slice-selective axis to be along the transverse direction, or x-direction, swapping conventional read and slice-select axes. Each color in the plots corresponding to y axis represent a separate TR period. The panels on the right are area under the gradient traces (time integrals) and are shown to demonstrate the relative location in k-space referenced to the center of k-space. That is to say, the right hand plots in Fig 3.7 and 3.8 are traces of $\frac{2\pi}{\gamma}k(t)$ (Eq 3.32).

Similarly, the gradients applied prior to signal detection in a slice-selective 2D CSI acquisition can be simulated and the resulting traces are shown in Fig 3.8. The two

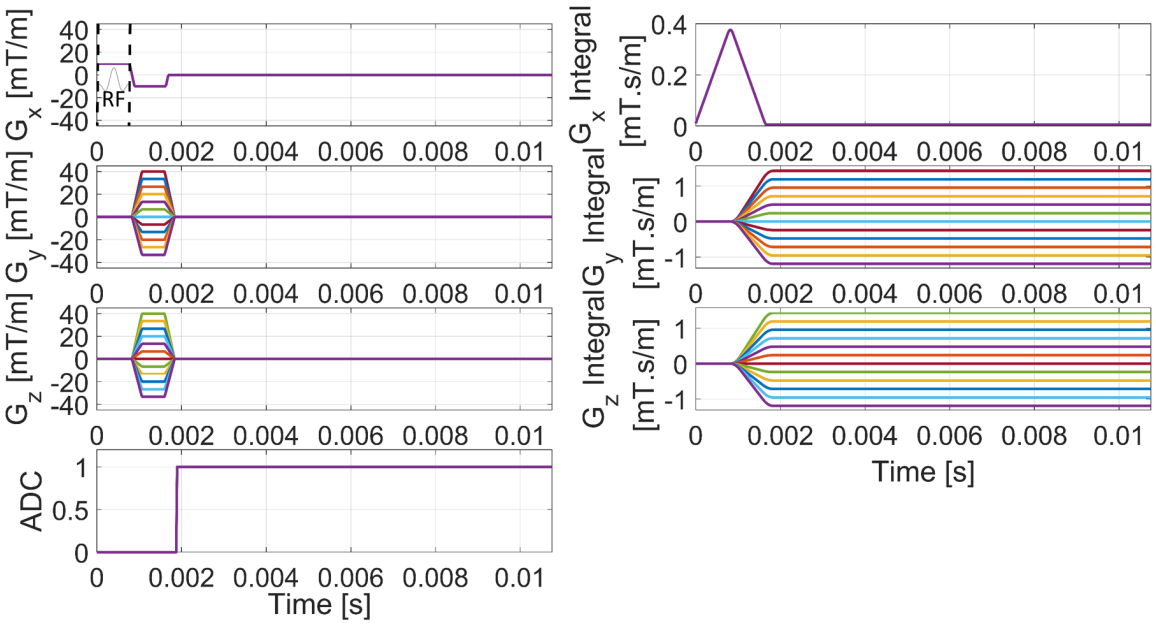

Figure 3.8: Simulated gradients applied for slice-selective 2D CSI acquisition. The application of RF pulse in each TR is assumed instantaneous (but shown on the plot for reference where the RF pulse would have been if not instantaneous). Slice selection is done along the x axis and phase encoding along both y and z axes. No frequency encoding is done except for slice-selection.

imaging gradient simulations have the exact same orientation, image resolution, and image field-of-view. Even though the specifics of the gradients like the timing, the waveform, and the number of the gradients applied in each acquisition method are vastly different, the exact same k-space locations are visited in both methods. This is

seen in both Figs 3.7 and 3.8 where the area under the gradient traces plotted on the right panels have the exact same lower and upper bounds, indicating that the same edge of k-space is reached in both acquisition schemes.

3.4 Combining simulations of magnetostatics, diffusion, and imaging

The iterative magnetic field calculation, the diffusion simulation, and the simulation of field gradients applied for imaging developed and presented in Secs 3.1, 3.2, and 3.3, respectively, are compatible with one another and can be combined. In this section, we combine the three to simulate diffusion of ^{3}He gas particles through the superposition of the susceptibility-induced magnetic field inhomogeneities of the the experimental setup, and the applied magnetic field gradients for imaging during image acquisition. We then simulate acquisition of two-dimensional slice-selective gradient-echo and CSI images while the ^{3}He gas diffuses through the calculated field. Lastly, signal strengths of the two images are compared to determine degree of signal attenuation caused by diffusion in each imaging technique.

Our goal is to simulate a slice-selective 2D CSI and GRE acquisition for the experimental setup where a 3-mm inner diameter tube is charged with ^{3}He and contains a 2-mm outer diameter pellet that's suspended by a bead that rests at the bottom of the tube. The cross-sectional slice has thickness of 2 mm and goes directly through the pellet. Since the tube and the bead have magnetic permeability that is different from that of ^{3}He, magnetic field inhomogeneities are present in and around the tube. This field inhomogeneity is, of course, overlaid on top of the static field of the magnet if the tube is at isocenter of the scanner.

Consider simulating the said experiment where there is only gas inside the tube and no gas has permeated, or is allowed to permeate into the pellet. First, let us populate the 2-mm slab that encompasses the pellet with uniform ^{3}He particles (par-

ticles with free diffusivity of ^{3}He in practice) as shown in the top row of Fig 3.9. This is equivalent to "exciting" a slice, where we have created available transverse magnetization for signal acquisition. This is done with the same field-of-view and

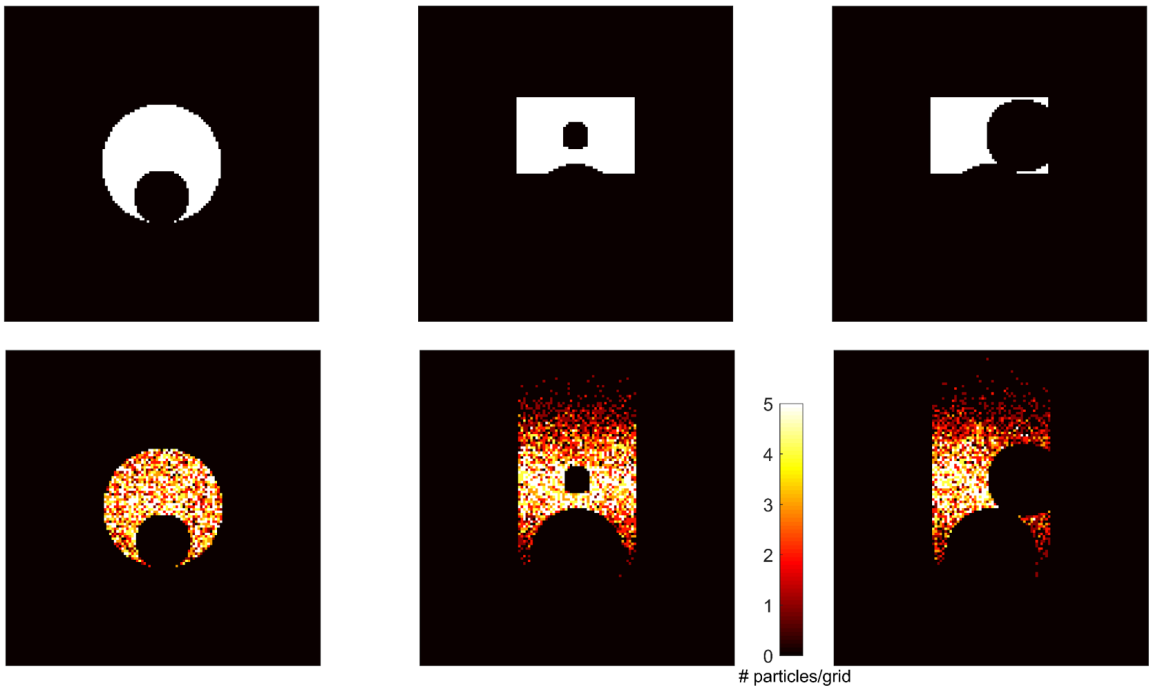

Figure 3.9: Central transverse, sagital, and coronal views of the spin density inside a 2 mm slab through the pellet. The pellet starts with no particles in it suspended by a solid bead sitting at the bottom of a 3-mm ID tube. There are initially 5 particles per grid point, uniformly distributed inside the slab. In this simulation, the pellet is also assumed impenetrable by the particles. All panels share the same color scale.

matrix size ($128 \times 128 \times 128$) as done in Sec 3.2. The particles in this slab represent the excited ^{3}He gas in the slice that have been knocked to the transverse plane using the RF pulse application of which is assumed instantaneous for the purposes of this simulation. Immediately after the excitation, these particles undergo 3D random Brownian walk and diffuse within and out of the slice with free diffusivity equivalent to that of ^{3}He gas as shown in the bottom row of Fig 3.9.

As these particles diffuse in the static magnetic field inhomogeneities created by the differences in magnetic permeability of glass and ^{3}He, they accrue phase strength

of which is proportional to the product of frequency and diffusion time. An example of the field inhomogeneities for the geometry of the experiment (as presented in Fig 3.9) is shown in the top row of Fig 3.10. At each step, the phase accrual of a particle with

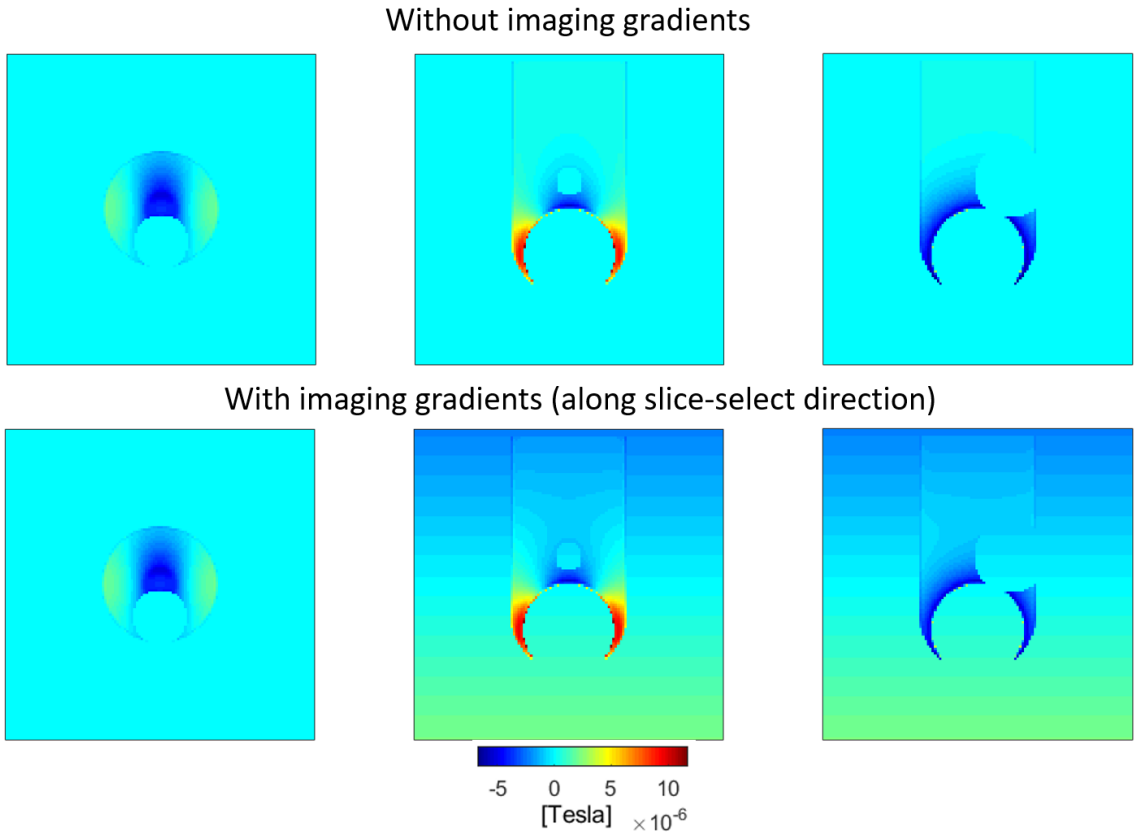

Figure 3.10: Top row: Transverse, sagital, and coronal views of the field inhomogeneities created by the difference between magnetic permeabilities of ^{3}He and glass in our experimental setup. Bottom row: Transverse, sagital, and coronal views of the same field inhomogeneities but with addition of an example of gradient applied along the slice-select ($\hat{x}$) for imaging.

transverse magnetization can be written as

$$\phi(r, \Delta t) = \Delta\omega(r)\Delta t = 2\pi\Delta f(r)\Delta t = \gamma(B(r) - B_0)\Delta t, \tag{3.35}$$

where γ is the gyromagnetic ratio of the said particles, in this case of ^{3}He. Since $B(r)$ is not uniform spatially, the phase accrual is not uniform for all particles that were

excited in the slice. That is to say, diffusion of particles in a nonuniform static field is inherently an irreversible dephasing process, one which causes signal attenuation as the particles lose coherence and resonate at different frequencies.

So far, the slab containing the particles is excited and particles are allowed to freely diffuse with the only exception being impenetrable glass bead, tube walls, and pellet where the particles are not allowed to permeate in. We point out that the pellet walls are only impermeable for the purpose of the simulation, that is to say, this is an artificial constraint and implemented only in this simulation, and in the actual experiment, the pellet walls are permeable to ^{3}He at room temperature. To acquire an image of this slice, one must acquire the collective signal produced by the particles at all appropriate spatial frequencies, i.e. k-space locations. This is done by applying the corresponding magnetic field gradients to traverse to the desired k-space location for signal acquisition. As demonstrated in Sec 3.3, for CSI acquisition, the application of the relevant gradients is done prior to ADC (i.e. phase encoding, see 3.8), while for gradient-echo acquisition, gradients are applied while ADC is on for signal acquisition (i.e. frequency encoding, see Fig 3.7). Unlike the static magnetic field inhomogeneities, the imaging gradients are time-dependent and their timing is very carefully computed in accordance with Eqs 3.32, 3.33, and 3.34, and their timing and waveforms depend on desired field-of-view and resolution.

This collective signal is generated by adding up magnetization of spins inside the entire slab. Signal acquisition for each TR period is done by keeping track of the phase of all particles and while the ADC is on, at time t, the signal is computed as

$$S(t) = \sum_{j=1}^{M} e^{-i\phi_j(t)} e^{-t/T_2^*} = \sum_{j=1}^{M} e^{-i\gamma[(B_j(t)-B_0)+G_j(t)\cdot r_j(t)]t} e^{-t/T_2^*}, \tag{3.36}$$

where e^{-t/T_2^*} term is included to account for T_2^* decay during signal acquisition, $B_j(t)$ is the superposition of the static and permeability-induced field inhomogeneity as seen by the j^{th} particle, $G_j(t)$ is the imaging gradient seen by the j^{th} particle, and

$r_j(t)$ is the position of the j^{th} particle all at time t.

For chemical shift imaging, the entire signal $S(t)$ is assigned to the appropriate k-space voxel as determined by the area under the gradient traces applied prior to ADC. Therefore, for a square field-of-view, isotropic slice-selective 2D CSI data set, an $N_\ell \times N_\ell \times N_s$ sized matrix is used to store the information, where N_ℓ is the number of voxels along each dimension and N_s is the number of sample points in $S(t)$. In this case, N_s is the number of iterations each with time step Δt in accordance with free diffusivity definition $D_0 \equiv \frac{\delta^2}{2N_d\Delta t}$. For the gradient-echo imaging simulation, the signal $S(t)$ read out in each line of k-space is allocated into N_ℓ pieces and the average value of signal in each piece is assigned chronologically to the appropriate k-space voxel.

Fully phase encoded imaging offers three unique strengths that are ideal for the purposes of our experiment. First and foremost, it is robust against diffusion attenuation, compared with gradient-echo imaging, because gradients are not on while image is being acquired. An example of the simulated signal acquired using gradient-echo imaging, and fully phase-encoded imaging with and without diffusion-attenuation is given in Fig 3.12. Second, it offers much higher SNR compared with gradient-echo imaging since

$$SNR/voxel \propto \Delta x \Delta y \Delta z \sqrt{t_{ADC}} = V_{voxel}\sqrt{t_{ADC}}, \tag{3.37}$$

where V_{voxel} is the volume of the voxel (bigger volume contains more spins and therefore more magnetization or signal) and t_{ADC} is the acquisition time (see Hacke [68]). Since $t_{ADC}/voxel$ is higher for phase-encoding than frequency-encoding, lower noise is achieved using the fully-phased encoded acquisition. Another strength of the CSI technique is providing spectral information at each voxel which as we will see in Chapter 4 turns out to be an asset in data analysis. Let us look at the simulated NMR signal and its associated frequency spectrum generated by the spins in the excited slab. This is done by plotting the NMR signal, which is the central k-space signal decay where there are no gradients applied prior to signal acquisition, and its

Fourier Transform that yields the frequency spectrum as shown in Fig 3.11. In this

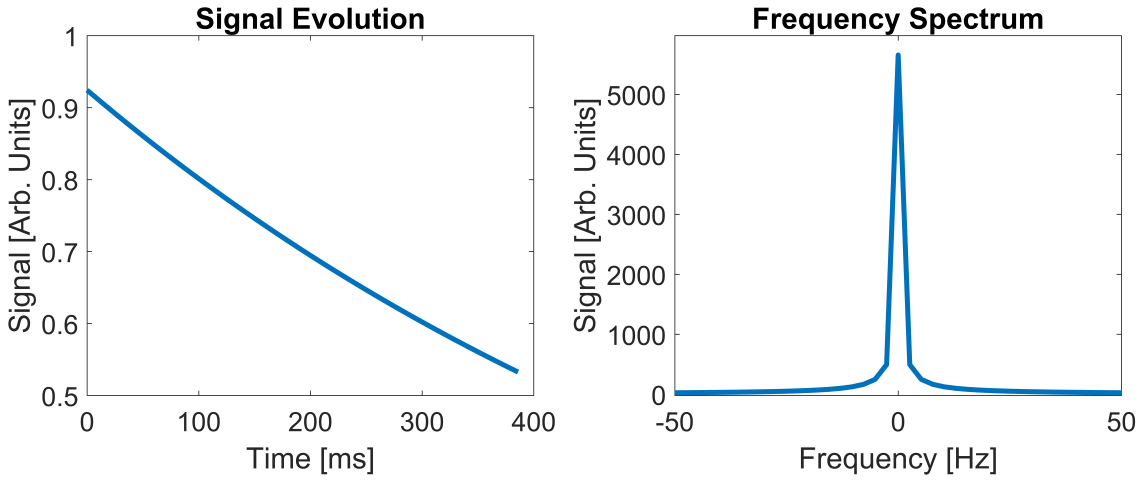

Figure 3.11: Simulated NMR signal (central k-space signal) from a slice-selective 2D CSI acquisition of ^{3}He gas inside a 3-mm ID tube and its corresponding frequency spectrum obtained by taking the Fourier Transform of the NMR signal. The geometry of the tube and the field inhomogeneities inside it, and diffusion of ^{3}He particles through the field inhomogeneities are presented earlier in Figs 3.9 and 3.10.

simulation, the transverse decay time constant is chosen to be $T_2^* = 700$ ms, which is perhaps higher than what T_2^* would be in our experiments. The purpose of that is to study the limiting case in which the dephasing mechanism introduced by diffusion is the dominant effect. It appears that within the parameters of this simulation, signal attenuation due to diffusion of gas particles through permeability-induced field inhomogeneities plays a negligible role, and even at such high T_2^*, the signal attenuation is dominated by T_2^* decay and not diffusion attenuation, another strength of this technique as compared with gradient-echo imaging where gradients are on during acquisition time causing severe signal attenuation.

The 2D k-space map for the CSI data set can be obtained by taking the first point of $S(t)$ and assigning it as voxel amplitude in each voxel, which in turn destroys the spectral information. This is called "single-point imaging". It is defensible to use only the first point in this simulation as an assignment for the voxel intensity because there is no measurement noise. In reality, only choosing a point to represent

the signal yields poor SNR and the image quality is severely compromised because as mentioned earlier, SNR in each voxel scales with square root of measurement time (i.e. $SNR \propto \sqrt{t_{ADC}}$). Instead, an average of several points of the signal $S(t)$ can be assigned to each voxel as intensity. Another way as mentioned in Sec 2.6 is to Fourier Transform the signal to obtain its frequency spectrum, fit the spectrum to a sum of complex Lorentzian functions, and assign the sum of areas under the curves to each voxel as intensity. Images can be obtained by taking the inverse Fourier Transform of the k-space maps corresponding to the slice-selective 2D CSI and gradient-echo imaging simulations.

The simulated k-space maps obtained in slice-selective 2D CSI and gradient-echo imaging simulations are plotted in the top row of Fig 3.12 and their corresponding images in the bottom row of the same figure. In this simulation, no regrowth or decay (in case of hyperpolarized imaging) of the longitudinal magnetization is considered in these acquisitions. This is done by ignoring RF loss of longitudinal magnetization at each excitation and assuming infinite T_1 in the case of hyperpolarized gas imaging (i.e. initial transverse signal after application of each RF pulse is the same). Fig 3.12 serves as another powerful demonstration of the robustness of the CSI technique to diffusion as opposed to the gradient-echo imaging technique.

3.5 Summary

In this chapter, we developed an iterative magnetic field calculation method based on the magnetic scalar potential. We implemented this technique to determine the magnetic field inhomogeneities pertinent to our experimental setup. We then developed a diffusion simulation to simulate the motion of the helium particles through the magnetic field inhomogeneities of our experimental setup. Additionally, we developed a technique to simulate the field gradients applied for imaging the gas, which is part of our experimental procedure for the permeation measurements.

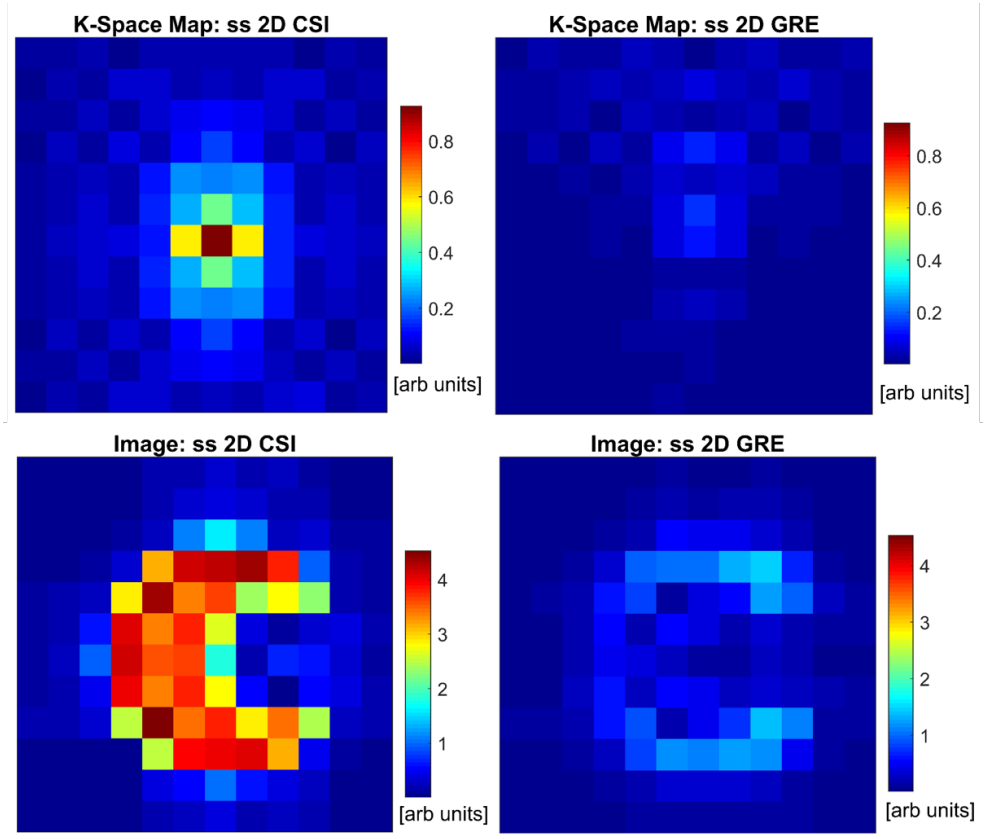

Figure 3.12: Simulated k-space maps and corresponding images using 2D slice-selective CSI and gradient-echo imaging of ^{3}He gas inside a 3-mm ID tube that houses a glass bead at the bottom suspending an impenetrable pellet. Perfect spoiling is assumed for both simulated acquisitions. Additionally, no regrowth or decay (in case of hyperpolarized imaging) are considered in these acquisitions (i.e. initial transverse signal after application of each RF pulse is the same).

Further we combined our field calculation with the diffusion and imaging gradients simulations to establish that for the polarized gas measurements, chemical shift imaging (CSI) is an imaging technique robust to diffusion and field inhomogeneities that offers higher signal intensity than gradient echo imaging. In particular, our simulations suggest that the signal intensity achieved using a two-dimensional CSI pulse sequence is substantially higher than using a gradient-echo pulse sequence, owing it to unfavorable signal attenuation due to diffusion of the gas through field inhomogeneities.

Several aspects of the simulations developed in this Chapter will be used throughout Chap 4 to draw conclusions and/or reason through our experimental results and observations.

Chapter 4

Permeation Measurements

The work presented in this thesis builds on the research collaboration efforts between University of Virginia, Jefferson National Laboratory, and General Atomics commenced in 2013 to design a polarized reactant fuel delivery mechanism [21, 23, 25, 28, 29]. The purpose of such research study is to demonstrate the feasibility of using inertial confinement fusion (ICF) polymer shells to encapsulate polarized ^{3}He and D suitable for cryogenic injection into the tokamak plasma core. Lack of a robust polarized fuel delivery mechanism is among the main obstacles standing in the way of spin-polarized fusion experiments to determine its potential in achieving fusion ignition.

The aim of the research project presented in this chapter is to study the feasibility of using ∼2-mm-diameter ICF polymer shells as a vessel for cryogenic transportation of polarized fuel. If the shells are proven feasible, they can be filled with polarized fuel and cryogenically injected into the core of the DIII-D tokamak, a magnetically confined fusion reactor, to test spin-polarized fusion.

To load the polymer shells with polarized ^{3}He, we must polarize ^{3}He first, and then permeate the polarized gas into the shells, because we use spin exchange optical pumping to polarized ^{3}He. There are three important questions the answers to which determine the feasibility: 1) how much polarization loss is associated with permeating polarized ^{3}He into these polymer shells, 2) what is the absolute polarization of the

reactant nuclei once the permeation process is complete, and 3) how long can the polarization last once inside the shells at temperature of 77 K.

The answer to the first two questions is important because fusion energy yield depends on degree of spin-alignment, or polarization along shared axis, between reactant nuclei. The higher the polarization of the reactant nuclei, the higher the fusion cross-section, and consequently, the higher the energy output. As we saw in Chapter 1, the energy yield could be 1.5 times larger for 100% reactant nuclei polarization.

The answer to the third question is of importance for the following reasons. If successfully loaded with polarized fuels, the polymer shells will have to be transported to the tokamak site, if the polarized-fuel loading station is not located at the tokamak facility. Even if the polarizer is located near the tokamak, there will be some delay between production and injection. This process has to be done cryogenically, because, as we will see in the next section, one of the properties of the said polymer shells is impermeability to helium at 77 K, such that no helium can enter or exit the shells. Once the shells are loaded, cooling them ensures encapsulation of the polarized gas. Further, the shells must be cryogenically injected into the plasma core through appropriate wave-guides. Therefore, how long the loaded fuels maintain their polarization inside the shells ultimately decides the degree of polarization entering the plasma.

We performed several experiments in which we aimed to load the said polymer shells housed inside a borosilicate glass tube with high pressure, high polarization ^{3}He gas. The permeation process was monitored using MRI to quantify the polarization loss in the permeation process along with decay time constant of the gas inside the tube, and inside the shell. In this chapter, we present the experimental apparatus, measurement plan including imaging techniques, data analysis, and results of permeation measurements performed using chemical shift imaging of hyperpolarized ^{3}He. This will provide the answer to the first question for our specific experimental setup. The answers to the second and third question are determined in the experimental results presented in Chapter 5.

We first begin by laying out the experimental apparatus in Sec 4.1 to describe the shells (also referred to as pellets throughout this chapter and the next), the glass vessels used for loading, polarizer, and the imaging hardware. In Sec 4.2, we describe the gas dispense procedure, MRI techniques used in measurements, and practical considerations. We then discuss how we analyze the MRI data used for quantification of permeation and decay parameters in Sec 4.3. Next, in Sec 4.4, we will develop a theoretical permeation and polarization evolution model to extract permeation parameters such as polarization retention rate and decay time constant from our experimental measurements. And lastly, in Sec 4.5, we present the results of the fit to the developed model and the extracted parameters.

The preliminary results laid out in this chapter were presented at the 23^{rd} International SPIN symposium in Ferrara, Italy (2018) [28].

4.1 Experimental apparatus

In this section we describe the components of the experimental apparatus for permeation measurements. This apparatus consists of polymer shells originally developed for inertial confinement fusion experiments, glass vessels used to contain the pellets while loading with high-pressure and polarized ^{3}He, polarizer for polarizing the ^{3}He gas, and MRI scanner and coil with which we perform our experimental measurements.

4.1.1 ICF shells

In inertial confinement fusion, polymer shells are used to encapsulate the fusion reactant nuclei, tritium and deuterium. These "pellets" are developed specifically for ICF experiments [30] and can hold up to 10 mg of fuel. An image of an ICF shell is given in Fig 4.1. These pellets are designed such that they are permeable to small gas atoms such as D and T at room temperature but impermeable at 77 K. At room

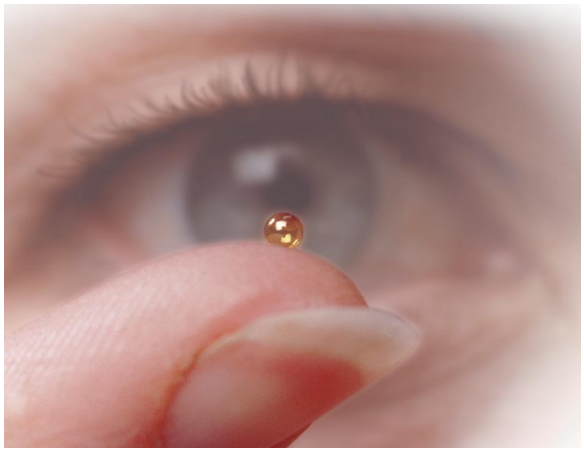

Figure 4.1: Image of an ICF pellet demonstrating its relative size. Image reproduced from [72].

temperature, pressure gradient causes net flow in or out of the pellet. Therefore, at room temperature, pressure gradient can be applied for buildup of ^{3}He or D inside the pellet. Therefore, once these pellets are cooled with liquid nitrogen, no reactant nuclei can permeate into or out of the shells.

These ICF shells can be used to contain polarized nuclei as well [21]. The pellets used in our experiment are developed by General Atomics [30] using the glow-discharge polymerization technique routinely used for ICF pellet fabrication [73]. They have an outer diameter of $\sim$2 mm with wall thickness of 15-16.8 μm or 26 μm. The permeation time constant of the pellets used in our experiments were measured by our collaborators at Jefferson National Lab and were found to be 225-232 s for 15-16.8-μm-thick-wall pellets, and 374-421 s for 26-μm-thick-wall pellets.

We exploit the temperature-dependent permeability of the ICF pellets for containment of polarized ^{3}He in our experiment presented in Chapter 5. That is, once the shells are loaded, we can immerse the glass vessel which houses the pellets in liquid nitrogen to seal the gas inside the pellet. Since the permeation time-constant at 77 K is in the order of hundreds of hours, the walls of the pellets are effectively sealed. Therefore, the gas inside the pellet can be cryogenically transported without

any leakage.

4.1.2 Borosilicate glass tubes

As discussed in the previous section, pressure gradient preferentially drives gas into or out of the pellets. Therefore, to load the pellets with ^{3}He, we expose the empty pellet to high-pressure gas, and the pressure difference between regions inside and outside the pellet will cause permeation into the pellet. In our experiment, we expose pellets to high-pressure, highly polarized ^{3}He inside borosilicate glass tubes with inner diameter of 3-4 mm. We experimented with a variety of tube designs before settling on the ones used for the measurements described here. All designs have a tubular section at the bottom of which the pellet sits, and the newer versions have a valved ante-chamber separate from the tubular section, creating a "buffer" volume. Two examples of the tube designs, one with, and one without the ante-chamber is shown in Fig 4.2.

We aim to quantitatively monitor the permeation process from the very beginning when the pellets are exposed to the high-pressure gas. This is done by imaging, where we acquire signal generated by excited spins inside and outside the tube (recall from Chapter 2 that "excited" spins have been tilted away from longitudinal direction and have transverse magnetization components). The purpose of the ante-chamber is to have control over the exact timing of pellet's exposure to high pressure gas, such that we have a definitive start time. The permeation process starts immediately after the pellet is immersed in gas. Since we would like to take polarization density measurements during the permeation process, an ideal time for the process to start is inside the scanner. That way, once we expose the gas to the pellet, we can immediately start the image acquisition. This capability is granted using a valve to the ante-chamber, which can be opened once inside the scanner to effectively immerse the pellet in high-pressure ^{3}He gas.

In a number of the permeation experiments, we placed a glass bead in the bottom

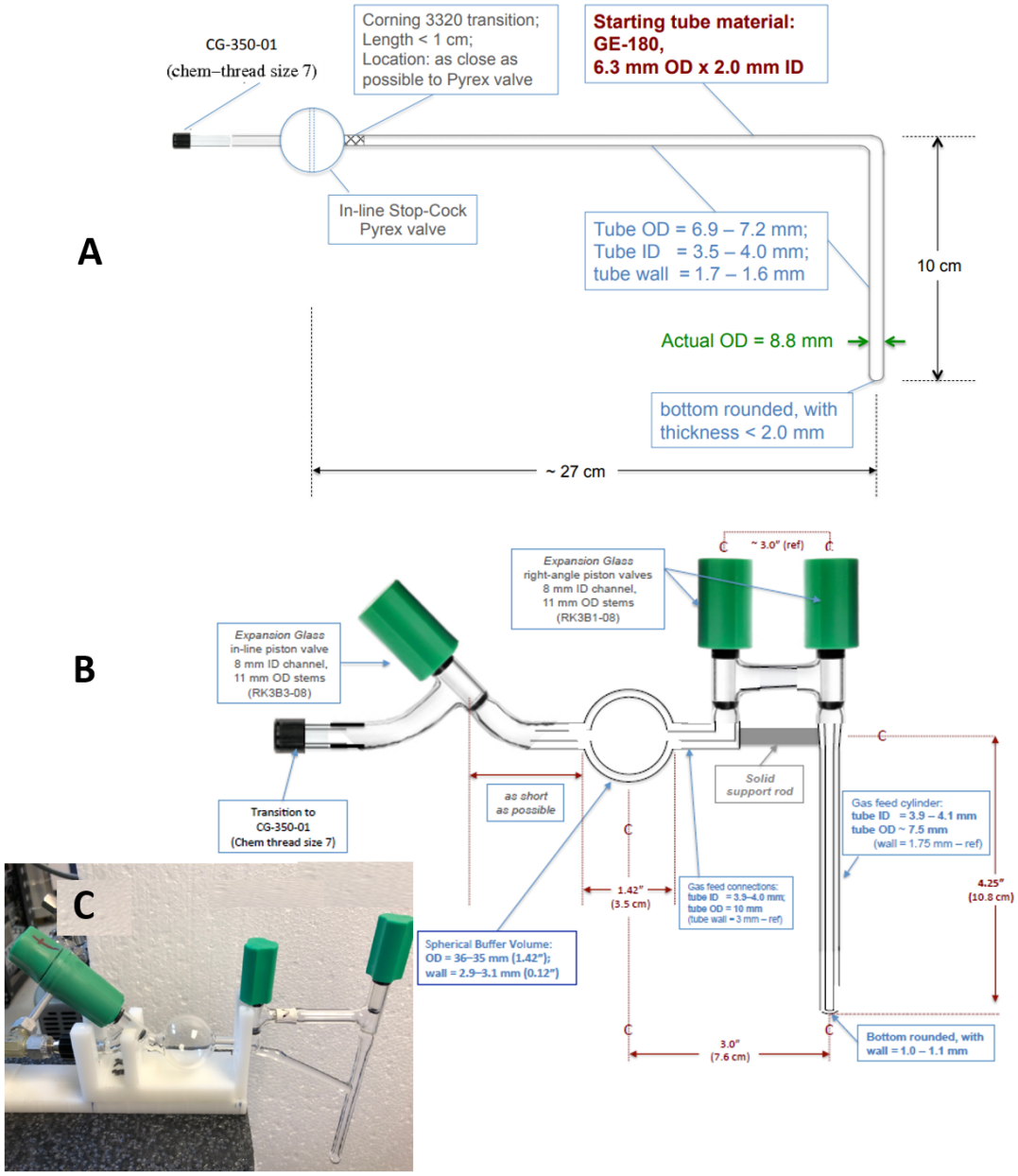

Figure 4.2: Tube designs. Diagram of A) an older version of the tube without the ante-chamber, and B) the latest version of the tube design with a spherical ante-chamber connected with a valve to the tubular part where the pellet rests at the bottom. C) image of the tube with design given in B).

of the tube to elevate the pellet away from the bottom of the tube (see Fig 4.3). This is done to minimize pellet's neighboring magnetic field inhomogeneities due to bottom of the tube's difference in magnetic permeability compared with permeability of ^{3}He. The bottom of the tube has a curvature such that substantial tube's surface

Figure 4.3: Image of the bottom of a tube which houses a pellet that rests on top of a glass bead.

is parallel to the static field. If two materials with different magnetic permeabilities share a boundary, and are immersed in an otherwise uniform static field, the most field disturbance is observed at and near the boundary that is parallel to the static field. As will be shown in Sec 4.1.4, the tubular part of the tube is normal to the static field of the magnet, therefore, near the bottom of the tube has the largest field disturbances and sharp field gradients, which act to depolarize the gas [74]. Therefore, the bead is placed at the bottom of the tube to move the pellet away from the region of high field disturbances.

In the next section, we will describe how we create a pressure differential between inside and outside the pellet such that the inside starts in vacuum while exposed to high pressure helium on the outside.

4.1.3 Polarized ^{3}He dispense mechanism

Here we describe how a tube containing a pellet can be filled with high pressure and highly polarized ^{3}He suitable for permeation experiments.

We polarize 121 psig of ^{3}He via spin-exchange optical pumping (see Sec 2.1.2) using our homebuilt polarizer located in the basement of Snyder building, down the hall from the MRI scanner room. The final polarization level is 40-60 % although the exact polarization is not measured for these experiments. Once the polarizer has been on for $\sim$ 5 polarization build up time constants ($\tau \sim 4$ hours), the oven and the lasers are turned off for at least 40 min to allow the rubidium to cool down and solidify. At this point, ^{3}He is ready to be dispensed.

While the polarizer is on, the tube of interest is vacuumed by connecting the tube to a vacuum turbo pump via aluminum tubing. This ensures that the starting state of the tube and the pellet is at vacuum, and using a turbo pump, we can achieve pressures in the order of 1e$-$6 mbar. Every time we place a pellet and/or a bead inside a tube, we expose both the tube and the pellet to room air. Tubes that are exposed to room air are vacuum pumped for at least 24 hours, while those that are reused in our experiments without a new pellet insertion, can be pumped in the order of an hour to reach mbar-level pressures. An image of the polarizer and the dispense system is given in Fig 4.4.

The vacuum pumping is done to remove all possible impurities, particularly those that are paramagnetic such as O_2. Presence of paramagnetic particles in the glass tube that contains the polarized ^{3}He is detrimental to the polarization of the ^{3}He gas [75–78]. For context, the limit of longitudinal spin-relaxation time of ^{3}He in polarizer cells are quoted $\sim$ 70 hours [79]. Whereas in our experiments presented in Chapter 6 of Part B, in which inhaled hyperpolarized ^{3}He or ^{129}Xe inside human lungs are imaged, T_1 values in the order of 20 s is observed due to presence of abundant oxygen molecules in the lung.

Once the pressure has stabilized at $\sim 1 \times 10^{-6}$ mbar at least for 30 minutes, we

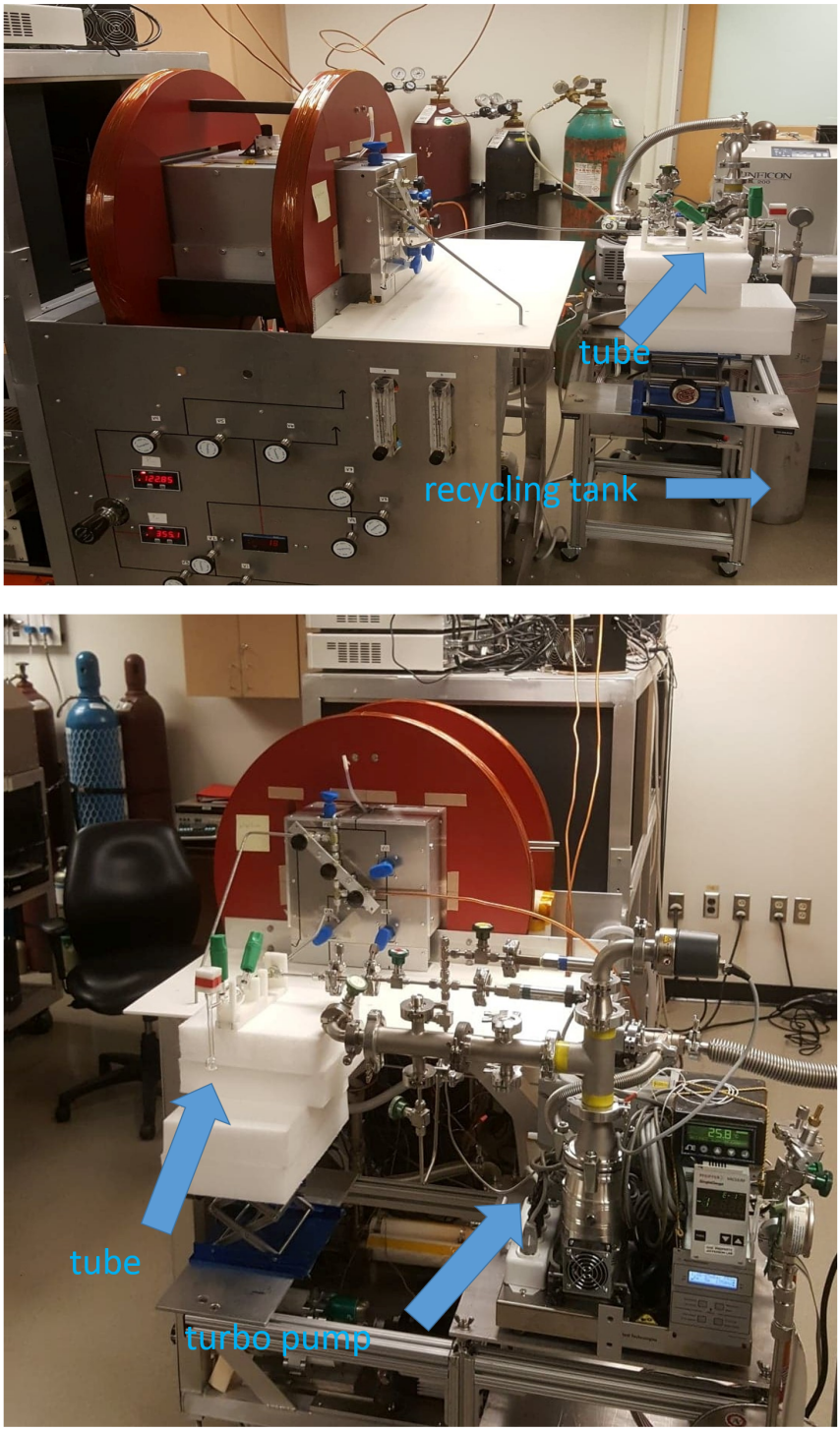

Figure 4.4: Shown are two views of the polarizer and the connected setup for dispensing polarized, high pressure ^{3}He gas into the tubes that house the pellet. Prior to dispensing gas, the tube is pumped down to $\sim$ 1e$-$6 mbar using the turbo vacuum pump. The remainder of the gas in pipes gets stored for future experiments in the recycling tank.

proceed to disconnect the vacuum pump from the tube. Next, from the polarizing cell, we dispense high pressure highly polarized ^{3}He and fill the glass tube. For tubes that have an ante-chamber, the valve to the tubular section where the pellet sits is closed prior to dispense. This gives us the capability to start the permeation inside the scanner, immediately followed by the first measurement of the spin-density in the tube and the pellet using MRI. For the tubes without the ante-chamber, the permeation process starts immediately after dispensing helium. Therefore, it is important to transport the loaded tube into the scanner and start the measurement as soon as possible. Typically in our experiments, the process to close the valve, disconnect the glass tube (filled with polarized ^{3}He) from the dispense mechanism, walk over the tube from the polarizer to the scanner, secure it onto the coil housing (which will be discussed in the next section), and send it inside the scanner takes ~ 90 seconds. The permeation measurement can commence shortly after the tube arrives at the center of the scanner.

4.1.4 MRI hardware

We use the MRI scanner to make polarization density measurements as a way of monitoring the permeation process inside the scanner. This section describes the MRI hardware necessary to perform an imaging-based polarization loss measurement of a given permeation experiment.

All imaging is done using a whole-body clinical 1.5 Tesla scanner (Siemens, Erlangen), which is also used for the experiment presented in Chapter 6, in which inhaled hyperpolarized ^{3}He or ^{129}Xe inside human lungs is imaged. An auxiliary RF coil is used for excitation and signal detection of the ^{3}He nuclei. Since ^{1}H and ^{3}He have different gyromagnetic ratios, and consequently resonate at different frequencies at a given field strength, conventional RF coils for body imaging are incompatible for imaging in our application. For our permeation experiments, and those presented in Chapter 5, a linearly polarized saddle-shaped coil was built on a cylindrical Acrylic

form. The coil was tuned to the resonant frequency of ^{3}He at 1.5T, which is 48.6 MHz.

The coil is secured inside a Styrofoam housing, positioned such that the bottom of the tube containing the pellet is suspended at the center of the coil. The tube sits on the Styrofoam coil housing which is taped onto the bed of the scanner table. The whole setup is positioned such that the center of the coil appears at the isocenter of the scanner, once the table is moved inside the magnet. Fig 4.5 shows the experimental set up for a typical permeation measurement.

4.2 Experimental Methods

In this section we lay out the experimental methodology used in our permeation measurements. This includes description of the general work flow of the experiment, as well as imaging techniques used to monitor the permeation process.

In the experiments presented in this chapter, we acquired and analyzed 2 datasets, the explanation of which is given in the following.

Data set A was taken on November 18 2016 with tube G filled with 1.54 (absolute) bar of polarized ^{3}He. The tube contained a 2.2-mm spherical glass bead, on top of which rested a 1.82-mm pellet with wall thickness of 15 μm, and permeation time constant of 227 s. This data set consists of 11 2D CSI images taken at times t = 1.5, 2.5, 3.5, 5.0, 7.0, 9.5, 13.5, 21.5, 33.5, 49.5, and 69.5 min all referenced to start of permeation (t = 0).

Data set B was taken on August 14 2016 with tube F filled with 2.18 bar of polarized ^{3}He. The tube contained a 2.2-mm spherical glass bead, on top of which rested a 1.82-mm pellet with wall thickness of 26 μm, and permeation time constant of 374 s. This data set consists of 15 2D CSI images taken at times t = 1.5, 2.5, 4.5, 75, 10.5, 16.5, 24.5, 36.5, 53.5, 54.5, 76.5, 105.5, 126.5, 151.5, and 176.5 min all referenced to start of permeation (t = 0).

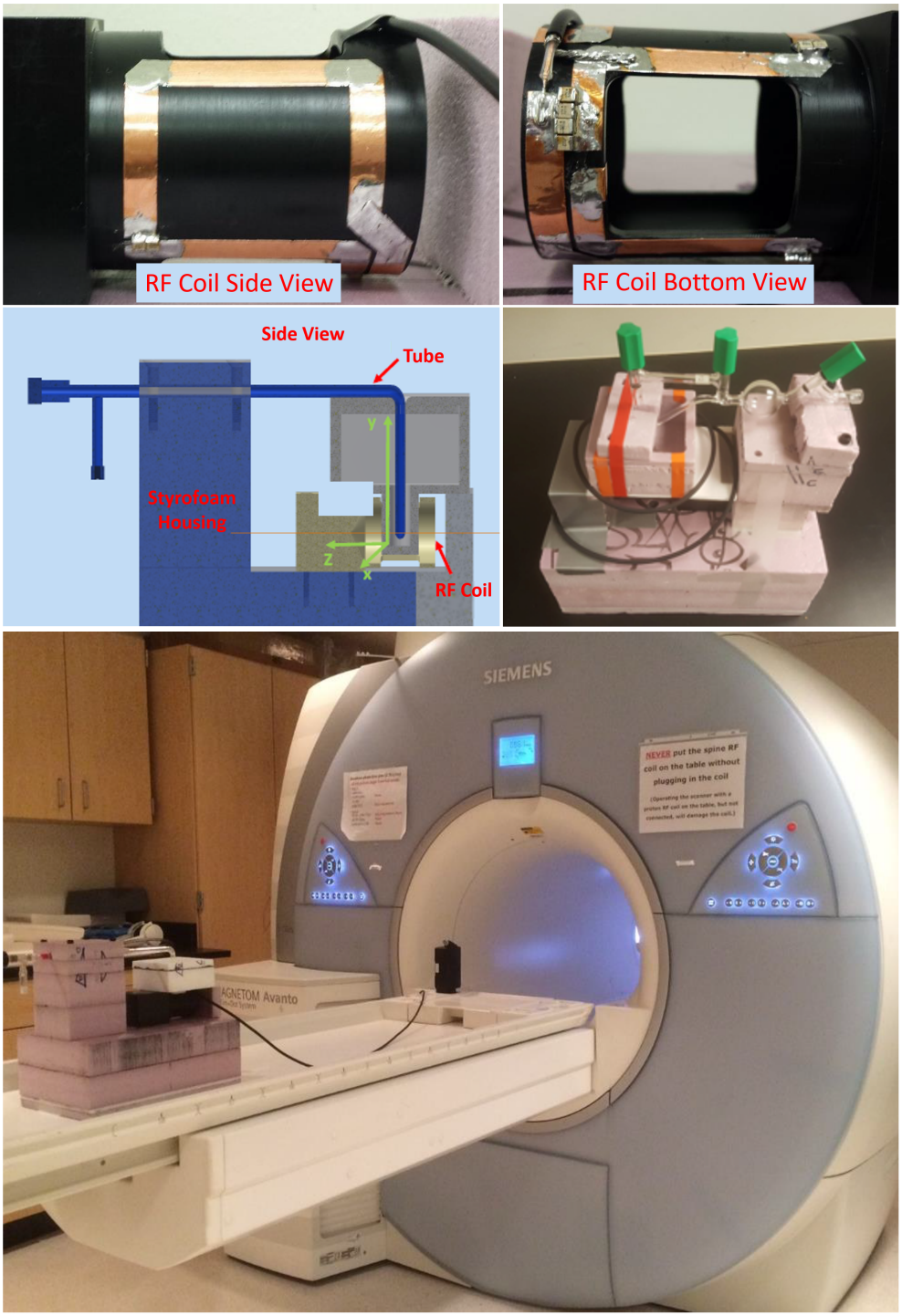

Figure 4.5: Top row: side and bottom views of our linearly polarized transmit/receive RF coil. Middle row: schematic diagram of coil housing setup with a tube without an ante-chamber (courtesy of [29]), and an image of the coil housing setup with our new-version tube atop. Bottom: the whole setup taped to the bed of the scanner. This setup is positioned such that once sent inside the scanner, the center of the coil (i.e. the pellets) would be at the isocenter of the scanner.

A tabular summary of the data sets is given in Table 4.1.

4.2.1 Gas dispense procedure

In this section, we describe the preparation work to set up the experiment for a permeation measurement. This includes loading the desired tube with a pellet, and charging the tube with highly polarized, high pressure ^{3}He.

The specific tubes to be used in an experiment are first loaded with the glass bead, if applicable, followed by placement of the pellet on top of the bead at the bottom of the tubular part of the borosilicate tube. This requires removing the valve stem leading to the tubular region. Since the tube and the pellet are naturally exposed to room air in the loading process, we then vacuum pump the tubes overnight, prior to the experiment day. The polarizer is turned on 16-20 hours (4-5 $\tau_{buildup}$) prior to the start of the experiment to achieve near-limit polarization buildup.

On the day of the experiment, the polarizer is turned off an hour prior to the start of the experiment to allow ^{3}He to cool to room temperature and for rubidium vapor to solidify. The valve to the vacuum pump is closed, and the valve to the polarizing cell is opened to connect the tube to the cell. For tubes that have an ante-chamber valve, the valve to the region containing the pellet is closed and maintained at vacuum until inside the scanner. Highly polarized, high pressure ^{3}He gas is dispensed from the polarizer cell into the tube and the pressure is read.

Immediately after dispensing the gas, the tube is disconnected from the dispense manifold and then taken as quickly as practical into the scanner room and moved into the center of the scanner magnet. This is because the presence of magnetic field gradients are a depolarizing mechanism (see Sec 5.5.5 and Eq 5.36). Since the tube is ∼30 cm away from the Helmholtz coils of the polarizer during dispense, with the tubular section of the tube normal to the axis of the Helmholtz coils, it is reasonable to expect the gas inside the tube will see field gradients at the dispense station. Further, T_1 scales with B^2, and the field anywhere near the Helmholtz coils are orders

of magnitude lower than the field of the scanner. Quick transportation to the scanner isocenter, where the field is very strong and uniform, inhibits undesirable relaxation.

For the tubes with an ante-chamber, when the setup is inside the scanner and the pellet sits at or near the isocenter of the magnet, the ante-chamber valve to the region of the tube containing the pellet (which, again, is maintained at vacuum until this moment) is cycled to immerse the pellet with polarized gas. For tubes without the ante-chamber, the permeation starts at the dispense time. At this time, the experimental preparation is complete, and we start acquiring images to extract the spin-density of ^{3}He inside and outside the pellet as a function of time throughout the permeation process, which will be the central topic of the following sections.

4.2.2 Flip-angle consideration for polarized ^{3}He MRI

Before moving onto describing the MRI techniques used in our permeation experiments, we will discuss a common consideration in all MRI of polarized (i.e. hyperpolarized) gas, which is the flip-angle of the excitation RF pulses used.

Recall from Chapter 2 that an RF pulse tips longitudinal magnetization away from the longitudinal direction, which creates precessing transverse magnetization. The MR signal generated from precessing transverse magnetization can be measured using RF coils. The signal S is proportional to $\sin\theta$, where θ is the flip-angle of the pulse. The magnetization that is tipped away from the longitudinal direction onto the transverse plane will regrow to its thermal equilibrium polarization level M_0, not its non-equilibrium hyperpolarized state $M(0)$. Therefore, the fraction $(1-\cos\theta)$ of the longitudinal magnetization used by the application of the RF pulse to generate transverse signal will no longer be available for future excitations since $M_0 \ll M(0)$. More broadly, for a series of n RF pulses applied to acquire an image, $(1-\cos^n\theta)$ fraction of the available longitudinal magnetization that is used to generate transverse signal is unrecoverable, and will no longer be available for future excitations.

For this reason, much lower flip-angles are used in MRI of hyperpolarized samples,

than are used in MRI of samples at thermal equilibrium polarization level. In our experiments presented throughout Sec 4.2, flip-angles between 1°-2° are used.

4.2.3 Initial experiment: confirmation of polarization survival in the permeation process

Our first goal in the permeation experiments was to determine whether any detectable polarized gas completes the permeation process. The buildup of the number density of ^{3}He molecules inside the pellet takes the exponential growth form

$$\rho^{in}(t) = \rho_0(1 - e^{-\frac{t}{\tau_{perm}}}), \tag{4.1}$$

where ρ_0 is the number density inside the tube, and τ_{perm} is the time constant of the pellet within the range 227 - 374 s (see Table 4.1), depending on the pellet batch, type, and wall thickness. Therefore, we expect that acquiring an image 10 min after the permeation process has commenced would show a considerable signal buildup at the location of the pellets in the image, if a substantial amount of the gas that has completed the permeation process retained its polarization.

To determine the outcome of the permeation experiment, we acquired a 3D gradient-echo image in an attempt to see signal where we suspect the pellet's position is after a few permeation time constants as shown in Fig 4.6a. While it is encouraging to see some signal where the pellets are, it would be more definitive to see the pellet gas signal isolated from the tube gas signal. To perform that experiment, we cooled the tube to 77 K by dipping it in liquid nitrogen to "freeze" the pellet walls such that they practically become impermeable to ^{3}He, and vacuum pumped the tube to empty the gas outside the pellet (leaving only the pellet with polarized gas anywhere in the tube). We then acquired the same image presumably with only gas existing inside the pellet as shown in Fig 4.6b. This is a direct, definitive confirmation that at least a measurable fraction of the polarization is retained in the permeation process.

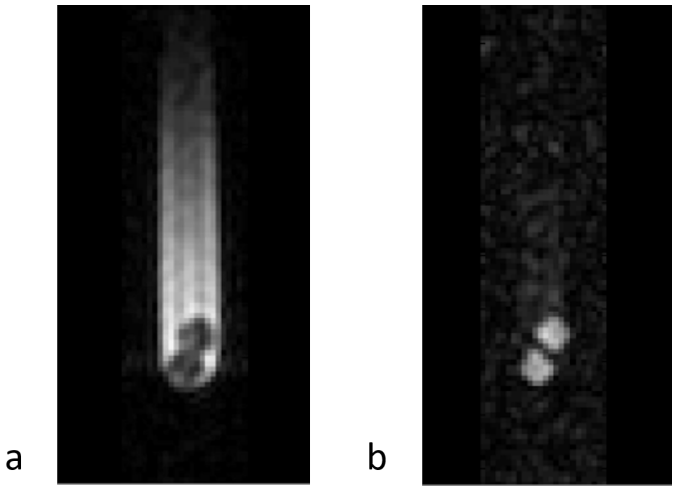

Figure 4.6: Single slice from a 3D image of hyperpolarized ^{3}He gas inside a tube with two pellets a) 10 min after the permeation process commenced, and b) after the tube is dipped in liquid nitrogen to seal the pellets and vacuum pumping on the tube to deplete the tube outside the pellet.

The next challenge then becomes determining exactly how much polarization loss is associated with the permeation process and what variables are at play that determine the degree of polarization retention. As motivated by the simulation results shown in Sec 4.2.4, it is important that we adopt the chemical shift imaging technique moving forward.

4.2.4 Motivation for using CSI

In this section, we discuss our motivation for using CSI rather than gradient-echo imaging for permeation measurements. Recall from Chap 2 that in MRI, SNR/voxel $\propto \sqrt{t_{ADC}}$. As will be discussed in Sec 4.3, polarized ^{3}He T_2^* in our experiments is rather large (typically 20-80 ms), which allows us to acquire this long-lasting signal at each k-space point by setting t_{ADC} to $\sim 4 \times T_2^*$.

On the other hand, this same time window is alloted for the entire line of voxels in gradient-echo imaging. Additionally, even though the time that the transverse signal is available for sampling is large, gradient-echo imaging should be used with

high bandwidth to avoid attenuation caused by diffusion, consequently, not taking advantage of the long T_2^*. Therefore, fully phase encoded imaging, even though requires application of n = FOV/L (where n is the number of voxels along a dimension for a square FOV, and L is the length along each dimension) times more RF pulses to acquire the same FOV image, the SNR/voxel is so much higher in the fully-phase encoded imaging sequence that if the extra acquisition time can be accommodated, a CSI pulse sequence is the favorable one.

The simulations presented in chapter 3 where the effects of gradients in imaging, diffusion of ^{3}He, and the field inhomogeneity superimposed on the static B_0 due to the presence of glass and pellet are all considered demonstrates this stark difference in signal alone as shown in Fig 4.7. It can be seen that a drastic signal attenuation is inevitable in gradient-echo imaging where gradients are applied while gas particles are diffusing compared with the gradient-echo image taken for stationary particles. On the contrary, the FID signal acquisition used in CSI is robust against diffusion-attenuation of the gas molecules since there are no gradients on during ADC no matter the strength and timing of the gradients applied prior to acquiring the signal at each k-space point. For this simulation, the average signal attenuation in gradient-echo imaging in the presence of diffusion is $\sim 60\%$.

4.2.5 Slice-alignment using 2D gradient-echo images

We have so far established that two-dimensional chemical shift imaging is a favorable alternative to 2D gradient-echo imaging for the permeation experiments. We aim to acquire 2D slice-selective CSI images through the cross-section of the tube where the pellet is located (Fig 4.8). To do so, we must first locate the pellet inside the tube for accurate slice-positioning, based on a "localizer" image. This has to be quick−permeation process starts the moment the ante-chamber valve is cycled, and ideally, the entire process would be monitored via a series of CSI images starting from the very beginning. Therefore we use a quick (<1 s), high-bandwidth gradient-echo

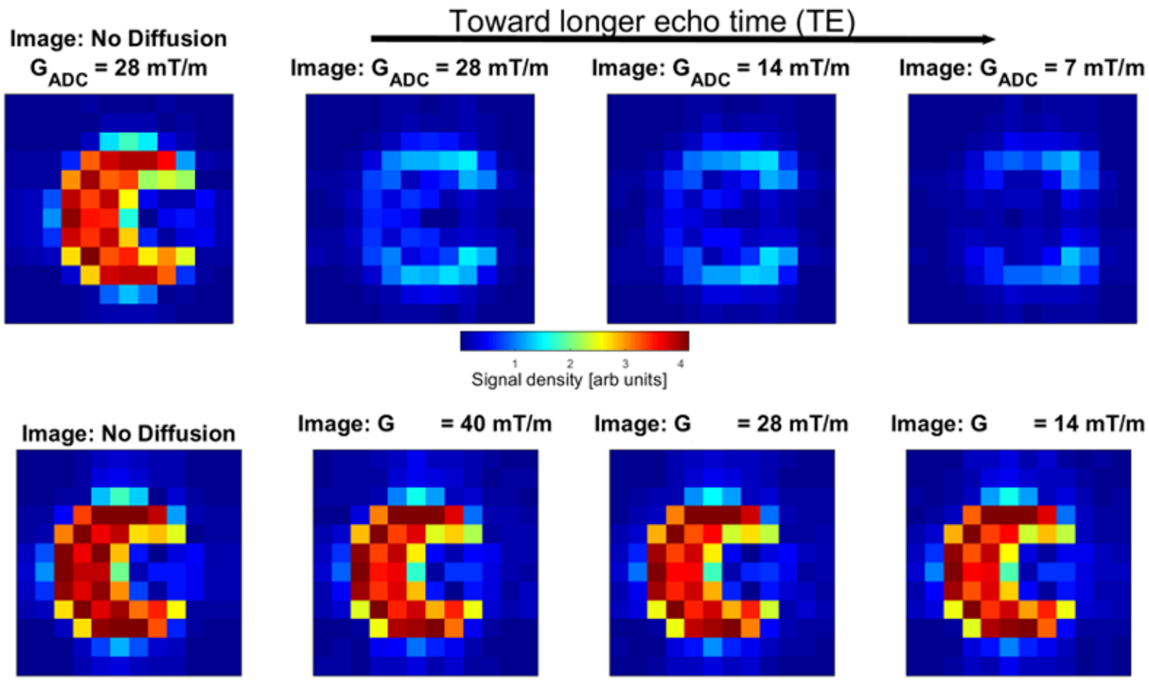

Figure 4.7: 2D simulations of gradient-echo (top row) and CSI (bottom row) as a function of TE (or product of gradient amplitude and time for the same area) for "frozen" and diffusing ^{3}He particles. The 2D slice is of gas surrounding an empty pellet, hence the 'Pacman' shape. All images share the same color scale. The images on the first column (top left, bottom left) do not allow diffusion of particles for reference. The gradients for the bottom row are applied to move to the desired location in k-space prior to acquiring signal, while G_{ADC} are gradients applied during signal acquisition. Mean signal attenuation between the gradient-echo and the CSI images is $\sim 60\%$, with the only difference between the two is diffusion of ^{3}He gas molecules.

pulse sequence with as short TE and TR as possible to acquire the localizer images. Only two localizer images are obtained, both as 2D projections using a non-selective excitation RF pulse. One is acquired in the vertical plane transverse to the scanner's magnetic field, and the other is acquired in the vertical plane parallel to the scanner's magnetic field.

A depiction of the 2D localizer images along with a diagram of the slice alignment is shown in Fig 4.8. Since the localizer images are taken very soon after the start of permeation, very little polarized ^{3}He has permeated into the pellet. Therefore,

the pellet shows up as a dark circle in the localizer images. A 2-mm slice is then positioned directly through the pellet, centering the 1.82-mm pellet inside the slice, and a time series of 2D slice-selective CSI images is then acquired throughout the permeation process, as will be discussed in the following section.

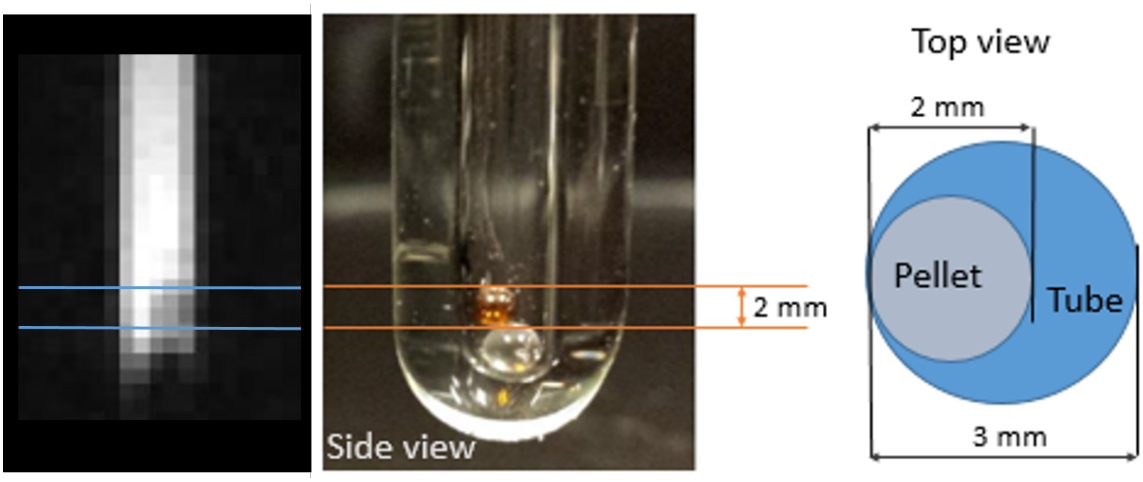

Figure 4.8: 2D gradient-echo projection image of the hyperpolarized gas inside the tube serving as a navigation localizer for slice alignment. The bead at the bottom elevates the pellet away from the field inhomogeneity introduced by the tube curvature at the bottom. A schematic top-view of the pellet and its position relative to the tube sides is shown on the right. The horizontal lines represent the slice location planned based on the gas image.

4.2.6 2D slice-selective CSI

This section focuses on the 2D slice-selective CSI pulse sequence which is used to acquire multiple images of ^{3}He gas inside the pellet and surrounding tube during the permeation process and subsequent T1 decay. These images can then be analyzed, as will be presented in Sec 4.3, to determine the polarization retention of the polarized gas completing the permeation journey, and the lifetime of the polarized gas once inside the pellet.

To precisely track the signal evolution, images must be acquired frequently with respect to the relevant time scales. These time scales are the permeation time constant

τ_{perm}, a property of the specific pellet of interest which is determined empirically prior to the permeation experiments described here, and the decay time constant of ^{3}He T_1 which also must be determined experimentally. We found that the decay time constant of ^{3}He gas inside a typical tube has a wide range of 20 - 50 min. As mentioned previously, the permeation time constant is considerably shorter at 227 - 374 s. Therefore, we aim to acquire images more frequently toward the beginning where the dominant behavior is polarization build up inside the pellet and increase the timing between the data points for $t >\sim 5\ \tau_{perm}$.

A custom 2D slice-selective CSI pulse sequence (diagram given in Fig 2.11b) is used to acquire data. To adequately resolve the pellet, imaging voxel size is chosen to be 0.5 mm, resulting in 36-64 voxels with gas signal (for inner tube diameter of 3-4 mm), ~ 9 of which will have pellet partial volume. To safely cover the gas both in the tube and the pellet in the imaging slice, FOV was usually set 1-2 mm larger than the inner diameter of the tube spanning 5 - 7 mm depending on the tube size. The temporal resolution of the free induction decay obtained at each voxel is 100 μs and total acquisition time is set to 0.192s per excitation, corresponding to 5.2 Hz and 10 kHz spectral resolution and field-of-view, respectively. Other relevant imaging parameters are repetition time TR = 200 ms and a matrix size = (10×10) - (16×16) (depending on tube type size). A full CSI image thus requires 100 - 256 points and a total of 19.2 - 49.1 seconds.

The slice thickness is 2 mm, nominally covering the gas in the entire pellet and some gas in the test tube (but outside the pellet). Recall from Sec 2.3.4 that for a boxcar slice excitation, a sinc pulse, infinite in time, must be used (Fourier transform of a sinc is a rect). Since it is impractical to generate such RF pulses, we use a truncated sinc pulse instead. The duration of the RF pulse is 1.3 ms with bandwidth-time product of 2 (i.e. just the central lobe of the sinc function), which results in a Gaussian-like frequency selection "profile" as seen in Fig 4.9. Since position is directly proportional to frequency due to the application of the linear gradient, the

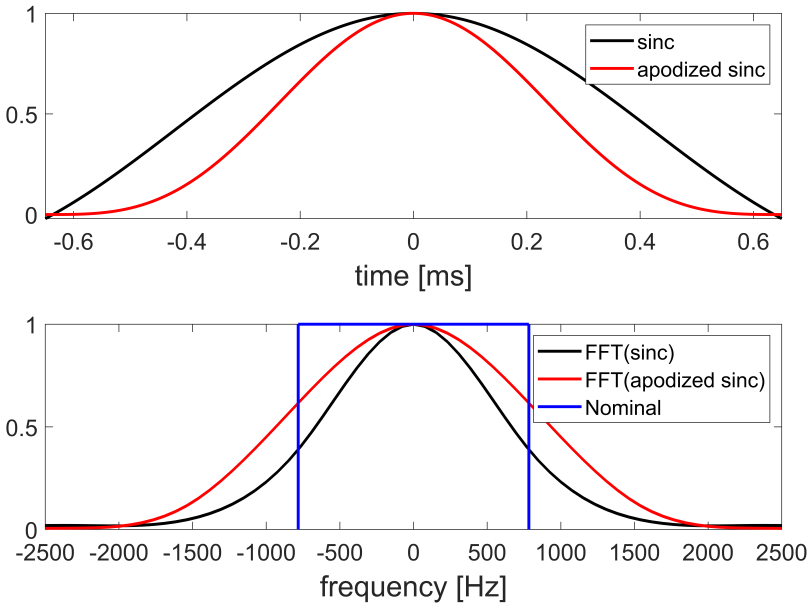

Figure 4.9: Truncated and apodized sinc RF pulse and its frequency response. The blue boxcar function is the nominal slice, if an infinite-in-time RF pulse (with infinite side lobes) was used to generate the excitation frequency range.

spatial slice has the same profile. Truncation in the time domain inherently causes unwanted oscillations in the frequency domain, although for bandwidth-time product $BWT = 2$ (i.e. two zero-crossings), oscillations are relatively small. Nonetheless, to achieve a smoother profile and remove all oscillations caused by the truncation, the RF pulse with a truncated sinc functional form can be apodized by multiplying the sinc envelope with the apodization function [69]

$$f(t) = \frac{1}{2}(1 + \cos\frac{\pi t}{BWT \cdot t_0}), \tag{4.2}$$

where t_0 is the time of the first sinc zero-crossing.

The data obtained from the 2D slice-selective CSI images are stored in a 3D matrix ($\mathrm{k}_x \times \mathrm{k}_y \times$ time). That is, for a 10×10 image, at each point in the 100 k-space points sampled, a complex FID is measured and stored, corresponding to a unique frequency spectrum. This implies that taking the Fourier transform along k_x and k_y

results in a spectrum at each point in 2D image-space. A simple illustration of an example of a chemical shift spectrum collected at every point in 2D image-space is given in Fig 4.10.

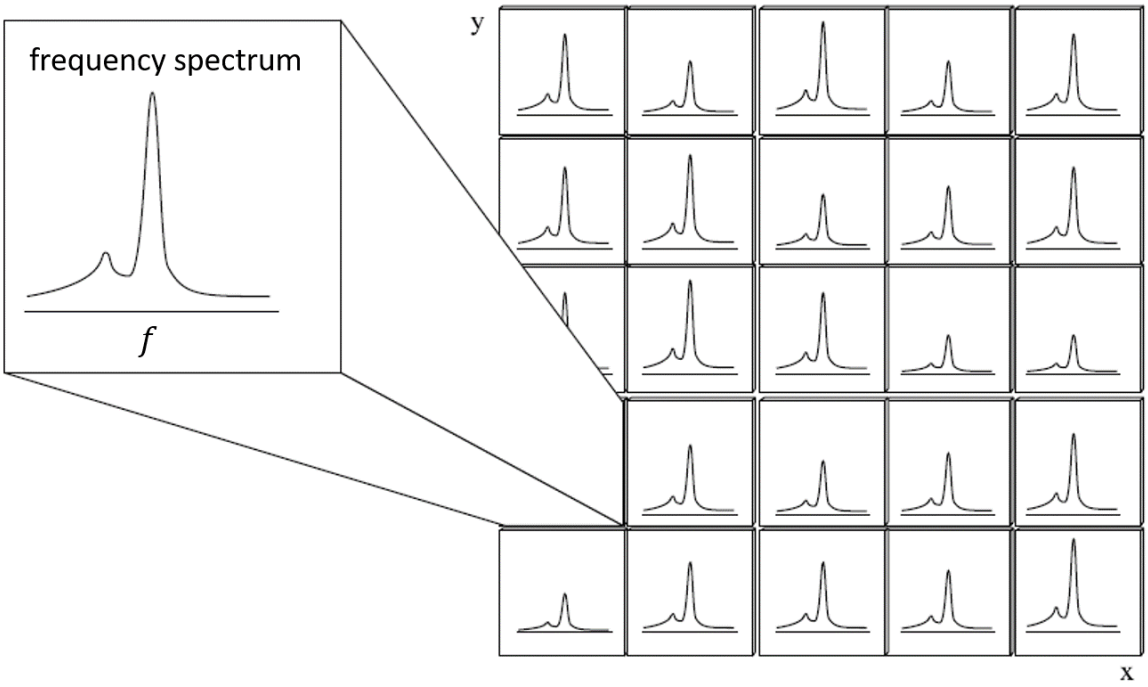

Figure 4.10: A simple illustration of an example of a chemical shift spectrum collected at every point in 2D image-space. Note that the spatially varying spectral distribution is illustrated by the varying shape and strength of peaks in the spectra shown for each voxel. Reproduced from [68].

4.3 Analysis of the 2D slice-selective CSI images

This section lays the groundwork for effectively analyzing the 2D CSI image sets to separately extract signal strength originated from spins outside the pellet and those inside.

4.3.1 Preview of the data analysis

As a preview to the data analysis procedure presented in the next section, let us now present some key features of a particular data set (data set A) where we used a 2.73-mm inner diameter tube (tube G) loaded with a 2.2-mm diameter pyrex bead that elevates a 1.8-mm pellet (A tabular summary of permeation data sets analyzed and presented in this thesis is given in Table 4.1 of Sec 4.5). The tube was filled with 1.54 bar of hyperpolarized ^{3}He and since there is no ante-chamber in this tube, the permeation starts at dispense time. The first slice-select 2D CSI image is acquired approximately 90 seconds after dispense time. After properly allocating the data matrix, we have a matrix size of $10 \times 10 \times 1920$ ($k_x \times k_y \times time$) with the first two being spatial dimensions and the last the time domain.

First, let us examine the NMR signal, i.e. signal at the center of k-space corresponding to the time-domain vector stored at $k_x = 6, k_y = 6$. Real part, imaginary part, and magnitude (i.e. absolute value) of the complex signal is plotted as a function of time and its Fourier Transform plotted (for magnitude, for example, absolute value of the Fourier transform, not Fourier transform of the absolute value of the signal, is plotted, to be perfectly clear) as a function of frequency as shown in Fig 4.11 for the first image of the series. There are a few important pieces of information that can be learned from these plots. First, it is evident that with this imaging technique, there is more than sufficient SNR to carry out the remainder of the experiment. Further, it can be seen in the magnitude of the time-domain signal that there are ripples in the decay suggesting that there are more than one decay processes involved. Additionally, there is a range of frequencies at which collections of spins are resonating (recall from Sec 2.6 that oscillations in the decay imply existence of off-resonant species in addition to on-resonant spins). The presence of off-resonant spin population is further bolstered by the signal behavior in the frequency spectrum where there are two distinct peaks immediately noticeable. Further, the entire spin population in the slice is resonating within $\sim$ 100 Hz range. It can also be seen that the T_2^* of the gas is

rather long which allows us to get above-noise-level signal all the way to the end of the ADC which is encouraging.

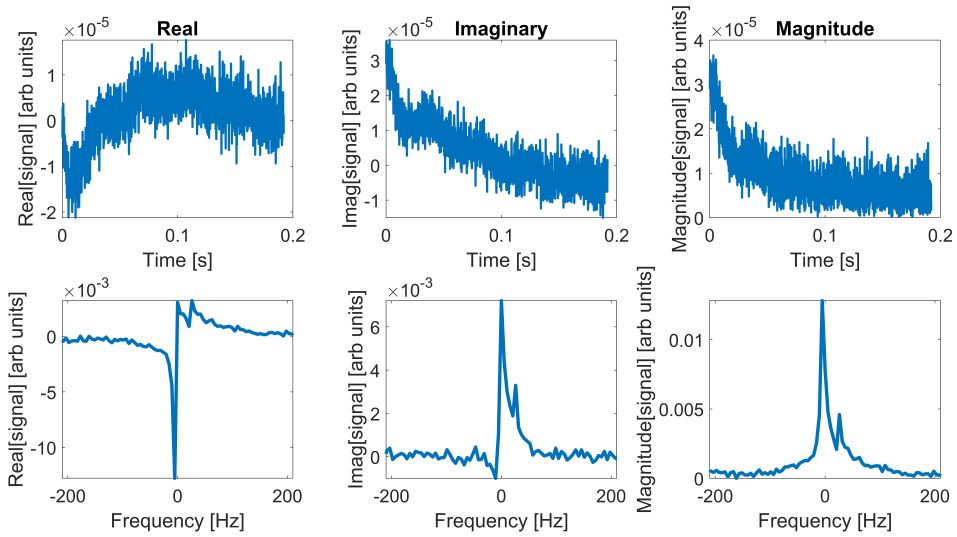

Figure 4.11: Top row: Center of k-space real, imaginary, and magnitude of signal plotted as a function of time. Bottom row: Real, imaginary, and magnitude (i.e. absolute value) of the Fourier Transform of the signal plotted as a function of frequency.

Let us now examine the same voxel but from the 5^{th} image in the series taken 7 min after the dispense time to see if there are any differences both in the time domain and frequency spectrum. Real, imaginary, and magnitude of the time-domain signal and the frequency spectra are shown in Fig 4.12 and it can been seen that the ripples (or oscillations) in the decay grew stronger. The consequence of that can also be seen in the frequency spectrum where the relative amplitude of the off-resonant signal to the resonant signal increased substantially. It seems as though the relative signal densities of the gas in the two regions are tractable and differentiable.

To examine the time-signal and the frequency spectrum as a function of position, we must take the inverse Fourier Transform along the first two dimensions to convert k-space data to spatial spin density (i.e. image space). In doing so, one can show the decay curves for specific locations in the image and their corresponding frequency

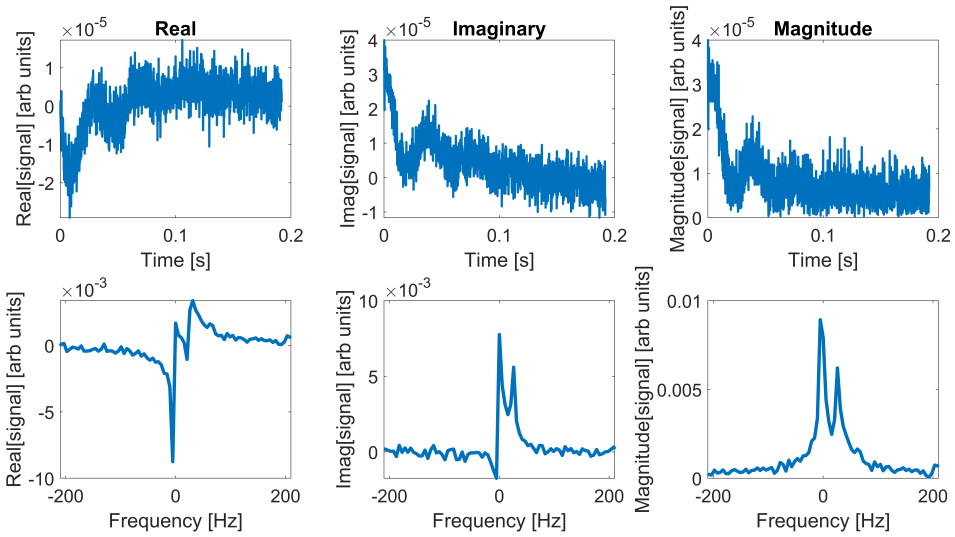

Figure 4.12: Top row: Center of k-space real, imaginary, and magnitude of signal plotted as a function of time. Bottom row: Real, imaginary, and magnitude of the Fourier Transform of the signal plotted as a function of frequency.

spectra. For example, Fig 4.13 and Fig 4.14 show the real, imaginary, and magnitude of signal plotted as a function of time and its corresponding Fourier Transform as a function of frequency for the central image voxel (x = 6, y = 6, or center of field-of-view) and a neighboring voxel (x = 3, y = 5), respectively.

It is evident, as expected, that there exist voxels that consist of spins in the imaging slice that are inside the tube (but outside the pellet) like voxel (x = 3, y = 5) and others that consist of partial volumes of both spins inside and outside the pellet like voxel (x = 6, y = 6). Further, it appears that at least in these series of images, the spins inside the pellet are resonating at a slightly different frequency than those outside and can therefore be differentiated by this frequency offset criterion.

Ultimately, our goal is to develop an analysis technique to determine the polarization loss due to the permeation process based on the 2D CSI image series. This requires establishing a robust method of tracking the strength of signal generated from spins inside the tube, but outside the pellet, and the signal generated from spins inside the pellet, as a function of time (i.e. as a function of image number, and its

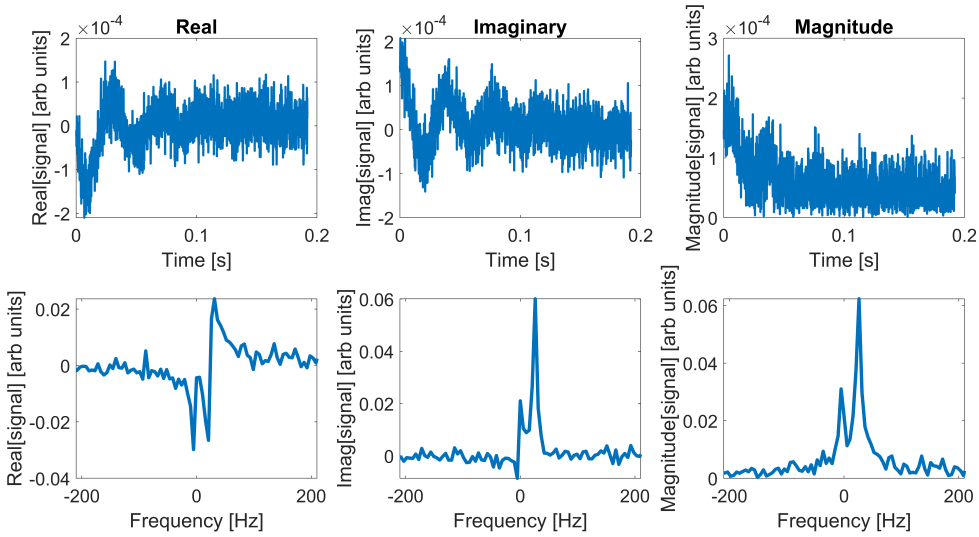

Figure 4.13: Top row: Real, imaginary, and magnitude of signal plotted as a function of time corresponding to the center of image voxel. Bottom row: Real, imaginary, and magnitude of the Fourier Transform of the signal plotted as a function of frequency for the corresponding voxel.

time of acquisition). Then the relationship between spin density (^{3}He number density), polarization, and signal strength need be examined to determine the relative polarization of gas inside and outside the pellet to extract the polarization loss.

In summary, it is apparent from the glance at the frequency spectra at several voxels that there exist an inherent shift in the frequency of the gas inside the pellet. We suspect that this off-resonant behavior is introduced by the difference in magnetic susceptibility of ^{3}He, pyrex glass tube-bottom, the bead at the bottom, and the pellet. Therefore, in Sec 4.3.3, we invoke the magnetostatics simulations developed in chapter 3 to examine the susceptibility-dependent off-resonant behavior. But first, in the next section, we describe the fitting routine which allows us to estimate the functional form of the frequency spectra.

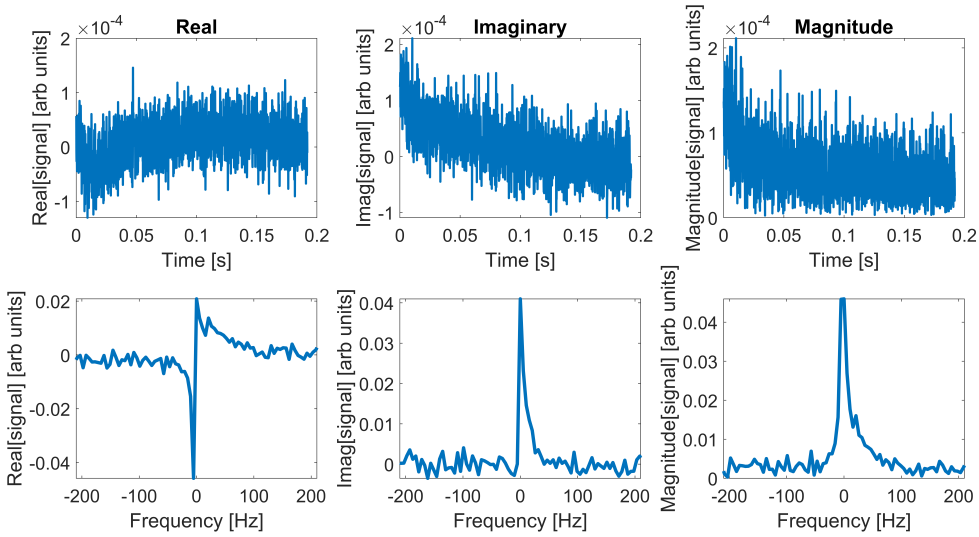

Figure 4.14: Top row: Real, imaginary, and magnitude of signal plotted as a function of time corresponding to voxel (x = 3, y = 5). Bottom row: Real, imaginary, and magnitude of the Fourier Transform of the signal plotted as a function of frequency for the corresponding voxel.

4.3.2 Fitting routine

Here we explain the function we use to approximate the functional form of the frequency spectrum at each voxel in the 2D image-space.

Recall from Sec 2.2 that the Fourier transform of a complex FID is a complex Lorentzian function. Extension of this relationship, which is mathematically derived in Sec 2.2, constitutes that the Fourier transform of sum of truncated complex decay function takes the form of a sum of n Lorentzian functions

$$\mathscr{F}(S(t)) = \sum_{k=1}^{n} A_k e^{-i\phi_k} \frac{1 - e^{-t(1/T_{2k}^* + i2\pi(f - f_{0k}))}}{1/T_{2k}^* + i2\pi(f - f_{0k})}, \tag{4.3}$$

where the k^{th} distribution has signal amplitude A_k, frequency offset $f_{0,k}$, phase ϕ_k, and decay time constant $T_{2,k}$. The basis of our analysis approach to extract permeation and decay parameters from the acquired 2D CSI images relies on fitting the frequency spectra to Eq 4.3 for one, two, or three peaks.

All analysis, including the fitting routine, is done in MATLAB. Least-squares-fit function "lsqcurvefit" is used which is based on the Levenberg algorithm [80]. This function takes several required parameters given in the following. It takes "x" and "y" arrays containing the raw data to be fit, in our case the functional form of the frequency spectrum as a function of frequency. It takes the functional form, in our case Eq 4.3. In addition, it takes initial values used as a starting point in the search for the global minimum of the optimization function. The initial "guess" values are thus consequential in convergence to a reasonable fit, as determined by plotting the residuals. If "bad" guess values are used, it is possible, and likely, for lsqcurvefit routine inputted with a fitting function that has multiple fit-parameters, to converge to a local minimum, yielding unsatisfactory fits. Given that in our application, anywhere between 4 and 12 fit parameters are at play, care must be taken to provide "educated" starting points for each parameter to increase the likelihood of convergence to satisfactory fits.

The lsqcurvefit function also takes optional input parameters for the lower and upper limits of the search range for each parameter. If no parameter limits are passed on to the function, it assumes $(-\infty, \infty)$ range for all parameters. This feature is implemented for certain parameters to enforce a logical range. For example, for T_2^*, a lower limit of 0 is passed since negative T_2^* is meaningless.

An optional output of the lsqcurvefit function, which is on the output end, is confidence interval (CI) defined as $CI = z\sigma$, for all fitted parameters. Specifically, the fit function outputs the Jacobian matrix, which is the real-valued matrix of partial derivatives at the solution. The Jacobian matrix is then the input to the MATLAB function "nlparci" (which stands for non-linear regression parameter confidence intervals) that outputs the 95 % confidence interval. For a given parameter x, we can obtain the range $x = x_m \pm z\sigma_x$, where x_m is the outputted value for the output fit parameter, $z = 1.96$ for 95% confidence interval, and σ_x is the standard deviation of the fit parameter based on the non-linear least-squares fit function. Therefore, from

the confidence interval, the error bars for each output parameter can be computed by dividing the confidence interval by $z = 1.96$ to get the error. This feature is exploited in reporting error bars for all the fit parameters throughout Chapters 4 and 5.

4.3.3 Off-resonance behavior of ^{3}He outside pellet

In this section we explore the different mechanisms that contribute to the frequency spread of the ^{3}He gas particles inside the tube and the pellet. In particular, we aim to determine the optimal number of Lorentzian functions in Eq 4.3 that most accurately estimates, or fits, the frequency spectrum observed in each voxel of the 2D image-space. Therefore, the underlying phenomenon responsible for creating the off-resonance behavior observed in the frequency spectra is the topic of interest in what follows.

Consider data set A where we used tube G filled with polarized ^{3}He that contained a 2.2-mm spherical glass bead, and a pellet resting on top of it. An initial transverse 2D projection image of the gas inside the tube serves as a localizer scan that shows the pellet is off-center from the tube axis normal to the field direction as seen in Fig 4.15.

Therefore, let us look at the frequency distribution in and around a 1.82-mm diameter pellet elevated by a 2.2-mm pyrex bead inside a flat-bottom tube where the pellet is tucked to the side of the tube normal to the field direction. The inner diameter of the tube is 3 mm, and it has a magnetic permeability $\mu = -11$ ppm, same as that of the glass bead. Fig 4.16 shows the results of the central cross-sectional views of the frequency distribution along the three principal axes. The frequency distribution of ^{3}He within a 2-mm cross-sectional slab through the pellet can be studied to shed light on the frequency spectrum of our data. Fig 4.17 shows the frequency distributions within the slab in different regions: the entire slab, the slab excluding the spins inside the shell, and only the spins inside the shell. It appears that the frequency distribution in the entire 2-mm slab which corresponds to the NMR signal at the center of the

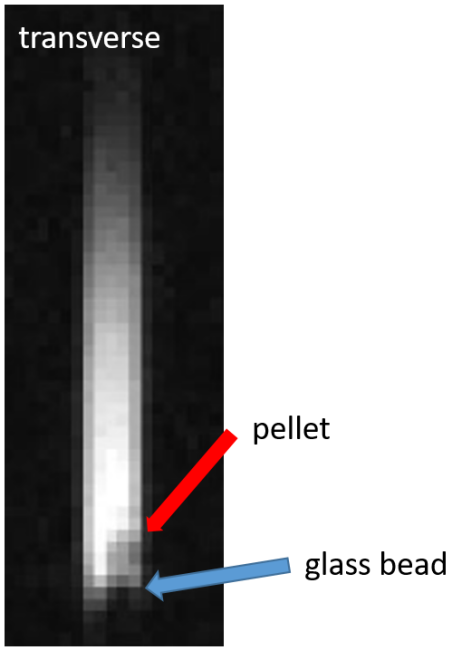

Figure 4.15: 2D transverse projection image of the gas inside tube G (data taken 11/19/2020, fill 2) shows that the pellet is elevated by a glass bead and is offset from the center of the tube normal to the field direction as indicated by the red arrow.

k-space has a bi-modal distribution. Another interesting observation is that the gas outside the pellet (second panel) appears to have an uneven distribution as though there are two distributions overlaid on top of each other but slightly offset from one another similar to the frequency spectrum of the voxel (x = 3, y = 5) that corresponds to the tube signal. The frequency distribution inside the pellet however seems to be a distribution with only one tail, although it looks like the range of frequencies can be approximated by a single distribution. Even though the relative sizes of the two distributions in the simulation and in our data are somewhat different, the simulation does provide some evidence of distinct peaks that correspond to different populations for the gas outside the pellet as well.

It is worth mentioning here that the effective field inhomogeneity as seen by the gas outside the pellet is not the exact static field inhomogeneities created by the tube and the bead at the bottom of the tube. That is because the gas almost freely diffuses

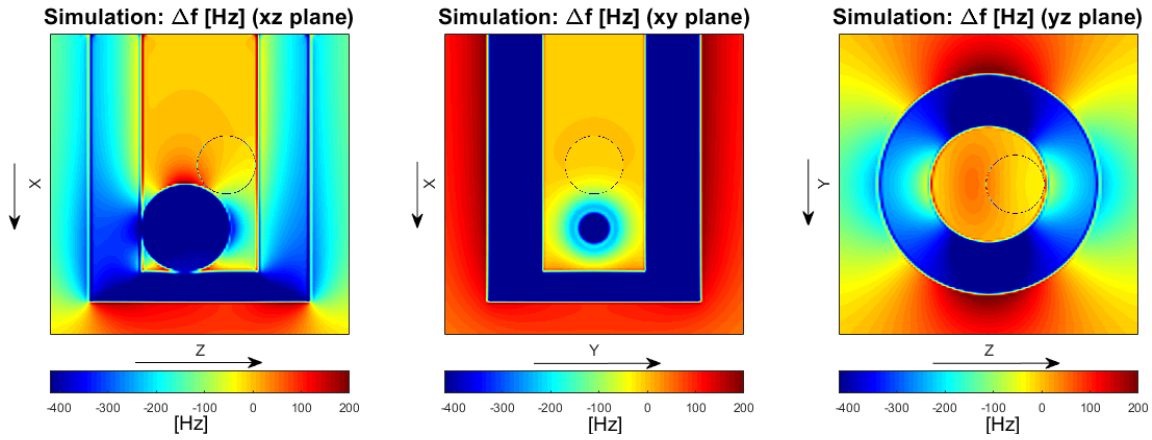

Figure 4.16: Central cross-sectional views of frequency distribution of a flat-bottom 3-mm ID pyrex tube containing a 1.82-mm OD pellet elevated by a 2.2-mm pyrex bead.

in and out of the imaging slice while acquiring signal, so not only does the gas see the inhomogeneities within the slice, it also sees dynamic frequency shifts during imaging as it travels through different regions of the tube. Diffusion of ^{3}He gas simulation for the imaging time as shown in Fig 4.18 shows that the gas that originated inside a 2-mm slice almost entirely disperses and fills up a 1-cm region of the tube within 100 ms (typical ADC time for our experiments).

Therefore, it is reasonable to assume that the magnetostatics simulation results shown in Fig 4.17 for the frequency distribution of the gas outside the pellet differ substantially from frequency spectra seen in our data, though the simulations provide tremendous insights into the processes and mechanisms by which the frequency spread and offset is created.

A better demonstration of the off-resonant frequency behavior of the gas outside the pellet can be seen in a data set which we do not have permeation measurements. Like data set A, this dataset used the same tube (tube G) loaded with the same bead and pellet (GDP 10-23-2). The purpose of this data set was to acquired 2D CSI images to examine the frequency behavior of the ^{3}He near the pellet, but also far away from it ($\sim$1 cm away from the pellet and the bottom of the tube where the bead sits). This

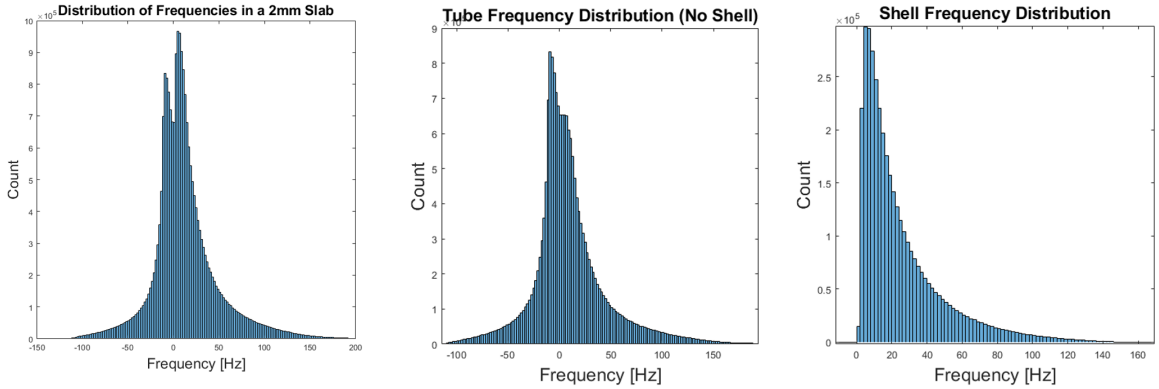

Figure 4.17: Central cross-sectional views of frequency distribution of a flat-bottom 3-mm ID pyrex tube containing a 1.82-mm OD pellet elevated by a 2.2-mm pyrex bead.

data set was therefore taken using a side-view slice-selective 2D CSI to cover more of the tube than just the cross-sectional slice. This gives us the capability to more carefully examine the signal generated by gas outside the pellet as seen in Fig 4.19. The magnitude of the frequency spectrum for select number of voxels show that as we get closer to the bottom of the tube where the bead sits, off-resonance behavior of the gas outside the pellet amplifies. This is consistent with magnetostatics simulations shown in Fig 4.16 where it can be seen that the field inhomogeneity decreases as we get farther away from the bottom of the tube where the bead and the pellet are. Since it is the field inhomogeneities that cause off-resonant frequencies, it is apparent that a more "pure" distribution of frequencies is seen near the middle and top of the tube. If the spectra of the voxels shown in Fig 4.19 were fit to either a complex Lorentzian function or a sum of complex Lorentzian functions, one can see that in fact, a single Lorentzian function fits the data better toward the top of the tube than the bottom. Near the bottom where the field inhomogeneity is stronger, the spectra are nearly perfectly fit with a sum of two Lorentzian functions.

In Sec 4.2.6, we observed that the gas inside the pellet resonates at a different frequency than the gas outside the pellet. In this section, we the help of magnetostatics and diffusion simulations, we demonstrated that the functional form of the frequency

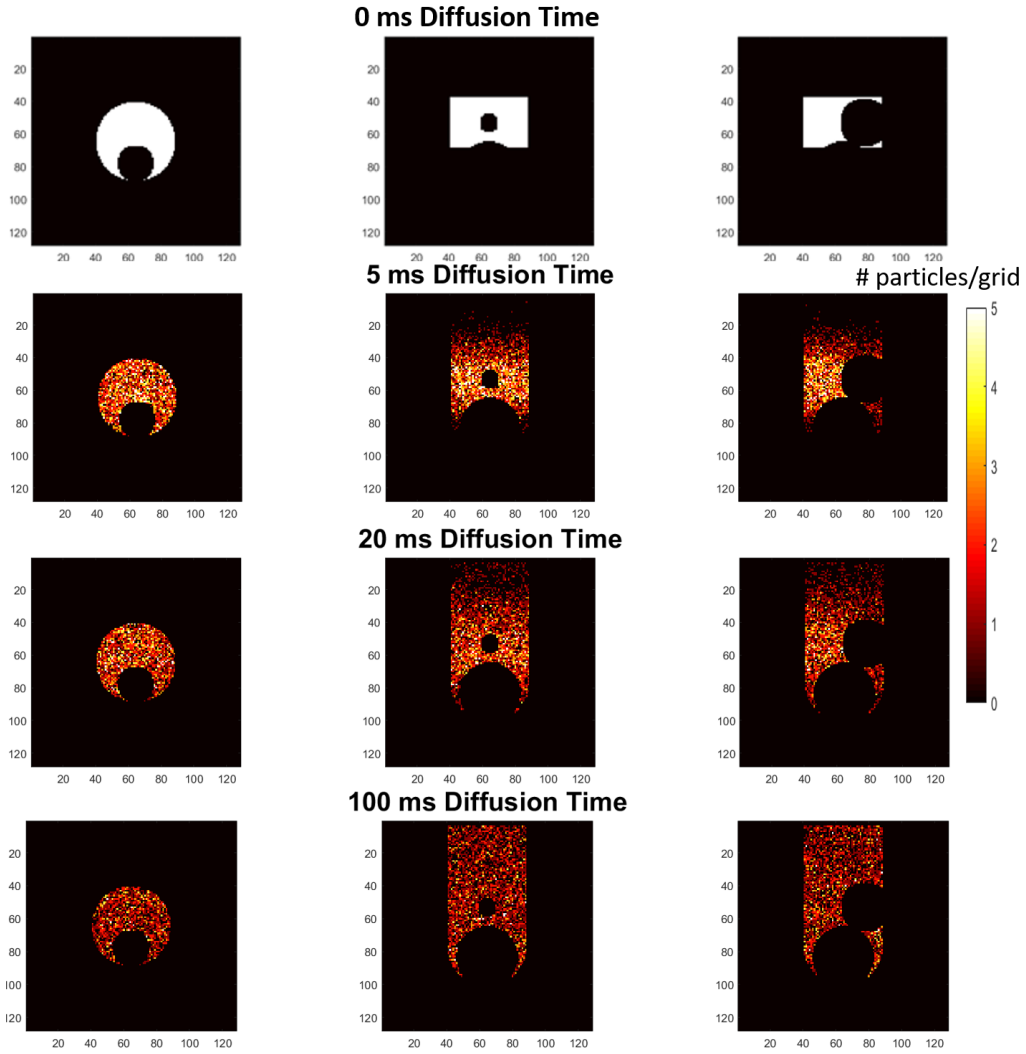

[p]

Figure 4.18: Simulation of ^{3}He gas diffusion starting from a 2-mm slab inside a 3-mm ID tube containing a pellet suspended by a bead. Each row consists of central cross-sectional views along the principal axes. At $t = 0$, the slab is occupied by 5 particles per grid point and the particles are allowed to undergo random Brownian motion in 3D. In this simulation, it is assumed that the bead, pellet, and the walls of the tube are impenetrable and no gas occupies the pellet in the beginning. All panels share the same color scale with white at each grid representing full occupancy (5 particles) and black representing no particles occupying the grid point. It is evident that in 100 ms, which is a typical ADC duration for our experiments, the gas initially occupying a 2-mm slab almost uniformly fills the field-of-view, a $\sim$ 6-mm region of the tube although there are particles that have spilled out of FOV and hence not shown here.

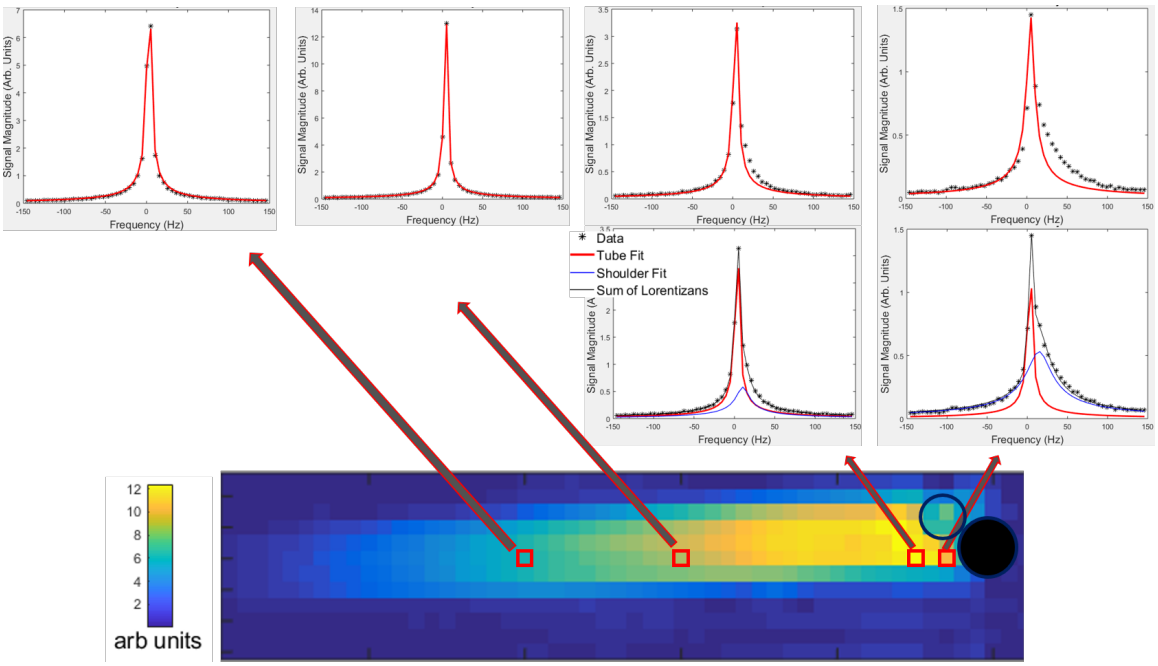

Figure 4.19: Slice-selective side-view 2D CSI image of hyperpolarized ^{3}He gas inside tube G with a 16 μ-wall pellet with OD = 1.82 mm elevated with a 2.2 mm glass bead. The magnitude of frequency spectrum for select number of voxels show that as we get closer to the bottom of the tube where the bead sits, off-resonance behavior amplifies. The spectra are fit either to a Lorentzian or sum of two Lorentzian functions to demonstrate that signal from voxels containing gas with off-resonant frequencies can be fit to an additional peak that have a frequency offset (blue peak). Red indicates on resonance signal, blue indicates off-resonant signal, and black indicates sum of the two (if fit to two peaks). The empty circle denotes pellet's position while the solid circle denotes the pyrex bead.

spectrum of the signal generated by gas outside the pellet can be approximated by sum of two complex Lorentzian curves. On the other hand, it is evident that the frequency spectrum of the signal generated by gas inside the pellet can be approximated by a single Lorentzian. Therefore, in voxels that contain partial volumes of both gas both inside and outside the pellet, the frequency spectrum may be approximated by sum of up to three distinct Lorentzian functions.

In summary, here, we established that the gas outside the pellet is best estimated by sum of 2 complex Lorentzian functions, which constitutes a three-peak fit in voxels

that contain both gas from outside and inside the pellet.

4.3.4 Performance of two-peak fit vs three-peak fit

Here we compare goodness of fit for a two-peak fit vs a three-peak fit analysis. We also establish the need for a multi-step fitting routine with application of appropriate parameter limits for convergence to satisfactory fits.

Let us attempt to fit the frequency spectrum in each voxel to a functional form of sum of three Lorentzian curves (i.e. Eq 4.3 for $n = 3$). For a three-peak-fit, there are 12 fit parameters, namely, area under the curve A, decay time constant T_2^*, frequency offset from the demodulation frequency f_0, and phase ϕ for each Lorentzian function. However, due to our limited frequency resolution (spacing between frequency points), there are only a few data points, in the order of number of fit parameters.. Therefore, it is desired to reduce the number of fit parameters if possible. For instance, because we have images at multiple time points and multiple voxels in each image, we can reduce the total number of fit parameters if we can establish that some of the parameters are constant across space or time. Obviously the amplitude of the signal can't be assumed constant, because time-varying amplitude is what we are ultimately trying to measure. But it may be reasonable to assume that the phase, center frequency, or T_2^* is constant in time or across some region of space. We discovered that we could use this tactic effectively by making multiple passes through the data analysis. In the initial passes, we determine which parameters can be held constant across time and/or space and compute their averages. Then in the final pass we use the determined averages to reduce the degrees of freedom of the final round of fits. A flow chart summarizing the fitting procedure steps is given in Fig 4.20.

We suspect that T_2^* would be constant throughout the entire experiment since T_2^* is a function of the magnetic environment and is sensitive to field inhomogeneity. Since the static field, including the magnetic susceptibility induced field inhomogeneities, doesn't change over time, it is reasonable to expect T_2^* to be the same for all images.

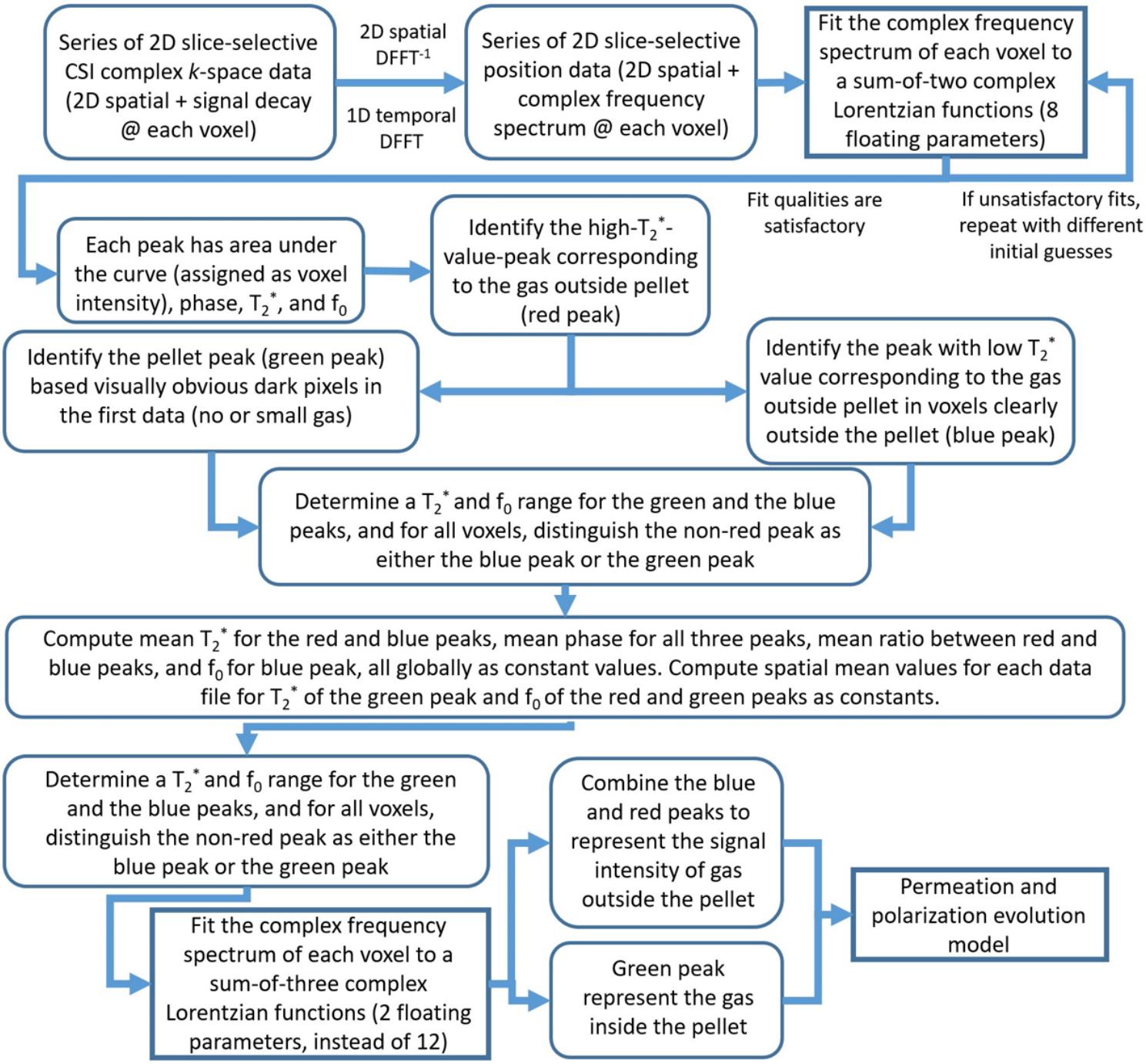

Figure 4.20: Flow chart summarizing the fitting procedure. DFFT = discrete Fourier transform, DFFT^{-1} = inverse discrete Fourier transform. Permeation and polarization evolution model presented in Sec 4.4.

Whether T_2^* has any spatial dependence, however, should be examined carefully since field inhomogeneity might arise from thicker glass in one region compared to the other, for instance. Another parameter we suspect should remain constant over time but may have regional differences is ϕ. Frequency offset on the other hand might be time-dependent due to static field drift. Historically, the scanner has shown evidence of static field drift in other experiments, therefore frequency offset should also be examined carefully.

At this point, let us adopt the following convention for the fitted peaks and their corresponding gas signal: The gas outside the pellet with a narrow frequency distribution is presented by a red peak (typically with a sharp-peak profile) and referred to as the 'tube' peak. The gas outside the pellet with a distribution of frequencies off-set from the 'tube' gas frequencies and with a broader frequency distribution (low T_2^*) is indicated by a blue curve and is referred to as the 'shoulder' peak which generally has a low amplitude. The gas inside the pellet which also has a frequency distribution centered at different frequency from the 'tube' gas peak is indicated by a green curve and is referred to as the 'pellet' peak throughout this chapter.

We start the analysis routine by fitting the frequency spectrum of each voxel of each image to Eq 4.3 to a sum of three peaks. Since the vast majority of the frequency spectrum is noise, and there is measurable signal only within a few data points spanning $100 \sim 200$ Hz depending on the data set, the frequency spectrum is truncated to have range $[-150, 150]$ Hz which should cover all signal above noise and some noise on either side of the tails to improve fit quality. Each fit parameter requires an initial guess. We start by finding the global maximum amplitude of the magnitude of the frequency spectrum signal, find its index, evaluate frequency at that index, and input that as frequency offset guess value for the most prominent peak.

The guess value for the area of that peak is determined by computing the trapezoidal area of the signal within the six neighboring data points (i.e. signal range $[f_{max} - 3 \times r_{freq}, f_{max} + 3 \times r_{freq}]$, where r_{freq} is the frequency resolution or spacing).

Since $T_2^* = 1/(2FWHM)$, the guess value for T_2^* is determined by computing FWHM of signal range $[f_{max} - 3 \times r_{freq}, f_{max} + 3 \times r_{freq}]$. And lastly, the guess value for ϕ is determined by computing the angle between the real and imaginary channels of the maximum amplitude data point. To determine the guess value for the fit parameters for the second and third peaks, signal in range $[f_{max} - 3 \times r_{freq}, f_{max} + 3 \times r_{freq}]$ is subtracted from the initial truncated frequency spectrum signal and the exact same routine is applied to the residual of the frequency spectrum signal.

As mentioned earlier, the fitting function can admit lower and upper limits for fitted fit parameters. For the initial run, the lower and upper limits are set the following way: $(-\infty, \infty)$ for all three peaks for ϕ, $(0, 2)$ s for all three peaks for T_2^* (the highest $T_2^* < 500$ ms in all of our datasets), $(0, \infty)$ for all three peaks for A, $(-10, 1)$ for the 'prominent' peak, $(1, 50)$ for the other two peaks for f_0. The reason for the relatively narrow allowed range for f_0 for the 'prominent' peak is to differentiate that peak using frequency.

However, as seen in Fig 4.21, the fit quality to this sum-of-three-Lorentzian-peaks function turns out to be compromised. It appears that the second peak associated with the gas outside (labeled the "shoulder" peak, thereafter) is very small in amplitude but has a very low T_2^* (the shoulder peak is broad and shallow) and is often below noise level in the voxels with partial volumes of gas inside and outside the pellet. Therefore, two of the peaks often assume opposite phases (one gets offset by $\pi/2$ from the other) and fight each others' amplitudes resulting in an unreasonable fit as seen in Fig 4.21 for a representative voxel. Even though the sum of the three peaks actually fits the data well as shown in the residuals (bottom row of Fig 4.21), the assignment of individual peaks to the pellet gas, and the off-resonant gas outside the pellet (green and blue curves, respectively) are unreasonable.

Alternatively, based on insights from both simulations and initial examination of our data, we know that only voxels containing partial volumes of gas inside and outside the pellet need be fit to three peaks for accurate extraction of relative signal

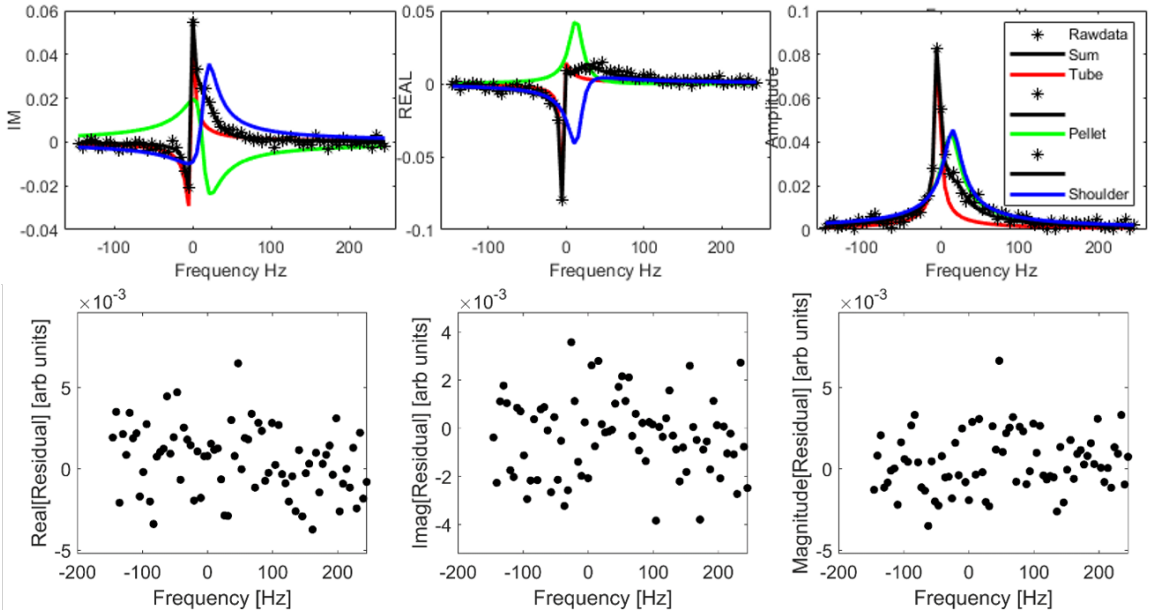

Figure 4.21: A representative sum-of-three complex Lorentzian functions fit to an image voxel depicting opposite phases that result in poor-quality fits. The voxel is from data set 'fill 2' of November 18 2106 experiment with tube G and pellet GDP 10-23-2 elevated by a glass bead. Note the merely $\pi/2$ phase difference between the green and blue curves corresponding to the pellet gas, and the off-resonant gas outside the pellet, respectively.

strengths. This inspires us to try a two-peak fit for the initial round of fitting, and a two-peak fit seem to fit the data well in voxels with partial volumes of gas inside and outside the pellet. The initial guess, and lower and upper bound limits are are set the same way explained for the three-peak-fit but with one less peak. The results of this first round fitting procedure is revealing: For almost all data sets, T_2^* for the shoulder peak is less than ~ 10 ms whereas for the pellet peak $25 < T_2^* < 120$ ms. Therefore, the two peaks can be differentiated from each other using T_2^*. This differentiation is done after the two-peak-fit is complete and is demonstrated by color-coding the pellet peak as green and the shoulder peak as blue to be consistent with our previous convention.

Based on the initial two-peak fit, it is evident that fits to frequency spectra in all voxels have reasonable quality demonstrated by residuals centered around zero and

low relative amplitudes. An example of fit to spectrum in a voxel containing mostly pellet gas but with some partial gas volume from the tube (based on proximity to the pellet as seen in the images) is given in Figs 4.22. Similar goodness-of-fit can be

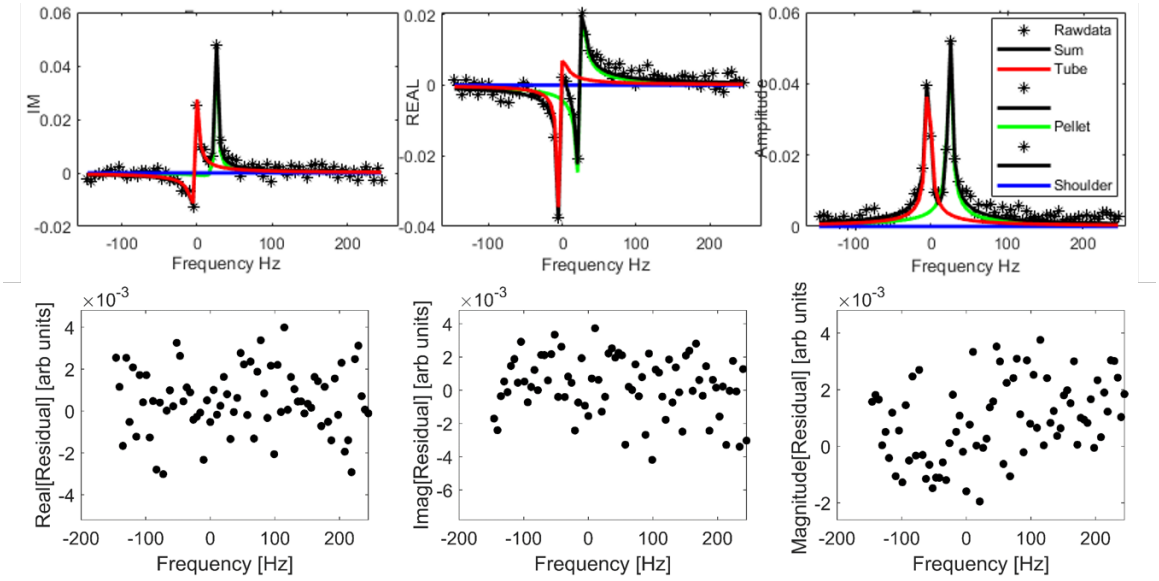

Figure 4.22: A representative sum-of-two complex Lorentzian functions fit to an image voxel containing partial volumes of gas inside and outside the pellet and associated residuals demonstrating high quality of fit. Based on its proximity to the pellet, the voxel is believed to contain mostly gas from inside the pellet. Based on T_2^*, the second peak is identified as the pellet peak, consistent with its location with respect to the pellet.

seen in fit to frequency spectrum for a voxel that contains only gas from outside the pellet is given in Fig 4.23.

In summary, we experimented with and presented both two-peak and three-peak fits to the frequency spectra. We discovered that a faithful three-peak-fit is challenging, and that a two-peak is capable of reasonably estimating the functional form of the frequency spectrum. In the next section, we will use the results of the two-peak-fits to improve the three-peak-fits for a faithful assignment of signal.

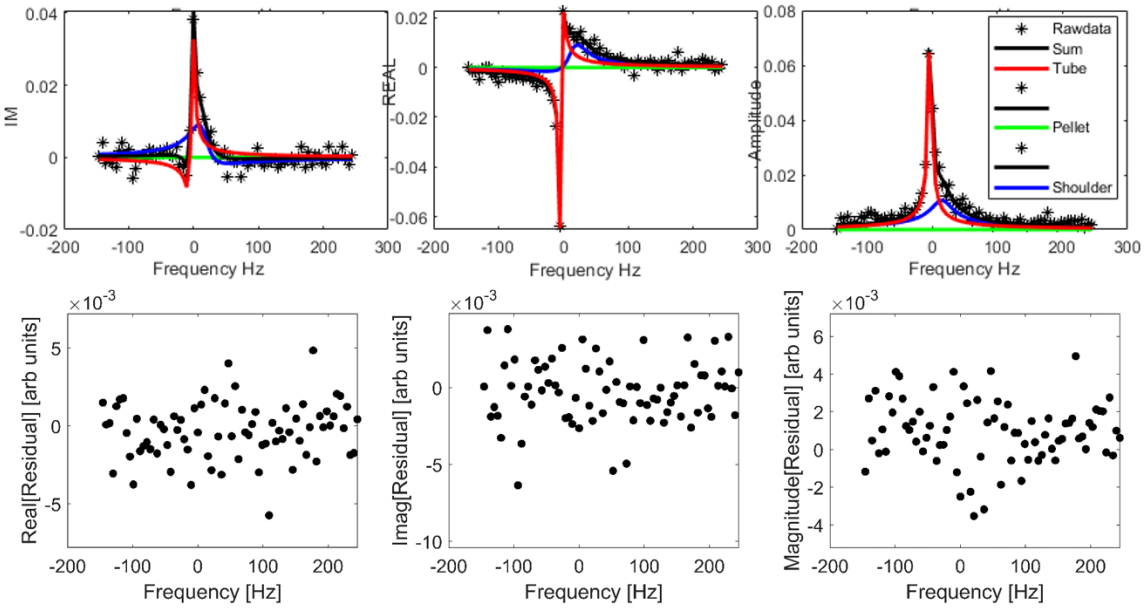

Figure 4.23: A representative sum-of-two complex Lorentzian functions fit to an image voxel containing only gas from outside the pellet and associated residuals demonstrating high quality of fit. Based on T_2^*, the second peak is identified as the shoulder, consistent with its location with respect to the pellet.

4.3.5 Temporal and spatial dependence of fit parameters

In this section, we will use the results of the two-peak-fits to compute mean values of some of the fit parameters, which allows us to reduce the number of fit parameters for the three-peak-fit. Here, we continue to consider data set A for the following.

As seen in Fig 4.24, it is evident that the intensity of the signal of both the tube peak and the shoulder peak decrease over time consistent with T_1 decay. The intensity of the 'pellet' peak signal increases for a limited time period in the beginning stages of the experiment and starts decreasing at some point. This also makes sense since initially there exists no ^{3}He gas inside the pellet, but as the gas rushes in retaining some polarization, the polarization density inside the pellet increases which leads to signal increase over a short period of time until the pellet gas density reaches the gas density inside the tube. At that point, the T_1 decay process becomes the dominant factor and the pellet polarization density, and hence the pellet signal strength

decreases for the remainder of the experiment.

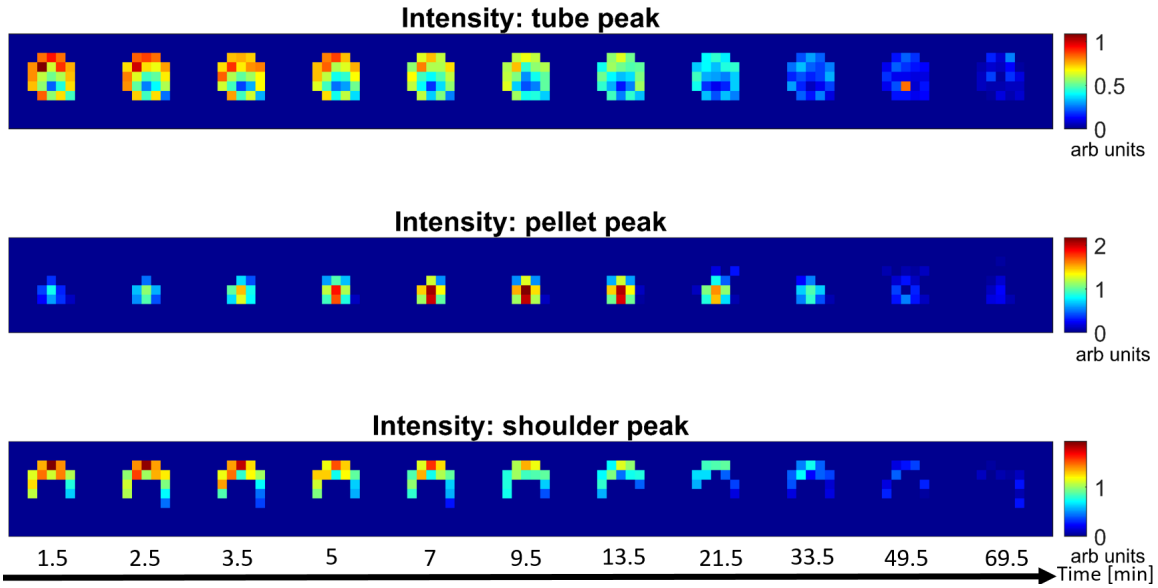

Figure 4.24: Fitted signal intensity map (i.e. parameter A or image) obtained from dataset A fit to sum of two Lorentzian functions. The intensities are masked using a t-cluster k-means algorithm based on the first tube peak image to omit noise.

As for the phase, it appears that the phase of neither of the peaks has significant spatial dependence as depicted in Fig 4.25. Further, ϕ does not seem to change over time either, as previously suspected. Therefore, the phase for all three peaks are excellent candidates to be summed over to reduce to global constants for the next fitting round.

The fitted T_2^* maps for the tube and the shoulder peaks seem to not vary spatially or over time, either. However, as seen in Fig 4.26 the T_2^* for the pellet peak decreases substantially with time suggesting that pellet gas T_2^* is density-dependent. Fig 4.27 shows the behavior of pellet peak mean T_2^* over time. Curiously, if fit to an exponential decay function with a y-offset $T_2^*(t) = Ae^{-t/\tau}+B$, one can find the decay time constant to be $\tau = 1.6 \pm 0.5$ min suggesting that this decay time constant is substantially different from the permeation time constant $\tau_{perm} = 227$ s $= 3.8$ min. Although T_2^* exhibits some regional variance consistently throughout all maps, T_2^* values for the

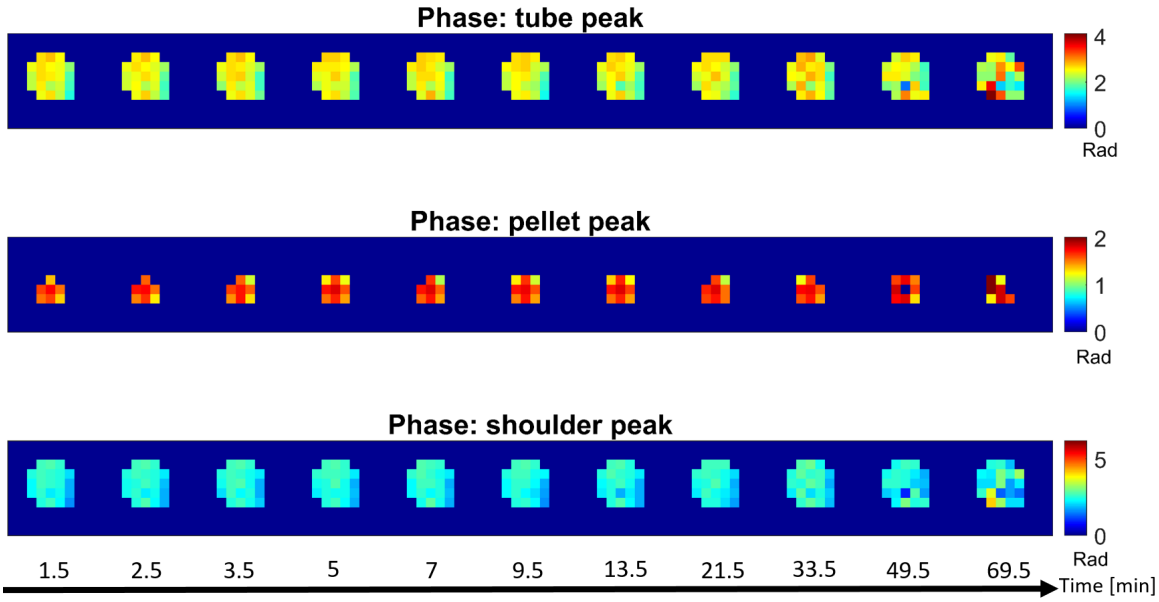

Figure 4.25: Fitted phase maps (i.e. parameter ϕ) obtained from dataset A fit to sum of two Lorentzian functions. The phase maps are masked using a 2-cluster k-means algorithm based on the first tube peak image to omit noise, the same mask applied to the intensity maps.

tube and the shoulder peaks may be good candidates for averaging, but not that of the pellet peak. Instead, one can compute mean T_2^* per time point and input each as a constant for the pellet peak in the second round of fits. Similarly, another fit parameter that can be examined is frequency offset. Fitted f_0 maps shown in Fig 4.28 demonstrate that the value of f_0 changes over time for the tube and the pellet peaks, although they seem to have no spatial variance. The value of the shoulder peak f_0, however, appears to be constant both temporally and spatially. Therefore, one can compute mean f_0 value for the tube peak and the pellet peak per time point and input each as a constant for the second round of fits, similar to the value for the pellet peak T_2^*.

Lastly, upon careful examination of the relationship between tube peak intensity and the shoulder peak intensity, it is evident that the ratio between the two stays constant both spatially and over time as seen in Fig 4.29. Therefore, the mean ratio

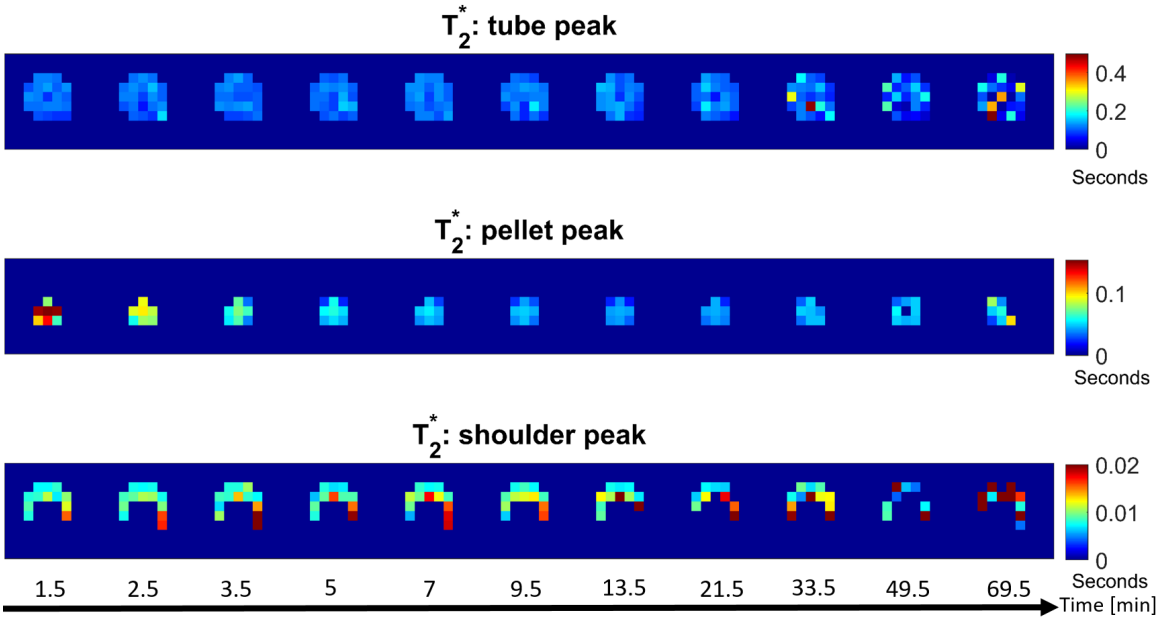

Figure 4.26: Fitted T_2^* maps obtained from dataset A fit to sum of two Lorentzian functions. The maps are masked using a 2-cluster k-means algorithm based on the first tube peak image to omit noise, the same mask applied to the intensity maps.

between shoulder peak and tube peak intensities can be computed and used as a constant for the second round of fits. We have now identified several parameters that can be averaged either spatially per time point, or globally averaging both regionally and over time. For the parameters to be averaged globally (ϕ for all three peaks, T_2^* for tube and shoulder peaks, f_0 for the shoulder peak, and the ratio of shoulder to tube peak intensities), we compute the mean and standard deviation (σ) of the masked maps, eliminate data points whose values differ by $> 2\sigma$ from the mean, and recompute the means which then serve as constants for the next fitting round, which is a three-peak-fit. Similarly, for the parameters to be averaged per time point (T_2^* for the pellet peak and f_0 for the pellet and the shoulder peaks), we compute mean and standard deviation of *each* masked map, eliminate values that are $> 2\sigma$ away from the mean, and recompute the mean at each time point as constant inputs for the final three-peak fit.

In this section, we used the two-peak fit results of the fit parameters to compute

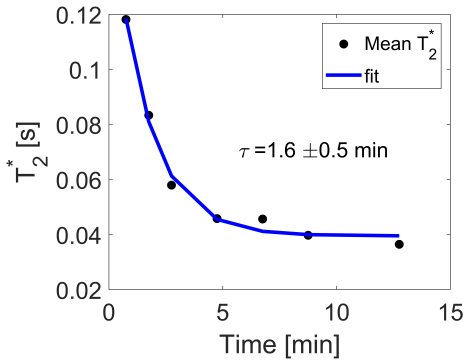

Figure 4.27: Mean T_2^* as a function of time for the pellet gas peak. Only the first seven mean values of T_2^* are plotted and used for the fit since due to lower SNR in later time points, the T_2^* appeared to be somewhat unreliable. The least-squares-fit function has the form $T_2^* = Ae^{-t/\tau} + B$, where τ is the decay time constant,A is the initial amplitude, and B is the y-offset

mean values of T_2^*, f_0, and *phi*, when reasonable (i.e. when there are no observable systematic spatial and temporal changes in the variables). These computed mean values can then be used as constants in the three-peak fit, reducing the number of required fit parameters, as we will show in the next section.

4.3.6 Polarization density maps obtained from multi-step three-peak fit

In the present section, we use the computed mean fit parameters obtained from two-peak-fits as constants, and input them into the three-peak fit in order to reduce the number of required fit parameters. We use the fit parameters A_k, which are proportional to spin density of the k^{th} spin population, to track the polarization density of the gas inside and outside the pellet as a function of time.

We can modify Eq 4.3 to write

$$\mathscr{F}(S(t)) = (A_3/R_{3/1})e^{-i\phi_1}\frac{1-e^{-t(1/T_{21}^*+i2\pi(f-f_{01}))}}{1/T_{21}^*+i2\pi(f-f_{01})}+\sum_{k=2}^{3}A_k e^{-i\phi_k}\frac{1-e^{-t(1/T_{2k}^*+i2\pi(f-f_{0k}))}}{1/T_{2k}^*+i2\pi(f-f_{0k})}, \tag{4.4}$$

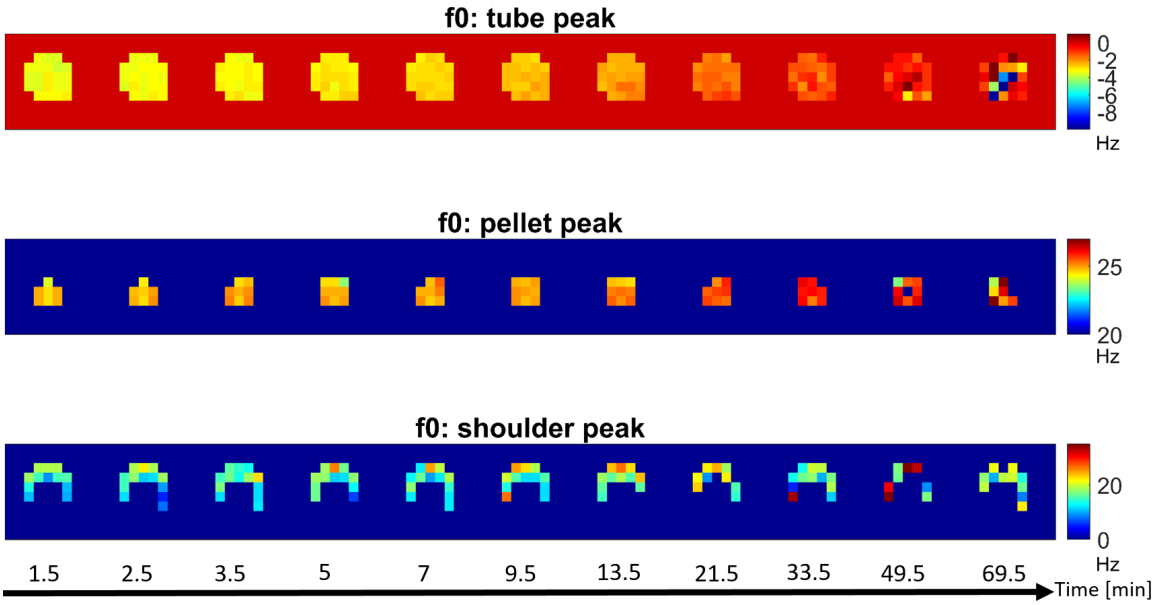

Figure 4.28: Fitted phase maps (i.e. parameter ϕ) obtained from dataset A fit to sum of two Lorentzian functions. The phase maps are masked using a 2-cluster$k$-means algorithm based on the first tube peak image to omit noise, the same mask applied to the intensity maps.

where subscripts 1, 2, and 3 correspond to the tube, pellet, and the shoulder peaks, respectively, $R_{3/1} = A_3/A_1$ is the ratio of shoulder peak intensity to tube peak intensity and is a computed constant (from the first two-peak-fit round), and T^*_{2k} and f_{0k} are the T^*_2 and f_0 for the k^{th} peak, respectively. In Eq 4.4, only A_2 and A_3 are fit parameters, drastically decreasing the number of parameters to be fit (from 12 to 2) and the degree of freedom in the problem.

For the second round of fitting routine, we fit our data to a three-peak-fit using a least-squares-fit function where the only fit parameters are the signal intensity for the pellet and the shoulder peaks. This is equivalent to having only two fit parameters A_1 and A_2, the only inconsequential difference being the ratio computed would have had to be A_1/A_3, instead of A_3/A_1.

An example of a voxel spectrum data fit to Eq 4.4 is given in Fig 4.30 demonstrating less-than-ideal fit quality. Although the fit quality seems to be somewhat

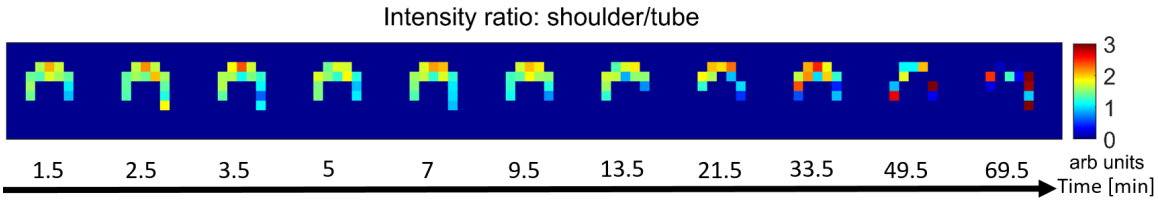

Figure 4.29: Ratio of fitted shoulder peak intensity to tube peak intensity maps obtained from fit to sum of two Lorentzian functions depicting no significant variance spatially or over time.

compromised compared with the two-peak-fit, the signal contribution from all gas inside and outside the pellet is considered. The signal maps for tube and shoulder

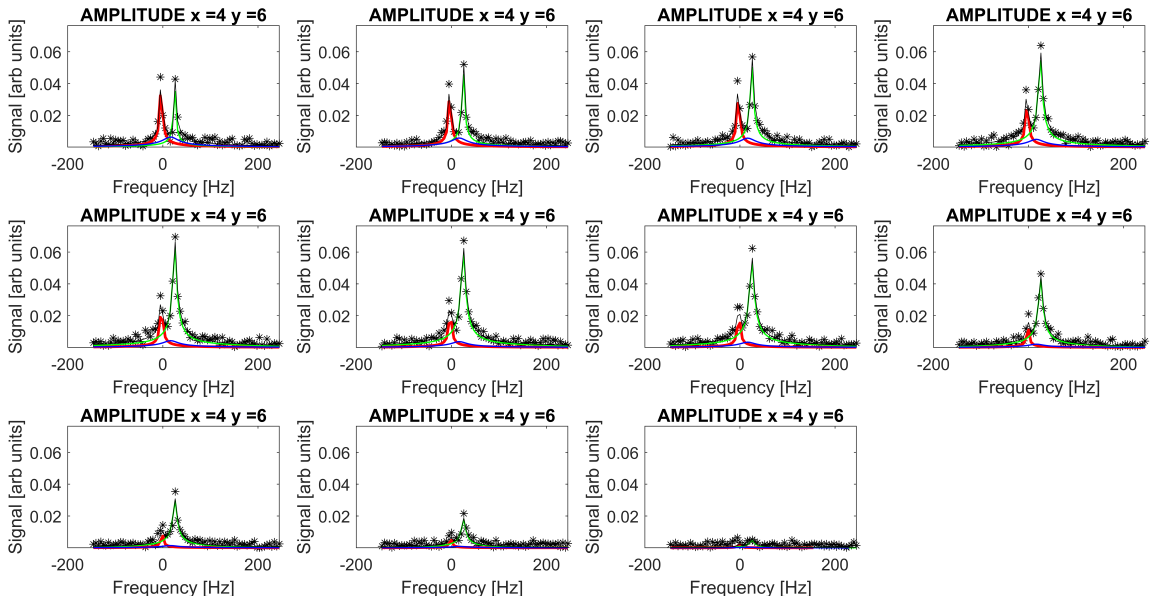

Figure 4.30: Time series of a voxel spectrum containing both pellet and tube gas fit to sum-of-three Lorentzian functions with only 2 fit parameters.

peaks are added to represent total signal outside the pellet. Inside the pellet, the signal is represented by the pellet peak. Signal intensity maps for the gas inside and outside the pellet is shown in Fig 4.31, where the total tube signal maps are sum of tube and shoulder signal maps. To determine signal density originated from gas inside and outside the pellet at each time point, sum of signal in all voxels in the

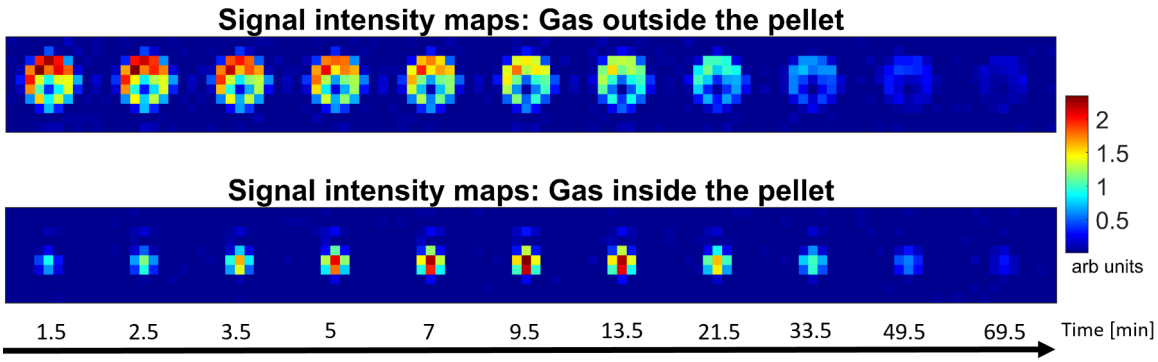

Figure 4.31: Time series of signal intensity maps for gas inside and outside the pellet. Signal intensity maps corresponding to gas outside the pellet are the tube and shoulder signal intensity maps.

mask is computed and divided by total volume of the 2 mm slice subtracted by the pellet volume. Recall that the excited slice has a profile (see Fig 4.9), which is also included in this computation. Similarly, signal density for the pellet is summed up for all voxels over the same mask and divided by the volume of the pellet, also corrected for slice profile.

Finally, the total signal density inside and outside the pellet obtained from analysis of each 2D slice-selective CSI data can be plotted as a function of time as seen in Fig 4.32. Since signal density is proportional to the amount of total magnetization available for imaging, and total magnetization is proportional to the product of gas density and polarization, the functional form of the polarization density inside and outside the pellet is also described by that of the total signal density (i.e. Fig 4.32).

Let us give a few remarks about the polarization density evolution inside and outside the pellet. First of all, it appears that a substantial fraction of the spins that complete the permeation journey retain their polarization. Secondly, it appears that the polarization of the gas that enters the pellet without loss of polarization decays with a time constant that is at least equal or longer than that of the polarized gas outside the pellet. Thirdly, at no time point does the polarization density inside the pellet noticeably surpass the polarization density outside the pellet. This implies

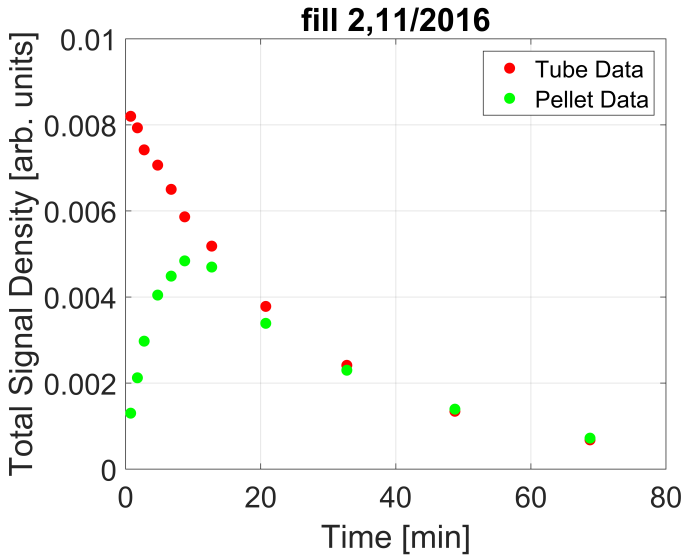

Figure 4.32: Time evolution of the total signal density inside and outside the pellet for dataset A. Each data point is obtained by summing up signal in all voxels inside the mask in intensity maps shown in Fig 4.31, weighted by its corresponding gas volume and corrected for the slice excitation profile.

that when the gas densities of the two regions equilibrate, gas exchange between the two regions due to self-diffusion of ^{3}He molecules in and out of the pellet does not change the polarization density inside the pellet. Another interesting observation is that the polarization density of the gas outside the pellet seem to not be affected by the presence of the pellet or the gas in it which is not surprising considering that the overall volume of the tube is much larger than that of the pellet or the excited slice. In other words, the gas outside the pellet serves as a reservoir of gas and polarization to the pellet.

We now examine another data set taken with the exact same experimental set up and pulse sequence but with tube F and GDP pellet 11-27-3 with a 26-μ-thick wall that's elevated by a pyrex bead (dataset B, see Table 4.1). Signal intensity maps for the gas outside (tube peak signal map + shoulder peak signal map) and inside the pellet are plotted in Fig 4.33. The signal density inside and outside the pellet plotted as a function of time is depicted in Fig 4.34. The polarization density curves for fill 13

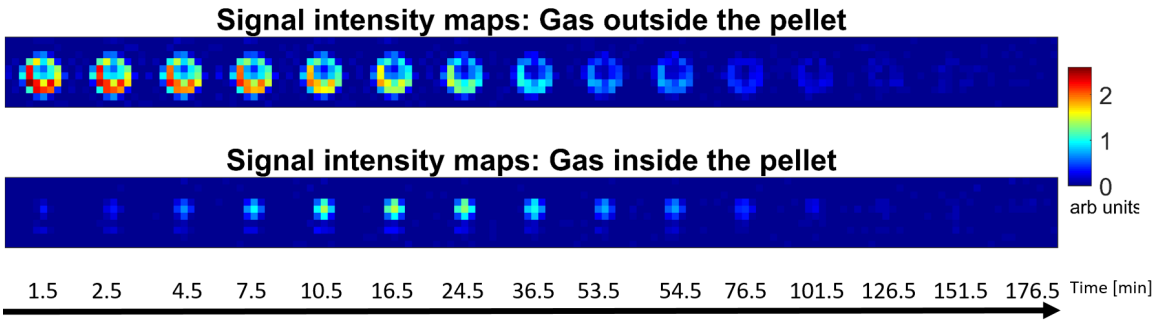

Figure 4.33: Time series of signal intensity maps for gas inside and outside the pellet for 'fill 13' data set. Signal intensity maps corresponding to gas outside the pellet are the sum of tube and shoulder signal intensity maps.

have a remarkably similar behavior to that of fill 2. The major difference between the two polarization density plots that is immediately noticeable is that the polarization density inside the pellet reaches the polarization density outside the pellet at a later relative time point for fill 13 data set than the fill 2 data set. This makes sense: We hypothesize that polarization loss associated with the permeation process is a function of wall thickness since it is the collisions with the wall material that seems to be the depolarizing mechanism. Another factor for depolarization could be impurities and existence of paramagnetic materials within the wall material and surface. Either way it takes more collisions to pass through the wall or more time to be exposed to the impurities and the paramagnetic material if the pellet has a larger thickness. Although until a mathematical model is not developed to accurately describe the permeation and polarization evolution, it is difficult to predict how polarization loss due to permeation is manifested in the polarization density functional forms.

We have now developed the capability to differentiate and quantify relative signal strength, and consequentially relative polarization density, inside and outside the pellet. Recall that our goal here is to quantify polarization loss associated with the permeation process as well as polarization decay rate once inside the pellet. In the next section, we develop a mathematical model that describes the evolution of permeation and polarization density as a function of time and use that model to

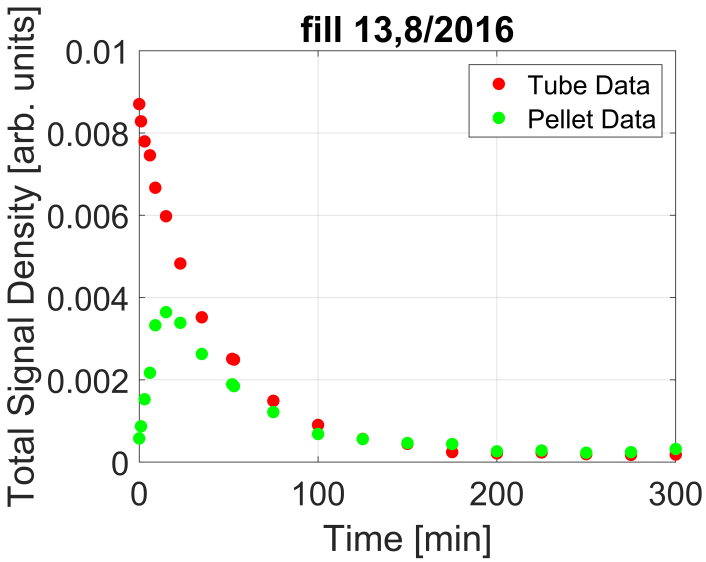

Figure 4.34: Time evolution of the total signal density inside and outside the pellet for dataset B. Each data point is obtained by summing up signal in all voxels inside the mask in intensity maps shown in Fig 4.33, weighted by its corresponding gas volume and corrected for the slice excitation profile.

quantify polarization loss associated with the permeation process.

4.4 Permeation and polarization density evolution model

In the previous section, by analyzing the 2D CSI images, we extracted polarization density inside and outside the pellet as a function of time. Here, we seek to determine the polarization loss due to the permeation process from the polarization density curves. Determining the polarization loss of the permeation process addresses one of the three feasibility criteria defined as the motivation of the presented experiments.

To do so, we develop a model to describe the permeation and polarization density evolution of the polarized gas permeating into the shell. We then present a simulated result of the permeation and polarization density evolution model for typical

parameters found in out permeation experiments.

This model assumes that the decay time constant of the gas in the tube is uniform throughout and there exists no polarization sinks anywhere in the tube. First, let us establish that throughout this section, we reference the evolution of polarization and spin density to $t = 0$, which we define as the time when the valve to the ante-chamber is cycled, or dispense time for the tubes without the ante-chamber. At this time, the pellet is immersed in the high pressure and polarized ^{3}He, which marks the start of the permeation process. The equation describing the flow of spins from the tube into the pellet is given by the following first-order, linear differential equation

$$\frac{d\rho^{in}}{dt} = \frac{\rho_0 - \rho^{in}(t)}{\tau_{perm}}, \tag{4.5}$$

where ρ_0 is the spin number density of the gas inside the tube and is assumed constant throughout the experiment, $\rho_i n$ is the number density of the gas inside the pellet, and τ_{perm} is the . Therefore, the spin number density of gas inside the pellet at time t is given by

$$\rho^{in}(t) = \rho_0(1 - e^{-\frac{t}{\tau_{perm}}}), \tag{4.6}$$

which is the solution to Eq. 4.5. Let us define P_0 to be the polarization of the tube gas at $t = 0$, i.e. $P_0 = P(0)$. We assume that the gas polarization inside the tube is completely independent of the gas inside the pellet (or the presence of the pellet itself), because the pellet volume and surface area are many fold smaller than those of the tube. Therefore, the dominant effect altering the tube gas polarization is longitudinal relaxation, which is probably dominated by wall interactions but the exact mechanism is unimportant to the model. Regardless of the cause, we assume that T_1 is uniform throughout the tube volume and can therefore be represented by a single parameter T_1^{out}. With this notation, the polarization of the tube gas at time t is given by

$$P^{out}(t) = P_0 e^{-\frac{t}{T_1^{out}}}. \tag{4.7}$$

The equation governing the behavior of polarization inside the pellet is rather more complicated and depends on exchange of polarized spins with the gas outside the pellet. We further assume that the gas inside the pellet sees a different polarization decay time constant (T_1^{pellet}) than the gas inside the tube does. Recall that polarization is defined as

$$P \equiv \frac{N_\uparrow - N_\downarrow}{N_\uparrow + N_\downarrow}, \tag{4.8}$$

where $N_\uparrow$ is the number of spins aligned with the field and $N_\downarrow$ is the number of spins anti-aligned. Therefore, the polarization of ^3He gas inside the pellet at time t is given by

$$P^{in}(t) = \frac{N_d(t)}{N(t)}, \tag{4.9}$$

where $N_d(t) \equiv N_\uparrow(t) - N_\downarrow(t)$ is the difference in number of aligned and anti-aligned spins inside the pellet, and $N(t) = N_\uparrow(t) + N_\downarrow(t)$ is the total number of spins inside the pellet and is given by $N(t) = \rho(t)V = \rho_0 V(1 - e^{-\frac{t}{\tau_{perm}}})$, where V is the pellet volume. To determine the behavior of $N_d(t)$, let us examine the effects influencing the spin excess N_d inside the pellet at a given time. Firstly, the gas that has already permeated into the pellet depolarizes with time constant T_1^{in}. Second, the gas that flows into or out of the pellet likely experiences some polarization loss in the permeation process due to collisions with the wall material. Let us assume the polarization survival represented by Γ to be the fraction of a "packet" of spins that retain their polarization traveling from outside to inside the pellet. Additionally, its polarization inside the pellet depends on its starting polarization before staring the permeation journey, i.e. P^{out}. Further, it also depends on the polarized spins flowing out of the pellet. Therefore, one can write the following first-order, linear differential equation to describe the fate of N_d inside the pellet

$$\frac{dN_d}{dt} = -\frac{N_d(t)}{T_1^{in}} + \frac{\Gamma\rho_0 V}{\tau_{perm}} P^{out}(t) - \frac{N_d(t)}{\tau_{perm}}. \tag{4.10}$$

The first term on the right-hand-side of the above equation is simply the longitudinal

spin relaxation rate of the polarized spins inside the pellet. The second term represents the spins permeating into the pellet, and the last term as the spins leaving the pellet. Plugging Eq. 4.7 into Eq. 4.10 yields

$$\frac{dN_d}{dt} = -\frac{N_d(t)}{T_1^{in}} + \alpha e^{-t/T_1^{out}} - \frac{N_d(t)}{\tau_{perm}}, \tag{4.11}$$

where $\alpha = \frac{\Gamma \rho_0 V P_0}{\tau_{perm}}$. Let us define τ^* such that $1/\tau^* \equiv 1/T_1^{in} + 1/\tau_{perm}$ to rewrite the above first-order, ordinary differential equation as

$$\frac{dN_d}{dt} = -\frac{N_d(t)}{\tau^*} + \alpha e^{-t/T_1^{out}}. \tag{4.12}$$

The solution to this equation assumes the form

$$N_d(t) = Ce^{-t/\tau^*} + De^{-t/T_1^{out}}. \tag{4.13}$$

Plugging $N_d(t)$ back into Eq 4.12 we write

$$-\frac{C}{\tau'}e^{-t/\tau^*} - \frac{D}{T_1^{out}}e^{-t/T_1^{out}} = -\frac{C}{\tau^*}e^{-t/\tau^*} - \frac{D}{\tau^*}e^{-t/\tau^*} + \alpha e^{-t/T_1^{out}}, \tag{4.14}$$

from which we can solve for D to find $D = \frac{\alpha}{1/\tau^* - 1/T_1^{out}}$. Enforcing boundary condition $N_d(0) = 0 = C + D$ enables us to find for $C = -D$. Therefore, the equation describing the evolution of the difference in number of spins aligned with the field and those anti-aligned inside the pellet, i.e. $N_d = N_\uparrow - N_\downarrow$ is given by

$$N_d(t) = \frac{\alpha}{1/\tau^* - 1/T_1^{out}}(e^{-t/T_1^{out}} - e^{-t/\tau^*}). \tag{4.15}$$

The polarization density is given by $P(t)\rho(t) = \frac{N_d(t)}{N(t)}\frac{N(t)}{V} = \frac{N_d(t)}{V}$. This is to say that ultimately, the polarization density inside the pellet is just $N_d(t)$ per unit volume.

It is useful to visualize the polarization evolution predicted by this model, for parameters similar to those in our experiments. We can calculate $N_d(t)$ for typical

values of $T_1^{out} = 30$ min, $\tau_{perm} = 227$s, and $\Gamma = 0.95$ as seen in our experiments and the results are shown in Fig 4.35 for a few different T_1^{in} values. Let us now examine the behavior of the model as a function of T_1^{in}. It is evident that for values of $T_1^{in} \geq T_1^{out}$, the model behavior is largely insensitive to change in T_1^{in} in that its functional form does not substantially change for varying values of T_1^{in}.

If T_1^{in} is large, the dominant decay process for the gas inside the pellet becomes similar to that of gas outside, explaining why the two tails of the polarization density curves of the gas inside and outside the pellet are overlaid on top of each other for all values of $T_1^{in} \geq T_1^{out}$.

4.5 Fit to permeation and polarization density evolution model

Now that we have developed the permeation and polarization evolution model, let us fit our polarization density curves obtained from the 2D slice-selective CSI images shown in Sec 4.3 to the model developed in the previous section.

One of the differences between the assumptions in the model and our measurements, is the excitation RF depletion of the longitudinal magnetization. This difference is ignored for the following reason. Gas continuously flows in and out of the pellet with a time constant in the order of minutes. Therefore, there is constant inflow of polarized gas into and out of the pellet, so the RF depletion inside the pellet approaches that outside, which is negligible, given the large reservoir of gas inside the tube. Presented in Fig 4.36 are the fitted polarization density curves.

There are four fitting parameters in the two way model presented in Fig 4.36: initial polarization density, T_1^{out} or tube T_1, permeation time constant τ_{perm}, and polarization retention rate Γ. The time constant of the pellet is set to ∞, since the behavior of the model is essentially insensitive to T_1^{in} for the range $T_1^{in} \geq T_1^{out}$.

Curiously, if the number of fit-parameters are reduced to 3 instead, where τ_{perm}

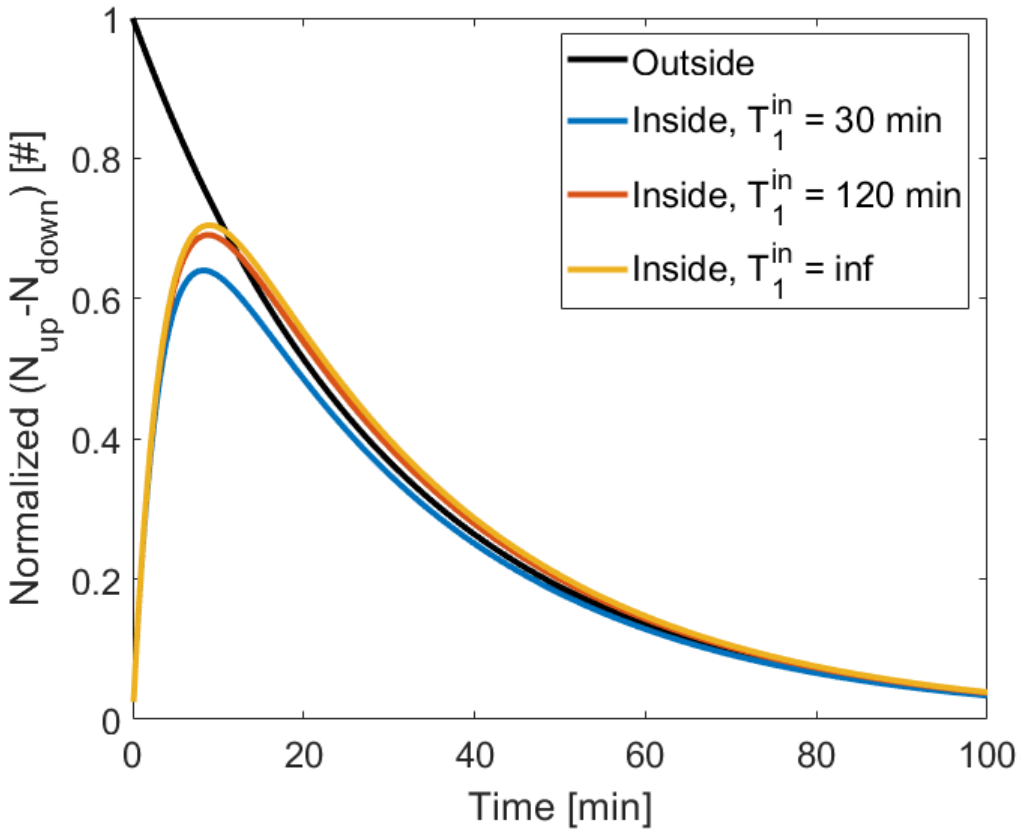

Figure 4.35: Permeation and polarization evolution one-way flow and two-way flow model simulations for typical values of parameters seen in our experiments for select number of T_1^{in} values. The dominant effect for tube gas polarization density is exponential decay (black solid line). The polarization density inside the pellet builds up as gas flows in while simultaneously experiencing T_1 decay. At some point the decay process is dominant and the polarization density falls off. Parameter values are: $T_1^{out} = 30$ min, $\tau_{perm} = 227$s, and $\Gamma = 0.95$. Note that the behavior of the one-way and two-way flow models is very similar in the regime where T_1^{in} and T_1^{out} values are comparable. Solid (with the exception of the black line) and dashed lines correspond to one-way and two-way flow models, respectively.

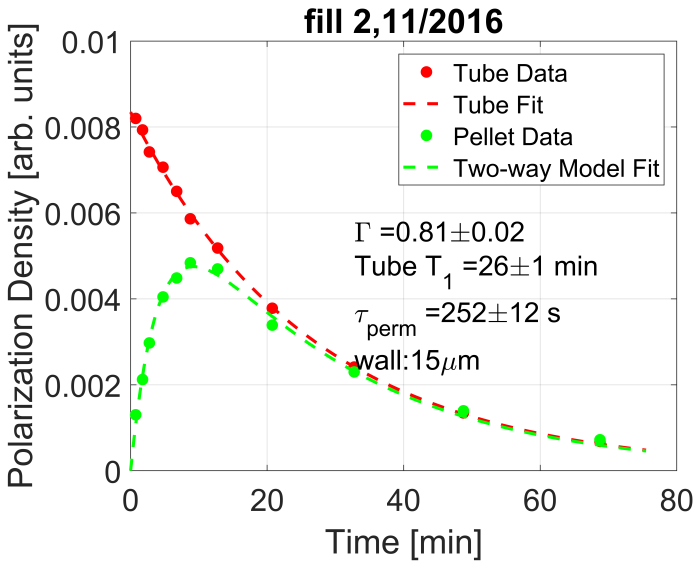

Figure 4.36: Polarization density as a function of time fitted to the two-way flow permeation and polarization evolution model. There are four fit parameters, initial polarization density, T_1^{out} or tube T_1, permeation time constant τ_{perm}, and polarization retention rate Γ. In this model, T_1^{in} is assumed infinite. RF loss is not taken into account in the fitted result.

is regarded as a constant and set to its measured value of 227 s, the fit quality remains more or less the same with a slightly-reduced Γ value as seen in Fig 4.37. It appears that the model with four fit parameters best describes the evolution of polarization density inside and outside the pellet. While it is worth noting that the fitted permeation time constant is not within error bars of the measured value, though it is close within a few percentage points, the permeation time constant was measured using ^{4}He and under different experimental conditions. Therefore, it is reasonable to allow τ_{perm} float as a fit parameter in the model.

Next we fit the polarization density curves obtained from fill 13 data set, where the pellet used in the experiment is GDP 11-27-3 with wall thickness of 26-μ, to the four-fit-parameter model as shown in Fig 4.38. It is encouraging to confirm our hypothesis formed in Sec 4.3 that polarization retention rate Γ associated with the permeation process is in fact lower ($\sim$ 20% higher loss) for the 26-μ-thick pellet than

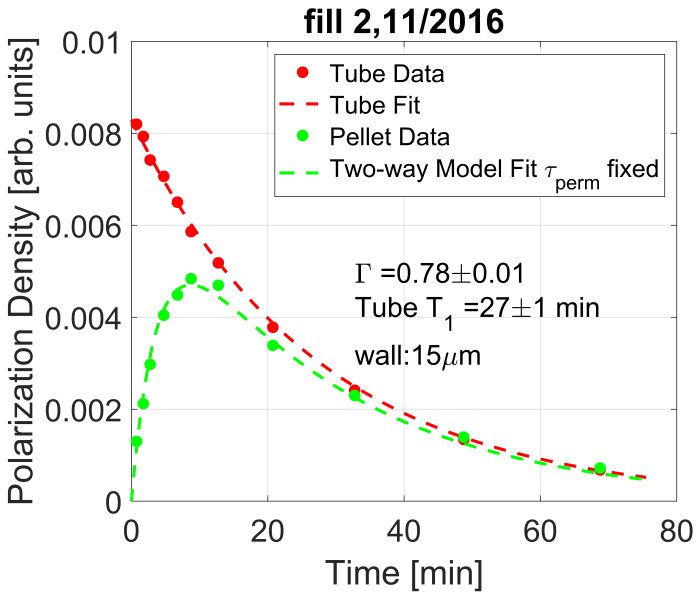

Figure 4.37: Polarization density as a function of time fitted to the two-way flow permeation and polarization evolution model with reduced number of fit parameters. There are three fit parameters, initial polarization density, T_1^{out} or tube T_1, and polarization retention rate Γ. In this model, T_1^{in} is assumed infinite. Notice that the fit through the points is essentially remained the same when compared with the 4-parameter two-way model fit. RF loss is not taken into account in the fitted result.

the 15-μ-thick pellet.

4.6 Conclusions

Our results indicate that the polarization retention of the permeation process depends on the pellet wall thickness. We report polarization retention of $\Gamma = 81\% \pm 2$ and polarization decay time constant of $T_1 = 26$ min ± 1 for a 15-μm pellet in tube G, charged with 1.54 bar of polarized ^{3}He. For a 26-μm pellet in tube F, charged with 2.18 bar of polarized ^{3}He, we measured polarization retention $\Gamma = 62\% \pm 2$ and polarization decay time constant of $T_1 = 42$ min ± 1. The decay time constants reported are for the gas inside the tube.

We discovered that the polarization decay time constant of the gas inside the

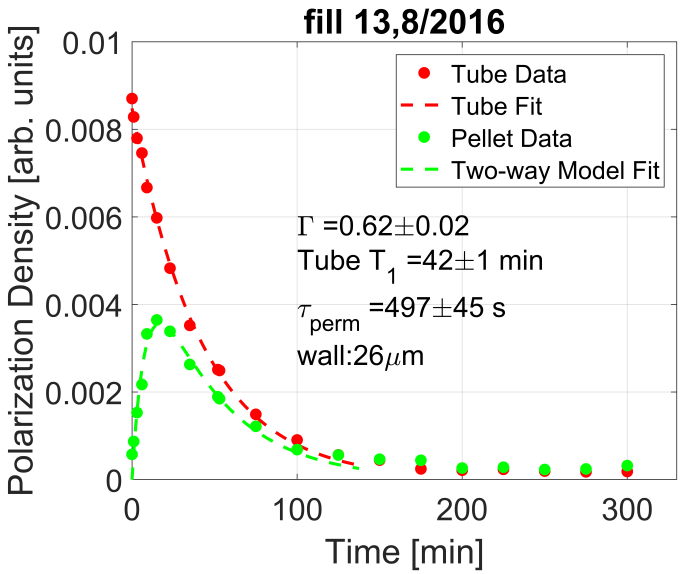

Figure 4.38: Polarization density obtained from fill 13 data set as a function of time fitted to the two-way flow permeation and polarization evolution model. There are four fit parameters, initial polarization density, T_1^{out} or tube T_1, permeation time constant τ_{perm}, and polarization retention rate Γ. In this model, T_1^{in} is assumed infinite. Only data points taken with the first 125 min of the experiment where fitted to the model since poor SNR in later signal intensity maps result in unreliable polarization density values. RF loss is not taken into account in the fitted result.

pellet tracks that of the gas outside the pellet (but inside the tube), presumably due to relatively rapid gas exchange across the pellet wall. We saw that at equilibrated pressures inside and outside the pellet, the gas particles diffuse in and out of the pellet, which indicates that the gas inside the pellet has a much longer polarization decay time constant if the gas was isolated inside. That is to say, polarized helium inside the pellet has a longer decay time constant, but because there is constant inflow/outflow of gas, the decay inside the pellet is dominated by the decay of the gas outside. We note that at room temperature, it is near-impossible to reliably measure the polarization decay time constant of the isolated gas inside the pellet independently, because the gas leaks out with a time constant ($= \tau_{perm}$) in the order of minutes, leaving no gas in the pellet for a robust T_1 measurement.

Based on our results, it is evident that polarization loss is substantially higher

data set	**acquired on**	**tube & fill #**	**tube ID [mm]**	**pellet identifier & wall TH [μm]**	**pellet OD [mm]**	τ_{perm} **[ms]**	**P [mbar]**	$\mathbf{T_1}$ **[min]**	Γ **[%]**
A	11/18/ 2016	G 2	2.73	10-32-02 15	1.82	227	1540	26 ± 1	81 ± 2
B	8/14/ 2016	F 13	3-4	11-27-3 26	1.82	374	2177	42 ± 1	62 ± 2

Table 4.1: Summary of permeation data sets analyzed and presented in this thesis. ID = inner diameter, OD = outer diameter, TH = thickness, τ_{perm} = pellet's permeation time constant measured for ^{4}He gas permeating out of the pellet into vacuum, P = pressure of the tubular part of the tube where the pellet sits, T_1 = longitudinal relation time of the gas inside the tube, and Γ = polarization retention rate of the permeation process given in percentage. The experimentally measured values T_1 and Γ are reported from results of the four-fit-parameter model, where τ_{perm} is allowed to float as a fit parameter.

in the pellet with larger wall thickness. Therefore, we conclude that for future experiments, pellets with thinner walls be used. In the event that polarization loss is inherent to the permeation process, given a polarization retention of $81\% \pm 2$, nominally, the maximum polarization achievable in the pellets is 81%. Using our polarizer, maximum polarization achieved inside the pellets is ∼48%, granted we start with 60% polarization.

Clearly, one way to improve the permeation process is to improve T_1 of the tube. Based on both our simulations and results, we expect that the polarization of the gas inside the pellet has a similar relaxation time to the gas outside the pellet. A glaring limitation of these experiments is that they used pressures of barely more than 1bar, whereas for an actual spin-polarized test, we need demonstrate similar degree of polarization survival in the permeation process at 5-10 times larger pressures than the pressures used in our experiment. We do no expect that polarization loss associated with the permeation process is dependent on pressure, however, future experiments must establish whether Γ is a function of pressure.

Here, we have demonstrated a robust method for monitoring the polarization

process. With our custom CSI pulse sequence, the analysis procedure, and the permeation and polarization evolution model, we have now created a robust testbed with which we can perform permeation measurements to faithfully determine the polarization loss in the permeation process.

Chapter 5

Absolute polarization and T_1 measurements

One of the milestones that need to be met to successfully perform a spin-polarized fusion experiment at the DIII-D tokamak located in San Diego is development of a robust method to deliver polarized fuel into the tokamak plasma. There currently exists no such method. As discussed previously in Chapter 1, our group is hoping to develop a delivery mechanism in which we load inertial confinement fusion (ICF) shells with spin-polarized, high pressure ^{3}He gas via permeation suitable for cryogenic injection into the plasma. In Chapter 4, we presented a method for loading the pellets with hyperpolarized ^{3}He via permeation, and developed a suite of highly sensitive MRI tools to monitor the permeation process with great precision. These tools were then used to quantify the polarization loss due to permeation through the shell wall. Although this is useful result, what we ultimately care about is the absolute polarization that can be loaded into the shell. In this chapter, we present the experiments carried out to determine (1) the absolute polarization of the gas that has been loaded into the pellet, and (2) how fast the polarization decays after it has been loaded.

To do this, we first develop the mathematical relationship between MR signal generated by a thermal sample and MR signal generated by a hyperpolarized sample, including imaging and physical dependencies, which is done in Sec 5.2. Based on the developed theory, we design a series of experiments as described in Sec 5.3, to acquire

images of a thermally polarized sample of ^{3}He (Sec 5.4) and hyperpolarized sample of ^{3}He (Sec 5.5) with known densities and temperatures, at the same field strength and using the same RF coil and receiver electronics (1.5-Tesla clinical MRI scanner) to determine the absolute polarization of the hyperpolarized ^{3}He sample (Sec 5.6).

This chapter presents a description and detailed analysis of the absolute polarization and T_1 measurements obtained from the hyperpolarized ^{3}He experiments performed during the weekend of Feb 14 2020 in addition to thermal equilibrium calibration measurements. First, let us give the motivation for the measurements presented ahead.

5.1 Motivation

In the present chapter we focus on the measurement of the absolute polarization of ^{3}He that has been permeated into the pellet.

Recall from Sec 2.1.2 that for our experiments, ^{3}He is hyperpolarized using our hybrid-alkali SEOP polarizer. Once the polarizer is turned off and the rubidium is no longer optically pumped, the ^{3}He will immediately start decaying due to wall relaxation mechanisms, with a time-constant of tens of hours. Before dispensing the gas, the polarization of ^{3}He in the polarizer cell can be measured via the polarizer's onboard NMR system calibrated to a previous electron paramagnetic resonance [81] measurement of absolute polarization.

However, once the hyperpolarized gas is dispensed, the polarization will start decaying via several different mechanisms, time-constants of which are mostly unknown. For example, once dispensed into a glass tube used for the permeation measurements, the gas will no longer be at the center of the Helmholtz coils, and will see a different magnetic field from the uniform field in the cell. More importantly, the gas will go through a variety of field gradients (a depolarizing mechanism) once the tube is detached from the dispense mechanism and walked over to the scanner. Additionally,

the gas decays due to wall interactions more quickly inside the tube than inside the polarizer cell due to its much larger surface-to-volume ratio. Therefore, even with the ability to measure ^{3}He polarization inside the cell, and knowledge of the polarization loss during permeation, the absolute polarization of ^{3}He permeated into the shell is unknown, because the starting polarization in the tube is unknown.

To measure the absolute polarization, we propose the following strategy. The thermal equilibrium polarization of ^{3}He at a known field strength and temperature can be calculated analytically to high accuracy. With the knowledge of thermal equilibrium polarization, we can design an experiment to determine the absolute polarization of hyperpolarized ^{3}He by calibrating measured MR signal generated by the hyperpolarized ^{3}He to that generated by the thermally polarized ^{3}He. That is, using the same imaging technique at the same field strength, if we acquire an image of a hyperpolarized ^{3}He sample with known density and temperature, and acquire an image of a ^{3}He sample at thermal equilibrium polarization also with known density and temperature, we can determine the polarization of the hyperpolarized ^{3}He sample by knowing thermal equilibrium polarization.

5.2 Theory

In this section, we establish the mathematical foundation for relating voxel signal strength in the hyperpolarized gas image to the voxel signal strength in the thermally polarized gas image, both obtained using a 3D CSI pulse sequence, from first principles. Recall from Sec 2.1.1, that for a given magnetic field strength and temperature, the thermal equilibrium polarization of a sample of spins can be precisely calculated as

$$P = \tanh(\frac{\gamma h B_0}{4\pi k T}) \approx \frac{\gamma h B_0}{4\pi k T}. \tag{5.1}$$

where k is the Boltzmann constant, T is the temperature in Kelvin, B_0 is the field strength, h is the Planck constant, and γ is the gyromagnetic ratio of the spins.

Recall also from Sec 2.1 that the NMR signal intensity S is proportional to the transverse magnetization $M_\perp$, and is given by

$$S \propto \omega_0 \int d^3r M_\perp B_\perp^{receive}, \tag{5.2}$$

where ω_0 is the resonant frequency, $M_\perp$ is the transverse magnetization, and $B_\perp^{receive}$ is the receive field sensitivity of the coil and often encompasses sensitivity in the electronics as well. We exploit the above expression to derive the elevant form of signal for thermally polarized case in Sec 5.2.1 and hyperpolarized case in Sec 5.2.2.

5.2.1 Derivation of the thermally polarized steady-state signal

Consider a thermally polarized spin population aligned with the longitudinal axis. In order to acquire an image, several excitation RF pulses are applied to create transverse magnetization for signal acquisition at desired k-space samples. Here we derive the expression for steady-state signal, which is the signal reached after several equally spaced excitation RF pulses have been applied, where the longitudinal magnetization right before application of an RF pulse and longitudinal magnetization right before application of the previous RF pulse are the same. Therefore, the signal generated by either of the RF pulses are also the same, hence the term "steady-state".

If we apply a series of excitation RF pulses to tip the longitudinal magnetization, the magnetization in the transverse plane after the application of the n^{th} excitation RF pulse is given by

$$M_\perp(n) = M_z^-(n) \sin\theta e^{-TE/T_2^*}, \tag{5.3}$$

where $M_z^-(n)$ is the longitudinal magnetization right before the RF pulse is applied, θ is the flip angle, TE is the time between the center of the RF pulse and the beginning of the signal measurement, and T_2^* is the decay rate of the transverse signal. $M_z^-(n)$

can be written as

$$M_z^-(n) = M_z^+(n-1)e^{-TR/T_1}\sin\theta + (1-e^{-TR/T_1})M_0, \tag{5.4}$$

where TR is the repetition time (time between RF pulses), T_1 is the time constant of the regrowth to thermal equilibrium magnetization, M_0, and $M_z^+(n-1)$ is the longitudinal magnetization right after application of the $(n-1)^{th}$ RF pulse. Note that the relationship between the longitudinal magnetization before and after the application of the RF pulse is given by

$$M_z^+(n) = M_z^-(n)\cos\theta, \tag{5.5}$$

and the longitudinal and traverse magnetization values are related as

$$M_\perp^+(n) = M_z^-(n)\sin\theta, \tag{5.6}$$

assuming perfect spoiling, which implies that there exists no transverse magnetization prior to the application of the excitation RF pulse. Let us now find the steady-state transverse magnetization by enforcing the steady-state definition: If the transverse magnetization has reached a steady-state value, the longitudinal magnetization right before (after) an RF pulse must equal the longitudinal magnetization right before (after) the previous RF pulse. Mathematically this condition is given by

$$M_z^\pm(n) = M_z^\pm(n-1). \tag{5.7}$$

Substituting the value of $M_z^-(n)\cos\theta$ for $M_z^+(n)$ (5.5) in Eq. 5.4 and applying the steady-state condition as in 5.7, we can write

$$M_z^-(n) = M_z^-(n)\cos\theta e^{-\frac{TR}{T_1}} + (1-e^{-\frac{TR}{T_1}})M_0, \tag{5.8}$$

where rearranging and isolating $M_z^-(n)$ gives

$$M_z^-(n) = \frac{(1 - e^{-\frac{TR}{T_1}})M_0}{1 - e^{-\frac{TR}{T_1}} \cos\theta}. \tag{5.9}$$

Substituting Eq. 5.9 in Eq. 5.6 yields

$$M_\perp^+(n) = \frac{(1 - e^{-\frac{TR}{T_1}})M_0}{1 - e^{-\frac{TR}{T_1}} \cos\theta} \sin\theta, \tag{5.10}$$

where $M_\perp^+(n)$ is transverse magnetization immediately after the n^{th} RF pulse which starts decaying as time goes on and can be rewritten at measurement time (or echo-time, TE) as

$$M_\perp(n) = \frac{(1 - e^{-\frac{TR}{T_1}})M_0}{1 - e^{-\frac{TR}{T_1}} \cos\theta} e^{-\frac{TE}{T_2^*}} \sin\theta. \tag{5.11}$$

5.2.2 Derivation of the hyperpolarized signal after application of the nth RF pulse

Unlike the magnetization in the thermal equilibrium polarization case, the signal in the hyperpolarized sample of spins will never reach steady-state since there is no regrowth in the longitudinal magnetization. In fact, the total magnetization constantly decays toward thermal equilibrium magnetization M_0 with time constant T_1. Instead, one can derive a recursive relationship for the longitudinal and transverse magnetization as follows.

Let us start by assuming that the longitudinal magnetization immediately before the application of the first RF pulse is M_{HP}, where $M_{HP} \gg M_0$. We can then write the longitudinal magnetization before the application of the n^{th} RF pulse for the first few terms to derive the recursive form:

$$M_z^-(1) = M_{HP}$$
$$M_z^-(2) = M_{HP} e^{-\frac{TR}{T_1}} \cos\theta$$

$$
\begin{aligned}
M_z^-(3) &= M_{HP} e^{-2\frac{TR}{T_1}} \cos^2\theta \\
M_z^-(4) &= M_{HP} e^{-3\frac{TR}{T_1}} \cos^3\theta \\
&\vdots \\
M_z^-(n) &= M_{HP} e^{-(n-1)\frac{TR}{T_1}} \cos^{n-1}\theta.
\end{aligned} \tag{5.12}
$$

The transverse magnetization at measurement time TE after the n^{th} RF pulse can be found by plugging Eq 5.12 in Eq 5.6 and including the transverse magnetization decay term as given below

$$
M_\perp(n) = M_{HP} \cos^{n-1}\theta \left(e^{-(n-1)\frac{TR}{T_1}}\right) \sin\theta \left(e^{-\frac{TE}{T_2^*}}\right). \tag{5.13}
$$

5.2.3 Mathematical relationship between voxel signal intensities in the thermally polarized and the hyperpolarized ^{3}He 3D CSI images

In this section, we relate the strength of the transverse magnetization at thermal equilibrium polarization derived in Sec 5.2.1 to the strength of the transverse magnetization of a hyperpolarized sample derived in Sec 5.2.2. Ultimately we seek to relate the voxel signal intensities obtained in each image by exploiting the relationship in expression 5.2 to write hyperpolarized signal in terms of thermally polarized signal, and imaging and physical parameters pertinent to our specific experimental design, starting from transverse magnetization.

The transverse magnetization for the gas with thermal equilibrium polarization with perfect spoiling derived in Sec 5.2.1, using the CSI pulse sequence shown in Fig 5.8 (this will be discussed in Sec 5.3.2), is given by

$$
M_\perp^{therm} = \frac{(1 - e^{-TR/T_1}) M_z^{therm}}{1 - e^{-TR/T_1}\cos\theta_{therm}} \sin\theta_{therm} e^{-TE/T_2^*}, \tag{5.14}
$$

where TE is the echo time defined to be the time between the center of the RF pulse and the beginning of the ADC, and M_z^{therm} is the longitudinal magnetization for the thermal gas. In the limit TR $\gg$ T_1, a condition that will be enforced in our experimental design as discussed in Sec 5.3.2 and 5.3.2, Eq 5.14 reduces to

$$M_\perp^{therm} = M_z^{therm} \sin\theta_{therm} e^{-TE/T_2^*}. \tag{5.15}$$

Similarly, the transverse magnetization after the n^{th} RF pulse for hyperpolarized gas using the same pulse sequence derived in Sec. 5.2.2 is given by

$$M_\perp^{pol}(n) = M_z^{pol} \cos^{n-1}\theta_{pol} e^{-(n-1)TR/T_1} \sin\theta_{pol} e^{-TE/T_2^*}, \tag{5.16}$$

where M_z^{pol} is the longitudinal magnetization for hyperpolarized gas. Since we use the center-out CSI sequence for the hyperpolarized gas image, where the first RF pulse in the imaging sequence is immediately followed by read-out without application of any gradients as will be discussed in Sec 5.3.2, only the magnetization after the first RF pulse is considered in our treatment. That is because the longitudinal magnetization loss from application of several RF pulses to acquire the 3D CSI image can be accounted for in the analysis. Therefore Eq 5.16 simplifies to

$$M_\perp^{pol} = M_z^{pol} \sin\theta_{pol} e^{-TE/T_2^*}. \tag{5.17}$$

Since TE is the same for both measurements, and T_2^* is assumed to be the same in thermally polarized and hyperpolarized gas, we drop the e^{-TE/T_2^*} term from both Eqs 5.15 and 5.17 and the two equations further reduce to

$$\begin{aligned} M_\perp^{therm} &= M_z^{therm} \sin\theta_{therm} \\ M_\perp^{pol} &= M_z^{pol} sin\theta_{pol}. \end{aligned} \tag{5.18}$$

The transverse magnetization is directly proportional to signal intensity measured in a given voxel, and Eq 5.18 can be rewritten as

$$\begin{aligned} S_{therm} &\propto M_z^{therm} \sin\theta_{therm} \\ S_{\text{pol}} &\propto M_z^{pol} \sin\theta_{pol}. \end{aligned} \tag{5.19}$$

It is now appropriate to include the variations in pressure (or density) and flip angle correction factors in 5.19 to write

$$\begin{aligned} M_z^{therm} &\propto \frac{S_{therm}}{\sin\theta_{therm} \cdot \rho_{therm}} \\ M_z^{pol} &\propto \frac{S_{pol}}{\sin\theta_{pol} \cdot \rho_{pol}}, \end{aligned} \tag{5.20}$$

where ρ_{therm} and ρ_{therm} are the ^{3}He gas pressures inside the thermal equilibrium phantom and in the isolated pellet, respectively. Recall that M_z^{therm} and M_z^{pol} are the longitudinal magnetization values which are directly proportional to the polarization of the gas in each case, namely

$$\begin{aligned} M_z^{therm} &\propto S_{therm} \propto P_{therm}^{^3He} \\ M_z^{pol} &\propto S_{pol} \propto P_{pol}^{^3He}, \end{aligned} \tag{5.21}$$

where $P_{therm}^{^3He}$ and $P_{pol}^{^3He}$ are the polarization values of the thermally polarized and hyperpolarized ^{3}He gas (please note that the following naming convention is adopted in this report: P = polarization, and ρ = pressure). Recall from Sec 2.1 that polarization is defined as $P = \frac{N_\uparrow - N_\downarrow}{N_\uparrow + N_\downarrow}$, and for thermally polarized ^{3}He gas at 1.5 Tesla and $T = 20°$, $P_{therm}^{^3He} = 3.98 \times 10^{-6}$ (see Table 2.1). Eq 5.20 can be rewritten as

$$\begin{aligned} P_{therm}^{^3He} &\propto \frac{S_{therm}}{\sin\theta_{therm} \cdot \rho_{therm} \cdot V_{voxel,therm}} \\ P_{pol}^{^3He} &\propto \frac{S_{pol}}{\sin\theta_{pol} \cdot \rho_{pol} \cdot V_{voxel,pol}}, \end{aligned} \tag{5.22}$$

where $V_{voxel,therm}$ and $V_{voxel,pol}$ are the voxel volumes for the images of the thermally polarized and hyperpolarized gas, respectively. The parameter that will ultimately bridge the gap between the signal intensities in the two images is the constant of proportionality between polarization and longitudinal magnetization α, where $P^{^3He}_{therm} = \alpha \cdot M^{therm}_z$. Therefore, one can write

$$\alpha = \frac{P^{^3He}_{therm}}{M^{therm}_z} = \frac{P^{^3He}_{therm}}{\frac{S_{therm}}{\sin\theta_{therm}\cdot\rho_{therm}}} = \frac{P^{^3He}_{therm}\sin\theta_{therm}\cdot\rho_{therm}}{S_{therm}}. \tag{5.23}$$

Since the constant of proportionality between polarization and longitudinal magnetization is the same for both thermally polarized and hyperpolarized gas, the following holds

$$P^{^3He}_{pol} = \alpha \cdot M^{pol}_z. \tag{5.24}$$

Therefore, substituting the value of α obtained from Eq 5.23, M^{pol}_z obtained from Eq 5.20, and the volume terms from Eq 5.22 in Eq 5.24 yields

$$\boxed{P^{^3He}_{pol} = \frac{P^{^3He}_{therm}\sin\theta_{therm}\cdot\rho_{therm}}{S_{therm}} \cdot \frac{S_{pol}\cdot V_{voxel,therm}}{\sin\theta_{pol}\cdot\rho_{pol}\cdot V_{voxel,pol}}.} \tag{5.25}$$

That is to say, if an experiment is carefully designed such that an image of the hyperpolarized gas sample and an image of the thermally polarized gas sample is taken with same RF received coil and known (measured) flip-angles, TR, T1, voxel size, and thermal equilibrium polarization, the polarization of ^{3}He in the hyperpolarized gas sample can be determined from signal intensities in the two images.

5.3 Experimental design

In this section, we describe the experimental apparatus and design pertinent to the T_1 and the absolute polarization measurements. The longitudinal spin relaxation measurement is done using hyperpolarized ^{3}He, whereas determining the absolute

polarization is done via a combination of measurements using both thermally polarized and hyperpolarized ^{3}He, which is motivated by the mathematical formalism developed in Sec 5.2. We first describe the experimental apparatus in Sec 5.3.1, followed by the general experimental design and related considerations in Sec 5.3.2.

5.3.1 Experimental apparatus

The majority of the experimental apparatus for the hyperpolarized measurements presented in this chapter is identical to the apparatus used in experiments presented in Chapter 4, and were described previously in Sec 4.2. Recall that the goal of the absolute polarization measurement is to determine the polarization of hyperpolarized ^{3}He that has permeated into the pellet. Therefore, once the permeation process is completed, for a faithful signal measurement, we seek to isolate the gas inside and outside the pellet, and acquire an image only of the hyperpolarized ^{3}He inside. To seal the permeated gas inside the pellet, we immerse the tube containing the pellet in a liquid nitrogen bath, effectively "freezing" the pellet walls, such that the walls are no longer permeable to ^{3}He.

The ICF shells' outer diameter is 1.82 mm, and given that the imaging resolution used in our experiments is 0.5 cubic millimeter, most voxels will have partial volume of region outside the pellet. To acquire an image of the gas only inside the pellet such that no voxel's signal comes from gas outside the pellet, we vacuum pump the tube to eliminate the hyperpolarized gas outside the pellet (remember, when the pellet is maintained at 77 K, the gas inside it cannot escape). Therefore, an additional experimental component for the absolute polarization measurement is a liquid nitrogen bath that sits inside the coil, mounted to the Styrofoam coil housing (see Fig 4.5).

As for the thermal equilibrium measurements, the gas-filling procedure of the ^{3}He phantom is as follows. Obviously, the polarizer is not needed for charging a tube with thermally polarized ^{3}He. We use the polarizer plumbing system to dispense ^{3}He

from a ^{3}He canister into the tube, precisely recording the pressure, similar to the gas dispense procedure described in Sec 4.1.3. For the thermal equilibrium measurements, tube V8C, which has a newer tube design, is charged with ^{3}He (see Fig 5.1) Recall

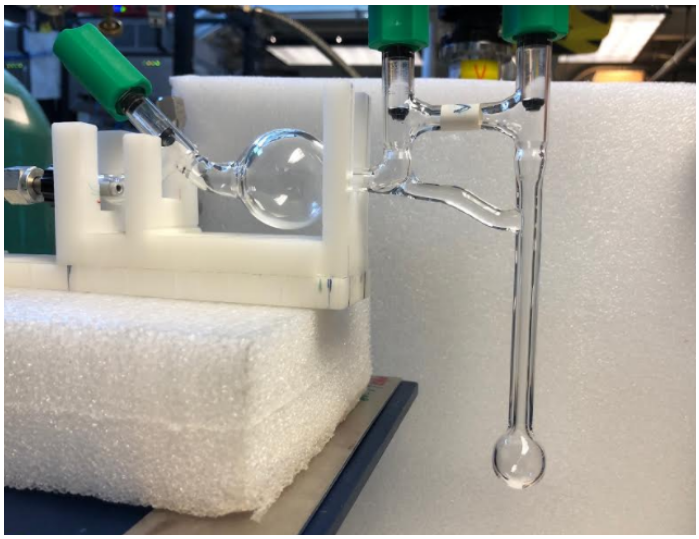

Figure 5.1: Tube V8C charged with thermally polarized ^{3}He and oxygen, and is used in the thermal equilibrium ^{3}He measurements. The bulb in the bottom sits at the center of the coil and is imaged as a component of the absolute polarization measurement.

from Sec 5.2.2 that we enforce the condition that $TR \gg T_1$ for the thermal equilibrium gas image acquisition, such that our approximations in deriving Eq 5.2.3 are valid. However, recall from the results presented in Sec 4.5, that the T_1 of the ^{3}He in the a typical tube used in our experiments is 20-45 min. Acquisition of a 10×10 (i.e. 10 voxels by 10 voxels) image requires 100 excitations. To enforce $TR \gg T_1$, the time between each RF repetition would have to be at least in the order of an hour, whereby a 2D CSI image with 100 voxels would take $>$ 100 hours, which is highly impractical.

We address this challenge by taking advantage of the accelerated longitudinal spin relaxation rate of a spin-1/2 particle in the presence of oxygen. Although oxygen acts unfavorably when the goal is achieving high T_1 in a hyperpolarized ^{3}He sample (see

Sec 4.1.3), it acts in our advantage to shorten T_1 when imaging a thermally polarized sample of ^{3}He. Therefore, to shorten the acquisition time for thermal equilibrium measurements, we dispense O_2 into the tube followed by ^{3}He. The exact amount of ^{3}He and oxygen dispensed to charge the tube is given in Sec 5.4.2, where the inverse relationship between oxygen partial pressure and T_1 is discussed. The tube used in the thermally polarized ^{3}He measurements presented ahead is charged with 0.912 Bar of oxygen and 6.017 Bar of ^{3}He.

Recall that the reason we perform the thermal equilibrium polarization measurements is to relate the MR signal in the thermally polarized gas, to the MR signal in the hyperpolarized gas, which has completed the permeation journey and resides in the pellet. The thermal equilibrium polarization measurement of MR signal can be done without the pellet. That is, we are concerned with measuring the MR signal inside a voxel that contains only thermally polarized ^{3}He. This measurement can be done for gas inside the tube, and the presence of the pellet makes no difference in the strength of the signal, whether the signal was generated by gas inside or outside the pellet. In fact, to increase SNR in the thermally polarized gas measurement, given that the signal available for measurement is orders of magnitude lower than the signal in the hyperpolarized case, the imaging voxel in the thermal case can be much larger (in our case, as will be discussed 8 times larger) than the imaging voxel in the hyperpolarized case to reduce required imaging time to achieve acceptable SNR. In the hyperpolarized permeation case, however, using a voxel size of 2 cubic millimeters would result in having one voxel encapsulating the gas inside the pellet, therefore unable to resolve the pellet.

5.3.2 Measurement procedure and imaging techniques

In this section, we are concerned with the general experimental procedure and imaging techniques used in the T_1 and the absolute polarization measurements. We begin by discussing the general measurement considerations followed by description of the

imaging techniques used to make the said desired measurement.

Let us begin with hyperpolarized measurements. Ultimately, our goal is to extract the polarization of spin-polarized ^{3}He in the pellet by invoking Eq 5.25. Accordingly, we acquire an image of the hyperpolarized gas isolated inside the pellet, and relate the image's signal intensity to signal intensity of an image of the thermally polarized gas inside the tube. For the assumptions and simplifications made in Sec 5.2.3 to be valid, a center-out CSI sequence is used to acquire the hyperpolarized image. The reasoning is as follows. The assumption in Eq 5.17 is that $n = 1$, meaning the signal is considered after application of the first RF pulse without application of any gradients, where the only source of transverse magnetization depletion is T_2^* decay. Experimentally, this assumption can be enforced by a center-out CSI sequence, where the center of k-space is sampled first (i.e. signal measurement at the center is done first), followed by sampling other points in k-space moving spirally out on a defined grid of points. We note that an excitation RF correction factor of $\cos^{-n}\theta$ is applied to each k-space sample to compensate for the magnetization loss and its effects on the reconstructed image intensity. To ensure a well-defined voxel size without slice-profile (see Sec 4.2.6), a 3D non-selective CSI sequence is used to acquire the image of the hyperpolarized gas isolated in the pellet as discussed in Sec 5.5.3.

Further, the flip-angle used in the hyperpolarized image acquisition must be known. We note that the RF pulse is generated by applying a voltage across the transmit coil, where the flip-angle of the RF pulse is determined by the magnitude of the applied voltage. One way to determine the actual flip-angle applied at the center of the coil is to first determine the reference voltage, which is the rect-waveform voltage that should be applied for one millisecond as a function of time to achieve flip-angle of 180° at the center of the coil. The flip-angle can then be computed based on the measured reference voltage, noting that the time integral of the applied voltage is directly proportional to the flip-angle. To measure the reference voltage, and consequently the actual flip-angle applied at the center of the coil, we use a series of

back-to-back NMR measurements, as will be discussed in Sec 5.5.2.

For determining the hyperpolarized ^{3}He longitudinal spin-relaxation time constant T_1, we acquire NMR measurements immediately after pumping out the gas in the tube and isolating the gas in the pellet. Since the pellet encompasses a small region of space at or near the iso-center of the magnet, we expect no systematic spatial variations in frequency, T_2^*, or phase. Therefore, the T_1 value can be determined globally using the strength of signal acquired in the NMR measurements as a function of time, as is done in Sec 5.5.4.

We now focus on the thermal equilibrium measurements. To acquire an image, the signal strength of which is consistent with the assumptions made in Sec 5.2.3 to derive the equation (Eq 5.25) relating the two signal strengths, we attempt to acquire the image of the thermally hyperpolarized ^{3}He using the same experimental apparatus and imaging sequence where possible. As such, we use the same coil and coil housing. We use the same non-selective 3D CSI sequence (although with different parameters), which will be discussed in Sec 5.4.3.

To acquire an image of the thermally polarized ^{3}He sample, we must first determine the effective T_1 of the thermally polarized ^{3}He-oxygen mixture so we can properly enforce the $TR \gg T_1$ assumption by our choice of TR. This is done using a series of back-to-back NMR measurements, as will be described in Sec 5.4.2. Next we must determine the actual flip-angle map, instead of a global flip-angle measurement, because the thermally polarized gas spans a much larger region of space than the hyperpolarized gas inside the pellet. Within that region, the coil sensitivity may vary, meaning that the actual flip-angle as seen by spins throughout the region can be substantially different. To measure the reference voltage, and consequently the actual flip-angle applied at the center of the coil, we use a 2D non-selective CSI sequence (i.e. projection), as will be discussed in Sec 5.5.2.

5.4 Thermal equilibrium measurements

In this section we present the thermal equilibrium experiment results including the flip-angle and the T_1 measurements, and the image acquired using a non-selective 3D CSI sequence. In Sec 5.4.1, we describe the non-selective 2D CSI imaging technique to acquire the flip-angle map along with the results of the flip-angle measurement. Next, in Sec 5.4.2, we discuss the NMR measurements used to determine the effective T_1 of the ^{3}He-oxygen mixture in the thermal phantom. And lastly, we describe the non-selective 3D CSI imaging technique used to acquire the image of the thermally polarized ^{3}He, and present the image in Sec 5.4.3.

5.4.1 Flip-angle measurement

The flip-angle measurement is performed to determine the scale factor between the applied coil voltage and the achieved flip-angle. Noting that the relationship between flip-angle and the applied time-integral of the voltage is linear, via the flip-angle measurement, we effectively determine the constant of proportionality between voltage and achieved flip-angle for a given voltage waveform. This will help us determine the actual flip-angle map based on the reference voltage map, which allows a reliable comparison between the signal intensity values generated by the thermally polarized ^{3}He and the hyperpolarized ^{3}He.

Contrary to the global flip angle measurement in 5.5.2, a flip angle map should be determined since the gas in the thermal phantom spans a much larger space inside the coil, and as such, the flip angle exhibits a profile with highest sensitivity at the center of the coil. To determine the flip angle map, a series of 2D CSI projection images were acquired at different voltages (Fig 5.2). Recall that the signal intensity is proportional to $\sin\theta$. For $TR \gg T_1$, a condition enforced in our measurement sequence, the intensity in a given voxel across the images in Fig 5.2 follows the same functional form as $\sin\theta$, where θ is proportional to the voltage applied to the coil.

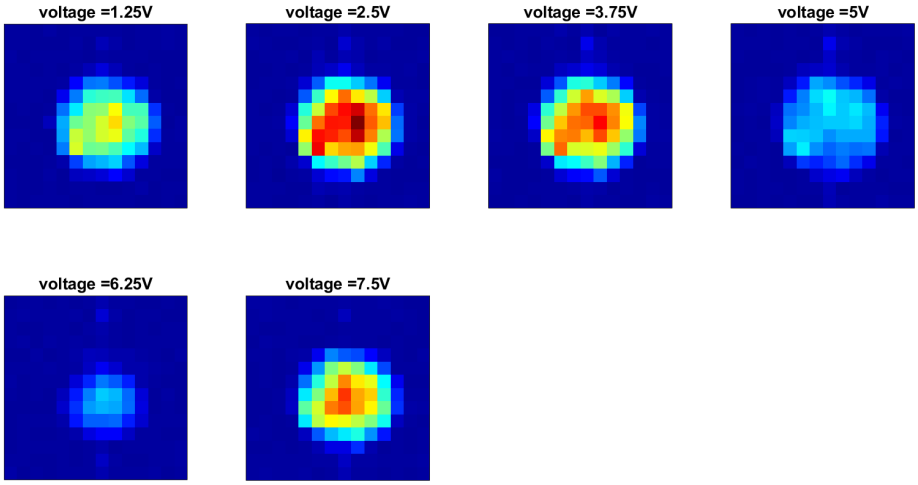

Figure 5.2: 2D CSI projection images acquired at varying voltages applied to the coil.

For this measurement, the nominal reference voltage input as a protocol parameter for the 2D CSI images is set to 6.1 V. This value is chosen somewhat arbitrarily for the following reason. The reference voltage applied to the coil depends on the loading of the coil, which alters its capacitance and impedance. For a typical loading of this particular coil, the reference voltage is known to be $\sim$ 6 V. The size of the image used for flip-angle measurement mimics that of the desired image for thermal equilibrium signal calibration, and is $14 \times 14 \times 2000$, with 2-mm resolution and 2.8 mm field-of-view (please see Sec 5.4.3 for rationale).

Reference voltage is the voltage that should be applied to the transmit coil for a 1-ms rect pulse to create a 180° flip-angle. Therefore, one can fit the signal intensity of all voxels across the images to $y = |A \cdot \sin(B \cdot \theta)|$, where zero signal is produced when the flip-angle is π produced by the reference voltage, $\mathrm{V}_{ref} = \frac{\pi}{B}$. The flip angle correction FA_{corr}^{therm} is the ratio between the nominal reference voltage and the actual reference voltage obtained from the fits in Fig 5.3. A reference voltage map can be obtained by plotting the reference voltage found in each voxel of the 2D CSI images and is given in Fig 5.4. The center of the coil appears to be at voxel

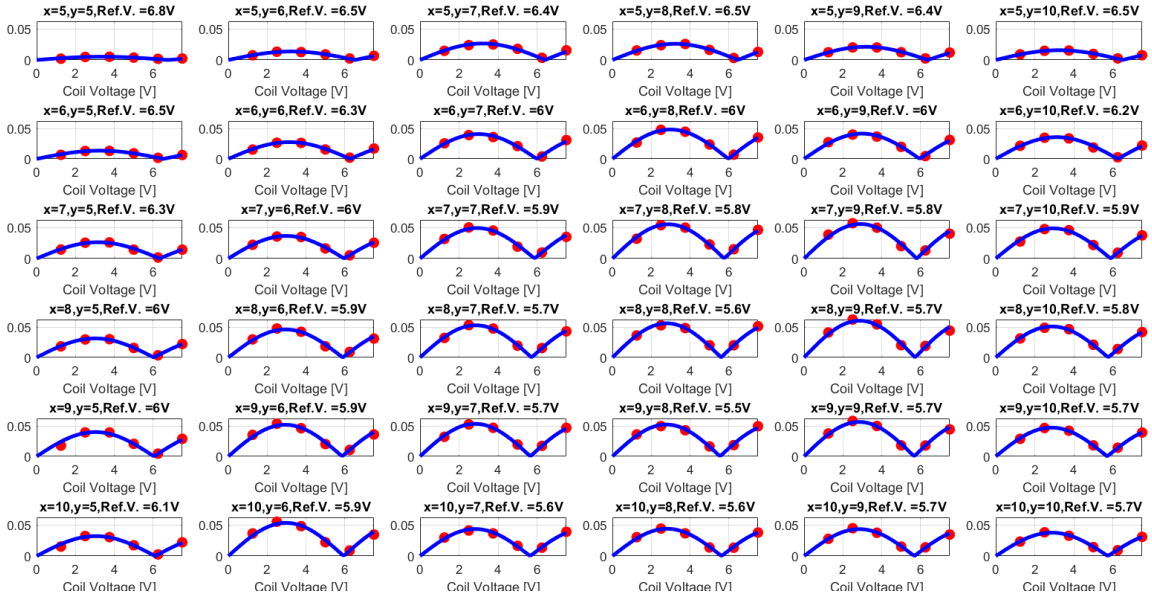

Figure 5.3: Signal response for select voxels. Each panel demonstrates the signal variation in a certain voxel as a function of voltage (i.e. the signal in the same voxel across all images in Fig 5.2). The reference voltage is the voltage that drives the signal to zero, which for most voxels near the center of the coil is ∼5.6 V. Red circles correspond to the data points and blue curves are the sinusoidal fits to the data.

$(x = 8, y = 9)$ with lowest reference voltge $V_{ref} = 5.6$ V where the coil has highest sensitivity. Therefore, the flip angle correction factor for the thermal equilibrium case is $FA^{therm}_{corr} = \frac{actual}{nominal} = \frac{5.6V}{6.1V} = 0.92$. That is to say, for the input reference voltage of 6.1 V, the nominal flip-angles setting used in our experiments would have to be multiplied by FA^{therm}_{corr} to yield the actual flip-angles as seen by the spins in the coil with the same spatial dependence (i.e."profile") as the reference voltage depicted in Fig 5.4.

5.4.2 T_1 measurement

Recall that in Sec 5.2.3, we set forth the condition $TR \gg T_1$ to derived Eq 5.25 which will be used in Sec 5.6 to extract the polarization of the hyperpolarized ^{3}He isolated in the pellet. Here we determine the effective T_1 of the thermally polarized

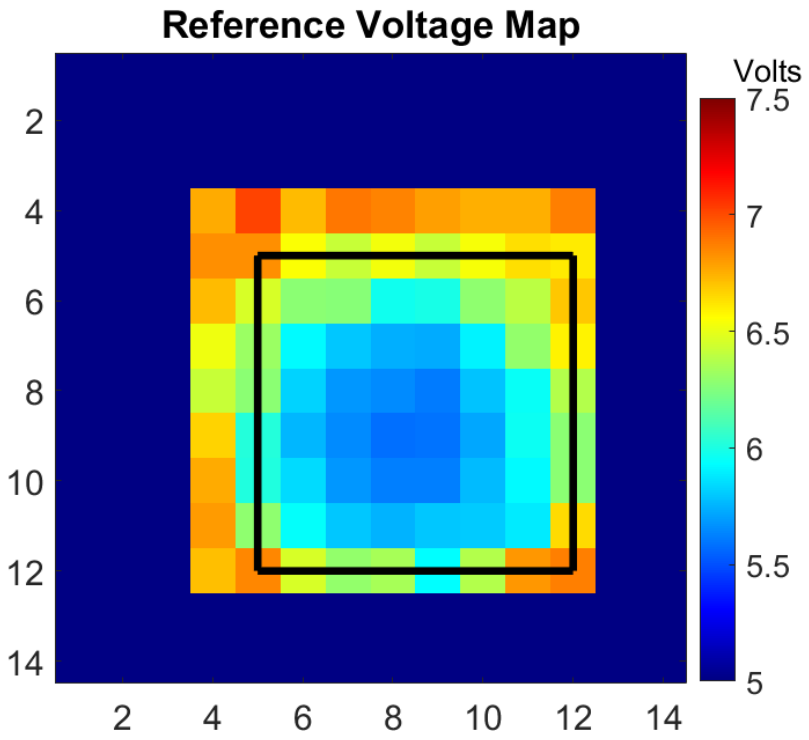

Figure 5.4: Reference voltage map (for select voxels). The reference voltage is the voltage that drives the signal to zero, which for most voxels near the center of the coil is ∼6 V. The box drawn in black is meant to demonstrate the relative position of the tube bulb in the map.

^{3}He-oxygen mixture so that the condition $TR \gg T_1$ can be faithfully satisfied when imaging the thermally polarized ^{3}He.

The steady-state signal intensity in the transverse plane is affected by the repetition time (TR), which is the time between consecutive RF pulses. One way to effectively eliminate the TR-dependence of the steady-state signal intensity is by making TR much larger than T_1. Recall that T_1 is the regrowth time constant of the longitudinal magnetization after application of an RF pulse. The T_1 of the thermally polarized gas can be determined by applying a series of back-to-back RF pulses, each followed by signal acquisition, for varying values of TR and plotting the steady-state signal as a function of TR. The relationship between steady-state signal and TR is

given by

$$S_{steadystate} = S_0(1 - e^{-TR/T1}), \tag{5.26}$$

as shown in Fig 5.5. The effective T_1 of the thermally polarized ^{3}He gas is obtained

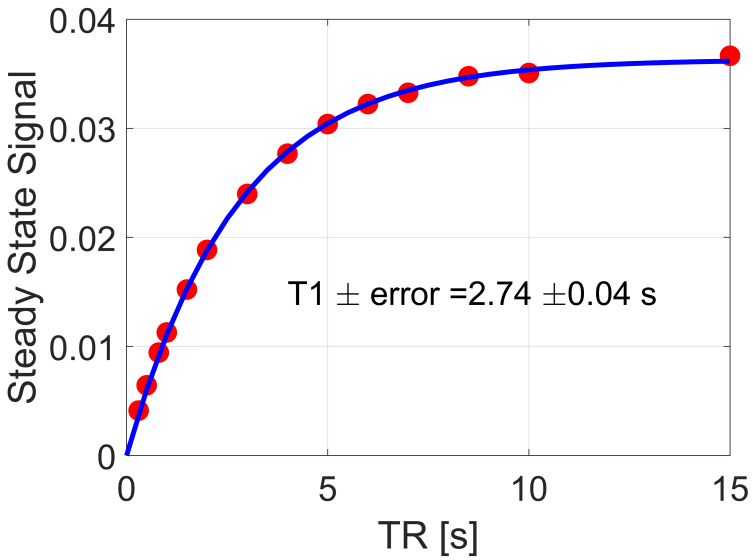

Figure 5.5: Steady-state signal as a function of TR of the thermally polarized ^{3}He-O_2 mixture (∼1 atm oxygen), from which the effective T_1 of the gas can be obtained. We refer to the T_1 measured in this experiment as *effective* because it represents the composite effect of inflow of fresh magnetization from the region of the tube outside the coil to the region of the tube at the center of the coil, and the longitudinal magnetization recovery.

from the fit to be 2.74 s ± 0.04. This value is not consistent with the expected T_1 for a phantom containing 0.912 Bar partial pressure of O_2 based on the empirical formula for longitudinal relaxation of ^{3}He in the presence of O_2 for T ≈ 200−400 K obtained by Saam [75]

$$\frac{1}{T_1} = 0.45[O_2](\frac{299}{T})^{0.42}s^{-1}/amagat. \tag{5.27}$$

At room temperature, which is the temperature at which our thermally polarized

measurements are performed, Eq. 5.27 yields $T_1 = 2.44$ s. A likely explanation for the discrepancy between the experimental measurement presented here and the empirical value is as follows. During the T_1 measurement, the diffusion of the gas introduces a constant inflow of fresh magnetization from a region of the gas in the tube that's outside the coil sensitivity range to the region of the tube that is inside the coil, and hence within the coil sensitivity range. Therefore, our measured value is better termed the *effective* T_1 as it represents the combined effects of longitudinal magnetization recovery and inflow of fresh magnetization into the region of the tube within the coil sensitivity range. The measurement of the effective T_1 here serves only one main purpose, and that is to guide us to choose a sufficiently large TR, and the exact value of T_1 is irrelevant for the purposes of thermal equilibrium calibration. Based on this T_1, the 3D CSI image of the thermally polarized gas is obtained with TR = 15 s which should well-satisfy the condition TR $\gg T_1$.

5.4.3 3D CSI image

Given the measured effective T_1 and the flip-angle map from the experiments mentioned above, we are now equipped with the necessary tools to satisfy the assumptions set forth in Secs 5.2.1 and 5.2.2, to acquire a 3D CSI image. The signal intensity of this image can be used to calibrate the hyperpolarized signal intensity of the 3D CSI image, which will be presented in Sec 5.5.3, to reliably compute the absolute polarization of the hyperpolarized ^{3}He sealed inside the pellet.

Recall that for this image, tube V8c charged with thermally polarized ^{3}He and oxygen is used with the same coil and Styrofoam coil housing as used in permeation measurements. Tube V8c, a newer version of our tube designs, has a near-spherical shape at the bottom, with approximate inner diameter of 18 mm. Recall from Sec 2.3.3 of Chapter 2, that phase-encoding is prone to aliasing without sufficient field-of-view to encompass all of the excited spins. To avoid aliasing, a 14×14×14×2000 matrix size image ($k_x \times k_y \times k_z \times time$) with 2-mm resolution is acquired, resulting in isotropic

field-of-view of 2.8 cm. This field-of-view should be robust against any excited magnetization at the stem of the tube getting "folded" back onto the image, granted that the coil sensitivity extends out the the edge of the coil form.

The actual flip-angle applied at the center of the coil is 82.6° (for a nominal setting of 90°). The repetition time between RF pulses, TR, is chosen to be 15 seconds, such that the condition $TR \gg T_1$ is satisfied (we measured effective T_1 to be 2.74 s). Recall that effectively, this condition eliminates the TR-dependence of the steady-state signal in the thermally polarized ^{3}He image, which will be used in Sec 5.5.3 to calibrate the pellet signal for absolute polarization extraction.

The 3D CSI image of the thermally polarized gas is obtained similar to that of the hyperpolarized gas inside the pellet (Sec 5.5.3), which is by taking the four-dimensional discrete Fast Fourier Transform of the data. Recall from Sec 2.6 of Chapter 2 that iFFT in first 3 dimensions resolves the spatial information, while the FFT in the fourth dimension transforms the temporal profile to the frequency spectrum. The frequency spectrum at each voxel can then be fit to a complex Lorentzian function, where the parameter representing the fitted area is assigned as signal intensity to each respective voxel.

There are four parameters to the fit: 1) phase which determines the relationship between the real and the imaginary channels of the complex data, 2) area under the curve (AUC) which determines the signal strength, 3) the inverse of the width of the frequency distribution T_2^*, which is indicative of the frequency spread of the spin population, and lastly 4) the frequency offset f_0. Depicted in Fig 5.6 are the central view of the coronal (left), sagittal (middle), and transverse (right) slices of the fit parameters 1) image, 2) phase, 3) T_2^*, and 4) f_0, from top row to bottom row, respectively.

Note that apart from frequency drift along the static field direction (i.e. vertical axis in coronal and sagittal images, or the X axis in the used convention), and the image intensity variations, no observable spatial dependence is present in other fit

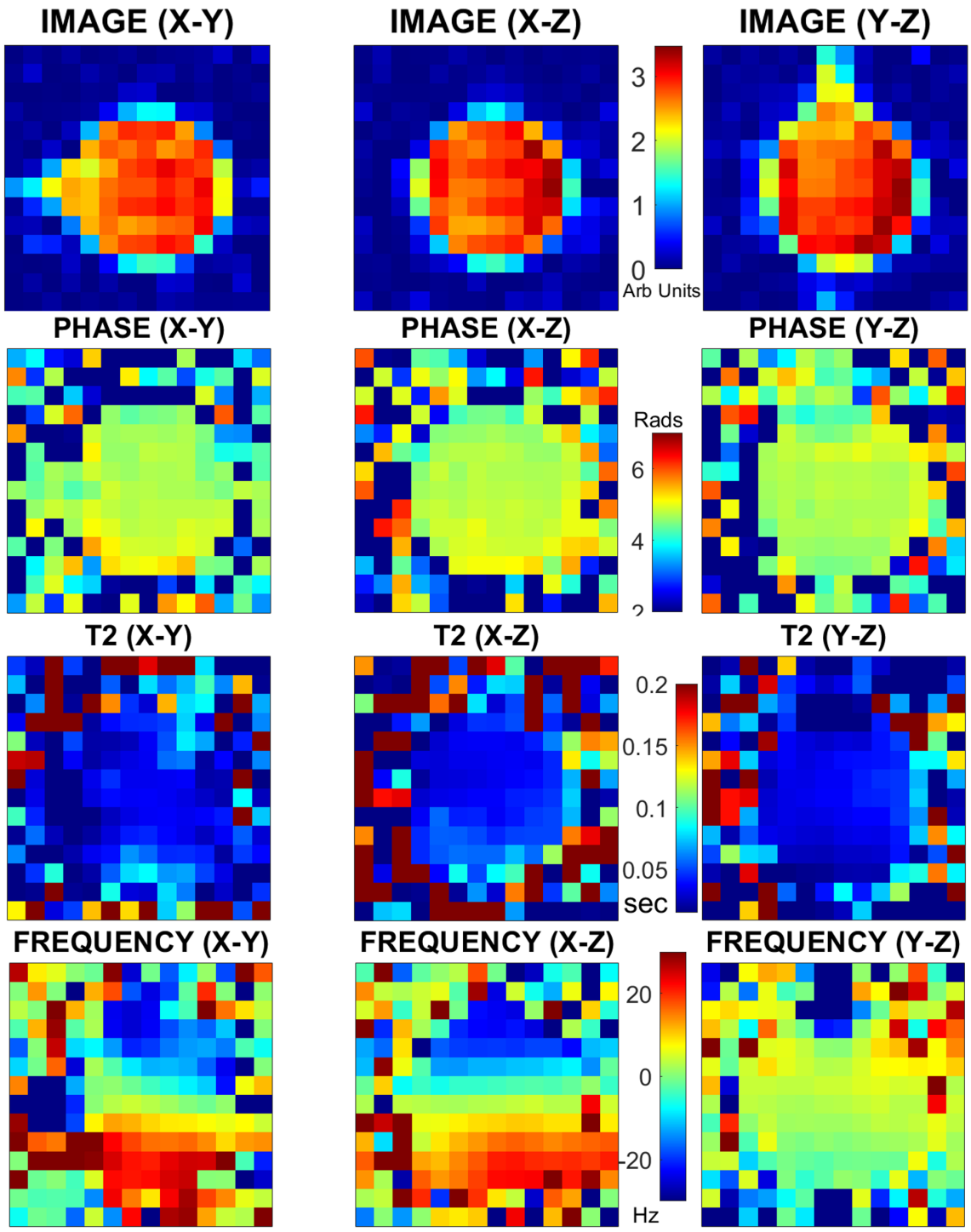

Figure 5.6: 2D cross-sectional coronal, sagittal, and transverse maps of the Lorentzian fit parameters obtained from 3D CSI data of the thermally polarized ^{3}He. Top to bottom: image, phase, T_2^*, and f_0. Left to right: Coronal, sagittal, and transverse views. Note that apart from frequency drift along the static field direction (i.e. vertical axis in coronal and sagittal images, or the X axis in the used convention), and the image intensity variations, no observable spatial dependence is present in other fit parameters.

parameters.

In summary, the voxel signal intensities of the image in Fig 5.6 are obtained from fitting the spectra to a Lorentzian function. In Sec 5.6, we use the mean of representative voxel signal intensities as S_{pol} in Eq 5.25 to extract the absolute polarization of hyperpolarized ^{3}He sealed in the pellet.

5.5 Hyperpolarized measurements at 77 K

Within this section is laid out the experimental procedure and the results of an image of the hyperpolarized ^{3}He gas that can be directly calibrated to the image of the thermally polarized ^{3}He gas obtained in Sec 5.4.3. Equation 5.25 can then be invoked to extract the absolute polarization of ^{3}He isolated in the pellet at 77 K, using the voxel signal intensities obtained in the two images.

First, in Sec 5.5.1 we describe the experimental procedure that is common to all hyperpolarized imaging experiments presented within the next few sections. Next, in 5.5.2 we report the exact flip angle used in the CSI image. Then in 5.5.3, we show two sets of 3D CSI images of hyperpolarized ^{3}He gas isolated inside the pellet at LN_2 temperature. We then determine the T_1 decay of the polarization of the gas sealed inside the pellet in 5.5.4. A phenomenon that contributes immensely to the polarization decay, and is particularly of interest for our application, is presence of magnetic field gradients and field inhomogeneity. In 5.5.5, the polarization loss while traversing the magnetic field gradient of the scanner is presented for a tube containing hyperpolarized ^{3}He at room temperature, and an isolated pellet containing hyperpolarized ^{3}He at 77 K.

5.5.1 Experimental procedure

The hyperpolarized measurements presented herein, with the exception of the field gradient-induced polarization loss measurement at room temperature, share the same

experimental procedure. Additionally, much of the experimental apparatus and setup is identical to the permeation measurements presented in Chapter 4. Specifically, hybrid-alkali SEOP polarizer is used to polarize the gas to $\sim$ 48%, and the same hyperpolarized gas dispense mechanism and procedure is used for the absolute polarization, flip-angle, and T_1 measurements. Additionally, similar to the permeation measurements presented in Chapter 4, a Borosilicate tube is used to permeate hyperpolarized ^{3}He into the pellet.

In this experiment, tube V10 with GDP 10-23-4b pellet resting on top of a 3-mm Pyrex bead at the bottom of the tube was used to load the pellet with hyperpolarized, high pressure ^{3}He. The tube was filled with 6.016 bar of ^{3}He gas believed to be hyperpolarized to $\sim$48%. Once inside the scanner, the valve connecting the antechamber and the tube was opened to submerge the pellet with high pressure gas. Precisely after 10 min ($1.881\tau_{perm}$), which is believed to be the approximate time that maximizes the polarization inside the pellet (balancing the fight between fresh polarization inflow and polarization decay), the liquid nitrogen bath surrounding the bottom of the tube was filled with LN_2, and for maintaining the LN_2 temperature, the bath was topped off every 45 min. The tube was then pumped to empty the gas outside the pellet, after about 5 min to allow liquid nitrogen to stabilize. That was done by a long tube, which was connected to the vacuum pump of the polarizer system, attached to the glass tube inside the scanner. Once the glass tube was immersed in liquid nitrogen, the valve of the glass tube to the vacuum was opened to empty the gas outside the pellet.

At this point, a 3D CSI sequence (Fig 5.8) was used to acquire an image of the polarized gas "frozen" and sealed inside the pellet, that is isolated in vacuum. Immediately after the image, the T_1 measurement commenced where we perform NMR measurements every $\sim$45 min to track the signal intensity as a function of time, for $\sim$ 11 hours. At the end of this time, we acquire a second image of the hyperpolarized gas using exactly the same 3D CSI sequence and protocol parameters

(e.g. flip-angle, TR, etc.). Next, a flip-angle measurement is done to determine the actual flip-angles used for the T_1 and absolute polarization measurements. And lastly, we seek to determine the degree of polarization loss experienced by the gas inside the pellet as it traverses through the field "gradients" of the scanner away and toward the center of the scanner bore. Here, the "gradients" refer to the rapid change of field at the bore opening (and not the imaging gradients), created by the field quickly dropping from 1.5 T at the center of the bore to near zero outside. The tube is mounted in the styrofoam holder, which is taped to the scanner table, and the setup is slid in and out of the magnet bore smoothly using the scanner's motorized system. Therefore, a series of NMR measurements were performed before and after a "round trip" travel, in which the pellet is moved along the axis of the scanner out of the bore, and back into the center of the scanner, to determine the field gradient-induced rapid longitudinal spin-relaxation of ^{3}He. To compare this polarization loss in gas isolated inside the pellet at 77 K, and polarization loss of hyperpolarized ^{3}He at room-temperature inside the tube, the following measurement was performed.

On a separate imaging session, the same tube charged with hyperpolarized ^{3}He was imaged prior and after a round trip travel. A 2D slice-selective CSI sequence was used to acquire the images to determine the signal intensity of the gas before and after the round trip travel through the same field gradients, to determine the polarization loss of hyperpolarized ^{3}He in the tube at room temperature.

5.5.2 Flip-angle measurements

For a accurate calibration of hyperpolarized ^{3}He signal to thermally polarized ^{3}He signal using Eq 5.25, an exact flip-angle measurement must be performed, similar to Sec 5.4.1. That's because, to reiterate, the magnitude of the precessing transverse magnetization as a result of an RF pulse, and the signal it generates, is proportional to $\sin\theta$, where θ is the flip-angle. The remaining longitudinal magnetization, denoted by M^+, which starts regrowing to the thermal equilibrium magnetization M_0 immediately

after excitation, is given by

$$M^+ = M^- \cos\theta, \tag{5.28}$$

where M^- is the longitudinal magnetization right before excitation. Now consider starting magnetization $M(0) >> M_0$ for a sample of hyperpolarized ^{3}He. If N RF pulses all with the same flip-angle θ are applied back-to-back, the remaining longitudinal magnetization after the N^{th} RF pulse is

$$M_N^+ = M(0)\cos^N\theta. \tag{5.29}$$

We design our flip-angle measurement based on Eq 5.29, where we apply a series of RF pulses, each followed by signal acquisition (i.e. NMR or "ping" measurements). Plotting the signal as a function of number of RF pulses, N_{RF}, and fitting it to

$$S(N_{RF}) = S_0\cos^{N_{RF}}(FA_{corr}^{pol}\cdot\theta_{nominal}), \tag{5.30}$$

we determine the flip-angle, θ, as seen by the spins that were excited and knocked onto the transverse plane. Here there are two fit parameters, one is S_0 which represents the signal after the very first excitation, and the other is FA_{corr}^{pol} which represents the flip-angle correction factor, such that the actual flip-angle as seen by the spins at the center of the coil is $\theta = FA_{corr}^{pol}\cdot\theta_{nominal}$.

The following measurements are done by applying 1000 and 2000 RF pulses using a nominal flip-angle setting of 1.5° and 1°, respectively (Fig 5.7). For these measurements, the nominal reference voltage, which is the voltage applied to the coil for 1 msec using a rect pulse to produce a 180° flip angle, is set to 5.8 V. The correction factor extracted from both measurements yield the same result, which is encouraging. Namely, $FA_{corr}^{pol} = 1.17/1.5 = 0.78/1 = 0.78$. Hereafter, FA_{corr}^{pol} will be applied to all flip-angles used for images/pings of the hyperpolarized gas in the presence of LN_2, and the actual (corrected) flip angles will be reported only.

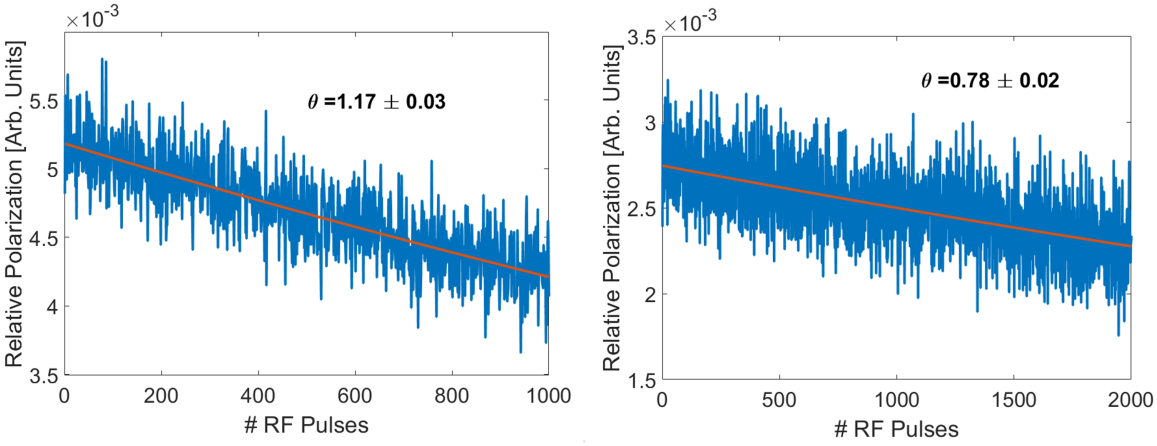

Figure 5.7: Global flip-angle measurements for nominal flip-angles of 1.0° and 1.5° in hyperpolarized ^{3}He. This is a precise way of determining the actual flip-angle the coil produces which can often be different from nominal values depending on the loading of the coil, and the reference voltage set as a protocol parameter.

5.5.3 3D CSI image

In this section, we describe the 3D CSI imaging sequence, the analysis of the CSI data, and the resulting images obtained of the permeated hyperpolarized ^{3}He gas sealed inside the pellet. The signal intensity of the image acquired here will be used in Eq 5.25 to extract the absolute polarization of the gas inside the pellet at 77 K.

Recall from Sec 5.5.1 that for the absolute polarization and T_1 measurements, tube V10 is charged with 6.016 bar of hyperpolarized ^{3}He and taken to the center of the scanner for image acquisition. Once inside the scanner, the ante-chamber valve is opened to immerse the pellet, which up until now was at vacuum, in high-pressure and hyperpolarized ^{3}He to begin the permeation process. The permeation time constant of the GDP 10-23-4b pellet used here is $\tau_{perm} = 319$ s. After 10 min, the bottom of the tube which sits at the liquid nitrogen bath is filled with LN_2 to cool the pellet, and seal in the permeated gas. Therefore, $\rho_{pol} = (1 - e^{-600/319}) \times 6.016$ bar $= 5.099$ bar is built up inside the pellet, prior to cooling to 77 K. Since the walls of the pellet will essentially become impermeable to ^{3}He at LN_2 temperature, the density inside the pellet remains the same throughout the remainder of the experiment.

There are two main measurements carried out after isolating the permeated gas inside the pellet: 1. acquiring a 3D image of the gas inside the pellet to determine its absolute polarization by comparing it with calibration image of the thermally polarized phantom, and 2. measuring the T_1 of the gas inside the pellet at LN_2 temperature to demonstrate potential feasibility for cryogenic injection into the tokamak plasma. Here we focus on the 3D image.

We use a non-selective 3D chemical shift imaging (CSI), or fully phase encoded, pulse sequence to acquire the images. A schematic diagram of the 3D CSI pulse sequence is given in Fig 5.8. In each repetition time (TR) of the pulse sequence,

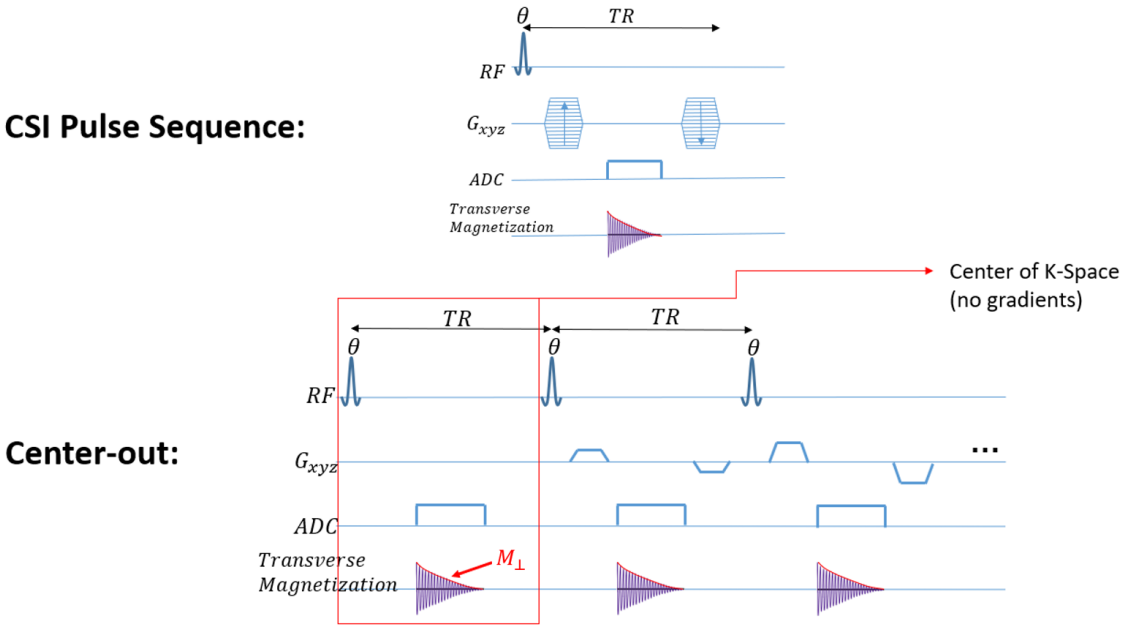

Figure 5.8: Top: A typical CSI acquisition. Bottom: The center-out CSI acquisition used in our experiment. The only difference between the two sequences is the order in which the gradients are applied. $M_\perp$ is the demodulated transverse magnetization. Although not shown here, constant spoiler gradients were applied immediately before each excitation RF pulse.

after application of an RF pulse, combination of gradients in x, y, and z direction are applied to move k-space acquisition voxel from the center to the desired location, and acquire precessing signal during the analog to digital converter (ADC), and then

applying the same gradients with opposite polarity to return to the center of k-space. We use a center-out CSI pulse sequence for the following reason. The excitation RF correction factor $\cos^{-n}\theta$ is applied to each k-space sample to compensate for the magnetization loss and its effects on the reconstructed image intensity. The center-out pulse sequence ensures that the correction factor is smallest at the most important k-space locations (aggregated near the center of k-space) that determine the image intensity, so the effect of imperfections is suppressed. The signal in the central k-space voxel of the 3D CSI data set of the pellet along with its Fourier Transform is given in Fig 5.9.

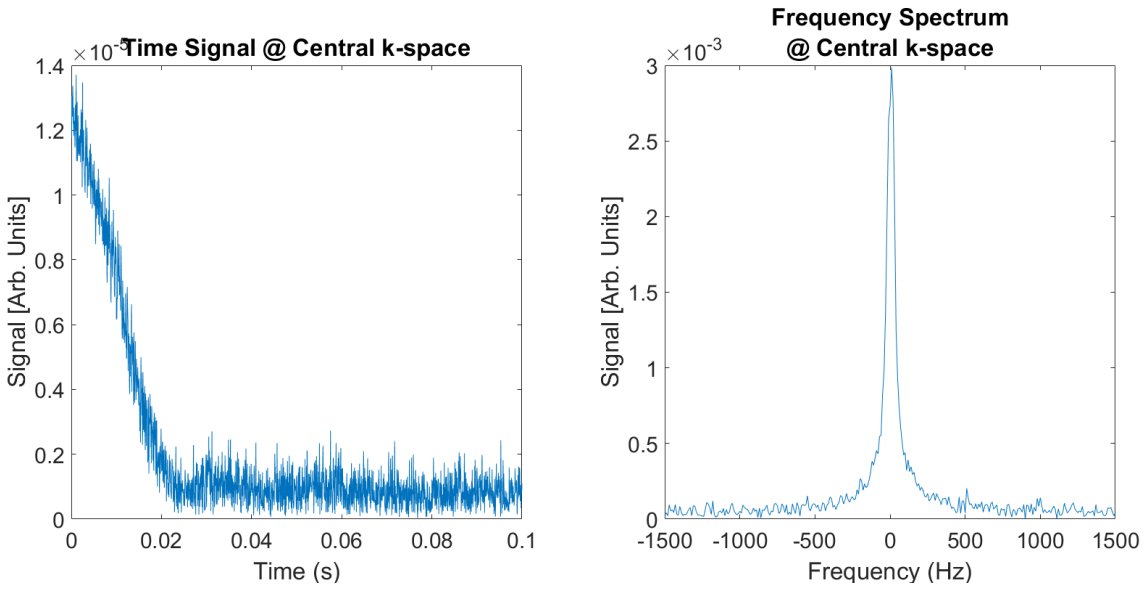

Figure 5.9: Central k-space voxel signal over time and its frequency response (Fourier Transform of the time domain). Note the absence of coherent oscillations in the time-signal, which in frequency spectrum corresponds to a distribution of frequencies that can be estimated with a single Lorentzian function.

Two datasets of the hyperpolarized ^{3}He gas inside the pellet were acquired with matrix size $10 \times 10 \times 10 \times 2000$ and 0.5 mm spatial resolution using the center-out pulse sequence, about 11 hours apart. The first three dimensions of the raw data for each one of these images correspond to the k-space x, y, and z coordinates and the last

dimension contains the temporal profile of the signal at those k-space coordinates. There are several ways of analyzing this dataset to represent the spatial intensity map (i.e. the image). All methods, however, include taking the inverse Fourier Transform of the data in the first three dimensions to resolve the spatial distribution of the signal intensities and similarly taking the Fourier Transform of the data in the fourth dimension to obtain the frequency spectrum of the signal in each image voxel (see Sec 2.6). One way to represent the image is demonstrated in Fig 5.10 which shows the first 3D image of the polarized gas in the isolated pellet where each image voxel intensity is plotted as the maximum value of the frequency spectrum at that voxel.

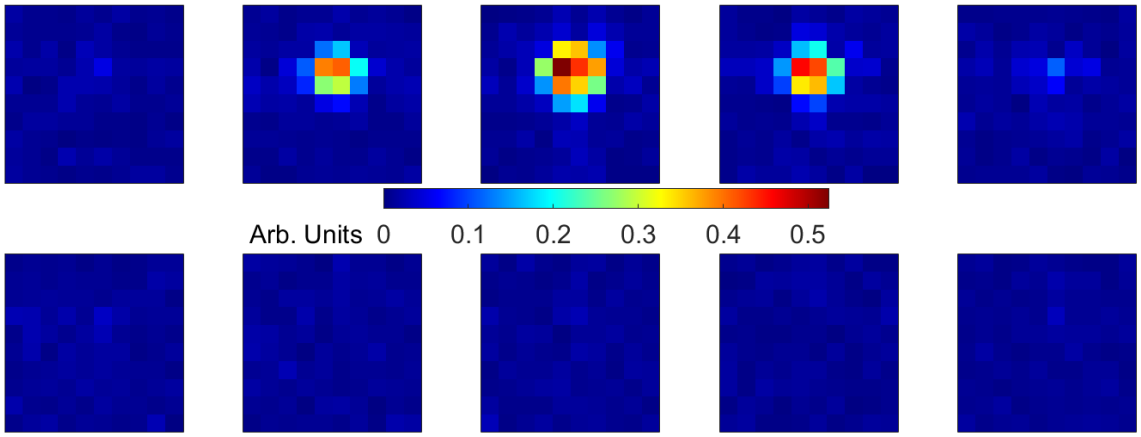

Figure 5.10: Cross-sectional views of the 3D image from one end to the other. This is the first 3D image of the hyperpolarized gas inside the pellet at LN_2 temperature acquired right after pumping out the gas in the tube surrounding the pellet. The image voxel intensity is the maximum value of the frequency spectrum at each voxel.

A more robust way of analyzing the data, however, is by fitting each voxel's frequency spectrum to a complex Lorentzian, where the fit-parameter that represents the area under the curve (AUC) of the fit, is assigned as signal intensity to the respective voxel. An example of a single complex Lorentzian fit is given in Fig 5.11.

Plotting the image voxel intensity as the area under the fits of the frequency spectra for each voxel in the 3D datasets, Fig 5.13 shows central cross-sections of the

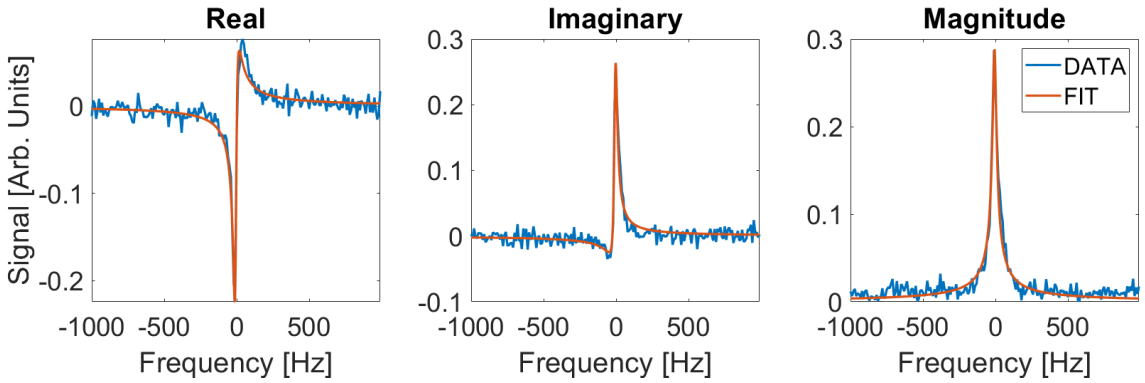

Figure 5.11: An example of a complex Lorentzian fit to the real and imaginary parts of the frequency spectrum as well as the magnitude in a representative voxel.

two images (transverse, coronal, and sagittal), one taken immediately after pumping out the gas inside the tube, and one after the conclusion of the T_1 measurement, ∼11 hours later. A 'pellet mask' is obtained by including all the voxels with pellet signal in them using the geometry of the pellet with respect to the voxels as shown in Fig. 5.12 and applied to both 3D CSI images in Fig 5.13. Notice that there are only $2^3 = 8$ voxels entirely encapsulated by the pellet and $4^3 = 64$ voxels with any pellet signal in them. It is noteworthy here to mention that one of the properties of the Fourier Transform is that the application of a linearly increasing phase shift in one domain creates a spatial shift in the other. The phase shift in all three dimensions can be applied as

$$k_{jp\epsilon}^{new} = k_{jp\epsilon} e^{i(j\eta_j + p\eta_p + \epsilon\eta_\epsilon)}, \tag{5.31}$$

where $k_{jp\epsilon}$ is the k-space complex amplitude at the k-space coordinates j, p, and ϵ, and η_j, η_p, and η_ϵ are the slopes of the linearly increasing phase along j, p, and ϵ coordinates, respectively. By applying a phase shift across all three dimensions as in Eq. 5.31, with the appropriate ϕ_j, ϕ_p, and ϕ_ϵ, both 3D CSI images were shifted such that their signal intensity is centered at the center of the spherical mask (i.e. pellet) in Fig 5.12.

Both images have been corrected for the polarization loss due to application of

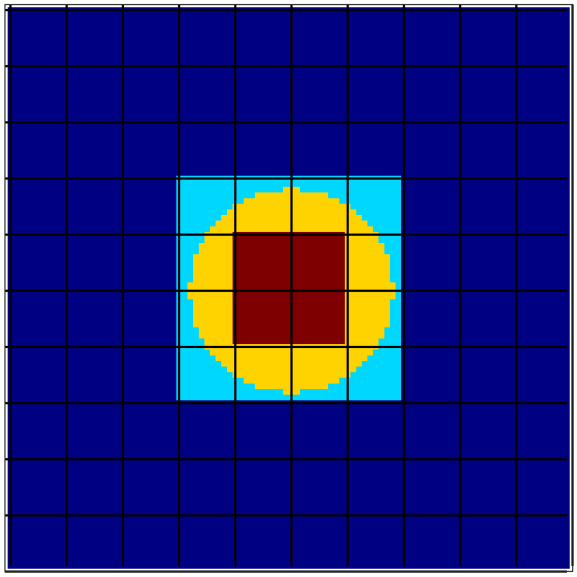

Figure 5.12: Central cross-sectional view of the pellet geometry. The circle has a radius of 0.91 mm and each voxel is 0.5 mm cubic in size. Notice that there are only $2^3 = 8$ voxels entirely encapsulated by the pellet and $4^3 = 64$ voxels with any pellet signal in them. The pellet mask is the square color-coded in blue.

1000 RF pulses, each with flip-angle of 1.17°, to acquire the image. The average intensity of the second image is $(24.9 \pm 1.6)\%$ lower than that of the first image (sum of all signal is 859.5 arb. units ±5.1 and 645.4 arb. units ±9.9 for the first and second image, respectively). This is somewhat consistent with the polarization loss due to the T_1 measurements (ping RF pulses applied to measure T_1 depolarizes some gas), and the T_1 decay of the polarization over the course of 11 hours (5.5.4). The T_1 measurement consisted of a total of 680 RF pulses each at $\theta = 0.78° \pm 0.02$ (nominal $\theta = 1°$), yielding to polarization loss of 6.20% ±0.01, and the T_1 decay in 11 hours assuming the measured T_1 = 83.5 hours ±10.0 amounts to a $12.3\% \pm 1.4$ polarization loss. Additionally, if the second image was acquired immediately after the first one, it would theoretically be $L = 1 - \cos^{1000}(1.17) = 18.8\% \pm 0.01$ dimmer than the first one. Therefore, the cumulative polarization loss amounts to $L_c = (100\% - 18.8\%) \times (100\% - 12.3\%) \times (100\% - 6.2\%) = 33.2\% \pm 7.6$ vs. the measured polarization loss based on the two 3D CSI images of $24.9\% \pm 1.4$ (see the following

subsection 5.5.3.1 for error propagation). It is evident that the error bars in the theoretical calculation and experimental measurement of polarization loss between the two images overlap, and the two values are not inconsistent.

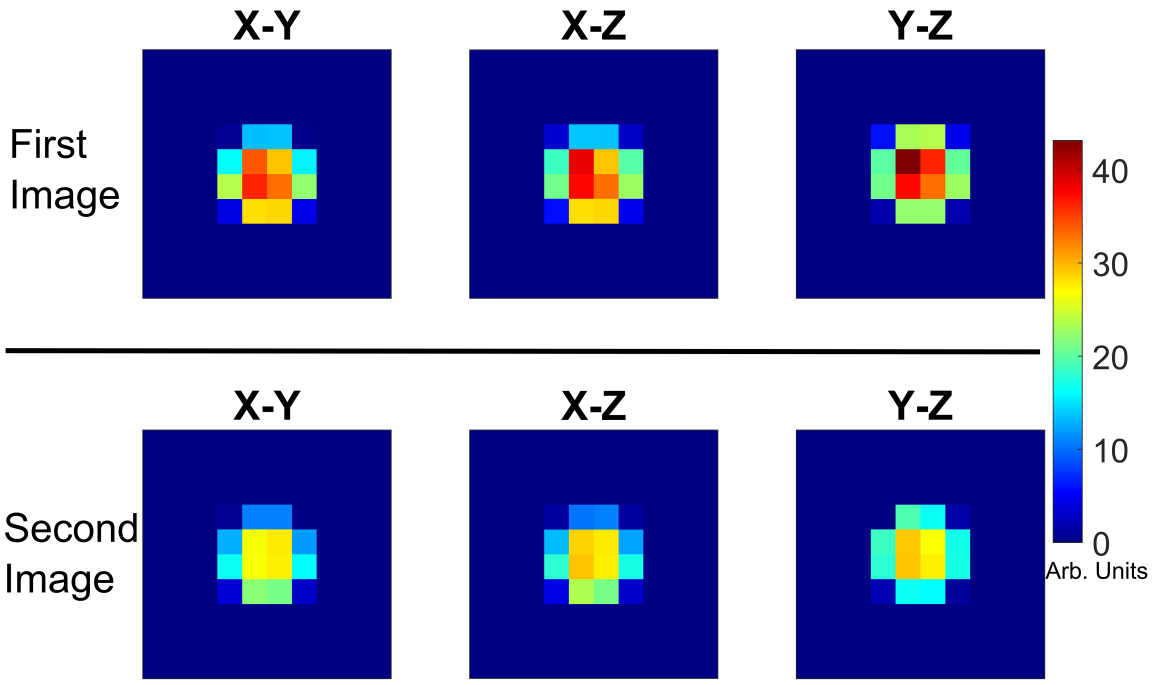

Figure 5.13: Central cross-sectional images (transverse, coronal, sagittal) of the two 3D CSI image sets acquired 11 hours apart (top-row and bottom-row are first and second image sets, respectively). Both images are corrected for RF loss during the acquisition of each image. On average, the second image is $24.9\% \pm 1.4$ dimmer than the first image. Both rows share the same color scale. The pellet mask in Fig 5.12 is applied to both images.

There are two notable differences between the 3D CSI imaging sequence used to image the thermally polarized gas in tube V8c, and the one used to image the hyperpolarized gas sealed in the pellet in tube V10. First, the voxel sizes are different. This can simply be accounted for by scaling the signal intensities with the voxel volumes. Second, the sequence used in Sec 5.4.3 is not a center-out one, but that doesn't matter since $TR \gg T_1$ and so each RF pulse produces the same signal intensity in the transverse plane. These differences are all tractable and can be easily accounted

for in image post-processing, as done in Sec 5.6 to invoke Eq 5.25 to calculate the absolute polarization of the permeated ^{3}He sealed in the pellet at 77 K.

5.5.3.1 Error propagation for the components of polarization loss

The error propagation for x in $f = A\cos(Bx)$ is given by:

$$\sigma_f \approx |AB\sin(Bx)\sigma_x|. \tag{5.32}$$

On the other hand, the error propagation for x in the exponential form $f = Ax^B$ is given by:

$$\sigma_f = fB\frac{\sigma_x}{x}, \tag{5.33}$$

The error for polarization loss $L = 1-\cos^{680}(0.78°)$ is the following: From Eq. 5.32 we can write $\sigma_{\cos\theta} = \sin x\sigma_x = 4.752e{-}6$, and from Eq. 5.33 we can write $\sigma_L = 6.2\% \times 680 \times \frac{4.752e-6}{0.999} < 0.1\%$. Similarly, the error for polarization loss $L = 1-\cos^{1000}(1.17°)$ is the following: From Eq. 5.32 we can write $\sigma_{\cos\theta} = \sin x\sigma_x = 1.069e{-}5$, and from Eq. 5.33 we can write $\sigma_L = 18.8\% \times 1000 \times \frac{1.069e-5}{0.999} = 0.1\%$.

The error propagation for multiplication/division of the form $f = \frac{x}{y}$ is given by

$$\sigma_f = f\sqrt{(\frac{\sigma_x}{x}^2 + \frac{\sigma_y}{y}^2)}. \tag{5.34}$$

From Eq. 5.34 the error in the fractional polarization $\frac{645.4}{859.5} = 24.9\%$ is $\sigma = 24.9 \times \sqrt{(\frac{5.1}{859.5}^2 + \frac{9.9}{645.4}^2)} = 1.4\%$. Similarly, the large error in the cumulative polarization loss due to imaging (1000 RF pulses at 1.17°), 680 ping RF pulses for T_1 measurement, and T_1 decay $L_c = (100\% - 18.8\%) \times (100\% - 12.3\%) \times (100\% - 6.2\%)$ is give by Eq. 5.34 as $\sigma_{L_c} = (1-0.188)\times(1-0.062)\times(1-0.123)\times\sqrt{(\frac{0.01}{18.8}^2 + \frac{0.01}{6.2}^2 + \frac{1.4}{12.3}^2)} = 7.6\%$.

Finally, the error in polarization loss due to the T_1 decay over the course of $t = 11$

hours with decay time constant $T_1 = 83.5$ hour ± 10.0 in $L_{T_1} = 1 - e^{-\frac{t}{T_1}}$ is given by

$$\sigma_{L_{T_1}} = \frac{t \cdot e^{-\frac{t}{T_1}} \cdot \sigma_{T_1}}{T_1^2} = 1.4\%. \tag{5.35}$$

5.5.4 ^{3}He longitudinal spin-relaxation

Here we focus on the ^{3}He longitudinal spin-relaxation measurement. Immediately after acquiring the first 3D CSI image of the isolated gas sealed in the pellet, a series of NMR measurements were performed to determine the T_1 of the hyperpolarized ^{3}He gas inside the pellet at LN_2 temperature. In this measurement, to achieve higher signal-to-noise ratio (SNR), a block of consecutive ping measurements were performed, each block of measurements spaced $\sim$45 minutes apart. After completion of each measurement series, the liquid nitrogen bath was refilled to maintain the bottom of the tube, where the pellet is located, at 77 K during the experiment.

At each time point, the ping measurements consisted of either 10 or 50 consecutive individual pings. The complex frequency spectra obtained from the pings were averaged resulting in a mean complex frequency spectrum. The first 8 data points were acquired using 10 NMR measurements, followed by 6 data points each with 50 consecutive measurements. Our decision to change to 50 pings mid-way through the experiment was to reduce measurement noise after some real-time preliminary analysis. Real, imagingary, and magnitude of the mean spectra of the 14 data points are shown in Fig 5.14. Note the reduced noise in the last 6 data points, compared to the first 8.

These frequency spectra were then fit to a complex Lorentzian and the area under the curve (AUC, which is a fit parameter) obtained from each fit was used to track the strength of the signal, which is proportional to the polarization of the gas, over time. The relative signal strength was monitored over the span of 11 hours as shown in Fig 5.17a. Since each RF pulse depolarizes a portion of the gas, a correction factor for each data point should be applied to account for the polarization loss, depending

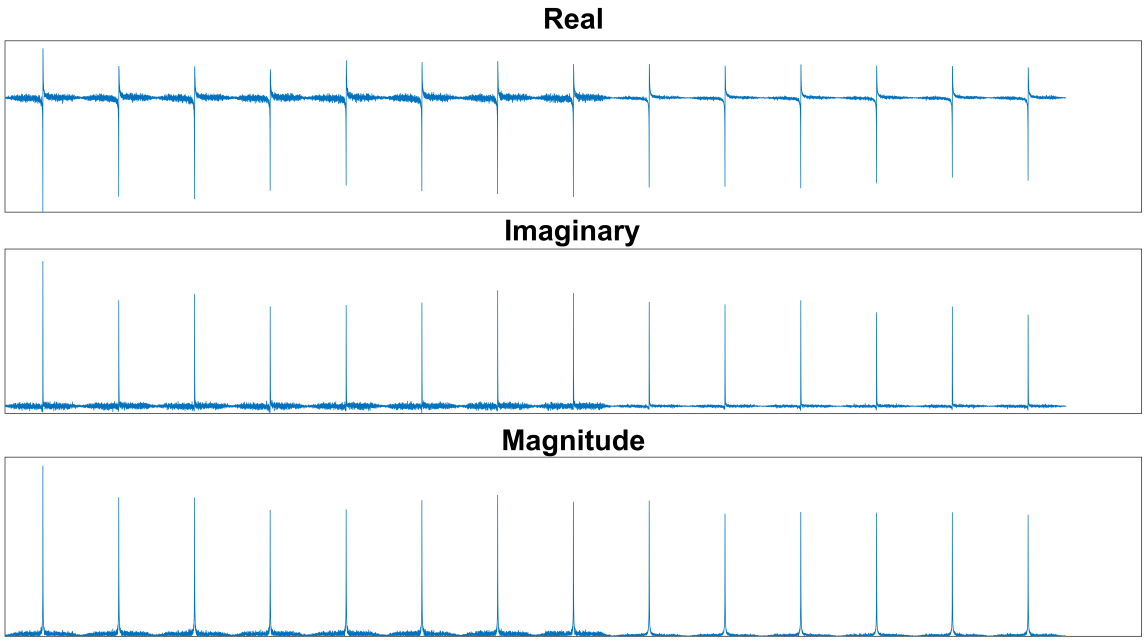

Figure 5.14: Real, imaginary, and absolute value of the mean frequency spectra obtained from NMR measurements for determining the longitudinal spin-relaxation of hyperpolarized ^{3}He sealed inside the pellet. Each spectrum is consists of either 10 or 50 frequency spectra average in complex form. Note the reduced noise level in the last 6 measurements compared to the first 8.

on the number of RF pulses and their flip-angles. Fig 5.17b shows the T_1 curve corrected for the RF loss for each measurement. The corrected T_1 is 83.5 hours $\pm$ 10.0.

5.5.5 Polarization loss through rapid field gradient of the scanner

It has been shown that the presence of magnetic field gradient and field inhomogeneity is depolarizing [74, 82–84]. A relevant depolarizing mechanism in our experiments is travel through field gradients and inhomogeneities. For example, transporting the tube charged with hyperpolarized ^{3}He from the polarizer room to the scanner room, and more importantly through the sharp field gradients at the bore opening of the

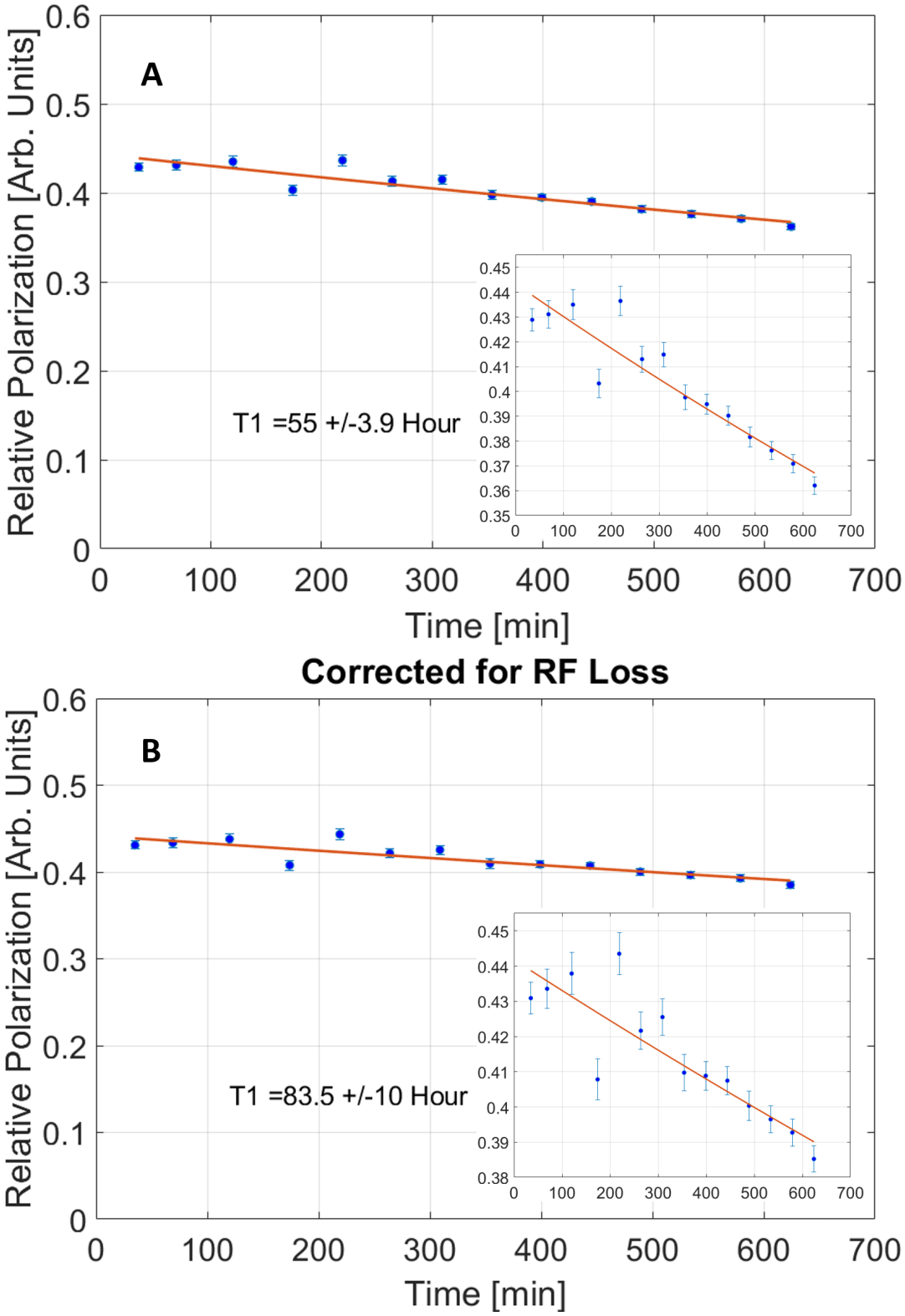

Figure 5.15: A) Uncorrected and B) corrected T_1 curves of the hyperpolarized gas inside the pellet at 77 K. The inset figures in each plot replicate the same figure but with zoomed-in y-range to show the dynamic range of the measured values. Error bars represent measurement error of each data point obtained from fitting the mean of the spectra to a single Lorentzian function, and the red curve is the exponential fit.

scanner into the magnet, are depolarizing steps inherent to our experiment design. As such, in this section, we measure and report the polarization loss arising from a round trip travel starting from the center of the magnet, out of and back into the bore. This is achieved by making a signal measurement prior to the round trip travel, and repeating the measurement after completion of the travel.

We first measure polarization loss of hyperpolarized ^{3}He inside the tube at room temperature undergoing a round trip travel out of and back into the scanner. In this experiment, a slice-selective 2D CSI image of polarized gas inside a typical tube, which is used to load the pellets, is acquired before and after sending the table out and back into the scanner. To acquire the image from the 2D CSI data set, similar to Chapter 4, we obtain AUC from the Lorentzian fits of the frequency spectrum in each voxel, and assign the AUC as signal intensity to the respective voxel. Fig 5.16 depicts the depolarization phenomena caused by the gas traversing the steep field gradient of the scanner at room temperature in two separate experiments (i.e. two separate image sets). The time elapsed between the first round trip image set is 132 s, the time elapsed between the second round trip image set is 371 s.

The measured polarization loss is $13.8\% \pm 0.5$ and $25.3\% \pm 0.5$ for the first and the second image sets, respectively. It is believed that for the first image set (i.e. I1 and I2 images), the table was maintained inside the scanner after the round trip, which implies that the tube was at or near the iso-center of the scanner. For the second image set, however, most of the time spent between the image taken before and image taken after the round trip, the table is believed to have been outside the scanner, prolonging exposure of the gas inside the tube to the steep field gradients order-of-magnitude smaller magnetic field outside of the magnet bore. This inconsistency between the measurement procedure in the two experiments may explain the discrepancy between the first and the second image sets (i.e. I1 & I2 set, and I3 & I4 set).

In the same imaging session where we acquired the 3D CSI images of the pellet gas in Sec 5.5.3, and performed the T_1 measurement in Sec 5.5.4, we also made

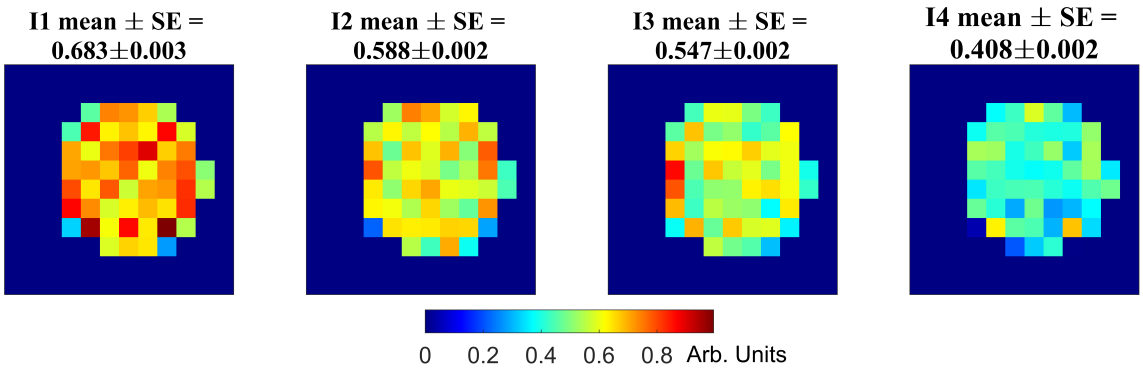

Figure 5.16: Slice-selective 2D CSI images of a tube containing hyperpolarized ^{3}He acquired before and after cycling the scanner table out and back into the scanner to measure polarization loss. I1 and I3 are images prior to cycling the table out and into the scanner, and I2 and I4 are images after cycling. The same mask, which is obtained by binarizing I3 image with a 35%-of-the-max intensity threshold, is applied to all images for computing the mean intensity of each image. SE = standard error of the mean.

polarization loss measurements due to round trip travel of the pellet out of and back into the scanner. This was the last measurement done in that imaging session. This measurement was done at 77 K, where the pellet was sent out and back into the scanner three times, each with acquisition of an image set (one before and one after the round trip). Contrary to the substantial polarization loss of the hyperpolarized gas in the tube at room temperature, there appears to be no measurable polarization loss of the isolated gas in the pellet. Fig 5.17 shows results from the three experiments in which ping measurements (composed of 50 consecutive individual pings and averaged to show each spectrum) are performed before and after sending the table out and back into the scanner. The frequency spectrum of each measurement is fit to a single Lorentzian and AUC is reported for each measurement as the strength of signal. The mean polarization loss of the three measurements is $(-0.8 \pm 2.2)\%$ demonstrating no measurable polarization loss in the round trip experiments.

This stark difference between the substantial polarization loss in the tube at room temperature and little or no polarization loss of gas in the pellet at 77 K may be

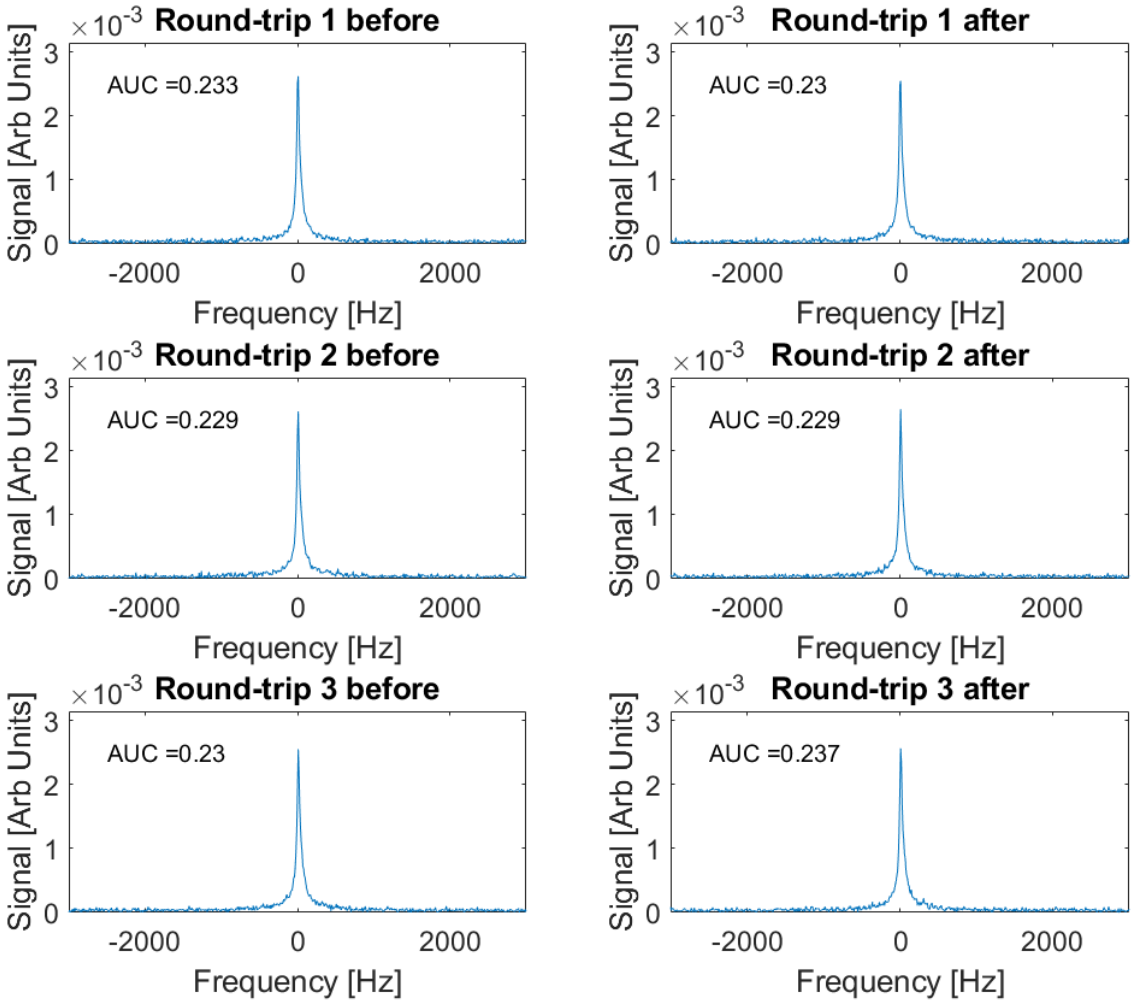

Figure 5.17: Ping measurements of the relative signal before and after cycling the scanner table out and back into the scanner. Each spectrum is an average of 50 pings to increase the measurement SNR. No measurable signal decay is observed in the 'after' pings implying no polarization loss caused by the field gradient. AUC = area under the curve.

explained by the equation governing the relaxation time constant T_1, as given in the work done by Cates et al. [74]:

$$\frac{1}{T_1} = D\frac{|\overrightarrow{\nabla} B_x|^2 + |\overrightarrow{\nabla} B_y|^2}{B_0^2}, \tag{5.36}$$

where D is the diffusivity, $\overrightarrow{\nabla} B_x$ and $\overrightarrow{\nabla} B_y$ are spatial field gradients, and B_0 is the static field. Equivalently, Eq. 5.36 derived in [82] in the rotating reference frame can be rewritten as

$$\frac{1}{T_1} = \frac{2}{3}\gamma^2 G^2 \langle U^2 \rangle \frac{\tau_c}{\omega_0^2}, \tag{5.37}$$

where γ is the gyromagnetic ratio of the nucleus of interest, G is the effective spatial gradient $G = \sqrt{|\overrightarrow{\nabla} B_x|^2 + |\overrightarrow{\nabla} B_y|^2}$, $\langle U^2 \rangle$ is the mean squared velocity of the particles, τ_c is the mean time between atomic collisions, and ω_0 is the resonant frequency of the said nucleus. Ultimately, the difference between the polarization loss in the two scenarios is dominated by the difference in the field gradients across the volume of the gas. In the case of the gas inside the pellet, the gas is limited to motion only within a 1.82-mm region inside the pellet, whereas the gas is free to diffuse in the tube which has inner diameter of 3 mm, but extends out ∼15 cm normal to the field axis.

Obviously, the diffusivity of the gas inside the pellet is much more restricted than that inside the tube. Since D scales inversely with T_1, it is expected that gas inside the pellet would have a substantially longer T_1 than the gas in the tube. More importantly, it is evident from both Eqs. 5.36 and 5.37 that G_z (or $\overrightarrow{\nabla} B_z$) has no effect on T_1. Since the long axis of the tube is normal to the static field, the Brownian motion of the gas molecules is overwhelmingly normal to the static field direction which further shortens the T_1 of the gas inside the tube. Another important factor evident in Eqs. 5.36 and 5.37 is the temperature. D is proportional to $\langle U^2 \rangle$ and by kinetic molecular theory, $\langle U^2 \rangle \propto T$, where T is the temperature in Kelvin. Therefore, T_1 is inversely proportional to temperature, and since the gas inside the pellet is maintained at 77 K, it is plausible that T_1 of the pellet is longer than that

inside the tube, all else being equal.

It is evident that the gas inside the tube will have a much shorter T_1 while it is traveling through the field gradient of the scanner than when it is sitting still at the center of it. However, it is worth noting that the gas inside the pellet sees no polarization loss primarily because the pellet sits at the axis of the scanner ($\pm$ a few mm) as it travels in and out of the scanner. This is because the experimental setup is designed carefully such that the pellet is at the coil center which has a cylindrical form and is concentric with the scanner solenoid sharing the same axes. Absence of x- and y-direction gradients along with extremely limited space encapsulated by the pellet in the path of its travel in and out of the scanner result in negligible polarization loss during a round trip travel.

5.6 Absolute polarization of ^{3}He

We have now laid out the theoretical groundwork and the experimental results necessary for extracting the absolute polarization of the hyperpolarized ^{3}He permeated into the pellet and sealed at 77 K. In this section, we invoke Eq 5.25 to compute the absolute polarization of ^{3}He after $t = 1.88\tau_{perm}$ of permeation.

The pellet has an outer diameter of 1.82 mm, and the voxels in the pellet image are 0.5 mm cubic wide which means that the majority of the voxels in the image are not fully contained within the pellet. On the other hand, there are several voxels fully contained within the thermally hyperpolarized gas phantom since the bulb of the tube has an outer diameter of $\sim$17 mm and 2 mm cubic voxels. When the pellet is centered on a corner of the voxel grid, there are exactly 8 voxels that are entirely within the pellet and 64 voxels that have partial pellet signal (see Fig 5.12). There are at least two ways to relate the signal intensities in the pellet image and the thermal equilibrium gas phantom image. One is to pick only voxels that are guaranteed to be completely inside the pellet, take the average of their intensity, and compare it

with the average intensity of voxels guaranteed to be inside the bulb of the thermal equilibrium phantom. This method ensures avoiding geometrical factors and partial volume voxels as done in Sec 5.6.1.

The alternative approach is to sum up all the signal in the pellet image (enforced by the pellet mask, please see Sec 5.5.3 and Fig 5.12) and divide it by the volume of the pellet and compare the volume-weighted mean value to the mean signal value of the voxels inside the thermal phantom bulb, also weighted by the volume size (in this case voxel size), as done in Sec 5.6.2.

5.6.1 Absolute polarization calculation avoiding all partial volume voxels in the pellet

Plugging the values $P^{^3He}_{therm} = 3.98 \times 10^{-6}$, $\theta_{therm} = 82.6° \pm 6.4°$, $\rho_{therm} = 7.161$ bar, mean of the voxel intensities entirely contained within the pellet $S_{pol} = 36.3$ arb units ± 1.5, $S_{therm} = 2.828$ arb units ± 0.019, $V_{voxel,therm} = 2^3$ mm^3, $V_{voxel,pol} = 0.5^3$ mm^3, $\theta_{pol} = 1.17° \pm 0.03°$, and $\rho_{pol} = 5.099$ bars in Eq 5.25 yields

$$P^{^3He}_{pol} = \frac{P^{^3He}_{therm} \sin\theta_{therm} \cdot \rho_{therm}}{S_{therm}} \cdot \frac{S_{pol} \cdot V_{voxel,therm}}{\sin\theta_{pol} \cdot \rho_{pol} \cdot V_{voxel,pol}} = 22.2\% \pm 1.1, \tag{5.38}$$

where the error is computed using Eqs. 5.32, 5.33, and 5.34 as

$$\sigma_{P^{^3He}_{pol}} = P^{^3He}_{pol} \cdot \sqrt{\left(\frac{\cos\theta_{therm} \cdot \sigma_{\theta_{therm}}}{\sin\theta_{therm}}\right)^2 + \left(\frac{\cos\theta_{pol} \cdot \sigma_{\theta_{pol}}}{\sin\theta_{pol}}\right)^2 + \left(\frac{\sigma_{S_{therm}}}{S_{therm}}\right)^2 + \left(\frac{\sigma_{S_{pol}}}{S_{pol}l}\right)^2} = 1.1. \tag{5.39}$$

5.6.2 Absolute polarization calculation including all partial volume voxels in the pellet

The alternative method to that presented in Sec 5.6.1 is to sum up the signal in all the pellet voxels, including the ones with only partial volume of gas, divide it by the nominal volume of the pellet assuming $OD = 1.82$ mm, and use the weighted signal

intensity as the pellet signal. $V_{voxel,therm} = 0.5^3$ mm^3, of course, will no longer be the correct volume term for the pellet.

Plugging the values $P^{^3He}_{therm} = 3.98 \times 10^{-6}$, $\theta_{therm} = 82.6° \pm 6.4°$, $\rho_{therm} = 7.161$ bar, the sum of signal containing any gas, $S^{sum}_{pol} = 859.5$ arb units ± 5.1, $\overline{S_{therm}} = 2.828$ arb units ± 0.019, $V_{voxel,therm} = 2^3$ mm^3, $V_{voxel,pol} = 4/3 \cdot \pi \cdot (0.91 \text{ mm} \pm 0.1)^3 = 3.16$ mm^3, $\theta_{pol} = 1.17° \pm 0.03°$, and $\rho_{pol} = 5.099$ bars in Eq 5.25 yields

$$P^{^3He}_{pol} = \frac{P^{^3He}_{therm} \sin\theta_{therm} \cdot \rho_{therm}}{\overline{S_{therm}}} \cdot \frac{S^{sum}_{pol} \cdot V_{voxel,therm}}{\sin\theta_{pol} \cdot \rho_{pol} \cdot V_{voxel,pol}} = 20.8\% \pm 0.6. \tag{5.40}$$

where similar to Eq. 5.39, the error is given by

$$\sigma_{P^{^3He}_{pol}} = P^{^3He}_{pol} \cdot \sqrt{((\frac{\cos\theta_{therm} \cdot \sigma_{\theta_{therm}}}{\sin\theta_{therm}})^2 + (\frac{\cos\theta_{pol} \cdot \sigma_{\theta_{pol}}}{\sin\theta_{pol}})^2 + (\frac{\sigma_{S_{therm}}}{S_{therm}})^2 + (\frac{\sigma_{S_{pol}}}{S_{pol}})^2 + (\frac{3 \cdot V_{voxel,pol} \cdot \sigma_{r_{pellet}}}{r_{pellet}})^2)} = 0.6. \tag{5.41}$$

It is encouraging and noteworthy that the values computed in 5.38 and 5.40 fall within error bars of each other.

5.7 Discussion and conclusions

Based on the Fourier analysis of the 3D CSI images, we report the absolute polarization of the hyperpolarized ^{3}He, that is sealed in the pellet after permeation, to be $P = 22.2\% \pm 1.1$, using a 15-μm pellet. The polarization of the dispensed gas, i.e. the starting polarization before the pellet is immersed in high pressure gas, is believed to be $\sim$48%. Further, from the NMR measurements, we determined the decay time constant of the hyperpolarized ^{3}He isolated in the pellet to be $T_1 = (84 \pm 10)$ hour. We note that the starting polarization quoted here is based on a crude estimate of the performance of the hybrid-alkali polarizer, since our electron paramagnetic resonance

system, which measures the polarization of the gas in the cell precisely, was nonfunctional at the time of the experiment. It is worth mentioning that one of the three lasers used for optical pumping malfunctioned prior to the experiment day, and was replaced with a "backup" laser of the same nominal power. And none of the lasers have been recalibrated for several years, so degradation of the laser performance is possible.

We now focus on the implications of the absolute polarization achieved in the pellet, and the mechanisms that affect the polarization. We demonstrated that starting from polarization $P_i \simeq 48\%$ at dispense time, the final polarization achieved in the pellet is 22%. It is important to discuss loss mechanisms. First and foremost, for the 15-μm pellet used in this experiment, it is expected that $\Gamma_{perm} = 82\%$ of the gas polarization is retained going from outside the region outside the pellet to the region inside. We sealed the pellet by cooling it to 77 K with LN_2 after 1.88 $\times\tau_{perm}$ of exposure to the high pressure gas inside the tube. We found that gas inside and outside the pellet has an *effective* decay time constant T_1. For tube V10 used in the absolute polarization measurement, T_1 is 24 minutes. Therefore, during the permeation process, $\Gamma_{T_1} = (1 - e^{-10\text{min}/24\text{min}}) \times 100 = 66\%$ of the polarization is retained. Further, at room temperature and averaged over the whole tube, we discovered that traversing through the steep field gradients of the scanner is a highly depolarizing mechanism, noting a round trip polarization loss of 14% was measured. Therefore, the polarization retention after the tube is sent into the scanner bore is $\Gamma_G = \sqrt{0.86} = 93\%$. At this point, the polarization retention is $\Gamma_{tot} = \Gamma_{perm} \times \Gamma_{T_1} \times \Gamma_G = 82\% \times 66\% \times 93\% = 50\%$, and the polarization is $P_f = \Gamma_{tot} P_i = 24\%$.

This polarization estimate of $\sim$24%, as opposed to the measured absolute polarization of 22%, does not include the following polarization loss mechanisms, the strength of which cannot be determined, at least given our experimental setup. First, it takes an average of $\sim$90 seconds to disconnect the tube from the dispense mechanism, walk it over to the scanner room from the polarizer room, secure it onto the Styrofoam coil

housing, and send it into the bore of the scanner. During this time, the gas resides in the ante-chamber of the tube, which has a much larger surface-to-volume ratio than the bottom of the tube. It is evident from the results and our estimation, that the combined polarization loss mechanisms not included in our estimation is in the order of a few percentage points, granted that the starting polarization is 48%.

We acknowledge that the retention rate of $\Gamma_{tot} = 50\%$ is not ideal, though note the following. The low value of Γ_{tot} found in our experiment is attributed to the short T_1 at the bottom of the tube, and presence of field inhomogeneities, particularly while entering the scanner. Both of these processes that act to depolarize the gas quickly are not inherent to the permeation process for loading the pellets, rather they are a consequence of performing the MRI measurements to our specific experimental design. In an actual hyperpolarized test, where imaging the pellets for measurements of retention and absolute polarization is not necessary, the pellets can be housed in a cell, for example, with a much larger surface-to-volume ratio, and inside a strong and uniform holding field. That is to say, we expect that if a cell with T_1 in the order of dozens of hours (like our polarizing cell) is used to load the pellets in a region of strong and uniform field, polarization retention values approaching Γ_{perm} is achievable, and expected. Second, there are ways we can improve our experiment to increase Γ_{total}. For example, tube V10 with a larger surface-to-volume ratio at its bottom, where the pellet is located, could have been used instead of tube V8c, to increase T_1.

In general, one of the most notable challenges in our experiments was achieving high T_1 values in our tubes. The tubes used in our experiments were custom-blown and treated by Mike Souza in Princeton University. Despite our efforts to increase surface-to-volume ratio at the bottom of the tube, and treating the inside coating of the tubes to release static and remove impurities, which are possible polarization sinks, we have not seen T_1 values higher than $\sim$50 minutes in the region of the tube where the pellets sit. This has made making permeation measurements, and achieving higher absolute polarization in the pellets more difficult.

Let us now focus on the implications of the long polarized ^{3}He T_1 achieved inside the pellet immersed in a strong and uniform field, sealed at 77 K. Although such long T_1 ($\geq$ 80 hours) is not required for the introduced hyperpolarized fuel delivery mechanism into the plasma core of the tokamak, it certainly is an advantage. We envision that a polarizer, dedicated for hyperpolarized fusion experiments, is built on-site at the DIII-D facility. Therefore, once hyperpolarized gas is produced for a given shot, the pellets are loaded on-site and taken to the cryogenic guns for injection into the core. However, such long T_1 offers the possibility of loading the pellets here at UVA, for example, and shipping the pellets inside a cryostat with a built-in magnet designed to have a relatively strong and uniform holding field.

It is evident from our results that we are able to successfully load the ICF polymer pellets with polarized ^{3}He, and seal in the hyperpolarized gas at 77 K for $\sim$ 80 hours with substantial polarization retention. However, there are a number of tasks and experiments that must be carried out before we are in the position to perform an *in-situ* hyperpolarized fusion demonstration, assuming availability of required resources and funding. For example, determining the upper limit of the polarization and the pressure (or density) at which the ^{3}He is sealed inside the pellet is a particularly important task. Theoretically, if the reactant nuclei are hyperpolarized to 100%, the fusion cross-section is 50% higher than if the spins of the reactant nuclei are randomly oriented. Our polarizer, at its peak, is able to produce polarized ^{3}He with 65% polarization at 135 psi (absolute pressure) [5]. The HDice group at Jefferson Lab can produce hyperpolarized deuterium crystals polarized to 40% inside the pellets [31]. That is to say, we are far from achieving 100% polarization in both reactant nuclei within our current polarization capability. But we are capable of determining the upper limit of the polarization we can achieve with our current equipment, a step that can be addressed in future work.

Additionally, to reach desirable density inside the plasma, larger-diameter pellet may be used with higher-pressure gas inside. That requires a ^{3}He polarizer with higher

optimal pressure in the polarizer cell than our polarizer can reach, which may require substantial research and experimentation to build such polarizer. And testing the performance of higher-diameter pellets in retaining high degree of polarization in the permeation process would be necessary. Another important project for future work is determining the polarization retention in the injection process using the cryogenic guns developed by Oak Ridge National Lab [32]. In our current plan for hyperpolarized reactant fuel delivery, after injection, the pellet would have to go through a wave-guide that connects the cryogenic gun to the plasma housing. This wave-guide would need to maintain a static field along its path for polarization retention, but it is highly conceivable that this field would not be uniform throughout the wave-guide. Simulations can be developed and performed to estimate the loss associated with travel through the waveguides, and experiments can be designed to determine the exact polarization loss.

Lastly, we remind the reader that ultimately, the fusion reaction T + D, and not ^{3}He + D, will be used for practical spin-polarized fusion experiments, and possibly energy production. Unlike established technology to polarize spin-1/2 noble gases such as ^{3}He and ^{129}Xe, there currently exists no standard technology to polarize tritium. Therefore, substantial research and development in tritium polarization, and the funding to undertake such research is of essence, though at least currently, is beyond the scope of our research collaboration.

In summary, we have developed and demonstrated success of a robust method to load ICF polymer pellets with hyperpolarized ^{3}He, and seal in the gas inside the pellets at 77 K, with substantial polarization retention. This is a major step toward performing the first *in-situ* proof-of-principle spin-polarized fusion experiment in the DIII-D tokamak in San Diego.

Part B

Diffusion-weighted MRI

Chapter 6

Diffusion-weighted MRI of human lungs: ADC-based emphysema index

For spin-1/2 noble-gas nuclei such as ^{3}He and ^{129}Xe, polarization levels orders of magnitude higher than their thermal equilibrium polarization is achievable via means of spin-exchange optical pumping. Additionally, since noble gases are chemically inert and nonradioactive, if polarized and inhaled, they could be used as contrast media for MRI studies as they offer remarkable signal-to-noise ratio owing to their high degree of polarization. Magnetic resonance imaging of inhaled hyperpolarized ^{3}He and ^{129}Xe has a rich history dating back to the mid 1990's. Ever since its conception in 1994, when Albert et al. demonstrated *in-vivo* imaging of hyperpolarized ^{129}Xe in mouse lungs [12], this non-invasive lung imaging technique has branched out to several research fields exploring lung function, structure, and disease.

The image of hyperpolarized gas inside the cavity of the lungs is referred to as a "ventilation image". Because the measured MR signal is generated by the hyperpolarized gas, only regions of the lungs where the gas is able to enter, i.e. ventilated regions, show up on the image, hence the name. Ventilation images can be used to visualize and characterize ventilation defects, which are lung regions where airflow is partially or entirely obstructed [85, 86]. For example, ventilation images based on both hyperpolarized ^{3}He [86,87] and ^{129}Xe [14,39,40] have been used for detecting and

characterizing chronic bronchitis, which is a subtype of chronic obstructive pulmonary disease (COPD), as well as cystic fibrosis [88] and asthma [38].

There exists another hyperpolarized-gas MR technique, referred to as diffusion-weighted MRI, that is based on the Brownian motion of the gas particles within the airspaces of the lungs. Recall from Sec 2.4 that Brownian motion in the presence of magnetic field gradients is a dephasing mechanism that attenuates the MR signal. This signal attenuation is often an unfavorable consequence of gradient application, which is needed for imaging. However, intentional use of gradients while gas atoms undergo Brownian motion, as described in Sec 2.5, is the basis of diffusion-weighted MRI, and allows us to measure the diffusivity of gas in different regions of the lungs [45].

Recall from Sec 1.2 that emphysema, which is another subtype of COPD, is a disease that causes irreversible destruction of the alveolar walls. In healthy regions of the lungs, the parenchymal tissue structure serves as a highly confining environment to the inhaled air or gas. On the other hand, in the regions of the lungs with emphysema-induced parenchymal tissue damage, the alveolar walls are much less restricting to diffusion of the gas particles present in the lung airspaces. As such, ADC maps obtained from hyperpolarized ^{3}He and ^{129}Xe can be used to visualize and characterize emphysema [45, 52, 89–91]. Since higher ADC values imply lower degree of gas confinement by external environment (in this case the alveolar microstructure of the lungs), ADC maps can be used as a qualitative and quantitative tool to probe the degree of damage to the lung parenchyma caused by smoking-induced emphysema [50, 54–56, 92, 93].

The present chapter describes an experimental study in which both ^{3}He and ^{129}Xe diffusion-weighted MRI was performed in a relatively large number of human subjects in order to develop a new way of measuring emphysema burden in COPD. This work has been published in the journal of Radiology [94], and some of the preliminary results of this work were presented at the Biomedical Engineering Society annual

meeting held in Phoenix (2017), AZ [95], the International Society for Magnetic Resonance in Medicine annual meeting held in Paris, France (2018) [96], and the 23^{rd} International SPIN Symposium held in Ferrara, Italy (2018) [97].

We begin by presenting the reader with the motivation for the research study in Sec 6.1. In Sec 6.2, we describe the experimental design of our research study in acquiring diffusion-weighted MRI images, CT images, and pulmonary function tests in our participants. Detailed description of the the algorithm to derive ADC maps from intensity images, and image processing and data analysis, including statistics, is given in Sec 6.3. Next, in Sec 6.4 we introduce our newly proposed ADC-based emphysema index, and present the results based on our technique, and those based on CT images and pulmonary function tests. And lastly, in Sec 6.5, we summarize our results and compare our findings to literature, and discuss the implications and potential of our method in emphysema assessment in clinical research and practice.

6.1 Motivation

Ventilation defect percentage (VDP) derived from ^{129}Xe or ^{3}He ventilation images (this technique will be described in Sec 6.3.4) has recently emerged as a clinically relevant whole-lung metric for quantifying ventilation impairment [54, 98]. To date, however, an analogous metric has not been developed for ADC measurements of emphysematous tissue destruction. Although hyperpolarized ^{129}Xe's clinical utility has recently entered it into clinical practice in the United Kingdom [99], it remains limited to research use in the vast majority of the world. One reason for this slow progress may be lack of a unifying framework within which to interpret ADC measurements. Whole-lung ADC metrics have been limited to mean and standard deviation, which are difficult to interpret in the absence of a unifying framework because the measured ADC value depends not only on airspace geometry but also on the b-value and timing of the diffusion-sensitizing gradients [100]. That is to say, the ADC value by

itself does not directly reflect emphysema burden. Furthermore, to our knowledge, beyond mean and standard deviation, a standardized scoring metric based on ADCs for quantifying emphysema severity has not yet been reported.

The motivation for this research study was to introduce and put to test a quantitative metric based on apparent diffusion coefficients that may prove useful in the clinical workflow: Inspired by emphysema index based on quantitative CT (this will be described in Sec 6.3.6), we propose an alternative method of defining emphysema index based on ADCs. Comparison of the proposed ADC metric with CT-based emphysema index and pulmonary function tests in healthy volunteers and participants with varying stages of COPD is presented. Additionally, we sought to show whether this method has any dependency on choice of hyperpolarized gas or b-value, in quantifying emphysema.

6.2 Experimental design

Total of 40 volunteers, including 27 patients with COPD and 13 healthy controls, were enrolled in this study. The study was approved by the University of Virginia Institutional Review Board, and complied with local and federal guidelines for human research studies. For each subject, hyperpolarized ^{3}He and ^{129}Xe diffusion-weighted MRI scans, computed tomography (CT) scan, and pulmonary function tests (PFTs) were obtained. Emphysema, and in general COPD, predominantly affects long-term smokers, and as such the age range of our participants (including the healthy volunteers) was chosen to be 45-70 years.

The following two sections describe the experimental design of the diffusion-weighted MRI of hyperpolarized ^{3}He and ^{129}Xe (Sec 6.2.1), and CT images as well as the pulmonary function tests (Sec 6.2.2).

6.2.1 Diffusion-weighted MRI

Using polarizers that work on the basis of spin-exchange optical pumping (SEOP), we produced ^{3}He gas polarized to 40-60% and ^{129}Xe gas polarized to 30-50%. We used our homebuilt ^{3}He hybrid-alkali SEOP polarizer [9] and one of two commercial ^{129}Xe polarizers (XeBox-10, Xemed, Durham, NH; or 9820 Hyperpolarizer, Polarean Imaging, Durham, NC) to produce hyperpolarized gas for each scan.

Hyperpolarized ^{3}He and ^{129}Xe diffusion-weighted MRI scans were obtained in separate breath holds during the same imaging session using a 1.5-Tesla clinical, whole-body scanner (Avanto; Siemens Healthineers, Erlangen, Germany). Since ^{3}He and ^{129}Xe have different resonant frequencies at a given field strength, two different transmit-receive, vest-shaped radiofrequency coils (Clinical MR Solutions, Brookfield, Wis) were used, one tuned to the resonant frequency of ^{3}He (= 48.6 MHz), and the other to ^{129}Xe (= 17.6 MHz) both at 1.5 Tesla (see Table 2.1).

Study participants were positioned supine in the scanner, and a brief ^{1}H scout image, which is a 2D projection coronal image acquired at very low resolution, was obtained at partial-inspiration breath-hold. The ^{1}H scan was used to guide the slice positioning of diffusion-weighted MRI images. For the ^{3}He (^{129}Xe) scans, 0.4 L (1 L) of the hyperpolarized ^{3}He (^{129}Xe) gas mixed with medical-grade nitrogen was dispensed into a plastic bag (Tedlar plastic bag; Jensen Inert Products, Coral Springs, Fla). The nitrogen acts as a diluting gas such that once the contents of the bags are inhaled, they fill up the lungs to 1/3 forced vital capacity, and the addition of nitrogen is inconsequential to the measured MR signal intensity. Xenon has a smaller gyromagnetic ratio than helium, and as such, same number density of hyperpolarized ^{3}He produces higher signal than hyperpolarized ^{129}Xe. Therefore, more ^{129}Xe than ^{3}He was dispensed to partially offset the signal difference in the two images.

Participants exhaled completely then inhaled the contents of the bag through flexible tubing and held their breath for up to 15 seconds during image acquisition. A two-dimensional spoiled gradient-echo pulse sequence with slice-selective excita-

tion RF pulse, equipped with bipolar trapezoidal diffusion-sensitizing gradient, as described in Sec 2.5, was used to acquire the diffusion-weighted MRI images. The diffusion-sensitizing gradients were oriented along the slice (i.e. head-foot) direction, and placed between RF excitation and signal readout. For a diagram of the pulse sequence, please refer back to Fig 2.10 of Sec 2.5.

For each gas scan, 5 separate images each corresponding to a unique b-value were obtained within the same breath-hold. For ^{3}He, the diffusion-sensitizing gradient ramp/flat-top (τ/δ) times were 300/980 μs with amplitudes (G) of 0, 14.3, 21.5, 26.8, and 31.3 mT/m, corresponding to b-values of 0, 1.6, 3.6, 5.6, and 7.6 s/cm^2. For ^{129}Xe, the diffusion-sensitizing gradient ramp/flat-top times were 300/4500 μs with amplitudes of 0, 16.8, 23.8, 29.2, and 33.7 mT/m, corresponding to b-values of 0, 12.5, 25, 37.5, and 50 s/cm^2. We paired each of the nonzero b-value images with the $b = 0$ image to obtain four different ADC maps. The b-values chosen here were consistent with those used in other multi-b diffusion MRI studies [55, 60]. Since the diffusivity of xenon atoms is nearly an order of magnitude lower than that of helium atoms, gradients with much larger time-integral are used for xenon scans (see Sec 2.5). Additionally, the factor of $\sim$3 difference between the ^{3}He and ^{129}Xe gyromagnetic ratios implies that to produce the same b-value for ^{129}Xe, gradient with 9 times larger time-integral must be applied, which explains the longer flat-top time for ^{129}Xe gradients.

Recall from Sec 2.5 that the b-value of a diffusion-sensitizing gradient is given by

$$b = (2\pi)^2 \int_0^t [k(t')]^2 dt'. \tag{6.1}$$

Therefore, for a bipolar diffusion-sensitizing gradient of trapezoidal waveform, the b-value is computed as

$$b = \gamma^2 G^2 [\int_0^\tau (1/2\tau)^2 dt + \int_\tau^{\tau+\delta} (\delta)^2 dt + \int_{\tau+\delta}^{2\tau+\delta} (1/2\tau)^2 dt]$$

$$+[\int_{2\tau+\delta}^{3\tau+\delta}(-1/2\tau)^2dt+\int_{3\tau+\delta}^{3\tau+2\delta}(-\delta)^2dt+\int_{3\tau+2\delta}^{4\tau+2\delta}(-1/2\tau)^2dt]$$
$$=2\gamma^2G^2[\frac{1}{2}\tau^3+\delta^3]. \tag{6.2}$$

The first nonzero b-value corresponding to ramp up/down time $\tau = 300$ μs, flat-top duration $\tau = 980$ μs, and gradient amplitude $G = 14.3$ mT/m, and $\gamma = 2\pi \cdot 32.4$ MHz for ^{3}He imaging is computed to be

$$b = 2\gamma^2G^2[\frac{1}{2}\tau^3+\delta^3] = 1.62 \text{ s/cm}^2. \tag{6.3}$$

Similarly for ^{129}Xe imaging, the first nonzero b-value corresponding to ramp up/down time $\tau = 300$ μs, flat-top duration $\tau = 4500$ μs, and gradient amplitude $G = 16.8$ mT/m, and $\gamma = 2\pi \cdot 11.8$ MHz is computed to be

$$b = 2\gamma^2G^2[\frac{1}{2}\tau^3+\delta^3] = 12.5 \text{ s/cm}^2. \tag{6.4}$$

Other nonzero b-values are computed using Eq 6.2. The diffusion-sensitizing gradient waveforms for the first nonzero b-value of ^{3}He and ^{129}Xe are given in Fig 6.1.

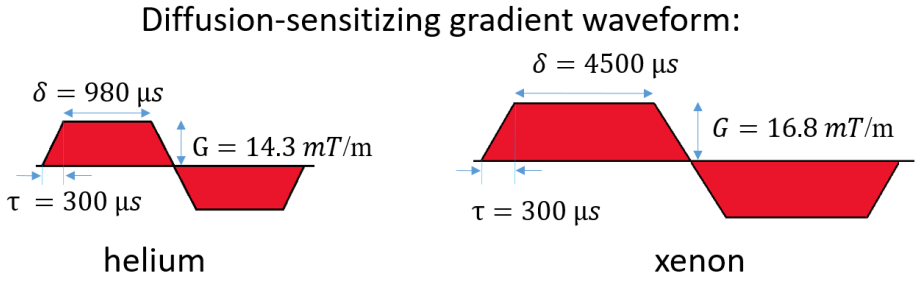

Figure 6.1: Diffusion-sensitizing gradient waveforms for inhaled hyperpolarized ^{3}He and ^{129}Xe diffusion-weighted MRI

Following an identical hyperpolarized-gas inhalation and breath hold, a second diffusion-weighted scan was obtained at the same slice positions as the multi-b scan (with b-values 0, 1.6 s/cm^2 for ^{3}He; and 0, 10 s/cm^2 for ^{129}Xe). This acquisition, whose

only purpose was to assess repeatability of the ADC measurements, was actually a "double-diffusion" pulse sequence consisting of a short-time-scale ADC measurement followed immediately by a long-time-scale ADC measurement [101]. The long-time scale ADC analysis is beyond the scope of this thesis and is not discussed.

Pulse sequence parameters for all hyperpolarized gas scans include the following. To span the majority of lung, five 40-mm axial slices with 8-mm interslice gap were acquired, with the top edge of first slice positioned at the apex of the lungs. The slice thickness and the resolution in our images are several times larger than those typically used in ventilation images [55] for the following reasons. First, like ventilation imaging, diffusion-weighted MRI acquisition time is limited to a breath-hold. It is challenging for human subjects, particularly those with COPD, to hold their breath longer than 15 seconds. Because we acquire 5 different images of each slice (corresponding to ADC measurements at 4 different b-values), it would take 5 times as long to perform our ADC scan, if we used the same imaging resolution and number of slices as a comparable ventilation scan. Therefore we use fewer slices and coarser resolution to keep the breath-hold time similar.

To maintain experimental consistency, the field-of-view and voxel size was the same for all subjects. The field-of-view was chosen to be 234-mm × 416-mm, which we knew from previous experience would be large enough for all subjects. Acuisition matrix size was 36 × 64, yielding in-plane resolution of $(6.5\text{ mm})^2$. The readout bandwidth was chosen to be 200 Hz/voxel (which implies application of a gradient such that the frequency range across each of 6.5-mm voxel is 200 Hz along the frequency-encode direction). Flip-angle was chosen to be 5°, which means that a fraction $\left(1-\cos^{(}36\times 5)5^\circ\right) = 0.50$ of the available longitudinal magnetization was consumed for each scan. [102]. Parameters for ^{3}He included repetition time $TR = 11$ ms and echo-time $TE = 6.8$ ms; and for ^{129}Xe repetition time $TR = 18$ ms and echo-time $TE = 14$ ms. Note that TE and thus TR are both longer for xenon to accommodate the larger diffusion-sensitizing gradients.

Rapid (1 sec) set of axial (= transverse) ^{1}H scans using a spiral k-space trajectory were obtained at the same slice positions during the same breath hold. These ^{1}H scans taken at same breath hold and position can be used to determine the percentage of lung with signal, and is the topic of Sec 6.3.4.

6.2.2 CT and pulmonary function tests

Along with diffusion-weighted MRI of inhaled hyperpolarized noble-gas images, we obtained other quantitative metrics that are typically used to diagnose and characterize COPD, and more specifically emphysema, in patients with lung disease. Computed tomography (CT) was obtained from all participants taken at the same lung volume as the MRI scans to ensure consistency across both imaging modalities. Chest CT images provide radio-density map of the lungs which serve as a characterization tool for emphysema burden. Further, all subjects underwent standard pulmonary function testing (PFT) which include spirometry and plethysmography. PFTs are currently the established non-imaging standard technique used to diagnose COPD, and its subtype emphysema.

6.2.2.1 Computed tomography

Computed tomography (CT) is a form of 3D x-ray, in which reconstruction of the cross-sectional (tomographic) x-ray images form a 3D radio-density of the object being imaged. The 3D radio-density image is reconstructed using the measured attenuation coefficients (μ) of the x-ray beams.

We use a linear transformation of the attenuation coefficient μ into a unit-less quantity called "Hounsfield unit", which is an absolute measure of the radio density. This linear transformation is constructed such that Hounsfield unit is zero for water and -1000 for air at standard pressure and temperature. The Hounsfield scale is

defined as

$$\text{HU} \equiv 1000 \frac{\mu - \mu_{water}}{\mu_{water} - \mu_{air}}. \tag{6.5}$$

Therefore, a CT scan displayed on the monitor or printed on film based on a gray color scale show brighter values in voxels with denser material (e.g. tissue or bone) and darker values in voxels that are translucent to x-ray (e.g. air). An example of a coronal slice from a 3D chest CT scan of a healthy subject is given in Figure 6.2. Note that the lungs, which have much less tissue density (∼3 times less dense than

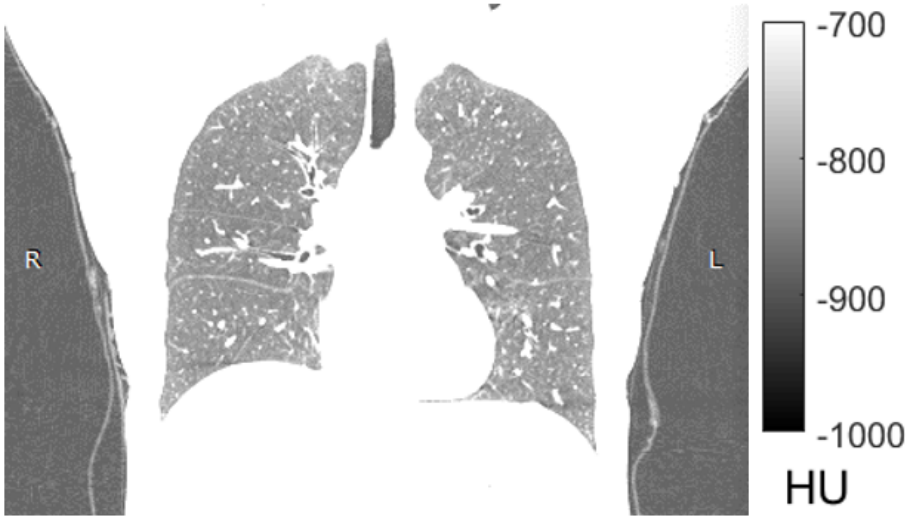

Figure 6.2: Coronal slice from a 3D chest CT scan of a healthy subject at 0.6-mm resolution. The brighter voxels correspond to more radio-dense matter. Therefore, the lung which is a much less dense organ than fat and muscle surrounding it shows up darker than the rest of the body. Note the relatively uniform tissue density in the healthy lungs.

muscle), appear darker than the rest of the body on the CT scan. The trachea, which contains only air, appears the darkest region of the body shown in this scan.

CT images provide exceptional, sub-millimeter resolution. In particular, CT is an ideal non-invasive imaging technique for visualizing fine-resolution dense media such as bones and implants inside the body. A notable downside of x-ray and CT imaging

is the ionizing radiation exposure to the human body. However, in recent years, the radiation dosage of CT has dropped significantly, while maintaining comparable resolution as that in high-dose CT [103]. Currently, CT is the most clinically prominent imaging technique for visualization and assessment of emphysema.

Therefore, in our study, within one week of MRI, chest CT scans were performed in the axial orientation using a 64-section multi-detector row CT scanner (SOMATOM Definition Flash; Siemens). Scan parameters included 0.75-mm slice thickness and 0.5-mm slice interval, as well as in-plane resolution of 0.6 mm. These are typical in-plane and through-plane resolutions for a CT scan acquired clinically for diagnosis and assessment of emphysema.

We sought to obtain CT images at the same lung volume as that in the MRI scans. The motivation for matching the lung volume in CT and MRI acquisitions was for better comparison between ADC and CT metrics, and matching lung volumes has also been done in similar studies done by Kirby et al. and Matin et al. [54,56]. Therefore, for each CT scan, we prepared a bag filled with N_2 (to 1/3 FVC), and had the subject inhale the contents of the bag using the same procedure as the MRI. We note that CT scans are commonly performed at full inflation level for assessing emphysema in clinical practice. However, we performed our scans specifically to match the lung volume in the diffusion MRI.

6.2.2.2 Pulmonary function tests

Pulmonary function tests (PFTs) provide global measures of lung function and are used extensively to diagnose and characterize lung diseases such as COPD and in particular emphysema [42]. PFTs were performed in all participants within one week of imaging, with the same procedure as would be done for clinical assessment. The most common measurement in PFTs is spirometry, in which a subject is asked to breathe out as fast as possible from maximum inspiration level to determine a parameter termed forced expiratory volume in one second (FEV_1). Since emphysema

causes loss of lung elastic recoil, patients with emphysema commonly have difficulty exhaling fast, which can be reflected in their FEV_1. This quantity is often reported corrected for age and sex as percentage predicted FEV_1, because what is considered "normal" varies with sex and age.

Another useful parameter determined by spirometry is forced vital capacity (FVC) which is the total amount of air the lungs are capable of exhaling between maximum inspiration and maximum expiration levels. Low FVC values can also be reflective of compromised lung elastic recoil in subjects with COPD. A plethysmography test is used to measure the functional residual capacity (FRC) of the lungs − the volume in the lungs when the muscles of respiration are relaxed − and total lung capacity (TLC). Other useful and relevant parameters are diffusing capacity of lung for carbon monoxide (DLCO), a quantity that indicates how fast molecules from alveolar gas can transfer to the hemoglobin of the red blood cells in the pulmonary circulation. This quantity is of particular interest in studying patients with emphysema. Recall that the large surface-to-volume ratio is a unique property of the lungs that enables sufficient gas exchange between the air in the lungs and the blood stream. In severe emphysema, since the alveolar walls are destroyed throughout the lungs, a parameter that indirectly reflects compromised surface-to-volume ratio is DLCO.

Additionally, due to the mentioned emphysema-induced loss of elastic recoil in lungs, patients with advanced emphysema empty much less of the inhaled air in their lungs at each expiration than healthy subjects. This phenomenon is directly reflected in the measured parameter called residual volume (RV)−volume of lung after maximum effort to deplete the lung. Both RV and DLCO are used clinically by pulmonologists to help diagnose and characterize emphysema, a subtype of COPD. Based on the global initiative for chronic lung disease, COPD diagnosis is determined using the conditions $FEV_1/FVC < 70\%$ and $FEV_1 < 80\%$. Within patients diagnosed with COPD, those with elevated percent predicted RV/TLC ($> 120\%$) and suppressed percent predicted DLCO ($< 80\%$) are more likely to have the emphyse-

matous subtype.

In this study, based on the clinical definition of COPD [42], all healthy volunteers had $FEV_1/FVC > 70\%$ and $FEV_1 > 80\%$ predicted, and all participants with COPD had $FEV_1/FVC < 70\%$. Further, the staging of COPD based on the global initiative for chronic obstructive lung disease is as follows: In patients with $FEV_1/FVC < 70\%$, those with $FEV_1 \geq 80\%$ are diagnosed as mild (COPD I), those with $50\% \leq FEV_1 < 80\%$ as moderate (COPD II), those with $30\% \leq FEV_1 < 50\%$ as severe (COPD III), and those with $FEV_1 < 30\%$ as very severe (COPD IV). A complete list of participant demographics, disease stage, and PFT results appears in Table 6.1.

Parameter	**Healthy**	**COPD I**	**COPD II**	**COPD III & IV**
Participants	10(27.8%)	7(19.4%)	9(25.0%)	10(27.8%)
Sex				
M	3	3	4	6
F	7	4	5	4
Mean age	57.6 ± 6.3	59.3 ± 3.6	59.4 ± 6.4	61.8 ± 8.0
Mean pack-years	0	33.7 ± 23.0	46.9 ± 28.5	47.8 ± 33.7
Smoking Status				
Current-smoker	0	5	6	5
Ex-smoker	0	2	3	5
FEV $_1^*$	101.7 ± 5.7	90.0 ± 7.9	69.0 ± 7.5	36.8 ± 7.6
FEV $_1$**/ FVC** (%)	77.5 ± 5.8	67.3 ± 8.9	61.8 ± 8.5	39.1 ± 9.9
RV/TLC *	$102.0 \pm$ 21.8	$105.1 \pm$ 10.2	$109.4 \pm$ 24.9	145.6 ± 20.3
DLCO *	91.1 ± 9.9	67.6 ± 18.2	69.4 ± 21.0	50.1 ± 9.5

Table 6.1: Data are means standard deviations. COPD = chronic obstructive pulmonary disease, packyears = number of cigarette packs smoked per day times years of smoking, FEV1 = forced expiratory volume in 1 second, FVC = forced vital capacity, RV = residual volume, TLC = total lung capacity, DLCO = diffusing capacity of lung for carbon monoxide. * Percentage predicted.

6.3 Image analysis

This section gives a detailed overview of the diffusion-weighted MRI image analysis, from which we obtain ADC maps, as well as CT image analysis. For the diffusion-weighted images, all analysis is done starting with the raw data stored in a matrix of complex values corresponding to the k-space signal output by the scanner. All analysis is done in MATLAB and the algorithms used for analysis are either built from scratch or based on MATLAB libraries.

6.3.1 Intensity images

The raw data for the axial slice-selective 2D gradient-echo image sets corresponding to the b-values presented in Sec 6.2.1 is stored in a matrix with dimensions $36\times64\times5\times5$. The first two dimensions represent the number of voxels along x and y axes, the third dimension represents the number of axial image slices to cover the lung, and the last dimension gives the number of b-values for the diffusivity measurements. To produce the magnitude image I for each of the slices and b-values, we take the discrete FFT^{-1} of the complex matrix as (see chapter 2)

$$I = \mathscr{F}^{-1}(K(:,:,m,n)), \tag{6.6}$$

for the m^{th} slice and n^{th} b-value (where ":" indicates all elements along the dimension). An example of the k-space map and the corresponding image (central slice) obtained from a ^{3}He scan for $b = 0$ is shown in Fig 6.3. The timing of all the diffusion-sensitizing gradients are kept the same for each gas but the amplitudes of the gradients increase progressively for the 5 images. Therefore, the intensity of the images progressively see higher attenuations with higher b-values. Axial inhaled hyperpolarized ^{3}He magnitude images for all 5 b-values for the middle slice of the lung is shown in Fig 6.4. The signal non-uniformity in each image may be the result from several factors. First and for most, there may be ventilation non-uniformity throughout the

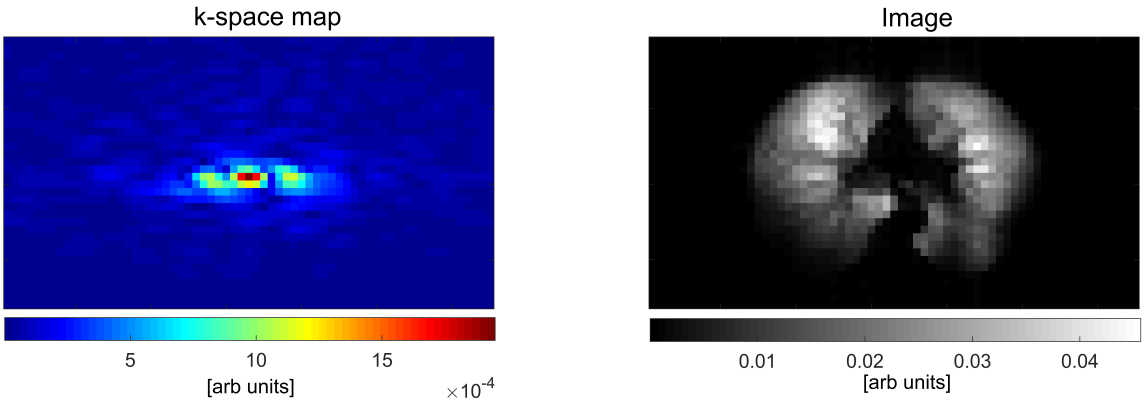

Figure 6.3: k-space map and the corresponding image of the inhaled hyperpolarized ^{3}He for $b = 0$.

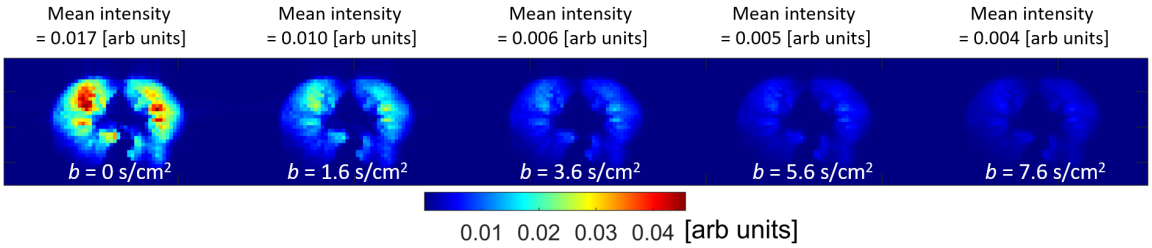

Figure 6.4: Axial inhaled hyperpolarized ^{3}He intensity images for 5 b-values demonstrating progressively higher diffusion signal attenuation for higher b-values.

lungs. Further, recall that the thickness of each axial image is 40 mm, meaning that the signal in each voxel is emanated by spins in a 6.5 mm $\times$ 6.5 mm $\times$ 40 mm region of space. Therefore, there will be a lot of partial-volume averaging in voxels that contain both gas inside the lung and other things like body tissue, particularly near the edges of the lungs where there is a steep curvature. Another factor contributing to signal non-uniformity is regional coil sensitivity – relative position of voxels with respect to the most sensitive and uniform region of the coil. This is an important ramification that need be considered carefully for ventilation imaging. However, for computing diffusivity values derived from pairs of these images, since the signal intensity profile is the same across all images, the non-uniformity in signal is simply inconsequential, especially if the lower signal intensities pass the noise level threshold discussed in the

next section.

6.3.2 SNR analysis and threshold

An important consideration for quantitative MR metrics is signal-to-noise ratio (SNR). Because the derived metric will be unreliable in portions of the lung where there is little or no MR signal (and completely inapplicable outside the lung), it is crucial to determine a threshold that faithfully separates noise from signal. In our experimental results, SNR is computed as follows. For each image set, SNR in each voxel is computed as the signal intensity inside the voxel I_{voxel} divided by the mean signal intensity $\bar{I}_{noise}$ inside a defined box that is well outside the lungs (near the perimeter of the field-of-view) corresponding to pure measurement noise

$$SNR_{voxel} = \frac{I_{voxel}}{\bar{I}_{noise}}. \tag{6.7}$$

There are numerous ways to determine the SNR threshold below which the signal intensity of a given voxel is classified as noise and consequently eliminated for diffusivity computation. Among them are the k-means algorithm which clusters signal intensity values into groups based on each group's mean value [104]. Another technique, specifically for diffusivity computation, is based on an empirical threshold [105] which reports that for ^{3}He diffusivity measurements derived from diffusion-weighted MRI, voxels with SNR < 15 in the $b = 0$ image should be eliminated for a faithful ADC computation. Since diffusivity measurements are done identically for both ^{3}He and ^{129}Xe scans, this SNR > 15 (for voxels to be included in analysis) criterion is adopted for the $b = 0$ image for both gases and all subjects. The same mask (with voxels that have SNR lower than 15 eliminated) is then applied to all other nonzero b-value images.

6.3.3 ADC maps

Four sets of ADC maps per slice were computed from each multiple-b-value diffusion-weighted scan by pairing the $b = 0$ image set with each of the nonzero b-value image sets as the following (see Sec 2.5):

$$ADC_m = \frac{1}{b_m} \ln \left(\frac{I_0 \cos^m \theta}{I_m} \right), \tag{6.8}$$

for m^{th} b-value b_m and the resulting image I_m, where $\theta = 5^\circ$ is the flip-angle which is assumed to have no regional non-uniformity. The flip-angle correction is applied to account for RF polarization loss associated with each image, since the k-space data is acquired in a line-interleaved manner. This is the standard manner in which ADC is computed [45, 52]. Similarly, one set of ADC maps was computed from the single-ADC scan (the one whose sole purpose is for repeatability assessment).

Eq 6.8 is applied on a voxel-wise basis and voxels with SNR < 15 in the $b = 0$ image were eliminated from all diffusivity analysis as described previously. The slice-positioning based on the initial ^{1}H scout and the general analysis work-flow from the intensity images to ADC maps for the first b-value corresponding to ^{3}He is shown in Fig 6.5. Voxels inside parts of the lungs with severe damage and compromised microstructure caused by emphysema can have ADC values approaching the free diffusivity coefficients mentioned earlier, since the gas inside those regions are only loosely confined by the lung parenchyma. Other places that ADC values can approach free diffusivity are the trachea and the bronchi, which contain only gas. However, since the main focus of this experiment is determining and developing a technique to assess emphysema burden in the lungs, the voxels in the large airways were manually eliminated, to yield a more faithful representation of emphysema. Examples of the masked and unmasked ADC maps for all four b-values for the central slice of the diffusion-weighted ^{3}He MRI are shown in Fig 6.6.

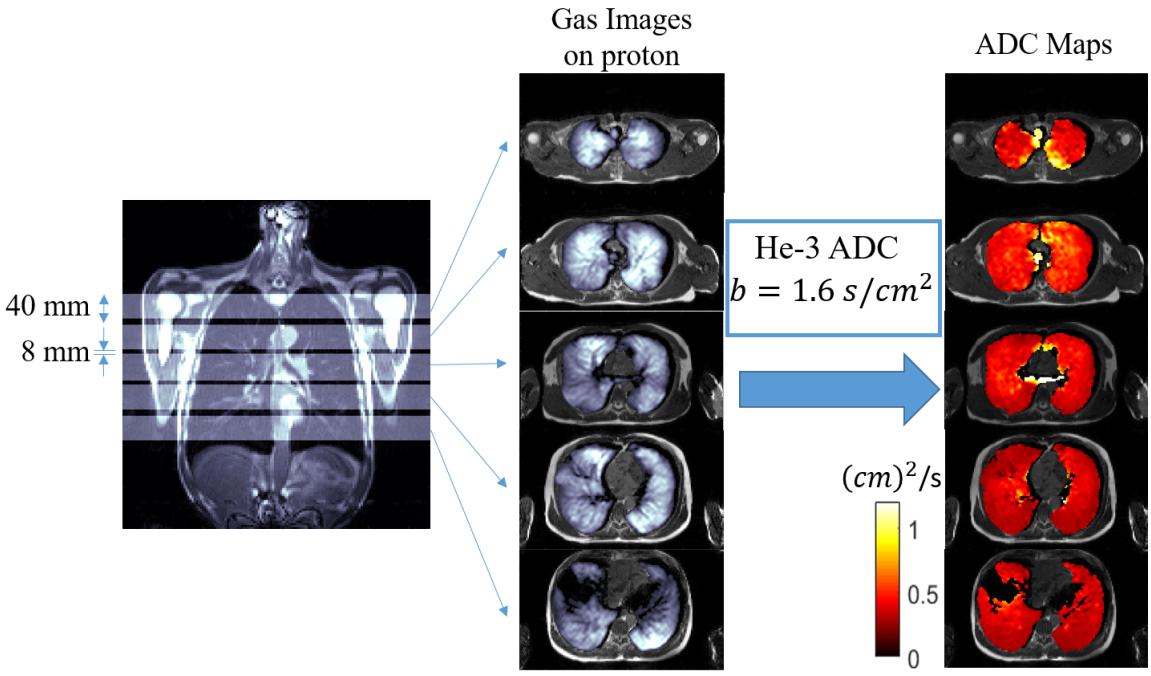

Figure 6.5: Slice-positioning and general work-flow of the analysis for inhaled hyperopolarized-gas MRI shown for ^{3}He. On the left, the slice positioning such that the first slice covering the top of the lungs starts at the apex of the lungs is shown based on the ^{1}H scout image. In the middle, the gas intensity images (5 axial slices) for the $b = 0$ are shown each overlaid on top of the same-breath-hold ^{1}H images taken for all slices. On the right, the Gas intensity ADC maps corresponding to their respective slice are shown for the first b-value each overlaid on top of the same-breath-hold ^{1}H images. The procedure for data analysis for diffusion-weighted MRI of inhaled ^{129}Xe is identical to that done for ^{3}He and presented in this Figure.

6.3.4 Percentage of available lung for analysis

Only regions of the lung where there is inhaled helium or xenon gas in the airspaces produce signal (generated by the gas). As such, in the unventilated regions of the lungs, lack of signal in the magnitude images, which arises from lack of transverse magnetization generated by the precessing spins of polarized ^{3}He or ^{129}Xe, makes ADC measurement impossible, regardless of b-value. Therefore, diffusivity measurements only for ventilated regions of the lungs are achievable.

Chronic bronchitis, which partially or completely obstructs the airflow in some

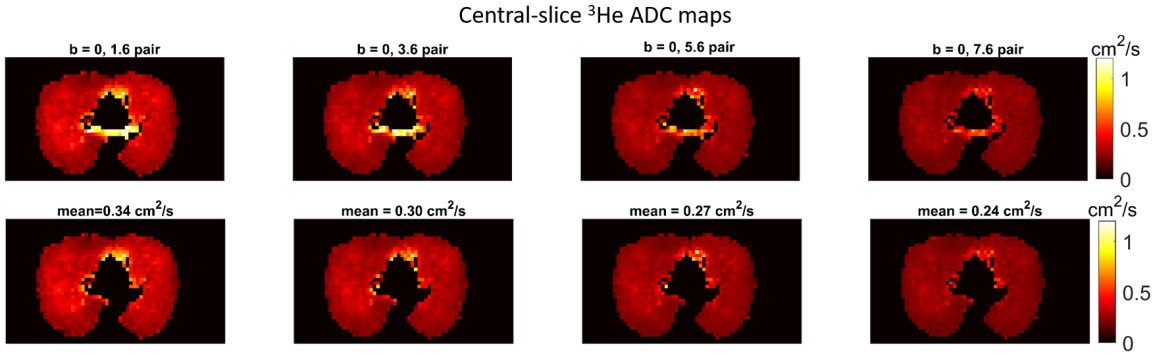

Figure 6.6: Central axial slice ADC maps derived from all four b-values. The top row represents the ADC maps without manual masking of the voxels inside trachea and the large airways and the bottom with those voxels eliminated and the mean value of the slice ADC shown on top. Note that as the nonzero b-value gets larger, the measured diffusivity gets smaller, hence the "apparent" in ADC. Apart from elimination of voxels in large airways, the two rows are identical.

of the conducting airways of the lungs, is a subtype of COPD that may accompany emphysema. Presence of chronic bronchitis, therefore, makes acquiring ADC measurements in patients with emphysema difficult. One useful metric to determine the extent of signal void in the measured ADC maps, which may reflect extent of bronchitis in COPD patients, is percentage of lung with signal above noise available for analysis. Therefore, we compute the percentage of lung available for ADC analysis based on the $b = 0$ magnitude image, and the ^{1}H images taken at same breath hold as the gas images.

There already exists a metric which captures percentage of lung with signal available for analysis based on the $b = 0$ magnitude image and is called ventilation defect percentage (VDP). Our method for calculating percentage of lung with signal available for analysis is similar to VDP computation; however, we acknowledge that VDP is more reliably computed for images with higher in-plane and through-plane resolution to minimize partial averaging effects. Nonetheless, because partial volume averaging is inconsequential in ADC calculation, we adopt the VDP computation.

In our analysis we compute percentage of lung with signal available for ADC

analysis based on the $b = 0$ intensity image and its counterpart same-breath-hold ^{1}H image on a whole lung basis.

Percentage of lung with signal above noise available for analysis Λ is computed as

$$\Lambda = \frac{V_I}{V_{Lung}}, \tag{6.9}$$

where V_I is the volume of the signal that passes the SNR > 15 criterion and V_{Lung} is the volume of the lungs as computed based on the cavity of the lungs in the ^{1}H images. Effectively, Eq 6.9 represents the fraction of the number of voxels N_I with signal above noise level to the total number of voxels N_{Lung} inside the lung, adjusted for differing voxel sizes of the two images, and we write

$$\Lambda = \frac{N_I \cdot V_{\text{gas voxel}}}{N_{Lung} \cdot V_{^1\text{H voxel}}}. \tag{6.10}$$

The numerator in Eq 6.10 is readily available by simply counting the number of voxels with SNR > 15 inside the $b = 0$ magnitude images. To find the denominator, we first need to segment the ^{1}H images to isolate the voxels making up the lung cavity. The ^{1}H images are acquired using a spiral pulse sequence with different imaging parameters including the voxel size (resolution). Fifteen axial slices spanning the lung from the apex to the bottom of the lung are acquired with in-plane isotropic voxel size of 3.9 mm (as opposed to 6.5 mm for gas images). The segmentation is done using the k-means algorithm [104] mentioned earlier, with 3 clusters. The number of clusters used was determined on a trial-and-error basis, and three was found to be most appropriate. One cluster will include the noise outside the body and the lung cavity, and the other two clusters corresponding to different signal intensity levels from the tissue inside the body as seen in Fig 6.7. If the two tissue clusters are combined, the images can be reduced to binary maps from which the lungs can be isolated using a three-dimensional flood-fill method to fill the region outside the body until the only non-filled region is the lungs as shown in Fig 6.8. Inverting the resulting binary image

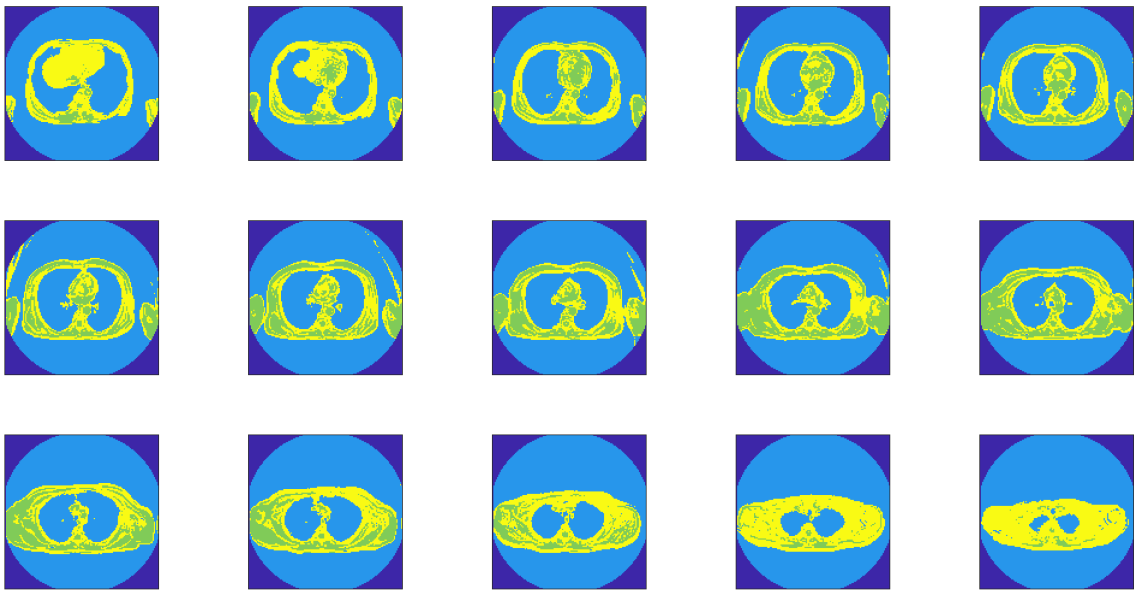

Figure 6.7: Demonstration of the three-cluster k-means segmentation algorithm in a ^{1}H lung axial image set: Shown are 15 axial ^{1}H slices spanning the lungs from the bottom (top-left panel) to the apex (bottom-right panel). The field-of-view includes regions from outside the scanner color-coded dark blue which does not enter the analysis in anyway. Each of the other three colors indicates one cluster of voxels grouped together by the algorithm. The two clusters inside the body can be combined into 2 to yield a binary mask.

will then yield the lung mask. Before counting the number of voxels in the ^{1}H lung mask, however, starting from the apex of the lungs, every three ^{1}H images (slices) are averaged to one image (slice) so that both gas and ^{1}H images consist of 5 slices. Number of voxels in the 5-slice ^{1}H lung mask can then be inputted in Eq 6.10 to compute the percentage of lung with signal available for analysis Λ for every subject in our experiment. The mean and median SNR values for all subjects broken down by disease stage/severity along with mean and median percentage of lung with signal available for analysis Λ is given in Table 6.2.

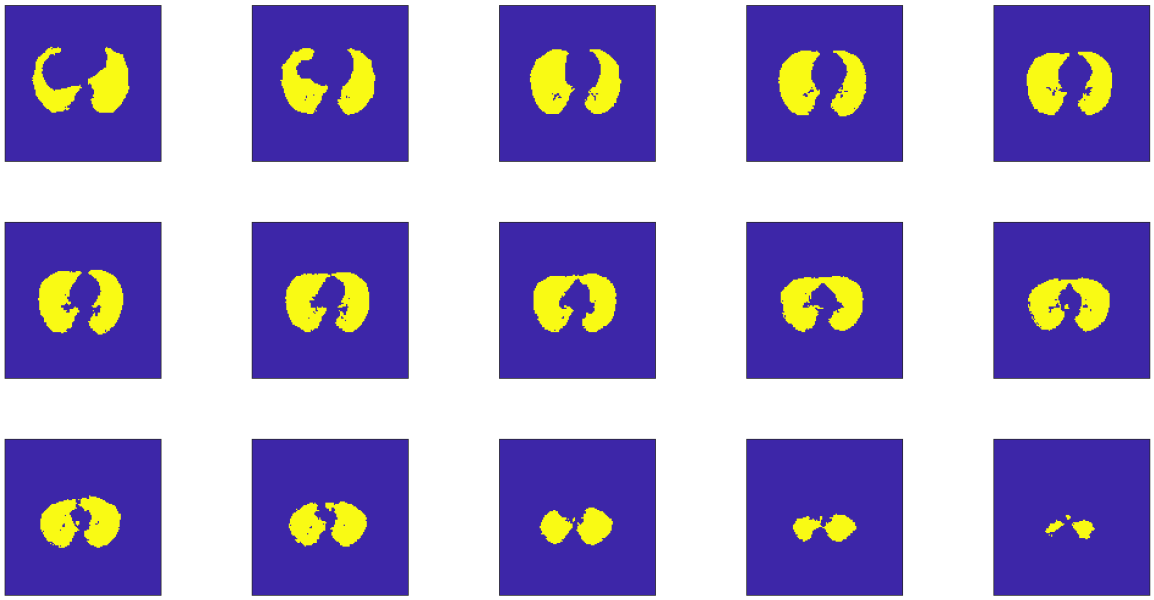

Figure 6.8: ^{1}H lung mask obtained from the k-means algorithm and the 3D non-lung flood-fill method. Every three images of this image set will be averaged to one image such that both gas and ^{1}H MRIs consist of 5 axial slices.

6.3.5 Dice coefficient

^{3}He and ^{129}Xe diffusion-weighted MRIs were performed with the subject exiting the scanner in between the two scans, but care was taken to position the subjects such that both scans have the same position and orientation. And as mentioned previously, both scans are acquired at the exact same nominal lung volume controlled by the volume of the bag. Therefore, it is reasonable to expect that the resulting gas images overlap substantially, or even completely. Although the work presented in this thesis does not include regional (voxel-to-voxel) analysis between the two gas images, the extent of overlap between the images is computed for good measure. The dice similarity coefficient (DSC) [106] is a useful quantitative metric to assess degree of overlap between two images A and B and is given by

$$DSC = \frac{|A \cap B|}{|A| + |B|}. \tag{6.11}$$

Parameter	**Healthy**	**Healthy**	**Mild-Moderate COPD**	**Mild-Moderate COPD**	**Severe COPD**	**Severe COPD**
Gas	^{3}He	^{129}Xe	^{3}He	^{129}Xe	^{3}He	^{129}Xe
SNR						
Mean†	118 ± 26	59 ± 24	105 ± 28	53 ± 15	120 ± 42	50 ± 14
Median‡	113 (106,133)	55 (44,70)	109 (84,127)	50 (39,63)	110 (76,120)	51 (45,60)
Λ*						
Mean†	97 ± 3	91 ± 8	95 ± 3	82 ± 8	87 ± 8	72 ± 11
Median‡	98 (95,99)	95 (86,97)	96 (93,97)	80 (75,87)	91 (79,94)	73 (65,81)

Table 6.2: SNR and fraction of available lung (Λ) for computing apparent diffusion coefficients broken down by COPD severity. COPD = chronic obstructive pulmonary disease, SNR = signal to noise ratio, Λ = percentage of lung with signal above noise available for analysis. † Data are means standard deviations. ‡ Data are medians with 25th and 75th percentiles of the distribution given in the parentheses. * Values given as percentages.

The dice coefficient calculated based on the binarized $b = 0$ ^{3}He and ^{129}Xe image masks after a rigid registration between the two images, which is done by maximizing the overlap between the binarized image masks. To register the two images, it is sufficient to iteratively apply a circular shift along two dimensions, compute the overlap between the two images, and maximize the computed overlap. For more complex geometries, non-rigid and affine transformations are often done which is beyond the scope of this work. The computed dice coefficients between binarized $b = 0$ ^{3}He and ^{129}Xe image masks for all subjects is given in Fig 6.9

6.3.6 Quantitative CT analysis

In order to use the CT images quantitatively, the lung parenchyma was extracted from the images. The lung parenchyma was extracted using a three-dimensional non-lung flood-fill method [56, 107], while bronchi and large airways were eliminated via condition of low HU and connectivity to the trachea as follows. First, we created a binary mask of the CT image using the global threshold of −300 HU. We then used

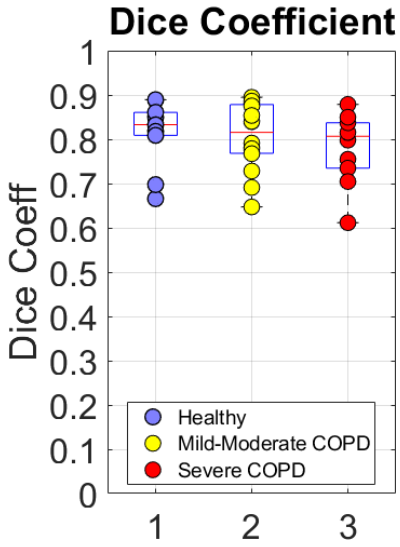

Figure 6.9: Dice coefficient between first b-value ^{3}He and ^{129}Xe ADC maps for all subjects. The horizontal lines inside the boxes are medians with the box edges indicating 25^{th} and 75^{th} percentiles of the distributions

a 3D flood-fill algorithm to fill the image from the edges of the field-of-view inward, and inverted the resulting image. We then found the largest connected object in the resulting binary map.

This mask contains the lung parenchyma, but it also contains the large airways leading to and within the lungs (trachea and bronchi). The trachea and the bronchi are eliminated by an iterative connectivity process. We start from the top-most axial slice of the CT image that contains any trachea voxels. We then iterate to the next slice and find all the voxels that might be in the airways by applying a -850 HU threshold. The voxels with values < -850 HU that overlap with the airway pixels identified in the previous slice are classified as airway. This iterative process is continued until the airway size gets below a certain threshold level chosen empirically via trial-and-error. All voxels that are connected in 3D and represent the airways will then be eliminated after the iterative process has concluded, leaving only lung parenchyma in the image.

Parenchymal tissue destruction is chiefly visualized with CT and its severity can be

assessed using quantitative CT methods including the relative area (RA) of lung with attenuation coefficients lower than a particular Hounsfield unit threshold (e.g. RA_{950}), which is sometimes referred to as emphysema index [43, 44, 108, 109]. Specifically, RA (a.k.a. emphysema index) based on segmented CT is computed as

$$RA_i = \frac{N_i}{N_{total}} \tag{6.12}$$

where i is the threshold, N_i is the number of voxels in the lungs with attenuation coefficient $< i$ HU, and N_{total} is the total number of voxels in the segmented lung. Currently, standard threshold for the RA definition is -950 HU [44, 109] assuming that the CT images are acquired at full inflation level (i.e. the subject inhales as much as they can, hold their breath, and the image is acquired), whereas the previous established standard for this threshold was -910 HU [43]. However, in our study, to match the lung volume of the gas images, the lung inflation for CT images were at 1/3 FVC which is substantially lower than full inflation level. For a complete and fair CT comparison, relative lung areas below -950 HU, -935 HU, and -910 HU (RA_{950}, RA_{935}, and RA_{910}) in lung parenchyma were computed from each segmented CT scan and used as the prominent quantitative CT metric in the results presented in Sec 6.4. Another CT quantitative metric is the mean parenchymal density reported (in units of HU) over the whole lung. Both these metrics are computed for the analysis and are used extensively throughout our study to compare MRI, CT, and PFT metrics and their strengths and weaknesses in characterizing emphysema.

6.3.7 Overview of the statistics used in the analysis

The main objective of the study presented in this chapter is to introduce and test a quantitative metric called "ADC emphysema index" for characterizing emphysema burden using hyperpolarized gas ADC and compare its performance against the established clinical metrics based on quantitative CT and pulmonary functions tests

(PFTs). This requires use of several statistical tools to assess significance of quantitative differences between performance of ADC-based, CT-based, and PFT-based metrics. An overview of the statistical tests used in the analysis and the results presented in Sec 6.4 is given in the following two paragraphs, while a detailed description of each statistic is given in App B.

As will be seen in Sec 6.4, to facilitate comparison between different emphysema metrics (RA_{950}, ^{3}He-based ADC emphysema index, and ^{129}Xe-based ADC emphysema index) across study participants, we selected the top of the 99% confidence interval of each metric's healthy-group distribution as a threshold to separate "apparently healthy" from "apparently emphysematous" ranges for each metric. That is, the participant was classified as "emphysematous" according to a given metric if its value was above that metric's emphysematous threshold. These classifications were also used to calculate measures of diagnostic performance: sensitivity, specificity, and area under the receiver operating characteristic curve (AUC), where RA_{950} was the reference standard and ADC emphysema index was the index test. Intraclass correlation coefficient was computed for repeatability data using SPSS (IBM SPSS Statistics 26.0; SPSS, Chicago, Ill; commercially available).

All other statistical analyses were performed in MATLAB. Spearman rank correlation coefficients and associated P values were calculated between all relevant MRI, CT, and PFT metrics. The P values represent the statistical significance of the reported metric and were computed based on the probability density function of each reported measurement. Healthy, mild-moderate COPD, and severe COPD group distributions were compared using Wilcoxon rank-sum test. Bland-Altman analysis was used to evaluate systematic bias between ^{3}He-based and ^{129}Xe-based ADC emphysema indices and repeatability comparisons. A P value of .05 was considered statistically significant.

6.4 Results

We start this section by computing our proposed metric, ADC-based emphysema index, based on the diffusivity measurements obtained from diffusion-weighted MRI of hyperpolarized ^{3}He and ^{129}Xe in Sec 6.4.1. We then compare the performance of ADC-based emphysema indices computed from ^{3}He and those computed from ^{129}Xe in Sec 6.4.2. Next, we compare the performance of ADC-based emphysema indices with the established quantitative CT metrics in Sec 6.4.3. And lastly, in Sec 6.4.4, we compare the performance of established quantitative results from pulmonary functions tests with quantitative CT metrics and ADC-based emphysema indices.

6.4.1 Calculation of ADC-based emphysema index

CT-based relative lung areas below -950 HU, -935 HU, and -910 HU (RA_{950}, RA_{935}, and RA_{910}) in lung parenchyma provide a quantitative measure of emphysema burden in patients with COPD, as described in Sec 6.3.6. Inspired by clinical utility of CT-based RA often referred to as emphysema index, we propose herein an alternative formulation of emphysema index based on ^{3}He or ^{129}Xe measurements with similar definition to RA. We define ADC emphysema index to be the fraction of lung voxels having ADC values greater than the 99^{th} percentile of all lung voxel values from all healthy volunteers, for a given gas and b-value. That is to say, voxels that have ADC values above the said threshold, as indicated by the vertical line in Fig 6.10 (i.e. voxels with ADC values that lie to the right of the vertical lines), are considered "emphysematous". Example histograms containing all lung-voxel ADC values, computed from the lowest b-value for each gas and grouped by COPD severity, are shown in Fig 6.10. ADC distributions for the mild-moderate COPD group and severe COPD group were broader and centered at progressively higher ADC values than the healthy group. This result is in agreement with the findings of Kaushik et al., where in a group of 7 healthy volunteers and 10 patients with COPD, they analyzed ADC values obtained

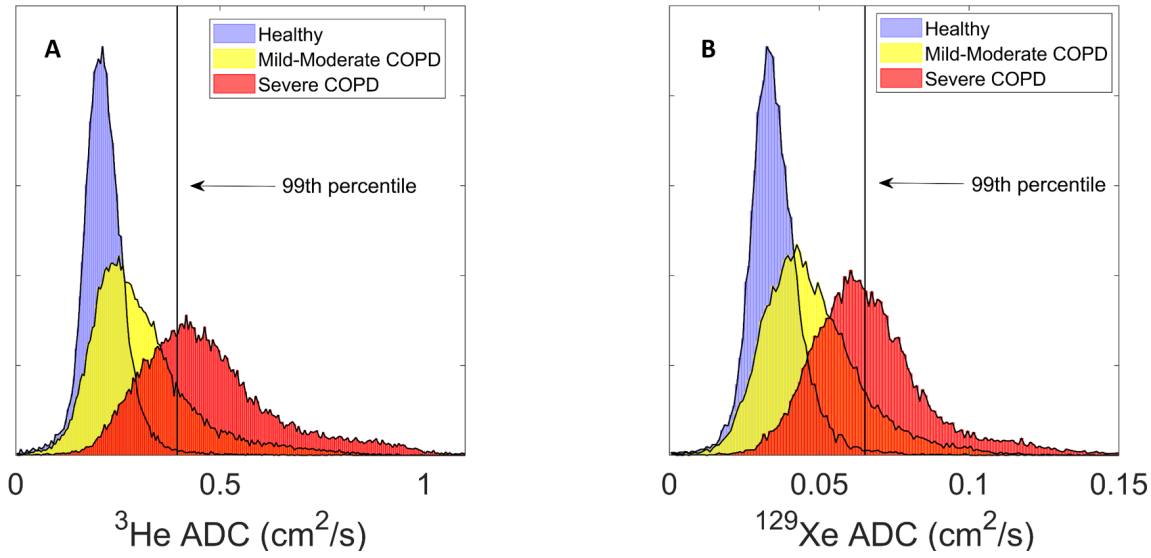

Figure 6.10: Histograms of all lung voxel apparent diffusion coefficient (ADC) values from all healthy volunteers (blue) and patients with chronic obstructive pulmonary disease (COPD) for (a) hyperpolarized ^{3}He and (b) hyperpolarized ^{129}Xe ADC computed from first (smallest) b-value. All distributions are self-normalized to have equal areas to facilitate visual comparison. Vertical lines mark 99^{th} percentile of healthy distribution. ^{3}He and ^{129}Xe ADC values at 99^{th} percentile of healthy distributions were 0.40 and 0.065 cm^2/sec for first b-value, 0.32 and 0.055 cm^2/sec for second b-value, 0.29 and 0.049 cm^2/sec for third b-value, and 0.25 and 0.047 cm^2/sec for fourth b-value, respectively.

from diffusion-weighted MRI of hyperpolarized ^{129}Xe [52]. They reported broader ADC distributions also centered at higher ADC values in patients with COPD than the distributions of ADC values in healthy subjects.

^{3}He and ^{129}Xe ADC values at 99^{th} percentile of healthy distributions were 0.40 and 0.065 cm^2/sec for first b-value, 0.32 and 0.055 cm^2/sec for second b-value, 0.29 and 0.049 cm^2/sec for third b-value, and 0.25 and 0.047 cm^2/sec for fourth b-value, respectively. The 99^{th} percentile was chosen because the paired Wilcoxon signed-rank test between CT emphysema index and ADC emphysema indices within the healthy group consistently yielded the highest P-value at this threshold, for both gases and all b-values as shown in Fig 6.11. High P-value based on the paired Wilcoxon signed-rank test between CT RA_{950} and ADC emphysema indices within the healthy group

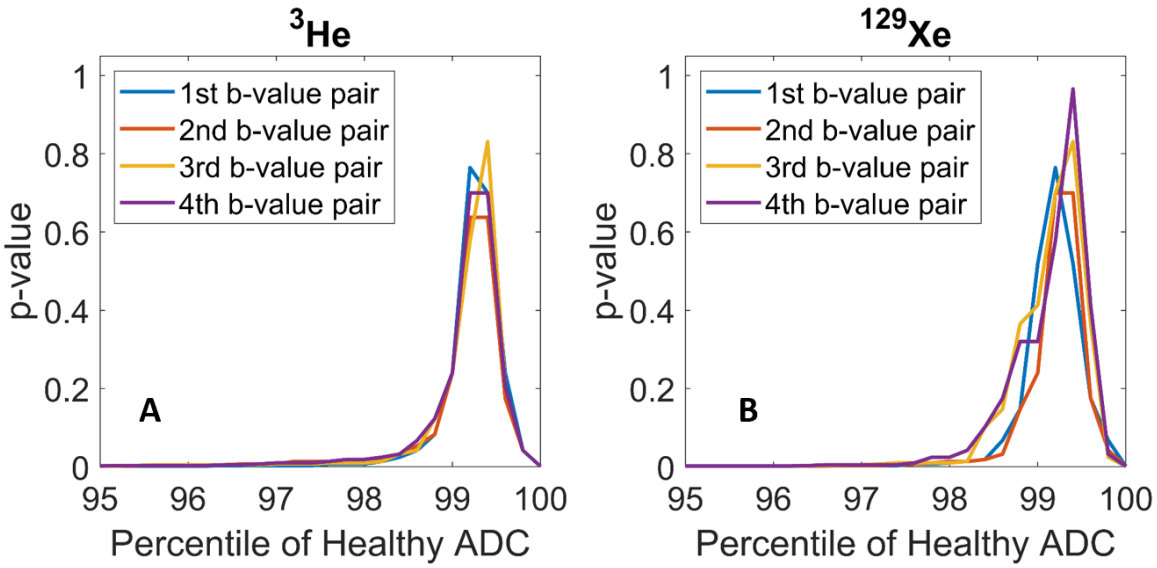

Figure 6.11: Plots of P-value versus apparent diffusion coefficient (ADC) emphysema threshold, obtained from correlation between CT RA_{950} and ADC emphysema indices computed using the indicated percentile of the aggregate ADC voxel distribution from all healthy volunteers for (a) ^{3}He ADC and (b) ^{129}Xe ADC. The plots show that CT RA_{950} and ADC-based emphysema indices are least distinguishable within the healthy group when an ADC-based emphysema threshold equal to the 99^{th} percentile is used, regardless of gas or b-value. At this threshold, the estimate of emphysema burden in healthy participants spans the same range (1%-3%) using all three metrics. RA_{950} = fraction of CT lung voxels with attenuation coefficients less than -950 Hounsfield units.

implies that for healthy subjects, both ADC- and CT- based emphysema metrics have identical performances, effectively calibrating the ADC-based emphysema index against CT RA_{950}. ADC-based emphysema index is a whole lung, unit-less metric with dynamic range between 0 and 1 with values $< 4\%$ in healthy volunteers of our study participants. In addition to providing regional qualitative information about the diseased lungs, ADC values can be used to define emphysema index to determine the global severity of emphysematous lung parenchymal damage based on an established normal range (which we determined based on the histogram of voxels in healthy volunteers).

6.4.2 ^{3}He ADC vs ^{129}Xe ADC emphysema indices

There is a near-unity Spearman rank correlation ($\rho = 0.99$, $p < 0.001$) between mean ^{3}He ADC and mean ^{129}Xe ADC for all subjects as seen in Fig 6.12, computed for the first b-value of each gas. Recall that mean ADC has been the standard quantitative

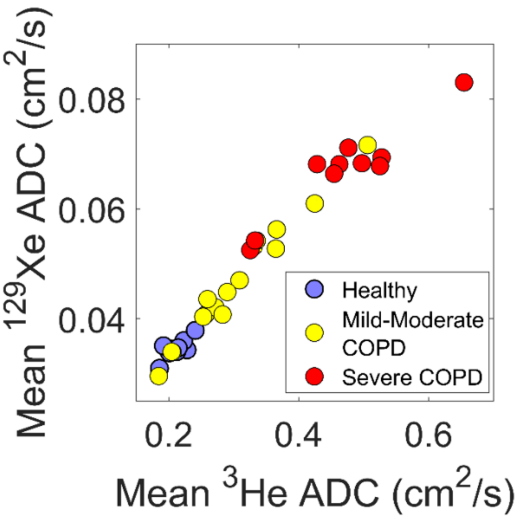

Figure 6.12: Scatter plot of mean ^{3}He and ^{129}Xe ADC showing excellent correlation with Spearman rank correlation coefficient = 0.99 at $p < 0.001$ confidence level.

metric used until now. Our finding is in agreement with those reported by Kirby et al., where they report Spearman rank correlation coefficient $\rho = 0.97$ ($p < 0.001$) [54], and Stewart et al., where they also reported $\rho = 0.97$ ($p < 0.001$) [57].

Even though the mean ADC values based on ^{3}He and ^{129}Xe have different scales, both show progressively higher values for patients with more advanced COPD stages, which is also observed by results reported in [54, 57]. Turning our attention to our newly proposed quantitative metric (ADC emphysema index), very strong correlation is observed between ^{3}He-based and ^{129}Xe-based ADC emphysema indices (Spearman rank correlation coefficient $\rho = 0.95$, $p < 0.001$) as shown in Fig 6.13A. Even though the two measures are highly correlated, it is evident that the helium-based ADC emphysema indices measure higher values as seen in Fig 6.13D. Bland-Altman analysis showed an average bias of 9.8%$\pm$8.6, and the difference between ^{3}He-based and ^{129}Xe-

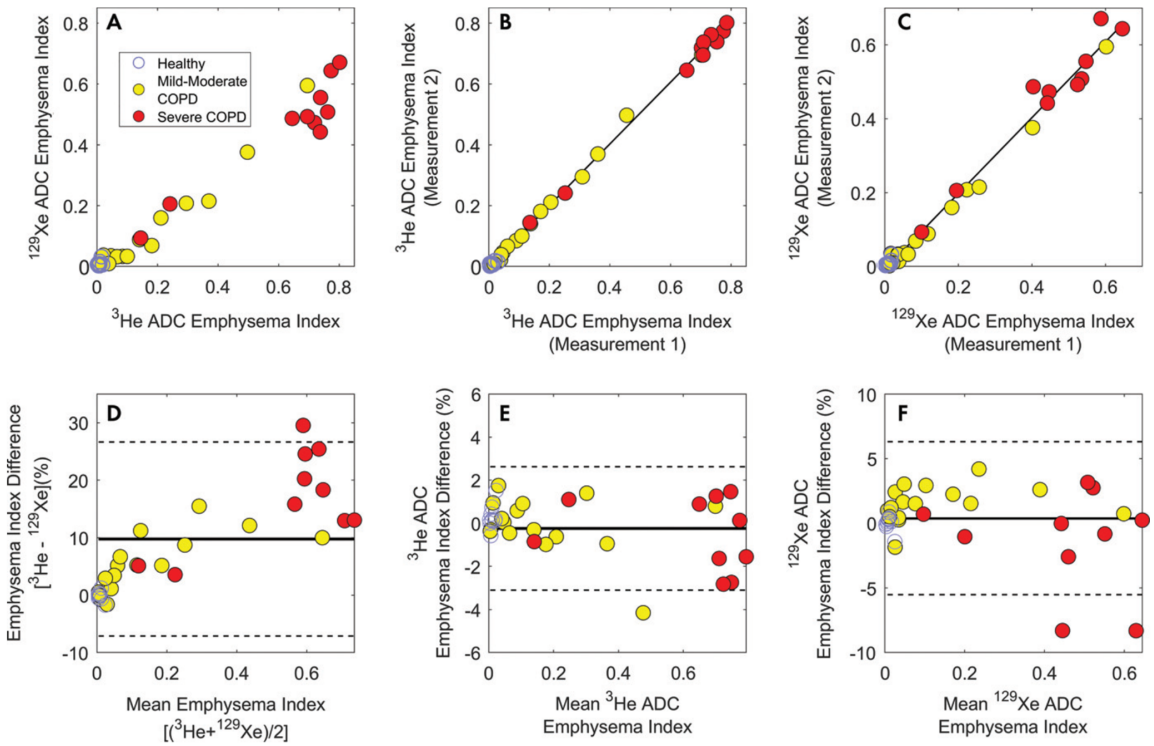

Figure 6.13: (a) Scatter plot and correlation of ADC emphysema indices based on ^{129}Xe versus ^{3}He in all participants. (b) Scatter plot of repeatability measurements of 3He-based ADC emphysema indices ($y = 1.01x + 0.00$, $r^2 > 0.99$). (c) Scatter plot of repeatability measurements of ^{129}Xe-based ADC emphysema indices ($y = 1.03x - 0.01$, $r^2 = 0.99$). (d) Bland-Altman plot depicts the bias between ^{3}He-based and ^{129}Xe-based ADC emphysema indices. Percentage mean $\pm$ standard deviation is 9.8 ± 8.6. Significant correlation is observed between percentage emphysema index difference and mean emphysema index ($r = 0.87, p < .001$). (e) Bland-Altman plot depicts no bias between ^{3}He-based ADC emphysema index repeatability measurements. Percentage mean $\pm$ standard deviation is 0.2 ± 1.4. (f) Bland-Altman plot depicts no bias between ^{129}Xe-based ADC emphysema index repeatability measurements. Percentage mean standard deviation is 0.43.0. Dashed horizontal lines represent 95% limits of agreement in all Bland-Altman plots. All plots share the same legend presented in (a).

based ADC emphysema indices was correlated with their mean ($r = 0.87, p < .001$). This bias probably relates to previous findings that ^{129}Xe images frequently show larger ventilation defects than ^{3}He images in participants with COPD, presumably because ^{3}He is more diffusible than ^{129}Xe and can better penetrate restricted airways or access obstructed lung regions via collateral ventilation [39,54]. Regions appearing ventilated using ^{3}He but non-ventilated using ^{129}Xe also tend to be emphysematous, which would increase emphysema burden measured using ^{3}He ADC. An example of this phenomenon is evident in the ADC maps displayed in the middle row of Fig 6.14, in which there are highly emphysematous regions in the ^{3}He ADC map that appear non-ventilated in the ^{129}Xe ADC map. Further, this phenomenon is also reflected in the percent of available lung used for ADC analysis as evident in Table 6.2, which was consistently larger for ^{3}He.

Repeatability was assessed by comparing emphysema indices computed from the single-ADC scan with those computed from the first b-value of the multi-ADC scan for each participant using the intraclass correlation coefficient (ICC). ^{3}He-based and ^{129}Xe-based ADC emphysema indices were both highly repeatable (ICC = 0.998 and 0.993 for ^{3}He and ^{129}Xe, respectively), as shown in Fig 6.13B-C. Further, Bland-Altman analysis revealed no significant bias between the two sets of repeatability measurements for either gas as seen in Fig 6.13E-F.

One of the major strengths of our research study as compared to others in the literature [54, 56, 57] is the extent of repeatability done in the ADC-based metrics for a large group of volunteers and patients with COPD. For example, Kirby et al. performed repeatability measurements of whole-lung mean ADC values for 8 healthy subjects and 10 subjects with COPD, though 8 of their 10 COPD subjects were stage II, with the other being stage I [54]. The study done by Matin et al. included more COPD subjects (total of 22) with stages II-IV, though they did not have any COPD stage I patients in their cohort, and their study did not include ^{3}He measurements [56]. Additionally, Stewart et al. reported repeatability measurements

for whole-lung mean ADC values, but their cohort only included total of 5 COPD subjects [57]. It is worth noting that our repeatability results were in agreement with their reported ICC coefficients for agreement (0.995 and 0.936 for ^{3}He and ^{129}Xe, respectively) significant at the $P<0.001$ level.

6.4.3 Performance of ADC-based emphysema index vs quantitative CT

Representative ^{3}He and ^{129}Xe ADC maps and CT images from a healthy volunteer and two participants with advanced COPD stage are shown in Fig 6.14. It can be seen in the healthy subject that dense and uniform tissue density is present as portrayed by the CT map while low and uniform ADC values are seen in both ^{3}He and ^{129}Xe ADC maps. The low measured diffusivity values are in agreement with the uniformly dense tissue across the lungs implying a robust lung parenchymal microstructure: Once the gas enters the lung and is confined by the structure, its diffusivity is low and uniform due to the confinement. Whereas in the patient with advance COPD (stage III) as seen in the CT map (second row), it is evident that there is severe, heterogeneous parenchymal damage throughout the lung caused by emphysema. These regions of the lung with near-translucent CT radiodensity approaching that of air are visually and qualitatively associated with regions of elevated ADC in the corresponding ^{3}He and ^{129}Xe ADC maps. In the other patient also with advanced COPD (stage III), lower degree of tissue destruction is seen in the CT map suggesting milder presence of emphysema. However, as indicated by both ^{3}He and ^{129}Xe ADC maps with relatively elevated values (compared to the healthy subject), it is evident that the lung parenchymal microstructure is compromised due to what we suspect is early-stage emphysema. This is an example of the potential ADC maps offer in diagnosing and characterizing early stage lung disease.

Mean parenchymal density (mean CT given in units of HU) was highly correlated with both mean hyperpolarized ^{3}He and ^{129}Xe ADC as seen in Fig 6.15. Similarly,

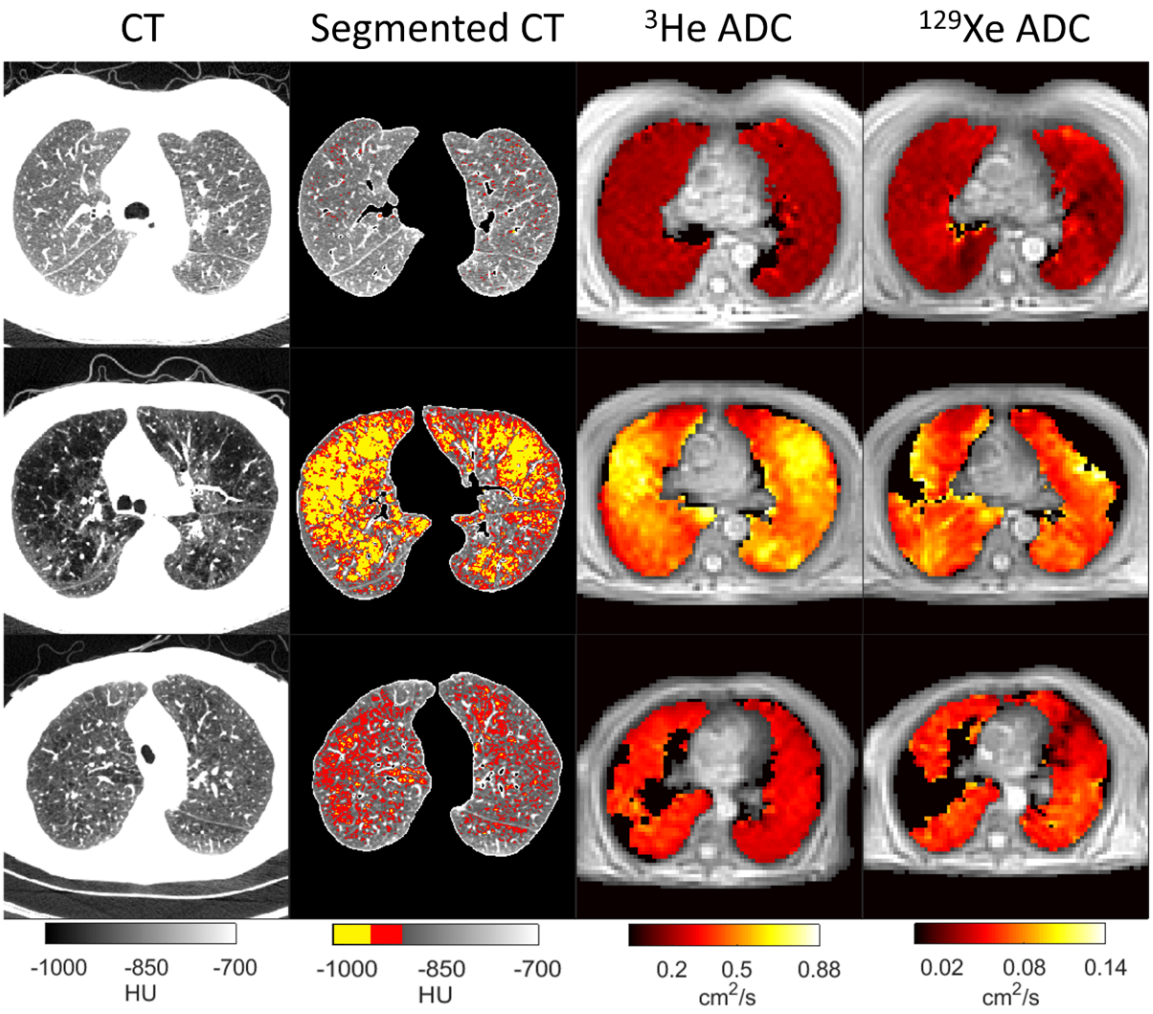

Figure 6.14: Representative axial CT lung images, segmented CT images with voxels having attenuation coefficient levels less than −950 HU and −910 HU displayed in yellow and red respectively, and corresponding ^{3}He and ^{129}Xe apparent diffusion coefficient (ADC) maps. In the top row, CT in a healthy 60-year-old man shows uniformly dense parenchyma throughout the lung and uniformly low ADC values in both ^{3}He and ^{129}Xe ADC maps. In the middle row, CT in a 75-year-old man with stage III COPD depicts large areas of lung parenchyma with low attenuation coefficients. Clear visual concordance is present between these areas in the CT image and elevated ADC values in the corresponding ^{3}He and ^{129}Xe ADC maps. CT RA_{950} and ADC emphysema indices are well outside the healthy range (> 0.03), indicating that all techniques identify the participant as emphysematous. In the bottom row, a clear difference in performance is seen in a 68-year-old woman with stage III COPD. Very few pixels in the CT image cross the −950 HU threshold, whereas both ADC maps show extensive lung regions with elevated values. Accordingly, both ADC-based emphysema indices for this participant lie well outside the healthy range, but the CT RA_{950} does not ($RA_{950} = 0.01$, ADC emphysema index $= 0.25, 0.21$ based on ^{3}He and ^{129}Xe, respectively).

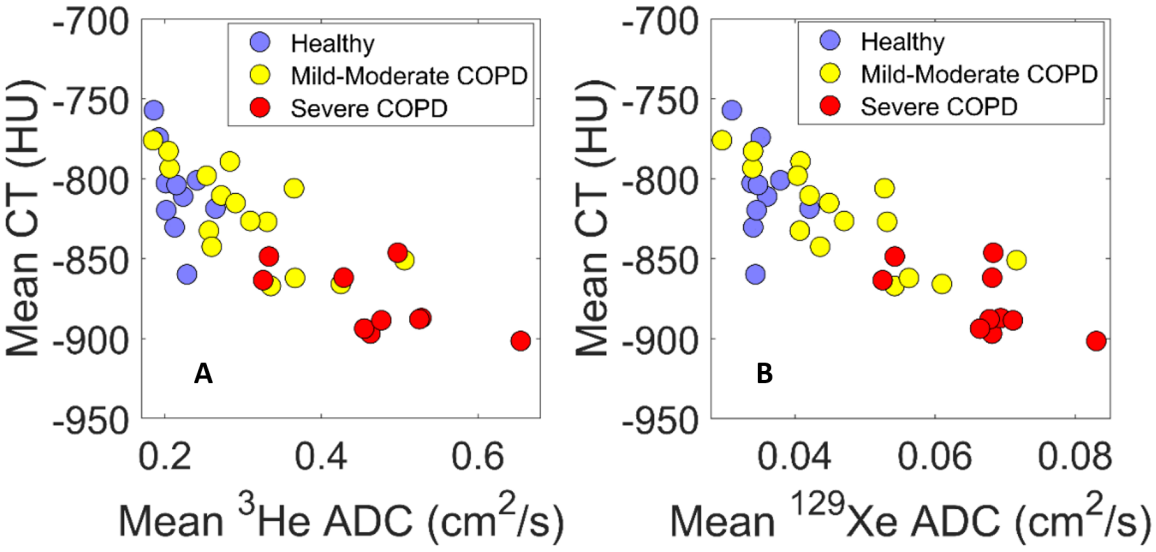

Figure 6.15: Mean CT vs hyperpolarized a) ^{3}He and b) ^{129}Xe ADC.

RA_{950}, RA_{935}, and RA_{910} were all strongly correlated with ^{3}He-based ($r = 0.86, p < .001$ for RA_{950}; $r = 0.86, p < .001$ for RA_{935}; $r = 0.84, p < .001$ for RA_{910}) and ^{129}Xe-based ($r = 0.85, p < .001$; $r = 0.87, p < .001$; $r = 0.85, p < .001$) ADC emphysema indices computed using the lowest b-value for each gas as seen in Fig 6.16.

These results further confirm our findings in Sec 6.4.2 that the performance of ^{3}He and ^{129}Xe emphysema indices are very similar. The high correlation coefficients between ADC-based and CT-based metrics ($\geq$0.85) establish that although CT directly measures tissue density while ADC is a relative measure of airspace size, both techniques can be used to assess emphysema, but through different processes. That is to say, CT may be used to characterize emphysema by determining regions of lung with low radiodensity implying loss of parenchymal tissue. Whereas, ADC may be used to characterized emphysema by measuring enlarged alveolar spaces, which is the consequence of parenchymal tissue destruction.

Furthermore, our results echo the findings in the study done by Kirby et. al, where for COPD ex-smokers, they reported that CT RA_{950} correlated with mean ^{3}He ADC ($\rho = 0.90, P = 0.008$) and ^{129}Xe ADC ($\rho = 0.85, P = 0.03$) [55]. In our

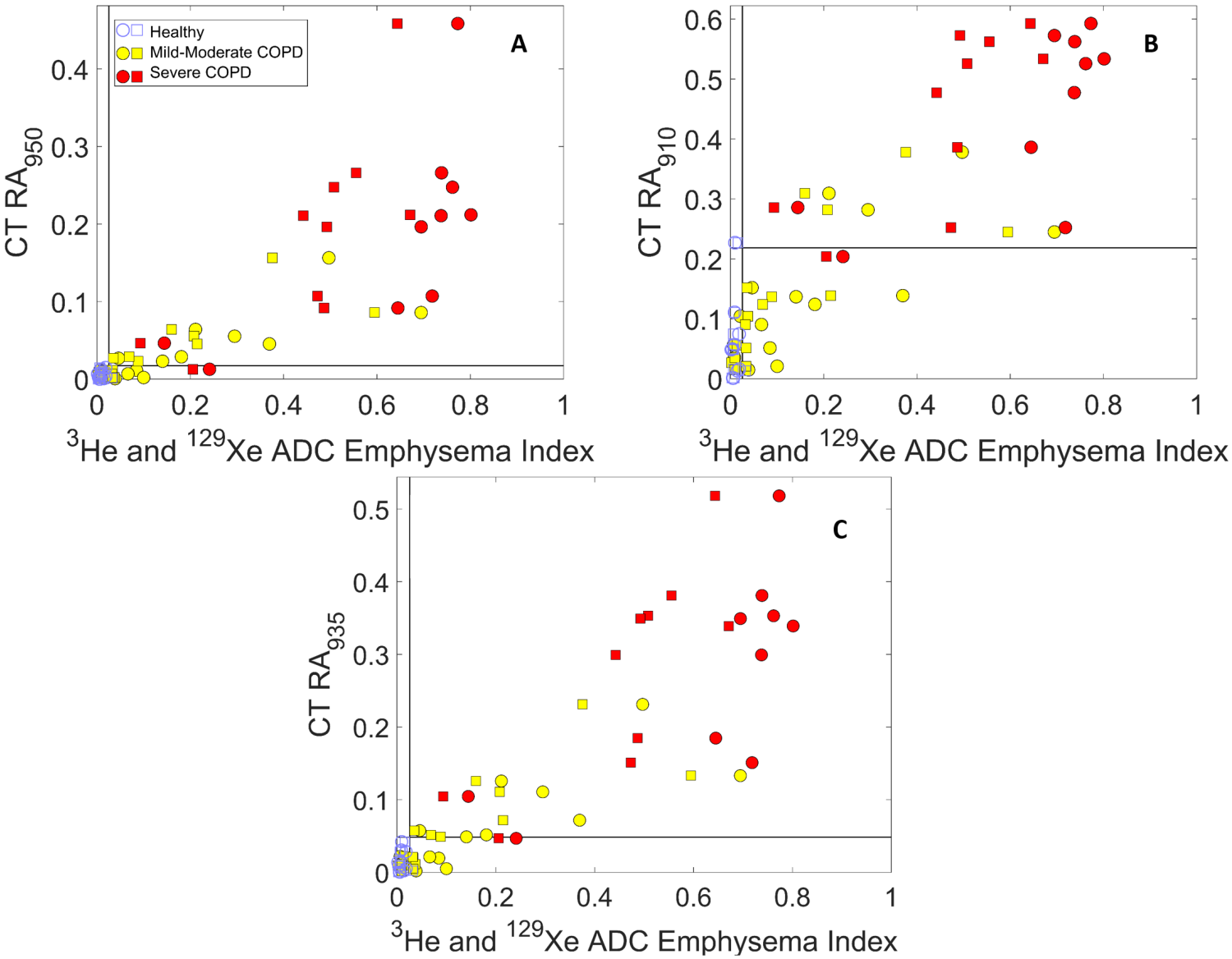

Figure 6.16: Superimposed scatter plots of CT RA_{950}, RA_{935}, and RA_{910} versus lowest b-value emphysema index based on both ^{3}He apparent diffusion coefficient (ADC) and ^{129}Xe ADC (circles and squares represent ^{3}He-based and ^{129}Xe-based ADC emphysema indices, respectively). Solid lines are drawn at upper limit of 99% confidence interval of healthy population to create "apparently healthy quadrant (lower left) and "apparently emphysematous quadrant (upper right). Lower right quadrant contains participants whose emphysema indices lie in healthy range based on CT but lie in emphysematous range based on ADC (five ^{3}He-based and five ^{129}Xe-based ADC emphysema index data points appear in lower right quadrant). No data points appear in upper left quadrant for A and C, and only one data point appears in the upper left quadrant in B. RA_{950}, RA_{935}, and RA_{910} = fraction of CT lung voxels with attenuation coefficients less than −950, −935 and −910 HU, respectively. All plots share the same legend as presented in A.

study, correlation with ADC emphysema indices computed using higher b-values were similarly strong (Table 6.3). The similarity between ADC-based emphysema indices based on all b-values and both gases indicates the robustness of our technique in relating airspace enlargement to emphysema-induced parenchymal tissue loss.

Parameter	^{3}**He EI** 1^{st} $\boldsymbol{b}$	^{129}**Xe EI** 1^{st} $\boldsymbol{b}$	^{3}**He EI** 2^{nd} $\boldsymbol{b}$	^{129}**Xe EI** 2^{nd} $\boldsymbol{b}$	^{3}**He EI** 3^{rd} $\boldsymbol{b}$	^{129}**Xe EI** 3^{rd} $\boldsymbol{b}$	^{3}**He EI** 4^{th} $\boldsymbol{b}$	^{129}**Xe EI** 4^{th} $\boldsymbol{b}$
Mean CT	−0.77	−0.80	−0.80	−0.83	−0.78	−0.81	−0.77	−0.83
CT RA$_{950}$	0.86	0.85	0.85	0.84	0.85	0.84	0.85	0.85
CT RA$_{935}$	0.86	0.87	0.85	0.86	0.86	0.85	0.85	0.87
CT RA$_{910}$	0.84	0.85	0.85	0.85	0.85	0.82	0.85	0.82

Table 6.3: Data given are Spearman Rank correlation coefficient. EI = emphysema index, HU = Hounsfield unit. RA = relative lung area with low attenuation. CT RA computed as fraction of voxels with attenuation coefficients less than threshold given in the subscripts. All Spearman Rank correlation coefficients are highly significant with $p < 0.001$.

However, a closer look at the data points in Fig 6.16 suggests important differences between healthy and COPD group distributions along each axis. Nearly all data points for healthy volunteers (10/10 for ^{3}He and 9/10 for ^{129}Xe), as well as 15% of patients with COPD (4/26), had data points in the lower left quadrant, corresponding to "apparently healthy" based on both CT and ADC. Most patients with COPD (17/26 or 65%) had data points in the upper right quadrant, corresponding to "apparently emphysematous" based on both CT and ADC. However, a substantial minority of the patients with COPD (5/26 or 19%, four with mild-moderate COPD) had emphysema indices solidly in the lower right quadrant, appearing "healthy based on quantitative CT but "emphysematous based on ADC, whereas no patients appeared "emphysematous based on CT but "healthy based on ADC (upper left quadrant). Therefore, ADC emphysema index showed near-perfect sensitivity in our study sample (17/17 = 100% for the lowest b-value using both gases; 95% confidence interval: 94-100%) but somewhat lower specificity (14/19 = 74% for ^{3}He and 13/19 = 68% for ^{129}Xe; 95% confidence intervals: 49-99% and 42-94% respectively).

Area under the receiver operating characteristics curve (ROC AUC) is a useful statistic used to assess performance of any proposed new metric, referred to as the "index test" (in our case, ADC-based emphysema index), against the ground truth metric, referred to as "reference standard" (in our case, CT RA). ROC AUC was also relatively high for both gases (≥ 0.94 for all ^{3}He b-values, 95% confidence interval: 0.86-1; ≥ 0.92 for all ^{129}Xe b-values, 95% confidence interval: 0.83-1) (please refer to Table 6.4, Fig 6.18).

Near-identical sensitivity, specificity, and ROC AUC measures were observed between CT RA_{935} and RA_{950}, and the diagnostic performance measures were similar when CT RA_{910} replaced CT RA_{935} or RA_{950} as the reference standard (Table 6.4). The -950 HU threshold is the current standard for CT emphysema index at full lung inflation [44, 109]. Because our CT scans were obtained at a lower inflation level, the higher (-910 HU) threshold corresponding to a previous standard [43] was analyzed for comparison. Additionally, lung-inflation-corrected threshold value of -935 HU was extrapolated from study done by Madani et al [109] and CT RA_{935} was included in all CT analysis. Linear extrapolation was used to determine the -935 HU threshold as shown in Fig 6.17. It can be seen that going from -935 HU to -950 HU, the false negative rate increases from 27% to 38% while -910 HU threshold increases the false positive rate from 25% to 40% reflecting the optimal threshold at or near -935 HU for CT based emphysema assessment. Using an RA threshold of -910 HU to calibrate the ADC emphysema index percentile threshold resulted in emphysema indices approaching 20% for healthy participants (Fig 6.16B). Therefore, calibration against the standard RA thresholds of -935 HU and -950 HU, which yielded much lower estimates of emphysema burden in the healthy group, seems more reasonable. It is evident that results from analyzing CT RA_{935} and RA_{950} are very similar (Tables 6.4 and 6.3, and Fig 6.16), therefore, we adopt the established CT threshold of -950 to present further results on comparing ADC-based emphysema index and CT RA. It can be seen from Fig 6.19 that the statistical separation between the healthy group

Parameter	**Sensitivity**	**Specificity**	**ROC AUC**
CT RA$_{950}$			
^{3}He ADC (1^{st}-*b*-val)	17/17 (100%; 94,100)	14/19 (74%; 49,99)	0.95 (0.88,1)
^{129}Xe ADC (1^{st}-*b*-val)	17/17 (100%; 94,100)	13/19 (68%; 42,94)	0.93 (0.85,1)
^{3}He ADC (2^{nd}-*b*-val)	17/17 (100%; 94,100)	13/19 (68%; 42,94)	0.95 (0.88,1)
^{129}Xe ADC (2^{nd}-*b*-val)	16/17 (94%; 77,100)	14/19 (74%; 49,99)	0.92 (0.83,1)
^{3}He ADC (3^{rd}-*b*-val)	17/17 (100%; 94,100)	13/19 (68%; 42,94)	0.95 (0.88,1)
^{129}Xe ADC (3^{rd}-*b*-val)	17/17 (100%; 94,100)	14/19 (74%; 49,99)	0.92 (0.83,1)
^{3}He ADC (4^{th}-*b*-val)	17/17 (100%; 94,100)	12/19 (63%; 36,90)	0.94 (0.86,1)
^{129}Xe ADC (4^{th}-*b*-val)	16/17 (94%; 77,100)	16/19 (84%; 63,100)	0.92 (0.83,1)
CT RA$_{935}$			
^{3}He ADC (1^{st}-*b*-val)	17/17 (100%; 94,100)	14/19 (74%; 49,99)	0.95 (0.88,1)
^{129}Xe ADC (1^{st}-*b*-val)	17/17 (100%; 94,100)	13/19 (68%; 42,94)	0.98 (0.92,1)
^{3}He ADC (2^{nd}-*b*-val)	17/17 (100%; 94,100)	13/19 (68%; 42,94)	0.97 (0.90,1)
^{129}Xe ADC (2^{nd}-*b*-val)	16/17 (94%; 77,100)	14/19 (74%; 48,99)	0.97 (0.91,1)
^{3}He ADC (3^{rd}-*b*-val)	17/17 (100%; 94,100)	13/19 (68%; 42,94)	0.95 (0.87,1)
^{129}Xe ADC (3^{rd}-*b*-val)	17/17 (100%; 94,100)	14/19 (74%; 48,99)	0.97 (0.91,1)
^{3}He ADC (4^{th}-*b*-val)	17/17 (100%; 94,100)	12/19 (63%; 36,90)	0.94 (0.86,1)
^{129}Xe ADC (4^{th}-*b*-val)	16/17 (94%; 77,100)	16/19 (84%; 62,100)	0.97 (0.91,1)
CT RA$_{910}$			
^{3}He ADC (1^{st}-*b*-val)	13/14 (93%; 72,100)	13/22 (59%; 34,84)	0.94 (0.86,1)
^{129}Xe ADC (1^{st}-*b*-val)	13/14 (93%; 72,100)	12/22 (55%; 29,80)	0.94 (0.86,1)
^{3}He ADC (2^{nd}-*b*-val)	13/14 (93%; 72,100)	12/22 (55%; 29,80)	0.95 (0.88,1)
^{129}Xe ADC (2^{nd}-*b*-val)	13/14 (93%; 72,100)	14/22 (63%; 39,88)	0.95 (0.88,1)
^{3}He ADC (3^{rd}-*b*-val)	13/14 (93%; 72,100)	12/22 (55%; 29,80)	0.95 (0.88,1)
^{129}Xe ADC (3^{rd}-*b*-val)	13/14 (93%; 72,100)	13/22 (59%; 34,84)	0.93 (0.85,1)
^{3}He ADC (4^{th}-*b*-val)	13/14 (93%; 72,100)	11/22 (50%; 25,75)	0.92 (0.82,1)
^{129}Xe ADC (4^{th}-*b*-val)	13/14 (93%; 72,100)	16/22 (73%; 50,96)	0.95 (0.88,1)

Table 6.4: CT RA$_{950}$ and RA$_{910}$ at 99^{th} percentile of the healthy group distribution is taken as the reference standard in determining the diagnostic accuracy of ADC emphysema indices in separating the healthy volunteers from those with emphysema. Data given in parentheses represent 95% confidence interval. ROC = receiver operating characteristics, AUC = area under the curve. RA = relative lung area with low attenuation. CT RA$_{950}$, RA$_{950}$, and RA$_{910}$ computed as fraction of voxels with attenuation coefficients less than -950, -935 HU, and -910 HU, respectively.

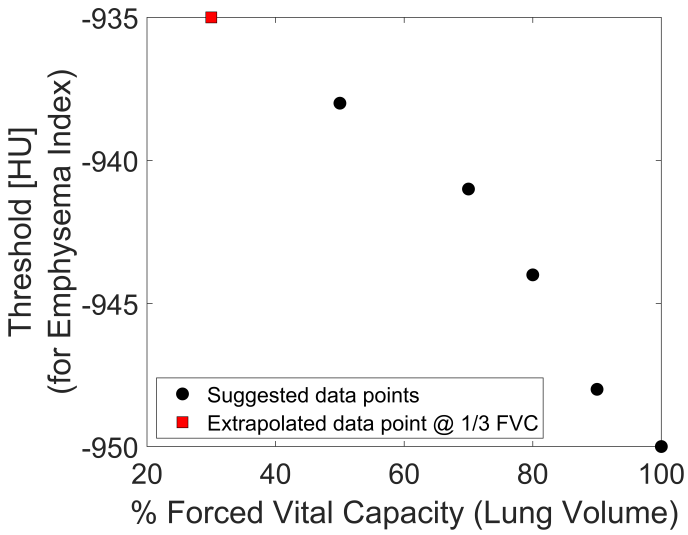

Figure 6.17: Extrapolating −935 HU threshold for CT-based relative area (RA) of lung with low attenuation. The black circles are the lung-inflation corrected values established by Medani et al. [109], the red square is the linear extrapolation of the threshold at lung inflation level of 1/3 FVC, based on the inflation level corrected values.

and the mild-moderate COPD group is greater based on ADC emphysema index ($p< 0.01$) than based on CT RA_{950} ($p< 0.05$). ROC analysis also revealed stronger separation between the healthy group and mild-moderate COPD group using either ^{3}He-based or ^{129}Xe-based ADC emphysema index (AUC= 0.87; 95% confidence interval: 0.71-1 for both) than RA_{950} (AUC=0.76; 95% confidence interval: 0.56-0.96). The stronger separation persisted regardless of the b-value used, for both gases as seen in Fig 6.20 (Table 6.6).

We remind the reader here that hyperpolarized gas ADC directly probes airspace size, whereas CT strictly measures tissue density. These two metrics are expected to be related and correlated, although subtle differences are possible. For example, if airway wall thickening accompanies airspace enlargement in the early stages of emphysema, this would partially offset the net decrease in tissue density due to airspace enlargement. In this case, quantitative CT may find similar density in healthy and early-stage emphysema, but ADC, which is not directly sensitive to airway wall

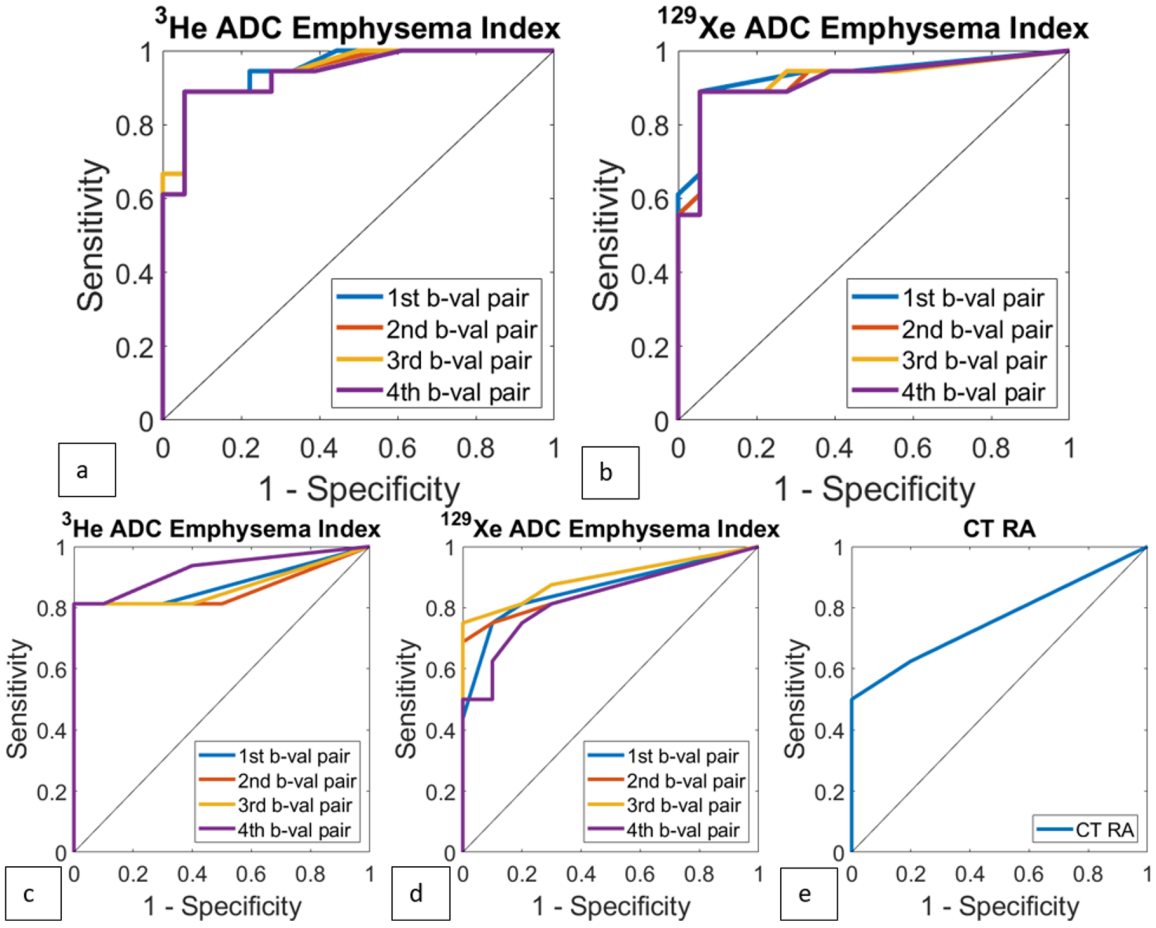

Figure 6.18: Receiver operating characteristic (ROC) curves for (a) ^{3}He-based ADC emphysema index and (b) ^{129}Xe-based ADC emphysema index assuming reference standard to be CT RA_{950}, to assess predictive power in separating "apparently healthy from "apparently emphysematous. ROC curves for (c) ^{3}He-based ADC emphysema index, (d) ^{129}Xe-based ADC emphysema index, and (e) CT RA_{950} to assess predictive power in separating healthy volunteers from participants with mild-moderate COPD. RA_{950} = fraction of CT lung voxels with attenuation coefficients less than -950 Hounsfield units.

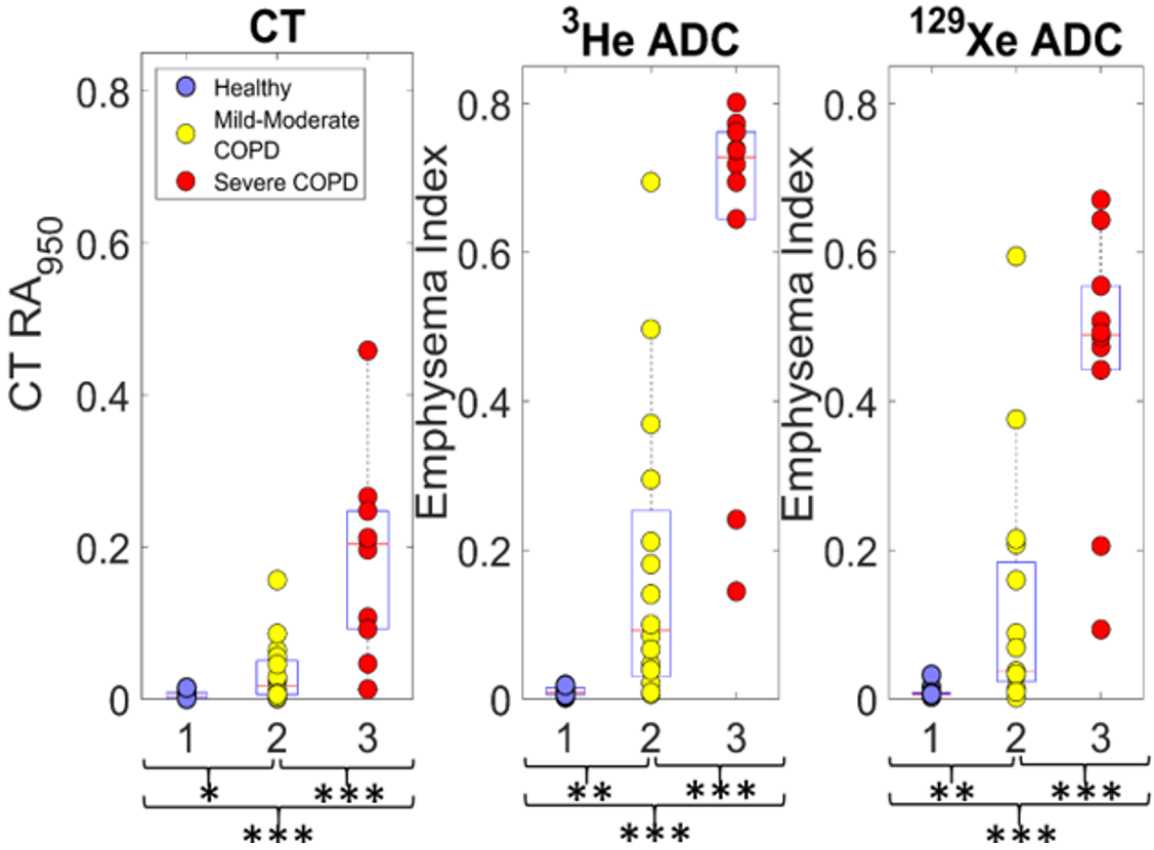

Figure 6.19: Boxplots of CT RA_{950} and emphysema index based on hyperpolarized ^{3}He and ^{129}Xe ADCs (first b-value). * $p < .05$, ** $p < .01$. *** $p < .001$. The horizontal lines inside the boxes are medians with the box edges indicating 25^{th} and 75^{th} percentiles of the distributions. ADC = apparent diffusion coefficient. RA_{950} = fraction of CT lung voxels with attenuation coefficients less than −950 Hounsfield units.

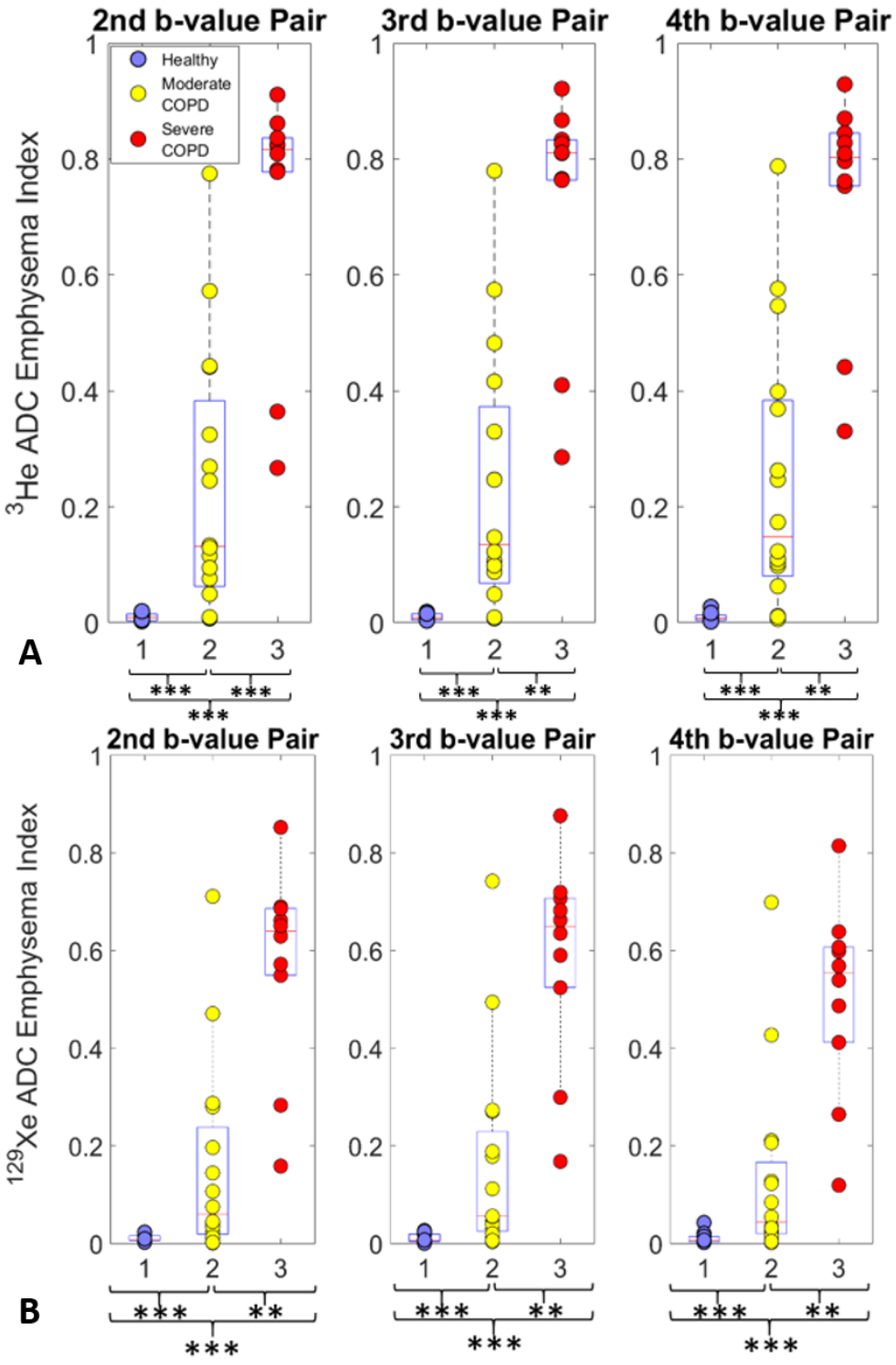

Figure 6.20: Boxplots of emphysema index based on hyperpolarized a) ^{3}He and b) ^{129}Xe ADCs for all four b-values. * $p < .05$, ** $p < .01$. *** $p < .001$. The horizontal lines inside the boxes are medians with the box edges indicating 25^{th} and 75^{th} percentiles of the distributions. ADC = apparent diffusion coefficient.

Parameter	**ROC AUC**
CT RA$_{950}$	$0.76(0.56, 0.96)$
^{3}He ADC (1^{st} *b*-value)	$0.87(0.71, 1)$
^{129}Xe ADC (1^{st} *b*-value)	$0.87(0.71, 1)$
^{3}He ADC (2^{nd} *b*-value)	$0.88(0.73, 1)$
^{129}Xe ADC (2^{nd} *b*-value)	$0.84(0.67, 1)$
^{3}He ADC (3^{rd} *b*-value)	$0.87(0.71, 1)$
^{129}Xe ADC (3^{rd} *b*-value)	$0.89(0.75, 1)$
^{3}He ADC (4^{th} *b*-value)	$0.88(0.73, 1)$
^{129}Xe ADC (4^{th} *b*-value)	$0.84(0.67, 1)$

Table 6.5: ROC AUC is presented as the predictive power of ^{3}He and ^{129}Xe ADC emphysema indices and CT RA$_{950}$ in separating the healthy group from that with mild-moderate COPD. Data given in parentheses represent 95% confidence interval. ROC = receiver operating characteristics, AUC = area under the curve. RA$_{950}$ = relative lung area with low attenuation coefficients < -950.

thickening, but is highly sensitive to airway enlargement, may detect subtle physiopathalogical changes in the lung microstructure in beginning stages of the disease. This situation is consistent with recent results shown by Ruppert et al. involving dissolved-phase ^{129}Xe, which showed that elevated alveolar wall thickness based on hyperpolarized ^{129}Xe MRI may be an indicator of early-stage lung disease and emphysema [58].

The first observations that measured diffusivity values from diffusion-weighted MRI scans are sensitive to early stage lung disease dates back to the mid 2000's. For example, Fain et al. demonstrated pre-symptomatic detection of degraded pulmonary function in smokers by using diffusion-weighted ^{3}He MRI in 2006 [50]. And later, in a longitudinal study of ex-smokers with COPD, Kirby et al demonstrated detection of early emphysematous changes using ADC values prior to any significant changes in pulmonary function tests [51]. Our results further establish the utility of ADC values in detecting signs of early stage physiological and structural changes in the smoker lungs.

6.4.4 Comparison of ADC-based emphysema index, quantitative CT, and PFT metrics

Although CT is the most widespread imaging technique to visualize and characterize emphysema burden in COPD patients with emphysema, non-imaging based pulmonary function tests (PFTs) are even more commonly used for diagnosing and characterizing emphysema. Therefore, it is vital not only to compare performance of hyperpolarized ^{3}He and ^{129}Xe ADC emphysema indices with quantitative CT, but to vet our ADC-based metric against PFT metrics such as percent predicted FEV_1, that are used to diagnose COPD, and percent predicted DLCO and RV/TLC, that is used to diagnose emphysema in particular.

In our study, percentage predicted DLCO was moderately correlated with each of ^{3}He-based ($r = -0.81, p < .001$), ^{129}Xe-based ($r = -0.80, p < .001$) emphysema index and RA_{950} ($r = -0.61, p < .001$) in participants with COPD (Fig 6.21a-c). Recall from Sec 6.2.2.2 that DLCO is a measure of gas exchange between the air in the lungs and the blood circulatory system. Compromised surface-to-volume ratio observed in lungs with substantial parenchymal tissue damage impairs gas exchange. Therefore, in COPD subjects with the emphysema subtype, this impairment is reflected in suppressed DLCO values, which explains the negative correlation between DLCO and ADC emphysema indices and CT RA. A noteworthy observation is the degree of correlation between our ADC-based metric and DLCO, compared with CT-based metric and DLCO. The higher degree of correlation between ADC-based emphysema index and DLCO (as compared to CT RA and DLCO) suggests that our ADC-based technique is a more sensitive (although indirect) measure of emphysema-induced gas exchange impairment, in addition to higher early-stage sensitivity to structural changes than CT RA.

Our reported values for correlation coefficients between DLCO and ADC-based metric are similar to that obtained in the study done by Matin et al., where they found the correlation coefficient between whole-lung ^{129}Xe mean ADC and DLCO to be

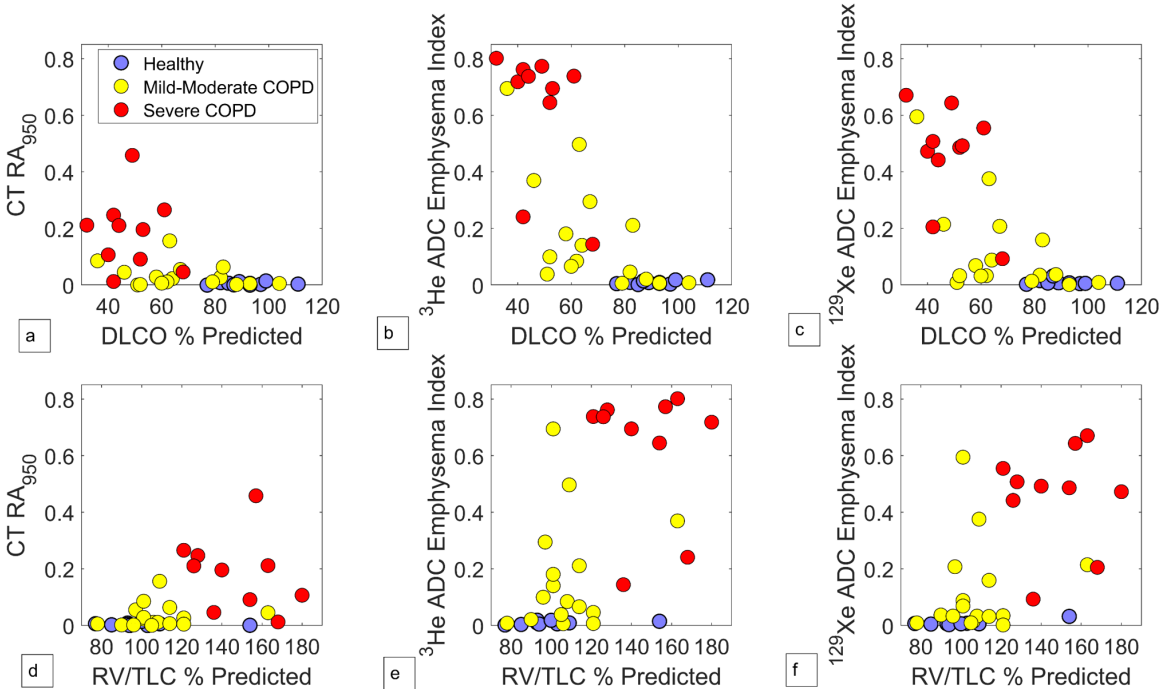

Figure 6.21: Scatter plots of (a) CT RA_{950} versus DLCO % predicted, (b) ^{3}He-based ADC emphysema index versus DLCO % predicted, (c) ^{129}Xe-based ADC emphysema index versus DLCO % predicted, (d) CT RA_{950} versus RV/TLC % predicted, (e) ^{3}He-based ADC emphysema index versus RV/TLC % predicted, and (f) ^{129}Xe-based ADC emphysema index versus RV/TLC % predicted. ADC = apparent diffusion coefficient, DLCO = diffusing capacity of lung for carbon monoxide, RV = residual volume, TLC = total lung capacity. RA_{950} = fraction of CT lung voxels with attenuation coefficients less than −950 Hounsfield units. All plots share the same legends as given in (a).

$\rho = -0.61$ at $p < 0.005$ confidence level [56]. In a similar study of healthy volunteers and patients with COPD, Kirby et al. reported similar correlation coefficient between ^{129}Xe ADC and DLCO ($\rho = -0.79, p = .03$) [54]. However, in another study done by the same group, much stronger correlation between both ^{3}He and ^{129}Xe ADC and DLCO were reported ($\rho = -0.95, p < .05$), even though they used near-identical b-values for both their ^{3}He and ^{129}Xe studies [55]. Another interesting observation is the order-of-magnitude difference in the statistical confidence level between the reported values in both of Kirby's studies compared with our study and that done by Matin

et al. And lastly, in a study of asymptomatic smokers, Fain et al. reported similar correlation between ^{3}He ADC and percent predicted DLCO ($\rho = -0.79, p < .001$) [50].

Percentage predicted RV/TLC, another marker of emphysema, was also moderately correlated with each of ^{3}He-based ($r = 0.65, p < .001$), ^{129}Xe-based ($r = 0.61, p < .001$) emphysema index and CT RA_{950} ($r = 0.57, p < .001$) (Fig 6.21d-f). As mentioned previously in Sec 6.2.2.2, percentage predicted RV/TLC is related to emphysema-induced loss of elastic recoil in the lungs due to substantial parenchymal tissue loss. The higher the degree of lung tissue loss, the higher ratio of gas left in the lungs to total lung volume (recall that RV is measured by instructing the subject to exhale as much volume of their lungs as they possibly can). The higher degree of correlation between our ADC-based metric and RV/TLC than CT-based metric and RV/TLC is another encouraging observation in demonstrating our metric's ability to assess and characterize emphysema.

6.5 Discussion and conclusions

Apparent diffusion coefficient (ADC) maps of inhaled hyperpolarized gases have shown promise for characterizing emphysema in patients with chronic obstructive pulmonary disease (COPD), yet an easily interpreted quantitative metric has not been previously established. Inspired by emphysema index based on CT Hounsfield units, we propose a similar definition of emphysema index based on ADC. In a study sample of 36 participants, we found that emphysema index based on ^{3}He and ^{129}Xe ADC were strongly correlated ($r = 0.95, p > .001$) and both showed strong correlation with relative lung area with low attenuation on CT ($r \geq 0.85, p < 0.001$). ^{3}He-based and ^{129}Xe-based ADC emphysema indices were also highly repeatable (intraclass correlation coefficient $> .99$) and showed highly significant differences between healthy, mild-moderate, and severe COPD groups, independent of the b-values used ($p < .01$).

Parameter	**Mean ^{3}He**	**Mean ^{129}Xe**	**Mean CT**	**^{3}He ADC EI**	**^{129}Xe ADC EI**	**CT RA_{950}**	**CT RA_{935}**	**CT RA_{910}**
FEV_1^*	−0.67 (<0.001)	−0.63 (<0.001)	0.53 (<0.001)	−0.72 (<0.001)	−0.69 (<0.001)	−0.63 (<0.001)	−0.64 (<0.001)	−0.65 (<0.001)
FEV_1/FVC	−0.75 (<0.001)	−0.72 (<0.001)	0.69 (<0.001)	−0.79 (<0.001)	−0.73 (<0.001)	−0.72 (<0.001)	−0.73 (<0.001)	−0.74 (<0.001)
FRC	0.34 (0.044)	0.34 (0.045)	−0.44 (0.007)	0.32 (0.055)	0.33 (0.052)	0.53 (0.001)	0.51 (0.001)	0.49 (0.002)
FRC*	0.72 (<0.001)	0.71 (<0.001)	−0.67 (<0.001)	0.73 (<0.001)	0.70 (<0.001)	0.61 (<0.001)	0.61 (<0.001)	0.59 (<0.001)
FVC	0.05 (0.77)	0.04 (0.82)	−0.16 (0.35)	0.03 (0.86)	0.01 (0.96)	0.22 (0.19)	0.19 (0.27)	0.13 (0.48)
RV/TLC*	0.64 (<0.001)	0.61 (<0.001)	−0.48 (0.014)	0.65 (<0.001)	0.61 (<0.001)	0.57 (<0.001)	0.57 (<0.001)	0.55 (0.002)
DLCO*	−0.80 (<0.001)	−0.79 (<0.001)	0.50 (0.002)	−0.81 (<0.001)	−0.80 (<0.001)	−0.61 (<0.001)	−0.61 (<0.001)	−0.58 (<0.001)
Pack-Years†	0.39 (0.051)	0.36 (0.067)	−0.21 (0.29)	0.30 (0.14)	0.28 (0.17)	0.24 (0.23)	0.23 (0.25)	(0.24) (0.24)

Table 6.6: Data given are Spearman Rank correlation coefficients with associated p-value in parentheses. EI = emphysema index, ADC = apparent diffusion coefficient, HU = Hounsfield unit, FEV_1 = forced expiratory volume in 1 second, FVC = forced vital capacity, FRC = forced residual capacity, RV = residual volume, TLC = total lung capacity, DLCO = diffusing capacity of lung for carbon monoxide, RA = relative lung area with low attenuation, pack-years = no. of cigarette packs smoked per day times years of smoking. CT RA computed as fraction of voxels with attenuation coefficients less than threshold given in the subscripts. * Percent predicted. †Values computed for participants with COPD only.

Both ^{3}He-based and ^{129}Xe-based ADC emphysema indices were also correlated with pulmonary function metrics traditionally used to characterize emphysema, including diffusing capacity of lung for carbon monoxide ($r \geq .80, p < .001$) and residual volume divided by total lung capacity ($r \geq .61, p < .002$) with similar degree of correlation as quantitative CT ($r \geq .57, p < .001$).

The excellent repeatability and strong correlation between ^{3}He and ^{129}Xe ADC emphysema indices in our study sample echoes previous findings based on mean ADC values [54,56,57], but in a larger study sample containing more patients with early stage

disease. In our data set, 25% of the mild-moderate COPD group (4/16) had ADC emphysema indices outside the healthy range but RA_{950} values inside the healthy range, yet there were no patients with COPD where the opposite was true. When RA_{950} and ADC emphysema indices were used to predict mild-moderate COPD, the AUC values for ^{3}He and ^{129}Xe were higher than for RA_{950}. Taken together, these findings suggest that ADC emphysema index may offer enhanced sensitivity to early-stage disease. Similarly intriguing results have been noted in previous ADC studies [50,58]. Sensitivity to early disease would be particularly useful for research, especially in pharmaceutical development. Since emphysema is currently a terminal disease with no reversible therapeutics commercially available, earlier detection would also facilitate earlier clinical intervention to slow disease progression.

Beyond COPD, which disproportionately affects older smokers, emphysema is frequently found in younger and more radiation sensitive patients with idiopathic pulmonary fibrosis (IPF) [110] and survivors of bronchopulmonary dysplasia [111]. Dissolved-phase ^{129}Xe has been investigated for characterizing fibrosis in IPF [112], and ADC emphysema index could provide a valuable adjunct for clinical management in these patients since comorbid emphysema is associated with poor outcomes [110].

An important limitation of our quantitative CT comparisons is that CT scans were performed at a lung inflation level of 1/3 FVC rather than the recommended inflation level of TLC [113]. Measurements at lower inflation levels are known to underestimate emphysema burden [109], and we acknowledge that our quantitative CT results might have been different at full inflation. Limitations of ADC relative to CT include much coarser spatial resolution and longer breath-hold times. However, our results indicate that the limited spatial resolution of ADC does not compromise its ability to quantify emphysema burden, and CT-like spatial resolution is probably not necessary for useful regional analysis. Further, all COPD subjects in our study tolerated the 15-second breath hold required for the ^{129}Xe ADC scan, and scan duration would be up to 60% shorter for a single-b-value non-research scan.

Hyperpolarized gas MRI is an expensive procedure, which raises the bar for clinical usefulness. However, it is clear that diffusion-weighted ^{129}Xe imaging, especially when combined with ventilation imaging, dissolved-phase imaging of gas exchange, and emerging ^{1}H MRI methods for parenchyma characterization [114], provides a unique and powerful combination of functional and structural information with segmental or subsegmental anatomical detail. Such a diagnostic platform could offer a more precise approach to emphysema therapies such as endotracheal valve placement and lung volume reduction surgery [108] in this nascent era of precision medicine [115]. In this context, the reduced ability of ^{129}Xe to penetrate highly emphysematous regions might not be a serious limitation, as persistent ventilation defects that do not permit ADC measurement would be candidates for regional intervention based on ventilation loss alone.

In summary, we propose herein a quantitative framework for characterizing emphysema burden in human subjects based on hyperpolarized gas diffusion measurements [94]. Within this framework, we found the basic performance of apparent diffusion coefficient (ADC) emphysema index to be largely insensitive to gas type and b-value. Widespread application of ADC emphysema index would still require standardizing on a particular gas (unequivocally ^{129}Xe, due to its abundance), inflation level, and diffusion-sensitizing gradient parameters, although our results indicate the precise choices are not crucial. Because the clinical definition of chronic obstructive pulmonary disease (COPD) encompasses both airflow limitation and emphysema, ADC emphysema index would provide a useful complement to ventilation defect percentage for staging COPD severity and monitoring disease progression.

Appendix A

Writing flux in terms of the magnetization

The magnetic flux Φ is defined as $\Phi \equiv \int_{\text{area}} \vec{B} \cdot d\vec{S}$. Invoking Stokes' theorem that states $\int d\vec{S} \cdot (\vec{\nabla} \times \vec{a}) = \oint d\vec{l} \cdot \vec{a}$, and realizing that $\vec{B} = \vec{\nabla} \times \vec{A}$, we write

$$\Phi = \int_{area} \vec{B} \cdot d\vec{S} = \int_{area} (\vec{\nabla} \times \vec{A}) \cdot d\vec{S} = \oint d\vec{l} \cdot \vec{A}, \tag{A.1}$$

where $\vec{A}$ is the magnetic field vector potential. Since we are interested in detecting signal generated by the magnetic field of the sample, we can write the magnetic field vector potential in terms of the magnetization. The current density in the coil is the curl of the magnetization ($\vec{M}(\vec{r})$) the coil sees and we write

$$\vec{J}(\vec{r}) = \vec{\nabla} \times \vec{M}(\vec{r}). \tag{A.2}$$

Therefore, the vector potential evaluated at position $\vec{r}$ originating from a current source $\vec{r}'$ can be written in terms of the magnetization as

$$\vec{A}(\vec{r}) = \frac{\mu_0}{4\pi} \int d^3r' \frac{\vec{J}(\vec{r}')}{|\vec{r} - \vec{r}'|} = \frac{\mu_0}{4\pi} \int d^3r' \frac{\vec{\nabla} \times \vec{M}(\vec{r})}{|\vec{r} - \vec{r}'|}. \tag{A.3}$$

As done in Haacke [68], invoking the vector identity, $\vec{a}\cdot(\vec{b}\times\vec{c}) = -(\vec{a}\times\vec{b})\cdot\vec{c}$, the magnetization flux is given by

$$\begin{aligned}\Phi_M &= \oint d\vec{l}\cdot\left[\frac{\mu_0}{4\pi}\int d^3r'\frac{\vec{\nabla}'\times\vec{M}\left(\vec{r}'\right)}{|\vec{r}-\vec{r}'|}\right] \\ &= \frac{\mu_0}{4\pi}\int d^3r'\oint d\vec{l}\cdot\left[\left(-\vec{\nabla}'\frac{1}{|\vec{r}-\vec{r}'|}\right)\times\vec{M}\left(\vec{r}'\right)\right] \\ &= \frac{\mu_0}{4\pi}\int d^3r'\vec{M}\left(\vec{r}'\right)\cdot\left[\vec{\nabla}'\times\left(\oint\frac{d\vec{l}}{|\vec{r}-\vec{r}|'\,|}\right)\right].\end{aligned} \tag{A.4}$$

The version of the vector potential $\vec{A}$ given in A.3 for current loops or a coil is given by

$$\vec{A}\left(\vec{r}'\right) = \frac{\mu_0}{4\pi}\oint\frac{Id\vec{l}}{|\vec{r}-\vec{r}'|}. \tag{A.5}$$

We define $\overrightarrow{\mathcal{B}}^{receive}$ as the magnetic field per unit current produced by the coil, representing the receive field coil sensitivity and write

$$\overrightarrow{\mathcal{B}}^{receive}\left(\vec{r}'\right) \equiv \frac{\vec{B}\left(\vec{r}'\right)}{I} = \frac{\vec{\nabla}'\times\vec{A}}{I} = \vec{\nabla}'\times\left(\frac{\mu_0}{4\pi}\oint\frac{d\vec{l}}{|\vec{r}-\vec{r}'|}\right). \tag{A.6}$$

Finally, in terms of the magnetization, the flux is given by

$$\Phi_M(t) = \int_{\text{sample}} d^3r\,\overrightarrow{\mathcal{B}}^{receive}(\vec{r})\cdot\vec{M}(\vec{r},t). \tag{A.7}$$

Appendix B

Statistics

B.1 Diagnostic performance metrics

All diagnostic performance metrics are based on a binary ground truth diagnosis. Consider a metric used to identify a subject either as healthy or emphysematous. If the metric correctly identifies the subject as emphysematous, the result characterized as true positive. If the metric correctly identifies the subject as healthy, the result is characterized as true negative. If the test instead incorrectly identifies an emphysematous subject as healthy, the result is a false negative. Lastly, if the test incorrectly identifies a healthy subject as emphysematous, the result is a false positive. With this convention, sensitivity and specificity are defined as

$$\text{sensitivity} = \frac{\text{true positive}}{\text{true positive} + \text{false negative}} \tag{B.1}$$

$$\text{specificity} = \frac{\text{false positive}}{\text{false positive} + \text{true negative}}. \tag{B.2}$$

Another useful statistic used to assess performance of a new metric referred to as the "index test" against the ground truth metric "reference standard" is the area under (AUC) the receiver operating characteristic (ROC) curve. The ROC curve is as parametric one obtained by plotting sensitivity as y vs $(1 - \text{specificity})$ as x. Since both sensitivity and $(1 - \text{specificity})$ range between zero and one, the maximum area under the ROC curve is unity, which corresponds to perfect performance of the new

metric taking the reference standard as the ground truth. The ROC curve effectively assesses the performance of the index test (i.e. the new technique) as a function of the threshold used in the index test to diagnose a subject healthy vs emphysematous. An example of the ROC curve, and its non-parametric counter parts (1 − specificity) and sensitivity plotted as a function of ADC-based emphysema index threshold given in Fig B.1.

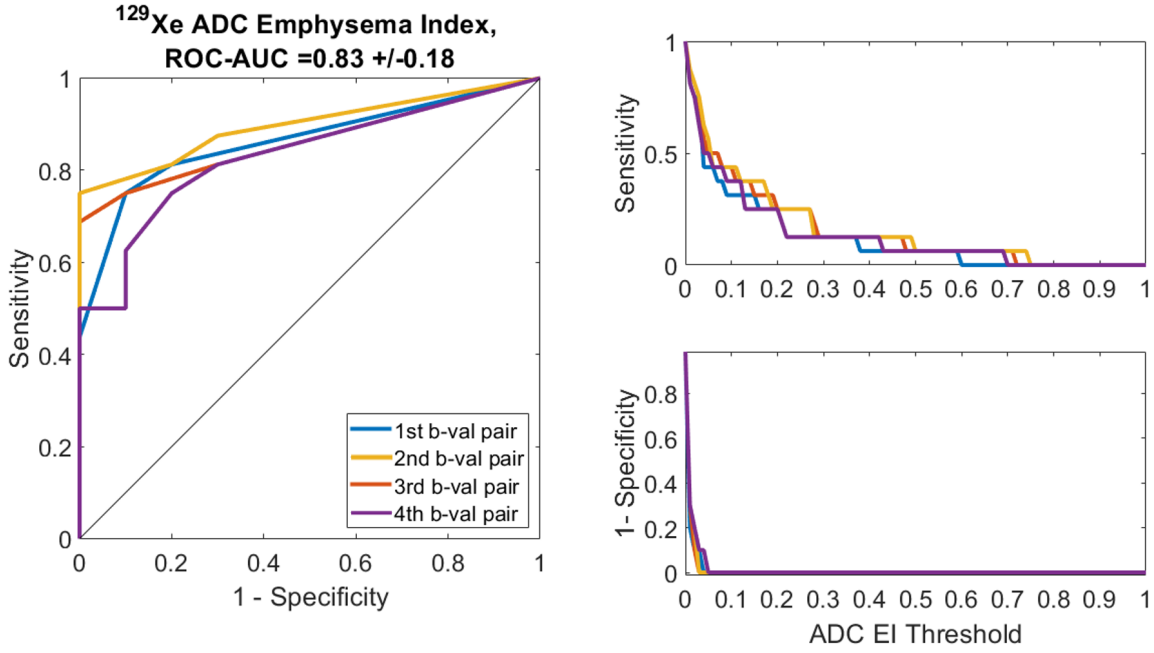

Figure B.1: An example of a ROC curve AUC and its non-parametric counterparts sensitivity and (1 − specificity) as a function of ADC-based emphysema index. The diagonal line represents the flip-of-a-coin performance (i.e. the index test's performance is 50-50 in correct diagnosis).

B.2 Intraclass correlation coefficient

Intraclass correlation coefficient (ICC) was first introduced by Fisher in 1950 and is a metric the determines correlations within a class of data, rather than correlations between two different classes of data [116]. Consider making several measurements of a the same class (e.g. weight) in a population of n subjects. For i^{th} subject and

j^{th} measurement, measurement values x_{ij} are given by

$$x_{ij} = \mu + r_i + v_{ij}, \tag{B.3}$$

where μ is a constant, namely the mean value of x for the whole population, $\mu + r_i$ is the actual value (true score) for subject i if there was no measurement error, and v_{ij} is the measurement error. If σ_r and σ_v are the the standard deviations in r and v, the sample intraclass correlation coefficient (ICC_s) is given by

$$ICC_s = \frac{k \cdot \sigma_r^2}{k \cdot \sigma_r^2 + \sigma_v^2 + (k-1)\sigma_v^2}, \tag{B.4}$$

where k is the number of measurements (in the case of repeatability data presented in chapter 6 k = 2). For large n (large population of subjects), ICC is reduced to

$$ICC = \frac{\sigma_r^2}{\sigma_r^2 + \sigma_v^2}, \tag{B.5}$$

independent of the number of measurements.

B.3 Spearman rank correlation

For sample size of n, the n raw scores X_i and Y_i having ranks R_{X_i} and R_{Y_i}, respectively, the Spearman rank correlation coefficient ρ is given by [117]

$$\begin{aligned} \rho &= \frac{COV(R_X, R_Y)}{\sigma_{R_X}\sigma_{R_Y}} \\ &= \frac{\frac{1}{n}\sum_{i=1}^{n}(R_{X_i} - \bar{R}_X)(R_{Y_i} - \bar{R}_Y)}{\sqrt{\sum_{i=1}^{n}(R_{X_i} - \bar{R}_X)^2}\sqrt{\sum_{i=1}^{n}(R_{Y_i} - \bar{R}_Y)^2}}, \end{aligned} \tag{B.6}$$

where $COV(R_X, R_Y)$ is the covariance between ranks R_X and R_Y of measurements (or scores) X and Y, and σ_{R_X} and σ_{R_Y} are their respective standard deviations.

B.4 Wilcoxon rank-sum test

The Wilcoxon rank-sum test is a nonparametric test for two populations when samples are independent. The Wilcoxon rank-sum (A.K.A. Mann-Whitney U-test) is a nonparametric test for equality of population medians of two independent samples X and Y. The statistic, U, for the X and Y distributions with N_x and N_Y number of samples, respectively, is given by the smaller of U_X and U_Y defined as [118]

$$U_X = N_X N_Y + \frac{N_X(N_X+1)}{2} - R_X \tag{B.7}$$

$$U_Y = N_X N_Y + \frac{N_Y(N_Y+1)}{2} - R_Y, \tag{B.8}$$

where R_X and R_Y are the sum of ranks in each distribution. The U statistic is then compared with the critical U value (for small sample sizes) given as a function of confidence level often chosen at $\alpha = 0.05$ in a typical statistics reference book (or based a normal distribution for large sample sizes, which is not the case in the statistics used in Chapter 6). For example, for two distributions of sample size $N_X = N_Y = 15$ at confidence level $\alpha = 0.05$ (i.e. "95% confidence"), the critical U value $U_{crit} = 64$. Therefore, if $U = min(U_X, U_Y) < 64$, the null hypothesis is rejected; the two distributions are not equal and have different medians at $\alpha = 0.05$ confidence level.

B.5 Bland-Altman analysis

The Bland-Altman analysis (often referred to as Bland-Altman plot) is a statistic used to determine if there is a bias between two measurement techniques that are designed to measure the same property. In two measurement samples, the ith measurements X_i and Y_i of the distributions, the difference $Y_i - X_i$ is plotted along the y-axis and the mean $\frac{Y_i+X_i}{2}$ is plotted along the x-axis. Often times, the 95% confidence intervals of the difference distribution is also plotted (horizontal lines at $\pm 1.96\sigma_d$, where σ_d is the standard deviation of the difference distribution). Since high correlation does

not necessarily imply that there is good agreement between the two methods, Bland-Altman plot is used to determine the degree of bias between the two measurements, and to see if this bias is dependent on the magnitude of the measured values.

Appendix C

Circularly polarized coil

A homebuilt bird-cage quadrature (circularly polarized) transmit-receive RF coil was designed and built on an acrylic cylinder form. The coil is tuned to the resonant frequency of ^{3}He at 1.5 Tesla, 48.64 MHz, as seen in as seen in Fig C.1. This coil was

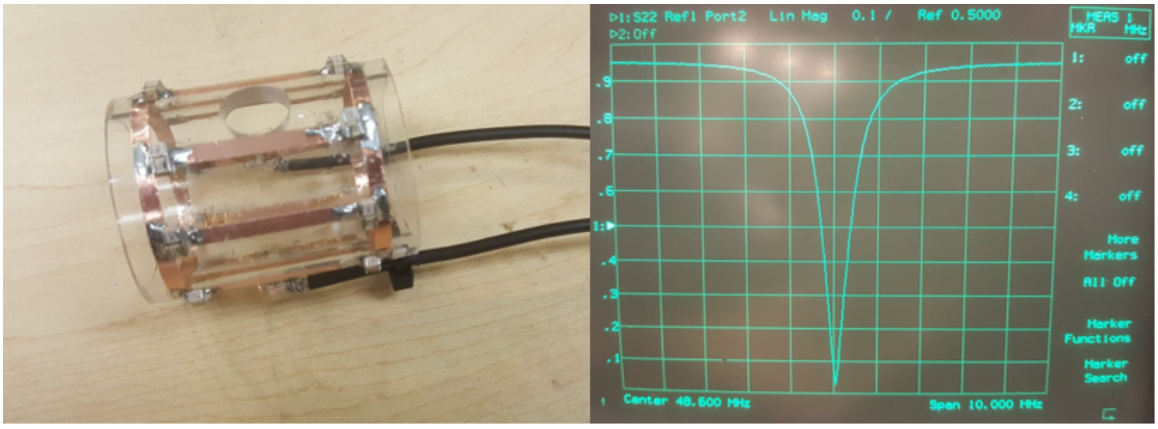

Figure C.1: Shown are the image of the quadrature coil and its frequency response as observed by a network analyzer. The resonant frequency is 48.64 MHz. The whole between the two top legs is where the phantom would be positioned such that the pellet would be centered with the center of the coil for optimal and homogeneous flip angle.

designed on a smaller cylindrical form than the linear coil used in our experiments presented in Chapters 4 and 5.

Since the overall size of the pellet chamber stayed roughly the same, we can gain signal-to-noise-ratio (SNR) by making our coil smaller and quadrature. I designed

and built a new quadrature coil with an outside diameter (OD) = 1.5 in (instead of previously OD = 1.75 in). For the same geometry, quadrature coils inherently have $\sqrt{2}$ higher SNR than linear coils. This increase in SNR combined with reduction of volume encapsulated with the coil should result in an SNR gain of 80%. However, due to unresolved noise spikes at the time of the experiment, and considering the time-sensitive nature of the experiment, this coil was not used in the experiments presented in this thesis.

Bibliography

[1] F. Bloch, "Nuclear induction," Physical Review, vol. 70, no. 7-8, p. 460, 1946.

[2] E. M. Purcell, H. C. Torrey, and R. V. Pound, "Resonance absorption by nuclear magnetic moments in a solid," Physical Review, vol. 69, no. 1-2, p. 37, 1946.

[3] P. C. Lauterbur, "Image formation by induced local interactions: examples employing nuclear magnetic resonance," Nature, vol. 242, no. 5394, pp. 190–191, 1973.

[4] P. Mansfield and P. K. Grannell, "NMR diffraction in solids," Journal of Physics C: Solid State Physics, vol. 6, no. 22, p. L422, 1973.

[5] K. Mooney, "Hyperpolarized gas diffusion MRI using steady state free precession pulse sequences," Thesis, University of Virginia, 2012.

[6] M. A. Bouchiat, T. Carver, and C. Varnum, "Nuclear polarization in ^{3}He gas induced by optical pumping and dipolar exchange," Physical Review Letters, vol. 5, no. 8, p. 373, 1960.

[7] E. Babcock, I. Nelson, S. Kadlecek, B. Driehuys, L. Anderson, F. W. Hersman, and T. G. Walker, "Hybrid spin-exchange optical pumping of He-3," Physical Review Letters, vol. 91, no. 12, p. 123003, 2003.

[8] J. Singh, "Alkali-hybrid spin-exchange optically-pumped polarized ^{3}He targets used for studying neutron structure," Thesis, University of Virginia, 2010.

[9] K. Mooney, G. Miller, and P. Dolph, "A 3-liter capacity, hybrid spin-exchange ^{3}He polarizer for medical imaging (abstract)," ISMRM, 2009, Honolulu.

[10] G. Cates, D. Benton, M. Gatzke, W. Happer, K. Hasson, and N. Newbury, "Laser production of large nuclear-spin polarization in frozen xenon," Physical Review Letters, vol. 65, no. 20, p. 2591, 1990.

[11] I. Ruset, S. Ketel, and F. W. Hersman, "Optical pumping system design for large production of hyperpolarized Xe-129," Physical Review Letters, vol. 96, no. 5, p. 053002, 2006.

[12] M. Albert, G. Cates, B. Driehuys, W. Happer, B. Saam, C. Springer, and A. Wishnia, "Biological magnetic resonance imaging using laser-polarized ^{129}Xe," Nature, vol. 370, no. 6486, pp. 199–201, 1994.

[13] J. P. Mugler III and T. A. Altes, "Hyperpolarized ^{129}Xe MRI of the human lung," Journal of Magnetic Resonance Imaging, vol. 37, no. 2, pp. 313–331, 2013.

[14] N. Peacock, D. Robinson, M. Forrest, P. Wilcock, and V. Sannikov, "Measurement of the electron temperature by Thomson scattering in tokamak T3," Nature, vol. 224, no. 5218, pp. 488–490, 1969.

[15] H. Eubank, R. Goldston, V. Arunasalam, M. Bitter, K. Bol, D. Boyd, N. Bretz, J.-P. Bussac, S. Cohen, P. Colestock, et al., "Neutral-beam-heating results from the Princeton Large Torus," Physical Review Letters, vol. 43, no. 4, p. 270, 1979.

[16] F. Wagner, G. Becker, K. Behringer, D. Campbell, A. Eberhagen, W. Engelhardt, G. Fussmann, O. Gehre, J. Gernhardt, G. v. Gierke, et al., "Regime of improved confinement and high beta in neutral-beam-heated divertor discharges of the asdex tokamak," Physical Review Letters, vol. 49, no. 19, p. 1408, 1982.

[17] Jet Team et al., "Fusion energy production from a deuterium-tritium plasma in the JET tokamak," Nuclear Fusion, vol. 32, no. 2, p. 187, 1992.

[18] M. Keilhacker, A. Gibson, C. Gormezano, P. Lomas, P. Thomas, M. Watkins, P. Andrew, B. Balet, D. Borba, C. Challis, et al., "High fusion performance from deuterium-tritium plasmas in JET," Nuclear Fusion, vol. 39, no. 2, p. 209, 1999.

[19] F. Romanelli, P. Barabaschi, D. Borba, G. Federici, L. Horton, R. Neu, D. Stork, and H. Zohm, "Fusion electricity: A roadmap to the realization of fusion energy," European Fusion Development Agreement, 2012.

[20] R. Kulsrud, H. Furth, E. Valeo, and M. Goldhaber, "Fusion reactor plasmas with polarized nuclei," Physical Review Letters, vol. 49, no. 17, p. 1248, 1982.

[21] A. Sandorfi, A. Deur, C. Hanretty, G. Jackson, M. Lanctot, J. Liu, M. Lowry, G. Miller, D. Pace, S. Smith, et al., "Polarized fusion, its implications and plans for direct measurements in a tokamak," arXiv preprint arXiv:1703.06165, 2017.

[22] R. Aymar, P. Barabaschi, and Y. Shimomura, "The ITER design," Plasma Physics and Controlled Fusion, vol. 44, no. 5, p. 519, 2002.

[23] D. Pace, M. Lanctot, G. Jackson, A. M. Sandorfi, S. Smith, and X. Wei, "Controlling fusion yield in tokamaks with spin polarized fuel, and feasibility studies on the DIII-D tokamak," Journal of Fusion Energy, vol. 35, no. 1, pp. 54–62, 2016.

[24] H.-S. Bosch and G. Hale, "Improved formulas for fusion cross-sections and thermal reactivities," Nuclear Fusion, vol. 32, no. 4, p. 611, 1992.

[25] A. Sandorfi and A. DAngelo, "Prospects for direct in situ tests of polarization survival in a tokamak," in Nuclear Fusion with Polarized Fuel, pp. 115–130, Springer, 2016.

[26] R. Kulsrud, E. Valeo, and S. Cowley, "Physics of spin-polarized plasmas," Nuclear Fusion, vol. 26, no. 11, p. 1443, 1986.

[27] C. D. Bass, C. Bade, M. Blecher, A. Caracappa, A. D'Angelo, A. Deur, G. Dezern, H. Glueckler, C. Hanretty, D. Ho, et al., "A portable cryostat for the cold transfer of polarized solid HD targets: HDice-I," Nuclear Instruments and Methods in Physics Research Section A: Accelerators, Spectrometers, Detectors and Associated Equipment, vol. 737, pp. 107–116, 2014.

[28] S. Tafti, A. Deur, J. Liu, M. Lowry, G. Miller, A. Sandorfi, K. Wei, X. Wei, and X. Zheng, "Progress toward spin-polarized fusion: Performance of laser-polarized He-3 during permeation into tokamak pellets," in ISPS, p. 181, 2018.

[29] J. Liu, "The proton spin structure function g_2 at low $Q2$ and applications of polarized ^{3}He," Thesis, University of Virginia, 2017.

[30] A. Nikroo, D. Czechowicz, E. Castillo, and J. Pontelandolfo, "Recent progress in fabrication of high-strength glow discharge polymer shells by optimization of coating parameters," Fusion Science and Technology, vol. 41, no. 3P1, pp. 214–219, 2002.

[31] M. M. Lowry, C. D. Bass, A. Deur, G. Dezern, C. Hanretty, D. Ho, T. Kageya, D. Kashy, M. Khandaker, V. Laine, et al., "A cryostat to hold frozen-spin polarized HD targets in CLAS: HDice-II," Nuclear Instruments and Methods in Physics Research Section A: Accelerators, Spectrometers, Detectors and Associated Equipment, vol. 815, pp. 31–41, 2016.

[32] L. Baylor, T. Jernigan, P. Parks, G. Antar, N. Brooks, S. Combs, D. Fehling, C. Foust, W. Houlberg, and G. Schmidt, "Comparison of deuterium pellet injection from different locations on the DIII-D tokamak," Nuclear Fusion, vol. 47, no. 11, p. 1598, 2007.

[33] Y. Ohno, H. Koyama, T. Yoshikawa, K. Matsumoto, M. Takahashi, M. Van Cauteren, and K. Sugimura, "T_2^* measurements of 3-T MRI with ultrashort TE's: capabilities of pulmonary function assessment and clinical stage classification in smokers," American Journal of Roentgenology, vol. 197, no. 2, pp. W279–W285, 2011.

[34] I. Benlala, P. Berger, P.-O. Girodet, C. Dromer, J. Macey, F. Laurent, and G. Dournes, "Automated Volumetric Quantification of Emphysema Severity by Using Ultrashort Echo Time MRI: Validation in Participants with Chronic Obstructive Pulmonary Disease," Radiology, vol. 292, no. 1, pp. 216–225, 2019.

[35] D. Kramer, "DOE begins rationing Helium-3," PhT, vol. 63, no. 6, p. 22, 2010.

[36] T. Feder, "US government agencies work to minimize damage due to Helium-3 shortfall," Physics today, vol. 62, no. 10, p. 21, 2009.

[37] A. Cho, "Helium-3 shortage could put freeze on low-temperature research," 2009.

[38] T. A. Altes, P. L. Powers, J. Knight-Scott, G. Rakes, T. A. Platts-Mills, E. E. de Lange, B. A. Alford, J. P. Mugler III, and J. R. Brookeman, "Hyperpolarized ^{3}He MR lung ventilation imaging in asthmatics: preliminary findings," Journal of Magnetic Resonance Imaging: An Official Journal of the International Society for Magnetic Resonance in Medicine, vol. 13, no. 3, pp. 378–384, 2001.

[39] M. Kirby, S. Svenningsen, N. Kanhere, A. Owrangi, A. Wheatley, H. O. Coxson, G. E. Santyr, N. A. Paterson, D. G. McCormack, and G. Parraga, "Pulmonary ventilation visualized using hyperpolarized helium-3 and xenon-129 magnetic resonance imaging: differences in COPD and relationship to emphysema," Journal of Applied Physiology, vol. 114, no. 6, pp. 707–715, 2013.

[40] T. Altes, J. Mugler, I. Dregely, S. Ketel, I. Ruset, E. deLange, F. Hersman, and K. Ruppert, "Hyperpolarized xenon-129 ventilation MRI: preliminary results

in normal subjects and patients with lung disease," in Proceedings of the 18th Annual Meeting of ISMRM, Stockholm, Sweden, p. 2529, 2010.

[41] Y.-S. Sun, S.-W. Peng, K.-H. Lin, and J.-Y. Cheng, "Electrotaxis of lung cancer cells in ordered three-dimensional scaffolds," Biomicrofluidics, vol. 6, no. 1, p. 014102, 2012.

[42] K. F. Rabe, "Global Initiative for Chronic Obstructive Lung Disease. Global strategy for the diagnosis, management, and prevention of chronic obstructive pulmonary disease. GOLD executive summary," Am J Respir Crit Care Med, vol. 176, pp. 532–555, 2007.

[43] N. Muller, "'density mask'. An objective method to quantify emphysema using computed tomography," Chest, vol. 94, pp. 782–787, 1988.

[44] D. A. Lynch and M. L. Al-Qaisi, "Quantitative CT in COPD," Journal of Thoracic Imaging, vol. 28, no. 5, p. 284, 2013.

[45] M. Salerno, E. E. de Lange, T. A. Altes, J. D. Truwit, J. R. Brookeman, and J. P. Mugler, "Emphysema: hyperpolarized helium-3 diffusion MR imaging of the lungs compared with spirometric indexes−initial experience," Radiology, vol. 222, no. 1, pp. 252–260, 2002.

[46] X. J. Chen, L. W. Hedlund, H. E. Möller, M. S. Chawla, R. R. Maronpot, and G. A. Johnson, "Detection of emphysema in rat lungs by using magnetic resonance measurements of ^{3}He diffusion," Proceedings of the National Academy of Sciences, vol. 97, no. 21, pp. 11478–11481, 2000.

[47] K. Emami, E. Chia, S. Kadlecek, J. P. MacDuffie-Woodburn, J. Zhu, S. Pickup, A. Blum, M. Ishii, and R. R. Rizi, "Regional correlation of emphysematous changes in lung function and structure: a comparison between pulmonary function testing and hyperpolarized MRI metrics," Journal of Applied Physiology, vol. 110, no. 1, pp. 225–235, 2011.

[48] J. F. Mata, T. A. Altes, J. Cai, K. Ruppert, W. Mitzner, K. D. Hagspiel, B. Patel, M. Salerno, J. R. Brookeman, E. E. De Lange, et al., "Evaluation of emphysema severity and progression in a rabbit model: comparison of hyperpolarized ^{3}He and ^{129}Xe diffusion MRI with lung morphometry," Journal of Applied Physiology, vol. 102, no. 3, pp. 1273–1280, 2007.

[49] S. Diaz, I. Casselbrant, E. Piitulainen, G. Pettersson, P. Magnusson, B. Peterson, P. Wollmer, P. Leander, O. Ekberg, and P. Akeson, "Hyperpolarized ^{3}He apparent diffusion coefficient MRI of the lung: reproducibility and volume dependency in healthy volunteers and patients with emphysema," Journal of Magnetic Resonance Imaging: An Official Journal of the International Society for Magnetic Resonance in Medicine, vol. 27, no. 4, pp. 763–770, 2008.

[50] S. B. Fain, S. R. Panth, M. D. Evans, A. L. Wentland, J. H. Holmes, F. R. Korosec, M. J. O'Brien, H. Fountaine, and T. M. Grist, "Early emphysematous changes in asymptomatic smokers: detection with ^{3}He MR imaging," Radiology, vol. 239, no. 3, pp. 875–883, 2006.

[51] M. Kirby, L. Mathew, A. Wheatley, G. E. Santyr, D. G. McCormack, and G. Parraga, "Chronic obstructive pulmonary disease: longitudinal hyperpolarized ^{3}He MR imaging," Radiology, vol. 256, no. 1, pp. 280–289, 2010.

[52] S. S. Kaushik, Z. I. Cleveland, G. P. Cofer, G. Metz, D. Beaver, J. Nouls, M. Kraft, W. Auffermann, J. Wolber, H. P. McAdams, et al., "Diffusion-weighted hyperpolarized ^{129}Xe MRI in healthy volunteers and subjects with chronic obstructive pulmonary disease," Magnetic Resonance in Medicine, vol. 65, no. 4, pp. 1154–1165, 2011.

[53] A. Ouriadov, A. Farag, M. Kirby, D. G. McCormack, G. Parraga, and G. E. Santyr, "Lung morphometry using hyperpolarized ^{129}Xe apparent diffusion coeffi-

cient anisotropy in chronic obstructive pulmonary disease," Magnetic Resonance in Medicine, vol. 70, no. 6, pp. 1699–1706, 2013.

[54] M. Kirby, S. Svenningsen, A. Owrangi, A. Wheatley, A. Farag, A. Ouriadov, G. E. Santyr, R. Etemad-Rezai, H. O. Coxson, D. G. McCormack, et al., "Hyperpolarized ^{3}He and ^{129}Xe MR imaging in healthy volunteers and patients with chronic obstructive pulmonary disease," Radiology, vol. 265, no. 2, pp. 600–610, 2012.

[55] M. Kirby, D. Pike, H. O. Coxson, D. G. McCormack, and G. Parraga, "Hyperpolarized ^{3}He ventilation defects used to predict pulmonary exacerbations in mild to moderate chronic obstructive pulmonary disease," Radiology, vol. 273, no. 3, pp. 887–896, 2014.

[56] T. N. Matin, N. Rahman, A. H. Nickol, M. Chen, X. Xu, N. J. Stewart, T. Doel, V. Grau, J. M. Wild, and F. V. Gleeson, "Chronic obstructive pulmonary disease: lobar analysis with hyperpolarized ^{129}Xe MR imaging," Radiology, vol. 282, no. 3, pp. 857–868, 2017.

[57] N. J. Stewart, H.-F. Chan, P. J. Hughes, F. C. Horn, G. Norquay, M. Rao, D. P. Yates, R. H. Ireland, M. Q. Hatton, B. A. Tahir, et al., "Comparison of ^{3}He and ^{129}Xe MRI for evaluation of lung microstructure and ventilation at 1.5 T," Journal of magnetic resonance imaging, vol. 48, no. 3, pp. 632–642, 2018.

[58] K. Ruppert, K. Qing, J. T. Patrie, T. A. Altes, and J. P. Mugler III, "Using hyperpolarized xenon-129 MRI to quantify early-stage lung disease in smokers," Academic radiology, vol. 26, no. 3, pp. 355–366, 2019.

[59] L. Mathew, M. Kirby, R. Etemad-Rezai, A. Wheatley, D. G. McCormack, and G. Parraga, "Hyperpolarized ^{3}He magnetic resonance imaging: preliminary evaluation of phenotyping potential in chronic obstructive pulmonary disease," European Journal of Radiology, vol. 79, no. 1, pp. 140–146, 2011.

[60] D. A. Yablonskiy, A. L. Sukstanskii, J. D. Quirk, J. C. Woods, and M. S. Conradi, "Probing lung microstructure with hyperpolarized noble gas diffusion MRI: theoretical models and experimental results," Magnetic Resonance in Medicine, vol. 71, no. 2, pp. 486–505, 2014.

[61] F. Colegrove, L. Schearer, and G. Walters, "Polarization of he 3 gas by optical pumping," Physical Review, vol. 132, no. 6, p. 2561, 1963.

[62] A. W. Overhauser, "Polarization of nuclei in metals," Physical Review, vol. 92, no. 2, p. 411, 1953.

[63] P. Anthony, R. Arnold, H. Band, H. Borel, P. Bosted, V. Breton, G. Cates, T. Chupp, F. Dietrich, J. Dunne, et al., "Determination of the neutron spin structure function," Physical Review Letters, vol. 71, no. 7, p. 959, 1993.

[64] M. Romalis, "Laser-Polarized He-3 Target Used for a Precision Measurement of the Neutron Spin Structure," tech. rep., Stanford Linear Accelerator Center, Menlo Park, CA (US), 2003.

[65] S. Appelt, A. B.-A. Baranga, C. Erickson, M. Romalis, A. Young, and W. Happer, "Theory of spin-exchange optical pumping of ^{3}He and ^{129}Xe," Physical Review A, vol. 58, no. 2, p. 1412, 1998.

[66] B. M. Goodson, "Nuclear magnetic resonance of laser-polarized noble gases in molecules, materials, and organisms," Journal of Magnetic Resonance, vol. 155, no. 2, pp. 157–216, 2002.

[67] M. Carl, "Characterizing microstructure of porous media using noble-gas-diffusion MRI at short time scales," Thesis, University of Virginia, 2008.

[68] R. W. Brown, Y.-C. N. Cheng, E. M. Haacke, M. R. Thompson, and R. Venkatesan, Magnetic resonance imaging: physical principles and sequence design. John Wiley & Sons, 2014.

[69] M. A. Bernstein, K. F. King, and X. J. Zhou, Handbook of MRI pulse sequences. Elsevier, 2004.

[70] J. D. Jackson, Classical electrodynamics. John Wiley & Sons, 2007.

[71] Wikipedia contributors, "Magnetic susceptibility — Wikipedia, the free encyclopedia." https://en.wikipedia.org/w/index.php?title=Magnetic_susceptibility&oldid=979431945, 2020. [Online; accessed 21-September-2020].

[72] Wikipedia contributors, "Inertial confinement fusion — Wikipedia, the free encyclopedia," 2020. [Online; accessed 20-August-2020].

[73] A. Nikroo and J. Pontelandolfo, "Fabrication of thin walled glow discharge polymer shells," Fusion Technology, vol. 38, no. 1, pp. 58–61, 2000.

[74] G. Cates, D. White, T.-R. Chien, S. Schaefer, and W. Happer, "Spin relaxation in gases due to inhomogeneous static and oscillating magnetic fields," Physical Review A, vol. 38, no. 10, p. 5092, 1988.

[75] B. Saam, W. Happer, and H. Middleton, "Nuclear relaxation of He-3 in the presence of O_2," Physical Review A, vol. 52, no. 1, p. 862, 1995.

[76] C. J. Jameson, A. K. Jameson, and J. K. Hwang, "Nuclear spin relaxation by intermolecular magnetic dipole coupling in the gas phase ^{129}Xe in oxygen," The Journal of chemical physics, vol. 89, no. 7, pp. 4074–4081, 1988.

[77] W. Fitzsimmons, L. Tankersley, and G. Walters, "Nature of surface-induced nuclear-spin relaxation of gaseous He-3," Physical Review, vol. 179, no. 1, p. 156, 1969.

[78] R. Timsit, J. Daniels, and A. May, "Nuclear Relaxation of ^{3}He Gas on Various Solid Surfaces," tech. rep., Univ. of Toronto, 1971.

[79] N. Newbury, A. Barton, G. Cates, W. Happer, and H. Middleton, "Gaseous ^{3}He magnetic dipolar spin relaxation," Physical Review A, vol. 48, no. 6, p. 4411, 1993.

[80] K. Levenberg, "A method for the solution of certain non-linear problems in least squares," Quarterly of Applied Mathematics, vol. 2, no. 2, pp. 164–168, 1944.

[81] S. Schaefer, G. Cates, T.-R. Chien, D. Gonatas, W. Happer, and T. Walker, "Frequency shifts of the magnetic-resonance spectrum of mixtures of nuclear spin-polarized noble gases and vapors of spin-polarized alkali-metal atoms," Physical Review A, vol. 39, no. 11, p. 5613, 1989.

[82] L. Schearer and G. Walters, "Nuclear spin-lattice relaxation in the presence of magnetic-field gradients," Physical Review, vol. 139, no. 5A, p. A1398, 1965.

[83] R. L. Gamblin and T. R. Carver, "Polarization and relaxation processes in He-3 gas," Physical Review, vol. 138, no. 4A, p. A946, 1965.

[84] G. Cates, S. Schaefer, and W. Happer, "Relaxation of spins due to field inhomogeneities in gaseous samples at low magnetic fields and low pressures," Physical Review A, vol. 37, no. 8, p. 2877, 1988.

[85] J. R. MacFall, H. C. Charles, R. D. Black, H. Middleton, J. C. Swartz, B. Saam, B. Driehuys, C. Erickson, W. Happer, G. D. Cates, et al., "Human lung air spaces: potential for MR imaging with hyperpolarized He-3.," Radiology, vol. 200, no. 2, pp. 553–558, 1996.

[86] H.-U. Kauczor, D. Hofmann, K.-F. Kreitner, H. Nilgens, R. Surkau, W. Heil, A. Potthast, M. V. Knopp, E. W. Otten, and M. Thelen, "Normal and abnormal pulmonary ventilation: visualization at hyperpolarized He-3 MR imaging," Radiology, vol. 201, no. 2, pp. 564–568, 1996.

[87] H.-U. Kauczor, M. Ebert, K.-F. Kreitner, H. Nilgens, R. Surkau, W. Heil, D. Hofmann, E. W. Otten, and M. Thelen, "Imaging of the lungs using ^{3}He MRI: preliminary clinical experience in 18 patients with and without lung disease," Journal of Magnetic Resonance Imaging, vol. 7, no. 3, pp. 538–543, 1997.

[88] L. F. Donnelly, J. R. MacFall, H. P. McAdams, J. M. Majure, J. Smith, D. P. Frush, P. Bogonad, H. C. Charles, and C. E. Ravin, "Cystic fibrosis: combined hyperpolarized ^{3}He-enhanced and conventional proton MR imaging in the lung-preliminary observations," Radiology, vol. 212, no. 3, pp. 885–889, 1999.

[89] J. Mugler, J. Mata, H. Wang, W. Tobias, G. Cates, J. Christopher, J. Missel, A. Reish, K. Ruppert, J. Brookeman, et al., "The apparent diffusion coefficient of ^{129}Xe in the lung: preliminary results," Proceedings of the 11^{th} International Society on Magnetic Resonance in Medicine, vol. 769, 2004.

[90] B. T. Saam, D. A. Yablonskiy, V. D. Kodibagkar, J. C. Leawoods, D. S. Gierada, J. D. Cooper, S. S. Lefrak, and M. S. Conradi, "MR imaging of diffusion of ^{3}He gas in healthy and diseased lungs," Magnetic Resonance in Medicine: An Official Journal of the International Society for Magnetic Resonance in Medicine, vol. 44, no. 2, pp. 174–179, 2000.

[91] A. Sindile, I. Muradian, M. Hrovat, D. Johnson, F. Hersman, and S. Patz, "Human pulmonary diffusion-weighted imaging at 0.2 T with hyperpolarized ^{129}Xe," in Proceedings of the 15th Annual Meeting of ISMRM, Berlin, Germany, vol. 1290, 2007.

[92] D. A. Yablonskiy, A. L. Sukstanskii, J. C. Leawoods, D. S. Gierada, G. L. Bretthorst, S. S. Lefrak, J. D. Cooper, and M. S. Conradi, "Quantitative in vivo assessment of lung microstructure at the alveolar level with hyperpolarized

^{3}He diffusion MRI," Proceedings of the National Academy of Sciences, vol. 99, no. 5, pp. 3111–3116, 2002.

[93] D. A. Yablonskiy, A. L. Sukstanskii, J. C. Woods, D. S. Gierada, J. D. Quirk, J. C. Hogg, J. D. Cooper, and M. S. Conradi, "Quantification of lung microstructure with hyperpolarized ^{3}He diffusion MRI," Journal of Applied Physiology, vol. 107, no. 4, pp. 1258–1265, 2009.

[94] S. Tafti, W. J. Garrison, J. P. Mugler III, Y. M. Shim, T. A. Altes, J. F. Mata, E. E. de Lange, G. D. Cates Jr, A. M. Ropp, C. Wang, et al., "Emphysema index based on hyperpolarized ^{3}He or ^{129}Xe diffusion MRI: Performance and comparison with quantitative CT and pulmonary function tests," Radiology, p. 192804, 2020.

[95] S. Tafti, W. Garrison, Y. Mugler, John Shim, T. Altes, J. Mata, N. Tustison, K. Qing, E. de Lange, G. Cates, and G. W. Miller, "Lobar Emphysema Index Based on Hyperpolarized He-3 Diffusion-Weighted MRI (Abstract)," Biomedical Engineering Society, 2017, Phoenix, Arizona.

[96] S. Tafti, W. Garrison, Y. Mugler, John Shim, T. Altes, J. Mata, N. Tustison, K. Qing, E. de Lange, G. Cates, and G. W. Miller, "Emphysema Index based on Hyperpolarized He-3 and Xe-129 ADC (Abstract)," ISMRM, 2018, Paris, France.

[97] S. Tafti, W. Garrison, Y. Mugler, John Shim, T. Altes, J. Mata, N. Tustison, K. Qing, E. de Lange, G. Cates, and G. W. Miller, "Emphysema Index based on Hyperpolarized He-3 and Xe-129 ADC (Abstract)," 23^{rd} International SPIN Symposium, 2018, Ferrara, Italy.

[98] R. S. Virgincar, Z. I. Cleveland, S. Sivaram Kaushik, M. S. Freeman, J. Nouls, G. P. Cofer, S. Martinez-Jimenez, M. He, M. Kraft, J. Wolber, et al., "Quantitative analysis of hyperpolarized ^{129}Xe ventilation imaging in healthy vol-

unteers and subjects with chronic obstructive pulmonary disease," NMR in Biomedicine, vol. 26, no. 4, pp. 424–435, 2013.

[99] J. Wild, G. Collier, H. Marshall, L. Smith, G. Norquay, A. Swift, F. Horn, F. Chan, N. Stewart, L. Hutchison, et al., "Hyperpolarised Gas MRI−a Pathway to Clinical Diagnostic Imaging (Abstract)," Thorax (BMJ Publishing Group Ltd), 2015.

[100] D. A. Yablonskiy, A. L. Sukstanskii, and J. D. Quirk, "Diffusion lung imaging with hyperpolarized gas MRI," NMR in Biomedicine, vol. 30, no. 3, p. e3448, 2017.

[101] C. Wang, T. A. Altes, J. P. Mugler III, G. W. Miller, K. Ruppert, J. F. Mata, G. D. Cates Jr, L. Borish, and E. E. de Lange, "Assessment of the lung microstructure in patients with asthma using hyperpolarized ^{3}He diffusion MRI at two time scales: comparison with healthy subjects and patients with COPD," Journal of Magnetic Resonance Imaging: An Official Journal of the International Society for Magnetic Resonance in Medicine, vol. 28, no. 1, pp. 80–88, 2008.

[102] G. Miller, T. Altes, J. Brookeman, E. De Lange, and J. Mugler Iii, "Hyperpolarized ^{3}He lung ventilation imaging with B_1-inhomogeneity correction in a single breath-hold scan," Magnetic Resonance Materials in Physics, Biology and Medicine, vol. 16, no. 5, pp. 218–226, 2004.

[103] T. Kubo, Y. Ohno, M. Nishino, P.-J. Lin, S. Gautam, H.-U. Kauczor, H. Hatabu, iLEAD study group, et al., "Low dose chest CT protocol (50 mAs) as a routine protocol for comprehensive assessment of intrathoracic abnormality," European Journal of Radiology (open), vol. 3, pp. 86–94, 2016.

[104] J. MacQueen et al., "Some methods for classification and analysis of multivariate observations," in Proceedings of the fifth Berkeley symposium on

mathematical statistics and probability, vol. 1, pp. 281–297, Oakland, CA, USA, 1967.

[105] R. L. OHalloran, J. H. Holmes, T. A. Altes, M. Salerno, and S. B. Fain, "The effects of SNR on ADC measurements in diffusion-weighted hyperpolarized He-3 MRI," Journal of Magnetic Resonance, vol. 185, no. 1, pp. 42–49, 2007.

[106] T. A. Sorensen, "A method of establishing groups of equal amplitude in plant sociology based on similarity of species content and its application to analyses of the vegetation on Danish commons," Biol. Skar., vol. 5, pp. 1–34, 1948.

[107] S. Hu, E. A. Hoffman, and J. M. Reinhardt, "Automatic lung segmentation for accurate quantitation of volumetric x-ray CT images," IEEE Transactions on Medical Imaging, vol. 20, no. 6, pp. 490–498, 2001.

[108] D. S. Gierada, R. D. Yusen, T. K. Pilgram, L. Crouch, R. M. Slone, K. T. Bae, S. S. Lefrak, and J. D. Cooper, "Repeatability of quantitative CT indexes of emphysema in patients evaluated for lung volume reduction surgery," Radiology, vol. 220, no. 2, pp. 448–454, 2001.

[109] A. Madani, A. Van Muylem, and P. A. Gevenois, "Pulmonary emphysema: effect of lung volume on objective quantification at thin-section CT," Radiology, vol. 257, no. 1, pp. 260–268, 2010.

[110] W. D. Travis, U. Costabel, D. M. Hansell, T. E. King Jr, D. A. Lynch, A. G. Nicholson, C. J. Ryerson, J. H. Ryu, M. Selman, A. U. Wells, et al., "An official American Thoracic Society/European Respiratory Society statement: update of the international multidisciplinary classification of the idiopathic interstitial pneumonias," American journal of respiratory and critical care medicine, vol. 188, no. 6, pp. 733–748, 2013.

[111] P. M. Wong, A. N. Lees, J. Louw, F. Y. Lee, N. French, K. Gain, C. P. Murray, A. Wilson, and D. C. Chambers, "Emphysema in young adult survivors

of moderate-to-severe bronchopulmonary dysplasia," European Respiratory Journal, vol. 32, no. 2, pp. 321–328, 2008.

[112] J. G. Mammarappallil, L. Rankine, H.-F. Chan, N. Weatherley, J. Wild, and B. Driehuys, "New developments in imaging idiopathic pulmonary fibrosis with hyperpolarized xenon MRI," Journal of Thoracic Imaging, vol. 34, no. 2, p. 136, 2019.

[113] D. A. Lynch, J. H. Austin, J. C. Hogg, P. A. Grenier, H.-U. Kauczor, A. A. Bankier, R. G. Barr, T. V. Colby, J. R. Galvin, P. A. Gevenois, et al., "CT-definable subtypes of chronic obstructive pulmonary disease: a statement of the Fleischner Society," Radiology, vol. 277, no. 1, pp. 192–205, 2015.

[114] K. M. Johnson, S. B. Fain, M. L. Schiebler, and S. Nagle, "Optimized 3D ultrashort echo time pulmonary MRI," Magnetic Resonance in Medicine, vol. 70, no. 5, pp. 1241–1250, 2013.

[115] G. R. Washko and G. Parraga, "COPD biomarkers and phenotypes: opportunities for better outcomes with precision imaging," European Respiratory Journal, vol. 52, no. 5, 2018.

[116] D. Liljequist, B. Elfving, and K. Skavberg Roaldsen, "Intraclass correlation−a discussion and demonstration of basic features," PloS one, vol. 14, no. 7, p. e0219854, 2019.

[117] D. Best and D. Roberts, "Algorithm AS 89: the upper tail probabilities of Spearman's ρ," Journal of the Royal Statistical Society. Series C (Applied Statistics), vol. 24, no. 3, pp. 377–379, 1975.

[118] M. Fay and M. Proschan, "Wilcoxon-Mann-Whitney or t-test? On assumptions for hypothesis tests and multiple interpretations of decision rules. Stat Surv 4: 1-39."